A Computational Modeling Approach of Fracture-Induced Acoustic Emission

A Thesis

Submitted to the Faculty

of

Drexel University

by

Jefferson A. Cuadra

in partial fulfillment of the

requirements for the degree

of

Doctor of Philosophy

June 2015

DOCTORAL COMMITTEE

Dr. Antonios Kontsos Chair and Advisor	*P.C. Chou Endowed Assistant Professor in Mechanical Engineering* *Department of Mechanical Engineering & Mechanics, Drexel University*
Dr. Ivan Bartoli	*Assistant professor* *Department of Civil, Architectural, Environmental Engineering, Drexel University*
Dr. Christopher Weinberger	*Assistant professor* *Department of Mechanical Engineering & Mechanics, Drexel University*
Dr. Cara Leckey	*Research Physicist* *Nondestructive Evaluation Sciences Branch, NASA Langley Research Center*
Dr. Matthew McCarthy	*Assistant professor* *Department of Mechanical Engineering & Mechanics, Drexel University*
Dr. Alan Lau	*Professor* *Department of Mechanical Engineering & Mechanics, Drexel University*

DEDICATION

Este logro no lo hubiese alcanzado sin el apoyo incondicional de mi familia, a los que quiero inmensamente y dedico esta tesis y meta trazada. Mi padre, Pedro Alberto Cuadra Cuadra, quien fue el que me enseñó a ver las consecuencias de la vida de una manera positiva; y quien tambien siempre me decía que valorase mis estudios y conocimientos, ya que estos nunca se me serán hurtados. Mi madre, Gleni Betty Montes Romero, tambien tuvo mucho que ver en mis estudios; ya que ella fue la que cultivó e inculcó en mí la importancia del trabajo arduo y el sacrificio a temprana edad, los cuales crearon en mí las bases de un estudiante a quien le gusta sobresalir dando todo su esfuerzo. Quisiera dedicar tambien esta tesis a mi hermano, Fremmy Alberto Cuadra Montes, quien para mí es el símbolo de la fortaleza y ha sido siempre para mi alguien quien admiro y un ejemplo a seguir. Y por último, quiero dedicar este meta de recibirme como Doctor y esta tesis a mi Mamá Goya, Gregoria Romero Mares Vda. De Montes, quien me crió y sembró en mí todos los valores y morales de un hombre de bien, que sin estos no hubiese apreciado y dado todo de mí para alcanzar todas mis metas.

Los quiere de todo corazón,

Jeffer

ACKNOWLEDGEMENT

I'm very thankful to all the people who have supported me in the past four years during my Ph.D. program at Drexel University. First, and most importantly, I would like to thank my advisor, Dr. Antonios Kontsos, for his unconditional and gracious support. He has been more than advisor during these years where he played a crucial role mentoring me, guiding me and inspiring me to push the limits of my capabilities. Undoubtedly, these words cannot express all of my deepest gratitude for him and the great experience and honor I had of working with him. Thank You Dr. Kontsos!

This also could have not been possible without the constant support of my dearest friends. I would like to start by thanking those who were the closest to this work and journey in my career. Dr. Kavan Hazeli, Dr. Prashanth A. Vanniamparambil and Dr. Matteo Mazzotti were more than colleagues and lab mates; they were always an example to follow and friends who guided me and motivated me to be an outstanding professional. From my research group, the Theoretical and Applied Mechanics Group, I would also like to thank Dr. Konstantinos Baxevanakis, Shane Esola, Dani Liu, Brian Wisner and Andrew Ellenberg for their help and numerous encouraging discussions; and for being great friends. I would also like to thank my closest friends who have always being there: Michael Cabal, Johanna Yarleque, Eduardo Mendez, Esteban Mendez, Yohan Seepersad, Marco Janko, Jonathan Campos, Utku Guclu, Selin Sahici, and Aditi Ramadurgakar. I would have not being able to reach all of my career goals without their friendships, supports and encouraging reminders of all my accomplishments in my career.

I would like to also acknowledge my fellowship program the Greater Philadelphia Region Louis Strokes Alliance for Minority Participation (LSAMP) and its directors, Dr. Venice Keene and Dr. Stephen Cox, for believing in me every step of my journey and giving me the opportunity to start my graduate studies at Drexel University as well as the funding support throughout my first two years. Furthermore, I would like to thank the National Science Foundation Graduate Research Program, XSEDE and my advisor at Drexel University, Dr. Tech Kah Lim, for the financial support, continuous advice and several career-related opportunities. I would also like to acknowledge the support from the College of Engineering Computing and Technical Services as well as the University Research Computing Facility at Drexel University for providing me with all the support related to the computational aspect of this dissertation.

I'm extremely proud and honor to be the first in family to obtain a Ph.D. degree which could have not been possible without the unconditional support and encouragement from my beloved family. I would like to thank my parents, Pedro and Gleni, my brother, Fremmy, and my wonderful grandma', Gregoria.

Jefferson A. Cuadra

LIST OF TABLES

LIST OF FIGURES

ABSTRACT

A Computational Modeling Approach of Fracture-Induced Acoustic Emission

Jefferson Cuadra

Antonios Kontsos, Ph.D.

Acoustic Emission (AE) has become a prominent Nondestructive Testing (NDT) technique with capabilities to be used for Structural Health Monitoring (SHM) applications that entail in-service monitoring, detecting damage-prone areas, and establishing damage prognostics of structures. The next generation of acoustics-based techniques for SHM will rely upon the reliable and quantitative characterization of AE signals related to dominant damage mechanisms. In this context, the forward problem of simulating AE activity is addressed herein by proposing advanced finite element models for damage-induced stress wave generation and propagation. Acoustic emission for this purpose is viewed as part of the dynamic process of energy release caused by damage initiation. To form the computational approach, full field experimental information obtained from monitoring the damage initiation process using digital image correlation is used to construct constitutive laws, e.g. traction-separation law, and to define other damage related parameters. Subsequently, *3D* FE simulations based on such experimental data are implemented using cohesive zone modeling and extended finite element method to create an initial failure. Numerically simulated AE signals from the dynamic response

due to the onset of damage are evaluated in the context of the inverse problem of source identification and localization. The results successfully demonstrate material and geometry effects of the propagating source and describe completely the AE process from crack-induced isolated source to transient and steady-state dynamic response. Furthermore, the computational model is used to provide quantified measures of the energy release associated with crack. In addition, the effect of plasticity on simulated traveling waves ahead of the crack tip was investigated and revealed nonlinear interactions that had been postulated to exist. Ultimately, the forward AE methodology is applied to an aerospace structural component to recreate the debonding process and associated stress release propagation. All damage-induced wave propagation simulations presented in this dissertation create a pathway for the quantitative comparison between experimental and theoretical predictions of AE.

TABLE OF CONTENTS

CHAPTER 1: INTRODUCTION

Acoustic emission (AE) consists of transient pressure waves that are released typically due to an irreversible process, for example fracture, and travel within a material or structure in the form of mechanical oscillations [1-4]. This physical phenomenon/process has been the basis for the development of a widely implemented Nondestructive Testing (NDT) method that bears the same name and has been demonstrated to be capable to detect various type of primarily damage sources. Based on its inherent characteristics, the AE method has been classified among the other NDT techniques as passive, in the sense that it does not require active interrogation of the inspected structure by imposing some type of energy and it can be detected by means of passively monitoring a material/structure under their normal operational conditions [2]. Consequently, AE has been demonstrated to have a great potential in real-time monitoring applications for diagnostics and prognostics of materials/structures as well as several manufacturing processes [5-8]. Although the AE method has found use in several applications, current challenges related to the acquisition and interpretation of large AE datasets have limited its suitability for implementation in complex materials/structures subjected to a variety of external loads. An appropriate approach to mitigate and tackle these challenges is the implementation of computational modeling that is capable to characterize and determine inherent properties of an AE source and the associated generated waves. Such computational model that is largely based on related experimental measurements and has key advantages with respect to previously reported approaches is developed, described and studied in this dissertation.

1.1 MOTIVATION

The intrinsic advantages of AE established it as a unique method compared to other NDT techniques for Structural Health Monitoring (SHM) [7-9] and Intelligent Processing of Materials (IPM) [6, 10] applications [5, 11-13]. For instance, current SHM infrastructure maintenance trends revealed the need to transition from periodic inspection to more advanced condition-based evaluations, in order to minimize inspection costs in addition to significantly reduce the actual maintenance time as this relates to service interruptions [14, 15]. Similarly, the needs and challenges faced in aging infrastructure is a topic of research at institutions such as the Air Force Research Laboratory (AFRL), where the concept of "Material State Awareness" (MSA) has been introduced and defined as the process for quantitative materials/damage characterization, regardless of (time and length) scale [12].

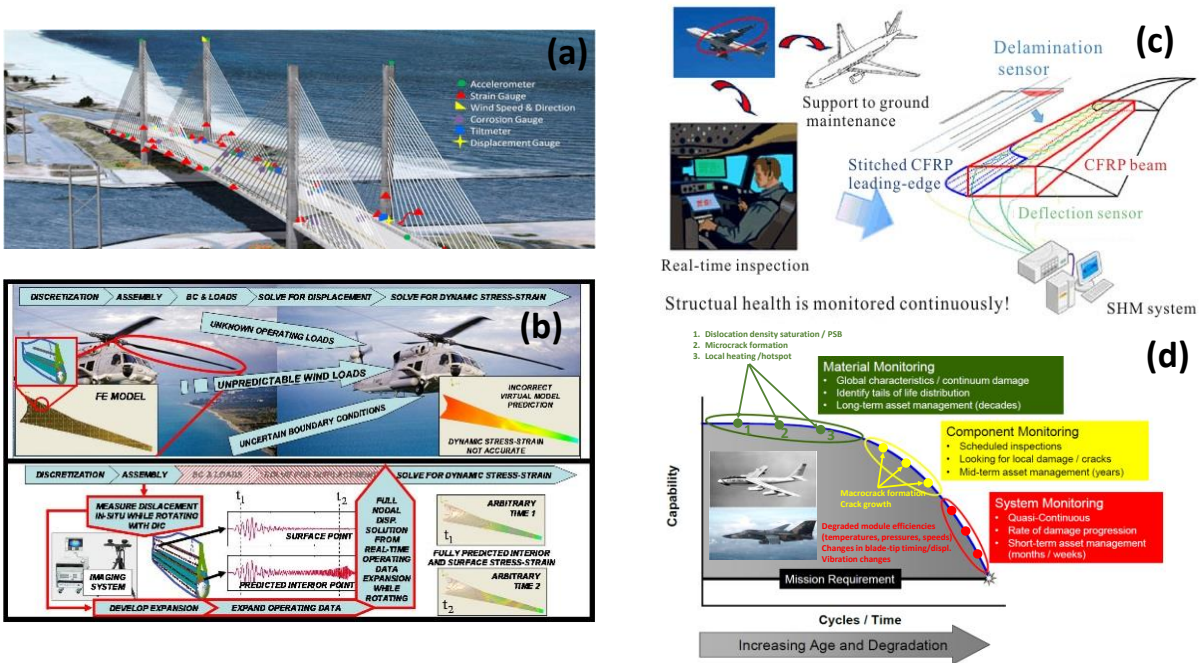

Figure 1.1: (a) Installed fiber optic SHM system on Delaware Bridge [16], (b) dynamic response and system load prediction for SHM of rotorcraft structures [17], (c) SHM of composite material components in aerospace applications [18], (d) MSA concept for different stages of time as defined by DARPA [12]

The MSA vision includes the complete characterization of damage (size, location, etc.) for metals, polymers, ceramics and composites in addition to metrics for reliability, including capability and precision. Although several approaches have been proposed and implemented to achieve such goals, current efforts to use NDT methods in SHM applications are still limited by the conventional approaches employed in periodic inspections, which tend to be costly and result in longer examination periods. Figure 1.1 presents some of the current and possible future NDT approaches applied in components and structures for both SHM and types of damage monitoring along with the current levels of capabilities regarding MSA. The combination of various sensors and sensing techniques for monitoring has been demonstrated but in most cases they still lack the capabilities and proficiency to describe and determine critical stages of components as they are aging or failing. In this context, the favorable characteristics of AE on the aforementioned needs in SHM and MSA applications, include: (i) the fact that it is naturally occurring across length/time scales, (ii) it could detect and locate damage in real time, and (iii) it has the potential for identification and characterization of the nucleation and evolution of damage. These distinctive attributes of the AE method are attractive and suitable for both SHM and MSA tools and applications (e.g. aerospace, mechanical, naval, etc.) since they can be used for: in-service monitoring, intelligent and efficient determination of critical regions for other NDT techniques, overall reduction of maintenance time, and formulation of damage diagnostics and prognostics.

Similar to the suitable attributes for SHM applications, AE is also a promising NDT method for real-time monitoring of various manufacturing forming processes. Specifically, the use of AE could potentially contribute in ensuring high quality products

while minimizing their total cost. This can be accomplished for example by using AE in situ during forming processes where the generated signal could serve to characterize overall the processes and to detect discontinuities or process abnormalities.

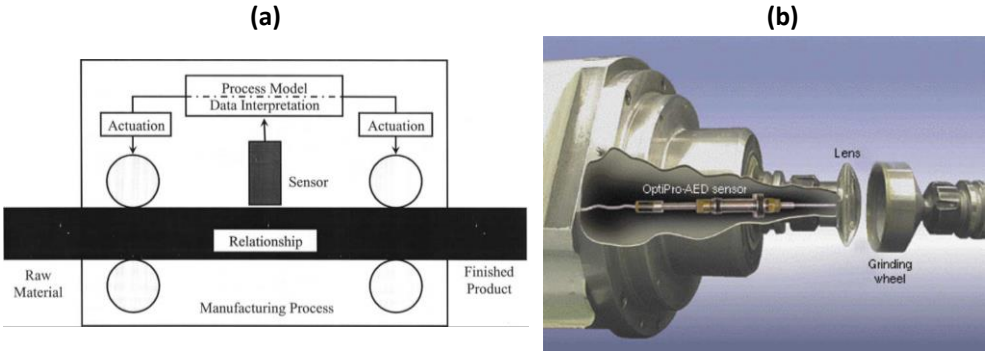

Figure 1.2: (a) Schematic diagram of AE as a monitoring and controlling tool in a manufacturing process. (b) Implementation of AE for fine grinding of precision lenses [6]

Figure 1.2 shows a schematic of AE as monitoring technique in a particular manufacturing process and its use of AE for a grinding process. The applicability of AE has been reported in various manufacturing processes (i.e. mostly forging and grinding processes) including punch stretching, deep-drawing, blanking, forging and grinding [6].

In spite of the advantages of AE and recent technological improvements in both hardware (sensing technologies), and software (signal processing), there are still issues and challenges regarding AE as a reliable NDT technique for SHM. Part of these challenge and difficulties in the application of AE as an advanced NDT method can be attributed to the complexity of the AE process from the source to recorded signal. Figure 1.3 illustrates the entire AE process which includes a signal shaping chain that is capable of altering the frequency content of an original source.

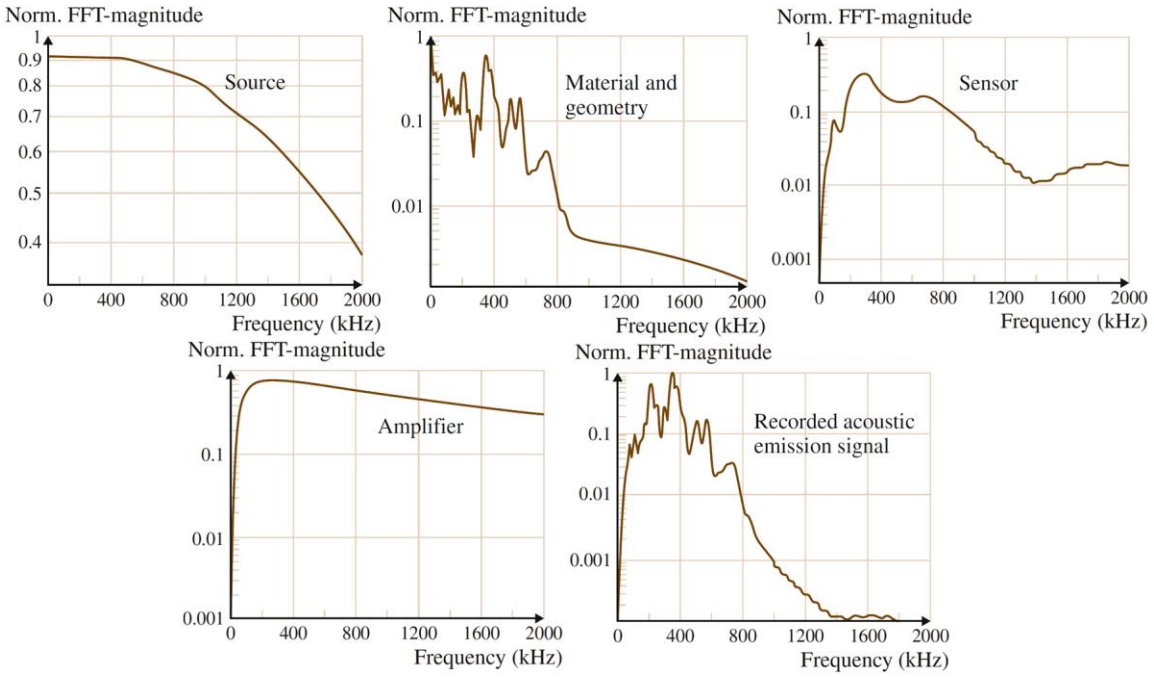

Figure 1.3: Signal shaping chain corresponding to the AE process [4]

Evidently, the modification of the signature of the original signal creates difficulties when attempting to interpret AE sources. In addition to the challenges that exist for a single source, the convolution, in the sense of the simultaneous activation of many sources in the AE experimental methodology creates even more complicated signals which can contain information from a combination of actual sources with environmental noise. Consequently, the AE method is yet to become a reliable tool for both material mechanical behavior characterization and structural health monitoring, due to some major issues associated which can be summarized as:

(i) The insufficient quantitative evaluation and validation of experimentally recorded AE signals.

(ii) The difficulty in interpreting the nature of AE information utilizing source inversion methods (e.g. backward or forward problem).

(iii) The lack of a quantitative deterministic model of the AE process that entirely describes the deformed state at the nucleation of damage, the dynamic characteristics of the source mechanisms, wave effects during media propagation, as well as the interactions and sensitivity of the sensor.

Another reason for the challenges encountered by the AE methodology is attributed to its own advantage of being a highly sensitive technique. However, regardless of the "noise" sensitivity of AE in in-service monitoring, AE can monitor structures over extended periods of time which may potentially assist in exploiting the repetitive nature of events. Consequently, the AE methodology in practice can fall into the categories of probabilistic/statistical or deterministic analysis which are closely related to the concepts of inverse (backward) and forward methods [3, 4, 19], respectively. For instance, the task of classifying unwanted signals (noise) from the authentic (primary) sources, is currently being addressed using advanced signal processing [20-22], statistical pattern recognition approaches [23, 24], as well as data fusion type methods [25-27]. In contrast, the deterministic methodology suggests suitable models to describe and quantify the complete AE process from source to received signal. In addition, accurate AE models simulating realistic waveforms from known source mechanisms will provide a platform to efficiently optimize the interpretation of AE data [19, 28, 29]. Such simulations can also be applied interactively with inverse methods for the determination of optimal placement of AE sensors, the scaling of AE results from laboratory coupons to structures of practical interest, and the recognition of extraneous noise and identification of source mechanisms.

1.2 RESEARCH STATEMENT AND OBJECTIVES

This dissertation presents an integrated computational method that attempts to address, and mitigate the aforementioned difficulties, challenges and limitations in interpreting experimental AE recordings by implementing a forward approach. The approach uses experimental data to construct, validate, and calibrate the numerical models for a specific isolated and targeted damage mechanism. In addition, the computational model is capable to simulate AE due to crack initiation and similar failure mechanisms. In general, forward modeling approaches that simulate primitive AE sources can be useful in: (i) optimizing sensor placement and selection, (ii) quantifying the wave propagation effects from geometrical structural or material features, and (iii) filtering recorded spurious signals (i.e. noise) [30, 31]. The forward modeling approach of AE in this work implements fracture-based methods including a cohesive zone model and the extended finite element method. These methods are used to link the quasi-static to dynamic models by successfully using fracture initiation as an input for transient dynamic analyses. In addition, such models are used to analyze and decompose simulated AE primitive signals for better interpretation and pattern recognition.

In summary the objectives of this dissertation are listed as follows:

- Develop computational models to simulate and characterize AE damage sources based on the concepts and methods of computational fracture mechanics.
- Analyze AE generation and wave propagation in the medium by analyzing both its frequency content and wave effects.

- Identify key AE parameters to discriminate amongst different primary sources of simulated AE primitive signals from different damage sources and geometries.

The results of this dissertation provide source-related AE waveforms in the form of displacement, velocity and acceleration components. These waveforms are analyzed both in time and frequency domains suggesting important information including attenuation, dispersion, geometric spreading, and dominant frequencies pertinent to a particular AE source. In addition, using both the static and dynamic solution, an energy balance analysis is implemented in order to quantify the energy emitted by the source and compared to the actual detected energy. Ultimately, the effect of plasticity on the propagating stress wave is evaluated using controlled sources as a function of distance, time and in the frequency spectrum.

To summarize, the major contributions of the computational approach in this dissertation include:

i. A validated crack initiation fracture model in addition to a debonding damage mechanism using state-of-the-art experimental procedures and computational fracture techniques.
ii. A dynamic computational model driven by the solution of isolated fracture/damage models. The corresponding analysis of such models also resulted in analysis and visualization tools for quantifying and understanding the wave propagation due to a targeted damage mechanism.

iii. The complete analysis of the AE process from generation to propagation which serves as a tool to identify the extracted/computed AE features that are most sensitive/descriptive of the damage process

iv. The development of a methodology to estimate the energy release associated to crack initiation in a quasit-static and transient environment.

v. The linkage of AE to fundamental material processes, e.g. plasticity, in order to deconvolve the AE process for accurately identifying the signature of damage sources.

This dissertation also contributes more generally to the end goal of enhancing the interpretation of AE sources, thus tackling the current challenges faced by both periodic and continuous data acquisition, as well as the sensor sensitivity and selection. Moreover, the methods developed attempt to assist in the identification of damage precursors and in structural damage diagnostics as a complementary tool for signal processing and qualitative source analysis at the initiation of critical stages. Consequently, the reported results are expected to contribute to the development of life prognosis from AE damage parameters which could potentially contribute to reliably retrofit, optimize the maintenance plan, and predict the remaining useful life of structures. It is important to note that the paramount significance of this work is not only to fundamentally understand AE but also to design improved acquisition methods including sensors and sensing procedures, which could assist in addressing the current challenges faced by AE as a NDT method in advanced structural applications.

1.3 THESIS STRUCTURE

In this dissertation, a computational model utilizing a forward AE approach was developed to describe and analyze the complete AE process from source to transient response in the propagating medium. Although this thesis mainly focused on a crack-induced source, the same methodology is also applied to a structure in order to study a debonding-related source as an application. Chapter 2 consists of background material on the AE method. It includes both experimental and modeling information in addition to relevant topics regarding the mechanics of the AE source and wave propagation. Chapter 3 presents the hypothesis of the thesis as well as an overview of the computational approach followed. Furthermore, the details of the integrated method, which includes an experimental procedure and computational approach, are described with brief background material about the techniques implemented in addition to the validation and calibration methodology of the final computational approach for the crack-induced AE model. Chapter 4 includes the description of the crack-induced dynamic model and corresponding results. This chapter also presents the complete analysis of the spatial, temporal and frequency domain calculated waveforms focusing mainly on the wave propagation problem. It also evaluates the effects of attenuation and dispersion. Chapter 5 focuses more on the crack-related AE source. This chapter evaluates and quantifies the energy associated to the disturbance caused by the crack surface creation. Two approaches are presented using the energy balance and energy release rate (i.e. energy flux) for both the static and dynamic analyses. Chapter 6 presents a case study to analyze the effects of the accumulated plasticity associated to the crack initiation problem. In this chapter, controlled signals with certain frequency content are utilized.

Ultimately, by contrasting the undeformed with the plastically deformed state the effects are analyzed in both the time and frequency domain. Chapter 7 is focused on the application of the computational methodology for a debonding source. An aerospace component, referred in the chapter as a stiffener, is studied to determine the AE signatures of debonding. In addition, a wave analysis of controlled disturbances is also evaluated and compared to the results obtained from debonding. Chapter 8 outlines a list of future research topics including multiscale modeling to better understand the AE process, the development of a piezoelectric sensor model or transfer function in order to compare the primitive AE signals with experimental results. Possible extensions of the current of the methodology to multiscale models, development of a sensor model and the novel sensor applications, or materials systems (composite materials) are further discussed.

CHAPTER 2: UNDERSTANDING OF ACOUSTIC EMISSION

2.1 THE ACOUSTIC EMISSION METHOD

Acoustic Emission is a physical phenomenon that occurs within a solid when subjected to an external loading such as mechanical, thermal, etc. AE is formally defined as the transient release of energy in the form of traveling stress waves in a material when subjected to external load due to mostly irreversible changes [2, 3, 32-36], associated to damage sources such as plastic deformation, phase transformation, fracture, delamination, debonding and others [34, 37, 38].

The origins of AE testing are closely related to the etymology of the word "acoustic" which refers to hearing. Structural failure for centuries has been associated to the sounds preceding it, which in essence is a precursor of damage. For instance, the cracking sound of a tree branch right before breaking and the rupture sounds of thin ice both warn impending failure and provide information about overall structural integrity [37]. AE is considered to be a passive technique compared to other NDT techniques, such as ultrasonic, and radiographic, among others. Active techniques rely on the external application of "interrogating" energy while AE detects the internal energy initiated within a material medium. AE is analogous to the concept of seismic waves or even to that of surface waves in water produced by the disturbance caused by a rock in a calm pond. For instance, Figure 2.1 depicts these concepts, as the stress waves caused due to the growth of a flaw move radially towards the boundary, i.e. a surface wave packet (Rayleigh or Lamb wave type) is created and then recorded by the AE sensor. Similarly, AE can be seen as the small amplitude (in the order of nm) vibration of material points in a solid

with which have high frequencies within range of 10 kHz to over 1 MHz (i.e. they are practically above the human audible range) [32, 36, 38].

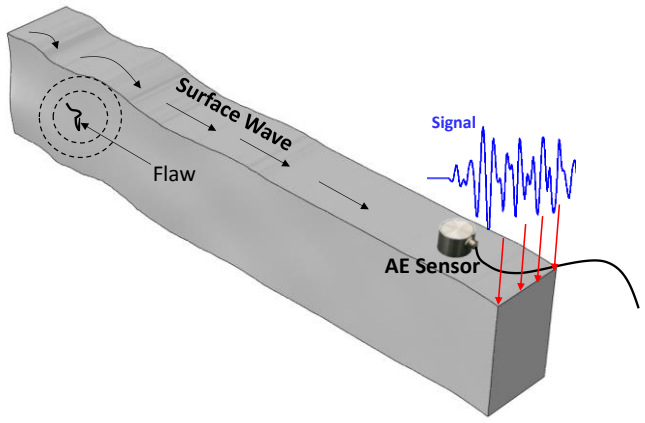

Figure 2.1: Schematic representation of the Acoustic emission process

Such surface mechanical vibrations are typically captured during testing by a variety of sensors e.g. piezoelectric, which convert them to electrical signals that are recorded by an appropiate data acquisition system. The signals obtained require postprocessing and analysis depending on their source location, voltage amplitude and frequency content; postprocessing includes the implementation of digital signal processing tools in order to extract critical parameters and features associated with particular sources.

The establishment of AE as a NDT method is attributed to the pioneering work performed by Joseph Kaiser in the early 1950s, who regardless of earlier studies of stress and sound waves sources was capable to link AE damage structural integrity of metals [2, 39]. By the 1960s, crack growth started to be extensively investigated and advances in technology led AE to become a more established NDT technique. Some of the first studies of AE included deformation tests of metals including the so-called “tin cry” using electronic transducers developed by Kaiser [2]. Similarly, Kaiser’s work extended to

other materials under deformation including zinc and steel where he recorded and detected the emitted sounds. Such investigations proved that AE is irreversible, and due to these contributions this effect is referred to as the *Kaiser effect* which is further explained in Figure 2.2. The *Kaiser effect* basically shows that when the load on a material/structure is increased from the value of B to D, AE activity is measured. However, as the material is unloaded from D to E and no AE activity is produced until the value of load when reloading is higher than the previously maximum load (point D).

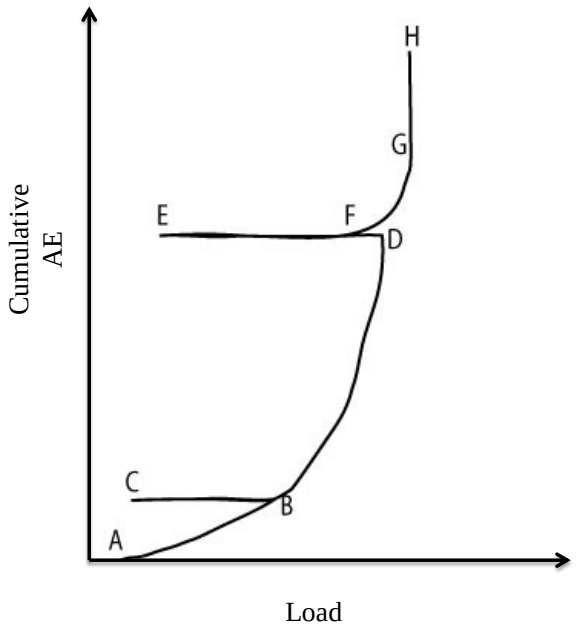

Figure 2.2: Kaiser Effect [39]

It was later found that less homogenous materials (e.g. composite materials, and anisotropic materials) subjected to fatigue conditions do not necessarily follow the Kaiser effect. For these reasons, the Felicity Ratio, also known as Modified Kaiser effect was first studied by Dunegan et al. in fatigue and by Fowler when testing fiber reinforced plastics [40, 41]. The Felicity Ratio, which has been mainly used as a type of damage index for life prognosis, is defined as the load ratio between the load value when AE

starts in reloading over the previously known maximum load for emissions [32, 33]. The smaller the Felicity Ratio is, the more damage occurs in the inspected material/structure.

2.2 EXPERIMENTAL METHODOLOGY

AE testing provides the dual advantage of being both a method for real time monitoring applications and an engineering tool to capture stress waves even from inaccessible locations. Furthermore, the implementation of multiple transducers/sensors and the use of source location algorithms allow calculations related to the location of primary AE sources. Multiple sensors are typically used to estimate the exact location of the defect producing AE activity using triangulation techniques. Moreover, the dynamics of the damage process can also be tracked through the monitoring of changes in features related to AE signals, typically consisting of parameterized time series of voltage values. Estimates of remaining life have been suggested in the prognostics part of the method, a fact that decisively sets apart AE as a NDT method which also qualifies for SHM applications.

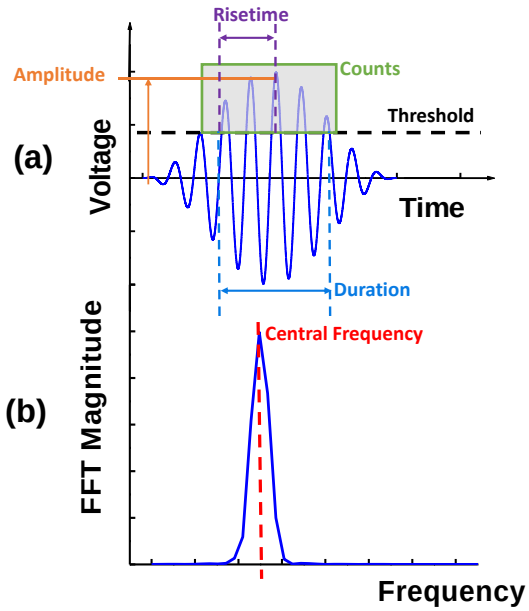

Figure 2.3: AE features on a waveform

Overall, AE has been well established as a prominent NDT technique and has been used for various applications including fatigue crack growth monitoring [42, 43], material characterization [44, 45], debonding in composite structures [46], wire breaks in bridge cables [47] and failure mode characterization in fiber reinforced composites [48-50]. There are various AE features which can be used for analysis of the information recorded. These features include emission counts, rise time, peak amplitude, duration, and energy. Figure 2.3a shows some of these features. In addition, other features in the time domain are also extracted such as energy, counts to peak, absolute energy etc. Furthermore, the acquired AE waveforms are typically also analyzed using Fast Fourier transforms (FFT) to extract frequency domain characteristics, such as the frequency centroid, and peak frequency, values which are then used to identify the AE sources in the material, as shown in Figure 2.3b. Furthermore, emissions from AE sources can be categorized as either transient/burst-type or continuous waveforms. Continuous waveforms are produced by rapidly repeated processes such as machine vibrations, fluid flow and continuous friction between surfaces. Some characteristics of such waveforms are the fact that their amplitude and frequency fluctuates without the signal ending, as shown in Figure 2.4.

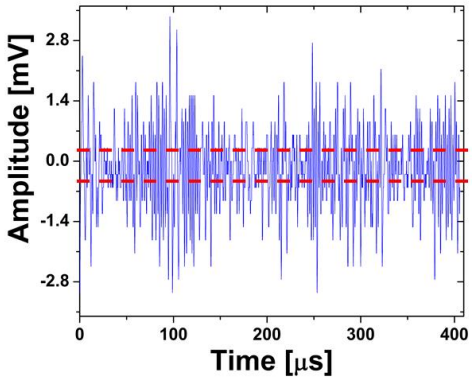

Figure 2.4: An example of a continuous waveform in AE

Burst type waveforms are typically generated by abrupt changes in a material/structure such as crack initiation. Burst-type signals are identified by their obvious start and end, while they evidently differ from the "noise" type continuous signal by their characteristic of sharp increase of amplitude (i.e. small rise time). Figure 2.5 depicts a burst-type signal.

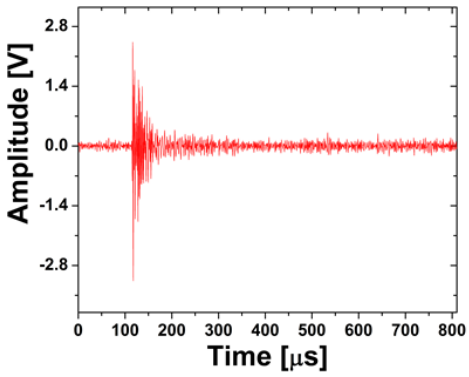

Figure 2.5: An example of a burst-type AE waveform

One of the basic AE acquisition parameters is the threshold, also referred to as the voltage threshold. This parameter indicates to an electronic comparator the voltage amplitude level at which the signals should be recorded and it is necessary for disregarding unwanted noise. Based on the definition of the threshold, the AE counts can

be obtained by determining the number of times the waveform exceeds it. In addition, the AE signal amplitude can be measured by reading at the maximum absolute peak value in the voltage-time waveform. This measure is usually reported in decibels (dB). Equation (2.1) shows the conversion used between voltage and dB

$$A = 20\log\left(\frac{V}{V_{ref}}\right), \tag{2.1}$$

where A is the amplitude in dB, V is the peak voltage, and V_{ref} is the reference voltage which is typically in the range of 1μV (i.e. Voltage generated by 1 mbar pressure of sensor surface). Other time domain parameters include the duration and the rise time which are the time from first to the last threshold crossing and the time it takes to reach the peak value, correspondingly. Other parameters are calculated also from the recorded waveforms such as the signal strength, the Measured Area under Rectified Signal Envelop (MARSE), and energy. For instance the signal strength is the area under the envelope of the linear voltage signal and can be calculated by:

$$S_o = \int_{t_1}^{t_2} \frac{1}{2} f_+(t)dt - \int_{t_1}^{t_2} \frac{1}{2} f_-(t)dt \tag{2.2}$$

in which the functions of time f_+ and f_- refer to the positive and negative signal envelope, respectively, while t_1 and t_2 are the time at first and last threshold crossing. The signal strength is closely related to the energy of the hit which is possible to trace back to the energy of the source (e.g. the energy release from a fracture process). Similarly, the MARSE can be expressed as,

$$S_r = \int_{t_1}^{t_2} \frac{1}{2} f_r(t)dt\,, \tag{2.3}$$

by defining a rectified envelop function f_r which is typically an approximation of the signal strength S_o. Among the various signal measurement parameters frequently used to describe a burst type acoustic signal, MARSE is a measure of both amplitude and duration. Experimentally, this parameter is less dependent on threshold settings as compared to counts, hits and duration. Different than the other two integrals, the AE signal energy is also classically measured for burst-type emissions and reported in joules or values which can be expressed in logarithmic form such as dB. The AE signal energy E_t as defined in,

$$E_t = \int_{t_1}^{t_2} \frac{1}{2} f_+^2(t)dt - \int_{t_1}^{t_2} \frac{1}{2} f_-^2(t)dt\,, \tag{2.4}$$

From (2.2) to (2.4) the function f is assumed to be continuous; however, all of these formulation can be implemented discretely in order to use them for waveforms data sets. Other AE definitions which are also useful include the sensor hit and AE event which correspond to the detection/measurement of an AE signal coming from a single and at least two channels, respectively. Changes in the values of these features have been directly related to the severity of damage induced in the material/structure, and they have been used for the development of damage indices in life prognosis. Correlations between extracted AE features such as counts, count rates, amplitude, absolute energy and damage parameters including crack-tip stress intensity factors and plastic region have been proposed and supported by the use of e.g. microscopy [26, 51, 52]. Furthermore, the use of signal processing and pattern recognition techniques coupled with fracture mechanics

have been used to formulate empirical equations relating, e.g., the number of AE counts with the stress intensity factor, as shown in Equation (2.5) [32, 53, 54].

$$\sum \#Counts = AK^m \,, \tag{2.5}$$

where K is the applied stress intensity, A is a proportionality constant and m is an empirical exponent. In addition, certain changes in the recorded/extracted/computed AE features have been also associated with the formation of a plastic zone ahead of a crack tip. Specifically,

$$V_p = B\sum \#Counts \,, \tag{2.6}$$

where V_p is the volume of the plastically deformed material, and B is a proportionality constant.

AE testing is a promising technique to monitor damage in complex and inaccessible sources since it can track in real time the various damage and failure mechanisms active under different loading conditions. In addition, AE counts have shown to be closely related to the crack growth and dissipated energy under fatigue conditions in which the sudden increase of activity directly relates to the final life stages. AE has long been applied to identify the initiation and development of damage in various materials and structures. In fact, the implementation of AE-based NDT has proved to be valuable for material behavior characterization [23, 45, 55-58], damage identification [21, 26, 31, 58-61], as well as for predicting the progressive failure and estimating the remaining useful life of material and structures [58, 62-65].

Similarly the AE time waveforms may be further analyzed in combined time and frequency domain using analyses for example the Wavelet Transform (WT). As an alternative approach to the interpretation of acoustic emission signals, the time-frequency behavior has been analyzed by a Short Time Fourier Transform (STFT). The following paragraphs will include a brief introduction of the techniques available and a corresponding comparative analysis. It is important to start from the definition of the Fourier-Transform (FT) which is used to convert AE waveforms from the time to the frequency domain. The FT can be expressed in a continuous form as

$$F(\omega) = \int_{-\infty}^{\infty} f(t) e^{-i\omega x} dt\,, \tag{2.7}$$

where *f(t)* is a continuous function of time and ω is the circular frequency (i.e. $f_{(Hz)} = \omega/2\pi$). Equation (2.7) can be formulated also discreetly by:

$$F(\omega_n) = \sum_{k=0}^{N-1} f(t_k) e^{-i\omega_n t_k},\ n = 0,1,2,...,N-1, \tag{2.8}$$

where $\omega_n = 2\pi n/T$ for a given sample window T and number of sampling points *N*, and t_k is the sample points (i.e. $t_k = k\Delta T$). In order to increase the computational efficiency, the Discrete Fourier Transform (DFT) in (2.8) can be solved using the Fast Fourier Transform (FFT), which is an effective algorithm that reduces the computational time from N^2 to $N\log_2(N)$, also referred to as the Butterfly algorithm. Consequently, the FFT algorithm was implemented for all numerical waveforms obtained in this dissertation. For correctness and implementation the algorithm requires both a sufficient sampling rate and for the data to have 2^n points (which can be zero padded when the data set size is not

of a power of 2). The minimum sampling ΔT can be defined by the Nyquist-Shannon sampling theorem and written as [66]

$$\Delta T_{\min} < \left(2(f_{\max} - f_{\min})\right)^{-1}, \tag{2.9}$$

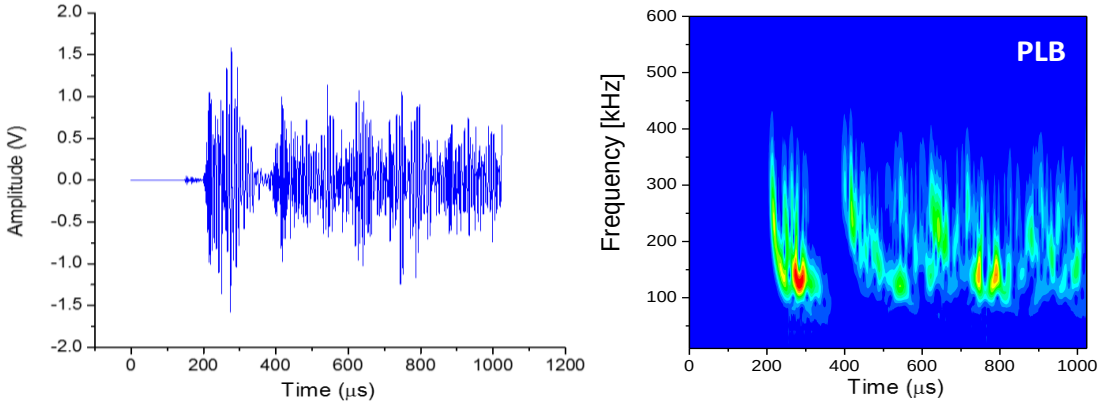

Figure 2.6: Wavelet analysis of AE time waveform from a pencil lead break (PLB) source in aluminum alloy plate [67]

The FFT provides an overall idea of the dominant frequencies in a given waveform; however, it is not sufficient to describe the evolution of those in time. Consequently, the time domain analysis may be implemented by the aforementioned techniques including the SFTF and/or WT, which are extensions of the FFT while it is capable to express the frequency as functions of time. Figure 2.6 shows an example of the WT for characterizing a particular time AE-related waveform in both time and frequency domain. This approach basically alters the temporal resolution and is adapted to a given frequency resolution. It is based on the concept of using a suitable scaled function for convolution at each point in the time-frequency domain. Such scaling functions, also called wavelets, are characteristic of a specific prototype-function known as mother-wavelet. Figure 2.7 shows the adaptive resolution in a WT compared to an equally distributed time-frequency resolution in the STFT approach.

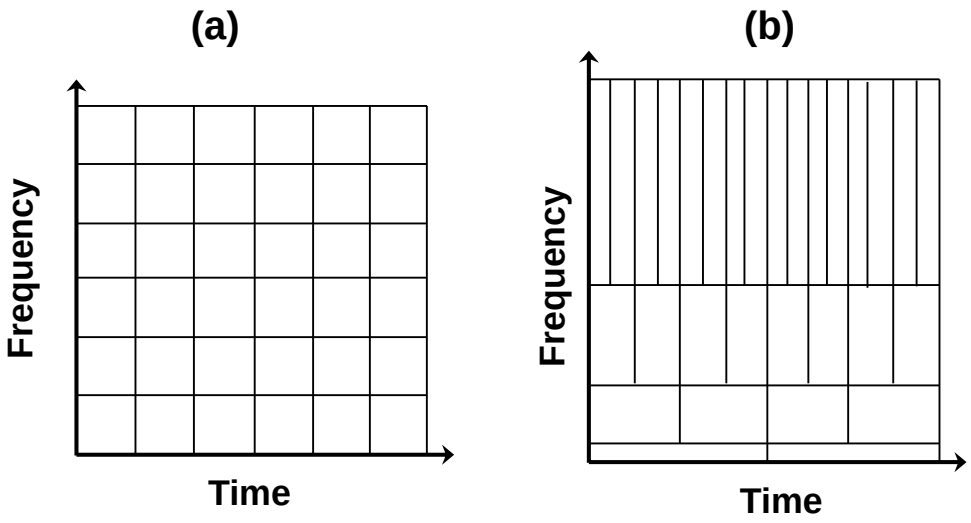

Figure 2.7: Frequency-time resolution for (a) STFT and (b) WT

It is important to note that the WT is more appropriate to transient/burst-type signals since the resolution at higher frequencies is increased to improve temporal accuracy (i.e. applying small wavelengths), while at lower frequencies the resolution is decreased to improve frequency accuracy. In the case of the STFT, the concept follows the idea of calculating a FFT distribution in time windows. In practice, the waveform is convolved with a Gaussian window or Hanning Window to remove the waveform information outside the time interval spanned by the window. Subsequently, the FFT is calculated for that window which is one distribution in the entire intensity contour. To achieve a continuous (i.e. quasi-continuous) intensity contour, the window is shifted in the time axis in order to obtain a FFT distribution for a given time slot. Although, this process results in a discrete time and frequency content, the dominant time-frequency can be reflected in the intensity contour plot. The two determining factors for such discretization are the window size and the finite frequency resolution.

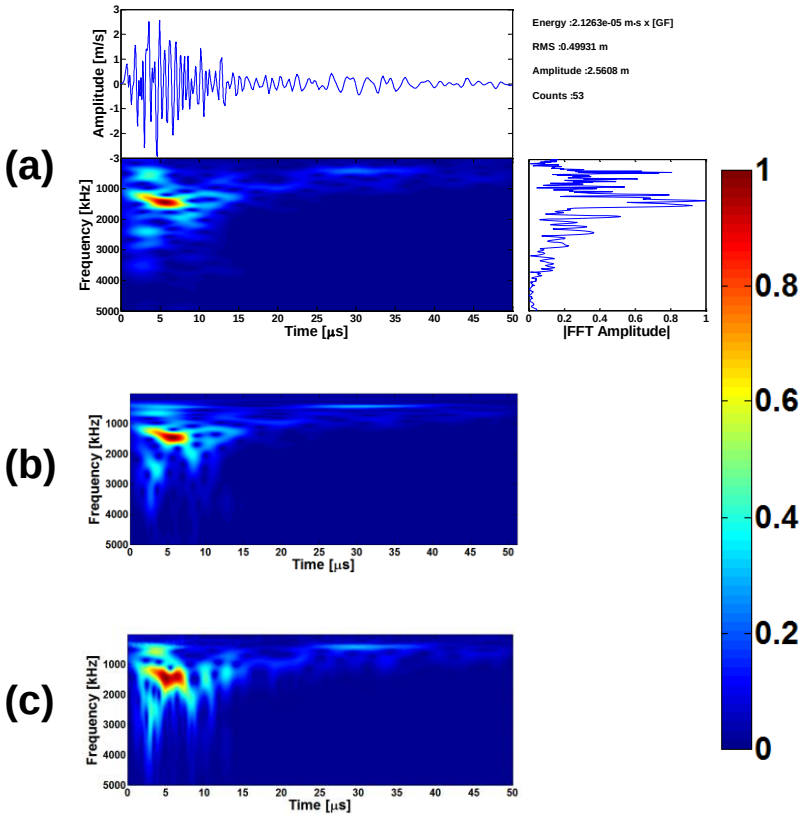

Figure 2.8: Comparison of frequency-time domain methods using (a) STFT, (b) WT with Morlet and (c) Garbor mother-wavelet for simulated waveform

Therefore, the time-frequency analysis is subsampled in a rectangular-type array as shown in Figure 2.7a. Although, there has been studies that show the WT and similar methods [68-72], such as the Choi-Williams Distribution, tend to have more accurate results and refined frequency-time domain resolution, this dissertation solely uses an adapted method for STFT. In this approach, the window size is fixed while the waveform is linearly interpolated in the time domain without affecting its dominant frequencies increasing in this way both temporal and frequency resolution. Figure 2.8 shows the three frequency-time distributions calculated with STFT and WT. The WT was applied using two mother-wavelet. It can be observed that one of the differences between the WT and the STFT distributions is at high frequencies which shows to have a

constant intensity above 2 MHz. Since the best validation method for the frequency-time content was the FFT itself, it was another reason to exclusively compute such distributions using the STFT. These wave analyses were performed using a customized code presented and described in Appendix B.

Prior to selecting and evaluating AE parameters, the implementation of the AE experimental methodology holds an important role to acquire data for post-processing. AE has the inherent advantage of being sensitive and the disadvantage of measuring unwanted data [4, 8, 73]. Consequently, the success of AE information relies strongly on the efficiency of the experimental setup and adjusted acquisition parameters to aid the post-processing analysis which can result in erroneous conclusions. The wide range of NDT techniques commonly used to characterize and evaluate the state and integrity of structures, components or materials implementing various methods of analysis, offers the possibility of coupling two or more of them to improve and validate their results. Along the same lines, each technique faces some limitations including material type, limited surface access, high sensitivity to noise, complex geometry and others. Overall, AE has many advantages for real time inspection of structures in addition to being able to discriminate the stages of both nucleation and growth of damage. Such characteristics align with the main objectives of SHM and have established AE as prominent technique for SHM applications. Although unwanted noise may be high during in-service monitoring, the fact is that monitoring can still be performed over extended periods of time. Therefore, AE in SHM can be implemented seeking the repetitive nature of events that may occur during service of a structure or component. In fact, AE falls into two categories, namely probabilistic or deterministic which stem from the approach(es) implemented. The

simultaneous use of several NDT methods therefore could potentially aid to mitigate related challenges and limitations for effective SHM. For instance, a hybrid acoustics framework could be the integration of non-contact full field optical techniques that can serve both as an independent monitoring technique and also provide visual and quantitative evidence to the unknown AE signals generated during a specific and targeted source [67]. The coupled methodology should be based on the extraction of damage-sensitive features and the successful data fusion of heterogeneous information for robust damage detection in order to achieve and address the aforementioned restrictions. For these reasons, NDT parameters and calculated features are commonly utilized as statistical variables and correlations with damage are established by using several approaches. Among these statistical tools and techniques, novelty detection methods have been extensively used in SHM. Novelty or Anomaly Detection [74] establishes whether or not a new configuration of a given system (in this case the structural component under observation) is discordant or inconsistent from the baseline configuration, which consists of an existing dataset (or patterns) that describe the normal operative conditions of the undamaged component. Examples of methods for novelty detection include: outlier analysis [74, 75], probability density estimation, and artificial neural networks [67, 76]. Even though NDT hybrid setups could essentially mitigate the challenges and limitations of the AE technique, the end goal is to minimize the equipment footprint and complexity (stage, data acquisition, power requirements, etc) in SHM applications [9, 14, 77, 78]. As a result, the hybrid approach remains useful for the initial step of cross-validating and enhancing the interpretation of the information from AE.

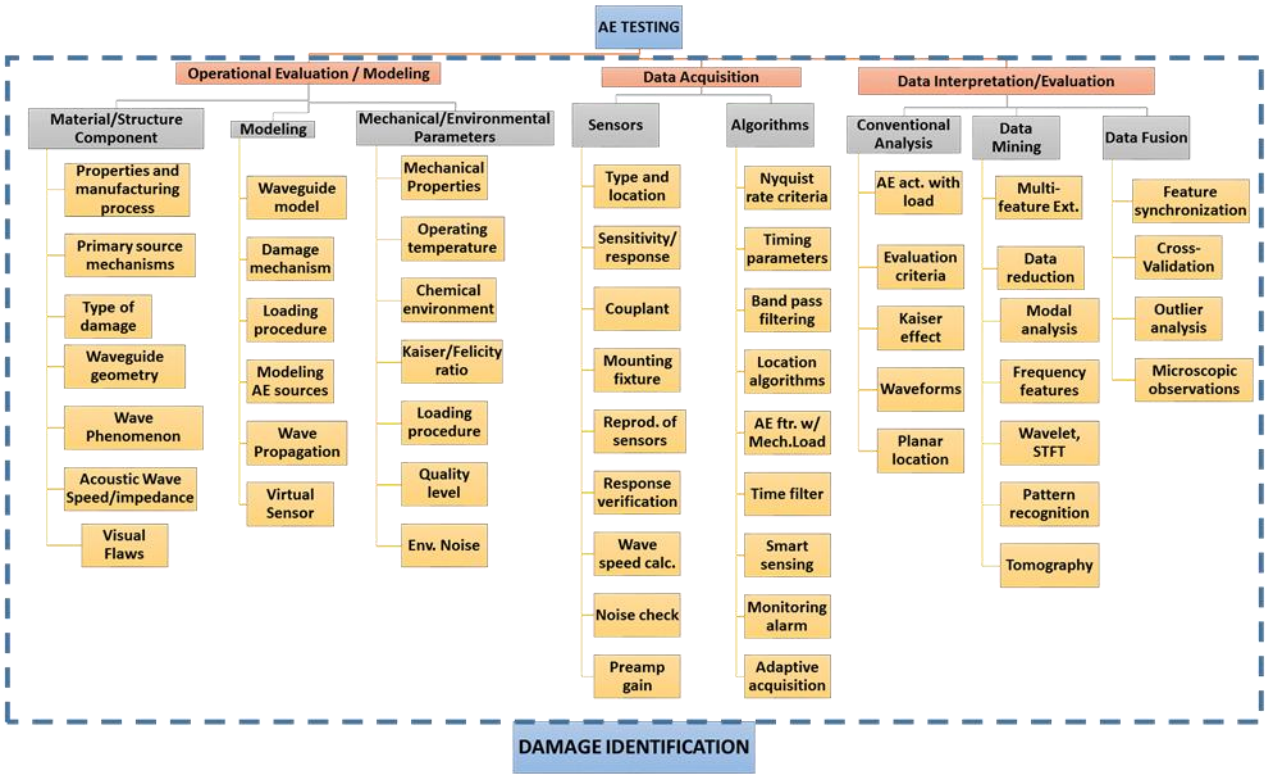

Figure 2.9: AE testing methodology [79]

In summary, the AE testing methodology for damage detection essentially entails identifying critical AE features, indices and innovative correlations for source mechanisms implicating the structure or material service conditions. Figure 2.9 shows a broad overview of the complex experimental methodology and includes the effective integration of both software and hardware approaches to reliably identify critical damage. It is important to note that the computational method in this dissertation offers an additional component to address the issues and improve both the interpretation and implementation of AE in real-time service applications.

2.3 MODELING METHODS

Acoustic emission is intrinsically related to wave propagation following generation from a source. Consequently, theoretical and computational modeling in relation to AE can be

divided into two problems, one related to evaluating the source and the latter dealing with AE-induced wave propagation. The numerical and analytical models found in literature consist of dynamic analyses of stress wave propagation which corresponds to the transient response of elastic media to simulated AE sources. One approach that was implemented intuitively to solve the wave propagation problem due to a source was the theory of elastodynamics based on the use of Green's functions [80-82] in semi-infinite media. Specifically, in an isotropic medium, appropriately defined Green's functions can be used to solve analytically the displacement at any point due to an arbitrary applied force. The displacement field can be defined in terms of point force F_0 and the Green's function G_{ij} for continuum body with surface Γ and volume Ω as the one shown in Figure 2.10.

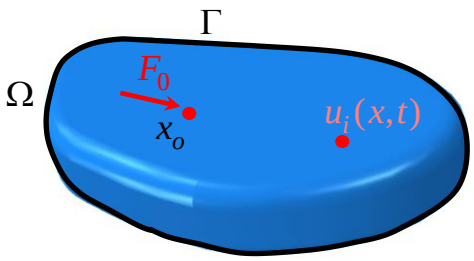

Figure 2.10: Continuum body subjected to a point Force at x_0

Using Helmoltz potentials and solving for the Green's function, the displacement field due to a point force in the x_1-direction for the Cartesian coordinate system can be expressed as [83, 84],

$$u_i(x,t) = \frac{1}{4\pi\rho}\left(\frac{\partial^2}{\partial x_i \partial x_1}\frac{1}{r}\right)\frac{1}{r^3}\int_{r/\alpha}^{r/\beta}\tau F_0(t-\tau)d\tau + \frac{1}{4\pi\rho\alpha^2}\left(\frac{\partial r}{\partial x_i}\frac{\partial r}{\partial x_1}\right)F_0\left(t-\frac{r}{\alpha}\right) - \frac{1}{4\pi\rho\beta^2}\left(\delta_{i1}\frac{\partial r}{\partial x_i}\frac{\partial r}{\partial x_1}\right)F_0\left(t-\frac{r}{\beta}\right), \quad (2.10)$$

where the ρ, α, and β are the material properties and r is magnitude of the position vector having x_0 as local origin. This formulation was then implemented by Rice [85] for microcracking and slip, by using the moment density tensor as the general representation of the AE event. Similarly, the work by Ohtsu and Ono for both the inverse/backward [80] and forward [29] problem introduced new approaches on how to use the Green's function both analytically and experimentally. A common empirical method to extract the Green's function between two points is, (i) via a direct pulse echo measurement, (ii) by using mathematical spectral methods, (iii) or via passive methods between two points using the cross-correlation approach. Other methods to extract the Green's function have included the work of Derode et al [86] who provided a direct physical interpretation of the development of the exact Green's function and the role of scattering in the reconstruction of the Green's function from far-field correlations. Furthermore, in the efforts of acquiring the Green's Function, Wapenaar et al. [87] evaluated and contrasted the principle of time-reversal and Rayleigh's reciprocity theorem, where the time reversal implemented the superposition principle in a homogenous medium, while the Rayleigh's reciprocity theorem utilized the equation of motion and the stress-strain relation in the space-frequency domain to obtain the Green's Function. In plate-like structures, AE waves are dominated by guided Lamb waves for which the signal reflections from the boundaries traveling in different modes are considered and correspond to more practical

applications. In this context, Prosser et al. [30] utilized and compared two different approaches to model AE waveforms in thin plates, including the Mindlin Plate Theory (MPT) and the Dynamic Finite Element Method (DFEM). The two approaches were implemented to model the flexural mode component of a simulated out of plane AE source in both isotropic and anisotropic plates. The resulting out-of-plane displacement w was formulated as:

$$w(x,y,t) = \frac{4P}{\rho hab}\sum_{n=1}^{\infty}\sum_{m=1}^{\infty}\frac{\sin\alpha_n x \sin\gamma_m y \sin\alpha_n \xi \sin\gamma_m \zeta (1-\cos\beta_{nm} t)}{\beta_{nm}^2}, \tag{2.11}$$

where P is the load amplitude of the step function, α_n and γ_m are geometrical factors and β_{nm} is the frequency for the given normal mode that depends on material properties. Some discrepancies were observed in the wave propagation at longer time intervals which were attributed to the differences of the boundary conditions for the two approaches and their corresponding signal reflections. This work however presents evidence that the DFEM approach has better agreement with experimental measurements, as formulation was based on exact linear elasticity providing all modes. On the other hand, the MPT approach was suited mainly for flexural modes at relatively low frequencies, where the basic assumption that the mid-surface plane remains straight is sufficiently accurate. In the case of viscoelastic plates, Giordano et al. [88] presented a model for AE wave propagation and predicted the displacement at a certain location based on the ray theory. In this approach, the displacement response produced due to a longitudinal wave generated at a certain distance from the source was assumed to be a superposition of the different rays produced by reflection at boundary surfaces.

Furthermore, Minozzi et al. [89] introduced a lattice model to study the AE process associated with the dynamic fracture in a disordered medium. Specifically, a *2D* lattice was subjected to mode III type loading and the resulting accelerations were captured at various locations. The cumulative AE energy calculated based on acceleration waveforms revealed a direct power relationship with the total number of disbonds (internal damage) in the model. Moreover, the acoustic energy distribution was noted to decay as a power function independent of the loading rate. Along a similar direction, Sause et al [20] stated that source radiation direction and the elastic properties of the medium cause distinct changes in the generated waveforms. Sause further reported that in isotropic media, the orientation of the in-plane sources produce a symmetric S_o wave mode along the normal to crack surface, while as the source sensor angle varied, the contributions of the S_o wave mode compared to the A_o wave mode remained constant.

At the atomistic level, Landa et al [90] performed wave propagation simulations due to various AE sources at the crack tip using a Molecular Dynamics (MD) method. To this aim, a single edge notch sample was modeled and loaded in mode II and the AE wave propagation due to eight local atomistic nodes was analyzed. Initially, scattering of the waves produced due to the loading process were observed at the crack faces. However, as the sample was further loaded, the waves produced by each of the eight atoms due to the crack extension were seen to interfere with the initial waves, In addition, the distances between each wave front were proportional to the time it took for the crack to grow through the atoms. It was noted that the waves produced by the crack extension were characteristic of very high frequency pulses. Actually, an important assumption that limits the contributions to AE by these models is the simplification of the simulated

source which is assumed to be a point or force/displacement excitation as shown in Figure 2.11.

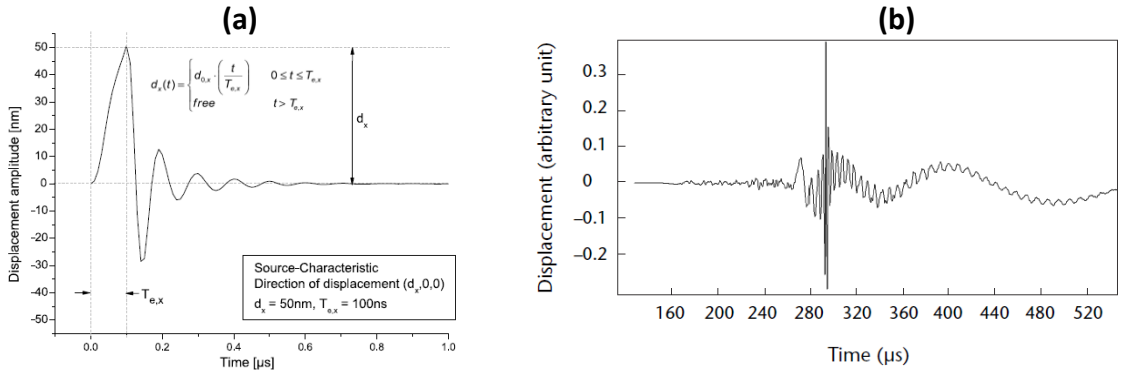

Figure 2.11: (a) Displacement-based function and (b) experimentally obtained excitation associated to a crack-induced AE source [2, 20]

Based on either an inverse or forward modeling approach using point or coupled sources [29, 80, 91], other investigations attempted to link AE from a damage source problem with the associated wave propagation. For example, Holian et al. [92] utilized a parallel MD model to study stress waves emitted by fracture at the atomic scale. This model used a seam crack that allowed to study fracture at the atomistic level, as well as its dynamic response due to the energy release from the crack growth. The interatomic potential used included a cohesive energy component to determine fracture between particles in Mode I. Figure 2.12 depicts the results obtained by Holian et al. for the atomistic fracture model.

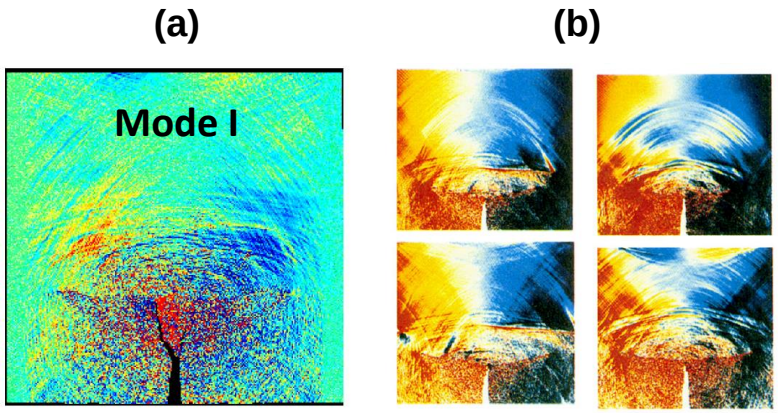

Figure 2.12: (a) Crack growth simulation results using MD, (b) in-plane velocity contour evolution as wave propagates due to crack initiation

Similarly, an investigation of microstructural fracture and stress wave propagation in *3D* in bcc iron crystals by Hora et al. [93, 94] integrated results from MD simulations to a continuum finite element model. In order to simulate fracture, the MD model applied concepts of linear elastic fracture mechanics. Critical parameters near the crack tip were extracted from the MD such as velocities and bond forces and then imposed as initial and boundary conditions in the continuum model. The final results for both the MD and the finite element models are illustrated in Figure 2.13.

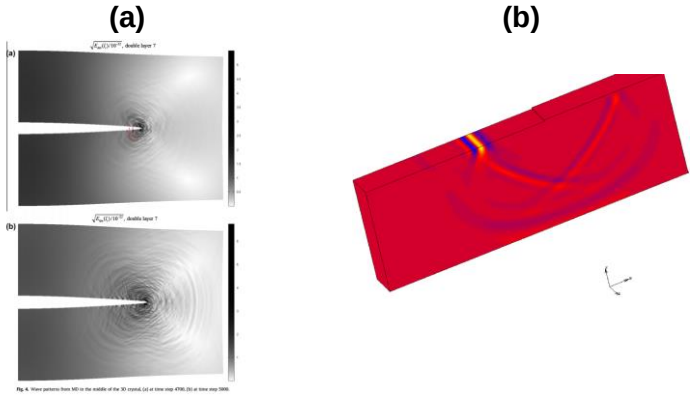

Figure 2.13: (a) Scaled kinetic energy map at two transient time instances during wave propagation for atomistic crack model and (b) velocity contour showing Rayleigh waves for continuum model

This model used the bonding forces from the MD simulation in order to couple them to the continuum scale. The MD simulations showed that the 3D cleavage-type crack initiation produces emissions. This model further demonstrated that the highest emissions are formed due to stress relaxation at the crack front after crack initiation. The normal residual forces coupled by MD in the crack plane and the associated wave patterns are illustrated in Figure 2.14.

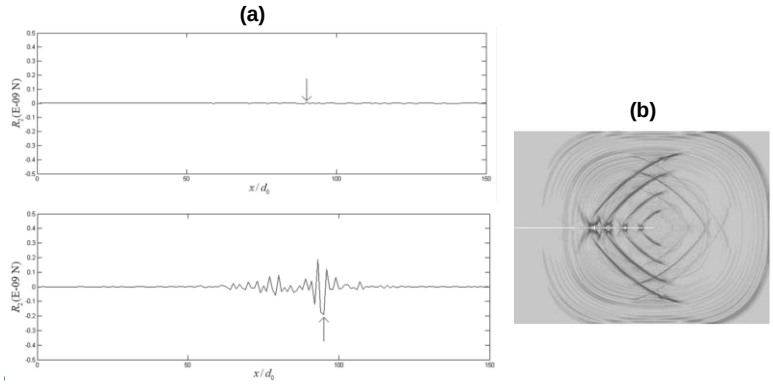

Figure 2.14: (a) Force-time evolution before and after the crack initiation (arrows denote the crack front) and (b) wave patterns plotted by the velocity contours

Similarly, the continuum simulations show that Rayleigh waves can also be generated at certain planes, which agreed with expectations according to continuum analysis. In the context of forward AE modeling, Wilcox et al. [95, 96] have attempted to implement a deterministic modular AE model using analytical formulations and finite element methods , which could potentially aid SHM applications by predicting the time waveforms at a sensor. The results that the model can be used to investigate the performance of probabilistic tools use for AE data classification. Recently, at the microlevel Sause et al. [97] introduced a model for micro-fiber and matrix failure implemented using the finite element method. The model included a cohesive-like interface in a fracture plane determined from experiments, as shown in Figure 2.15.

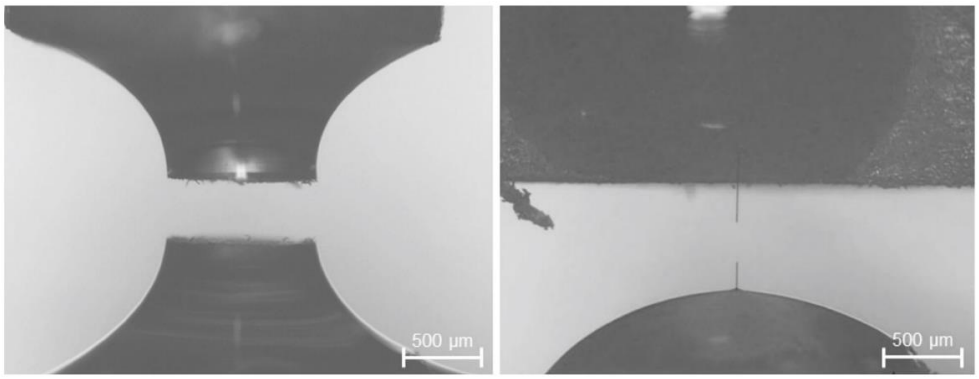

Figure 2.15: Microscopy image for matrix (left) and fiber (right) fracture [97]

The model linked the initial opening to the dynamic response. The results of the micro fracture model were compared to experiments using an acoustic sensor model. The results of the wave propagation due to fiber fracture are shown in Figure 2.16.

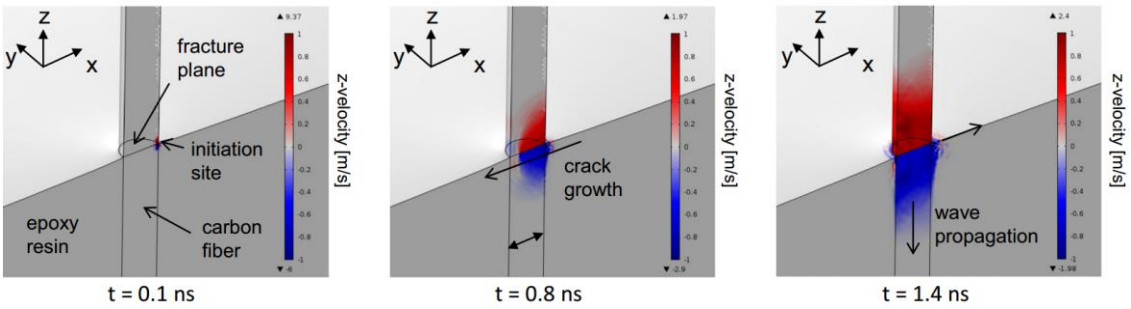

Figure 2.16: Wave propagation evolution due to fiber breakage. Velocity contours in the direction of the load (i.e. z-component) [97]

The simulated and experimental waveforms from the model and experiment showed good agreement for the considered micro-fracture mechanisms. However, there were no comparisons with experiments for validating the deformation state at fracture, thus validating the conditions of the AE damage source. AE consists of at least two components, the damage source characterization in addition to its subsequent transient response. Therefore, it is essential to accurately formulate both parts of the solution in order to obtain realistic emissions from a numerical source.

Within the context of modeling damage sources at initiation and growth as realistic AE sources, several computational approaches have been explored, such as peridynamics modeling, virtual crack closure technique, damage mechanics [98-102] in addition to the Cohesive Zone Modeling (CZM) and the eXtended Finite Element Method (XFEM) for elastoplastic materials [103-107]. In CZM and XFEM traction separation laws are defined by assuming fracture parameters (e.g. load to cause crack opening) or by extracting them experimentally. However, the direct connection between models that could be used to initiate a fracture mechanism in addition to investigate the associated characteristics including wave effects and energy release in have not yet been addressed.

2.4 RELEVANT MECHANICS CONCEPTS TO ACOUSTIC EMISSION

The following sections explain the background material of the pertinent topics to the two components of the AE model which include the AE source mechanism and the release of stress waves. The concepts of the AE source are inherently related to failure mechanisms, thus they are closely related to topics in fracture and damage mechanics. The second part is related to the wave propagation in solids and it is based on the concepts of Wave Mechanics.

2.4.1 ACOUSTIC EMISSION SOURCES MECHANISM

The assessment of structural integrity of critical components across time and length scales is indispensable to determine the type of service operations, thus it is important to determine the state of progressive damage. Although, fracture is one of the most critical AE sources there are several other dominant AE sources as schematically shown in Figure 2.17. In fact, AE is relevant to many localized sources as defined by the ASTM

E316 standard as “the class of phenomena whereby transient elastic waves are generated by the rapid release of energy from localized sources within a material, or transient waves so generated” [108]. Another formal definition of AE is that of redistribution of energy which is in fact related to the type of failure mechanism. Thus, the process of an elastic wave excitation due to a localized source can be thought of as an initial disturbance which then travels through a medium and thereby transferring energy further away.

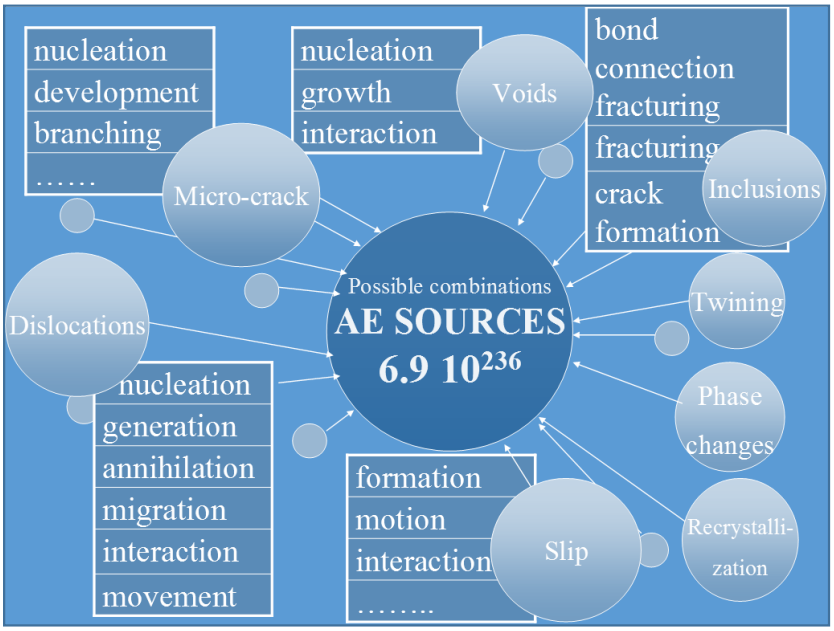

Figure 2.17: Acoustic emission sources schematic [109]

The amount of energy released in AE relies mainly on the intensity of the event, the speed of the local deformation process and the associated size. For instance, the formation and movement of a single dislocation does produce transient stress waves, but their overall intensity is not sufficient to be detected by standard e.g. piezoelectric transducers. However, when large number of dislocations accumulate and move in the form of avalanches or pile-ups, the occurring superposition results typically in detectable events at the meso- and macroscales [110]. In this context, Figure 2.18 provides a range

of damage mechanisms that have been investigated in the AE literature accompanied by suggested ranges of experimentally-measured energy magnitudes. In relation to the discussion on types and characteristics of primary AE sources, fracture mechanics will be briefly introduced in addition to energetic concepts to better describe from an engineering perspective the AE process.

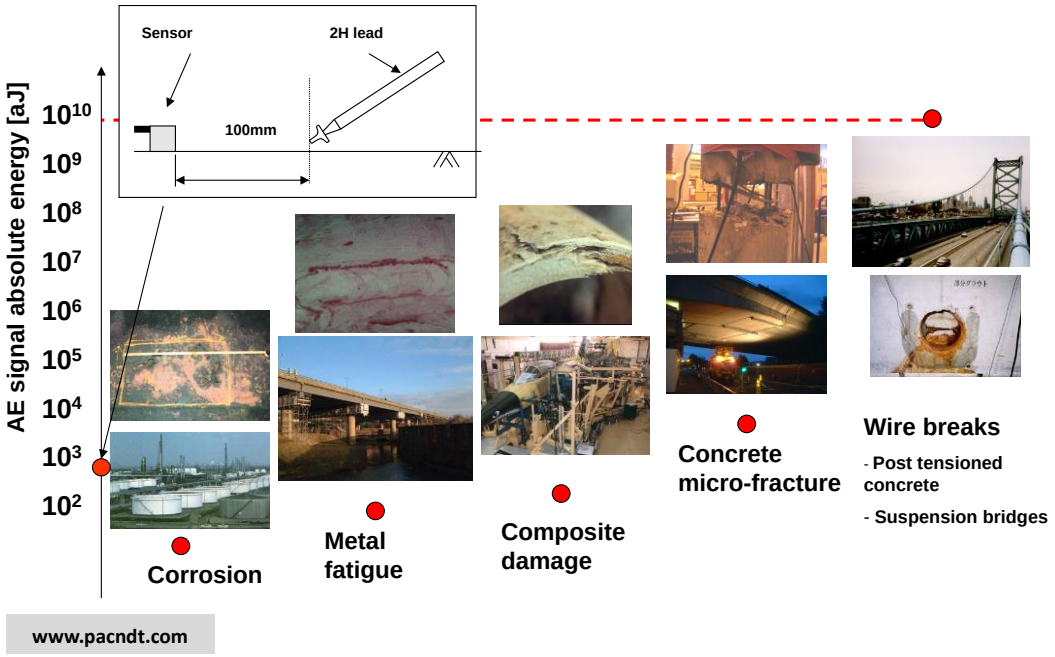

Figure 2.18: AE emission energy in atto-Joules for various damage mechanisms [111]

The main objective of fracture mechanics is to describe the fracture process from critical cracks that may cause structural failure [112], while damage mechanics focuses on the progressive deterioration process prior to ultimate failure. The origins of failure and damage in solid mechanics can be traced back to Leonardo da Vinci (1452-1519) who recorded fracture by performing strength tests of iron wires providing a qualitative analysis of the root cause of fracture, as well as Galileo (1638) who corrected the scaling laws for bars under tension and bending and noted limitation due to the size effect in fracture of structures [113-115].

The interest in fracture mechanics increased and it became an established discipline in the field of solid mechanics during World War II. Linear Elastic Fracture Mechanics (LEFM) particularly had been addressed and pioneered by the works of Inglis and Griffith with parameters such as energy release rate and stress intensity factor. A quantitative work on fracture stress and flaw size developed by Griffith in 1920 along with Irwin's extended work on Griffith's approach to metals by including plastic flow permitted the new field of fracture mechanics to get recognized. As a result, various engineering applications were found for fracture mechanics including the fuselage failure of a Comet jet aircraft and the failure of rotors in steam turbines[116, 117]. Such knowledge resulted in the formulation of the energy release rate, *G*, expressed as

$$G = -\frac{\partial \Pi}{\partial A} = 2\gamma_{surface} + G_{plastic} \tag{2.12}$$

where Π is the potential energy defined by the internal strain energy and external work that initiates or extends the crack by an area *A*, resulting in the formation of new surfaces, for which $\gamma_{surface}$ is the energy required to accomplish this task, while $G_{plastic}$ is the associated energy dissipation (for a general elasto-plastic/ductile fracture typical in metals). The energy release rate at a critical value for crack extension will dictate the instability, depending on how *G* and the material resistance (critical fracture energy) to crack growth evolve with crack extension. Thus, the critical fracture energy curve, also called R curve, in addition to other fracture toughness parameters, becomes a material property independent of the size or shape of the cracked body. Employing analytical tools, Westergaard, Irwin, Sneddon, and Williams focused on providing this type of relationships [113], resulting in a new parameter that describes the stress singularity

ahead of the crack tip, i.e. the stress intensity factor *K*. This development included three modes of loading for a crack for which a stress component and displacement could be calculated. The general form of the stress intensity factor is

$$K_{(I,II,III)} = Y\sigma\sqrt{\pi a} \tag{2.13}$$

where a, σ, Y are the characteristic crack dimension, applied stress and geometric factor constant, respectively. Both the stress intensity factor and energy release rate describe the crack behavior and are related by the crack size, thus $G=K_I^2/E$. Due to the limitations of LEFM, the analysis of stresses ahead of the crack tip is also confined for certain conditions and becomes inaccurate as the inelastic region grows. One approach to evaluate the plastic zone is the Irwin approach for first-order and second-order estimates. This approach provides a measure of the plastic zone and quantifies the limitation for LEFM to be valid, also referred as small-scale yielding or K-dominance region.

The post-World War II accomplishments and development of the fracture mechanics field included LEFM, which was limited to small nonlinear zone in front of the crack tip resulting from localized plastic deformation of materials. Numerous methods were suggested to mitigate and modify this formulation to account for large deformation and adjust the crack tip yielding. For instance, Irwin suggested the zone correction [118], while Well proposed the use of displacements of crack faces as a possible fracture criterion for large plasticity before failure occurs. Along the same lines, Rice [119, 120] derived a parameter based on a line integral contour to characterize nonlinear behavior around the crack by generalizing the energy release rate and proposing a power law to mitigate the associated plastic stress field singularities [119, 121]. All of these

contributed to the field called Nonlinear fracture mechanics also referred as Elastic-Plastic Fracture Mechanics (EPFM). EPFM adapted new formulations in order to account for the size of the plastic zone in nonlinear elastic materials, where it is no longer negligible. Although the LEFM parameters were modified to describe some nonlinear material behavior, most LEFM formulations fail to characterize the fracture process since plasticity and microcracking increase the size of the nonlinear zone. For instance, the nonlinear material deformation in most ductile metals or cementitious and other materials dictate that LEFM concepts are no longer valid and the plastic zone may not be confined to small region. Therefore, EPFM was developed and can be applied to materials that deform plastically with no time dependence. EPFM introduces two parameters to describe the nonlinear behavior: the crack-tip opening displacement (CTOD) and the *J* contour integral. These parameters describe crack-tip conditions in materials that plastically deform, and may be used to determine fracture criteria. Critical values of CTOD or *J* give nearly size-independent measures of fracture toughness, even for relatively large amounts of crack-tip plasticity. Although EPFM is not restricted to small deformation or small plastic zone, it is important to note that there are still limits on the validity of the *J* contour and the CTOD since the strain singularity still exists close to the crack tip.

The CTOD was studied and formulated in a work by Wells [122]. This study showed that the structural steels used were too tough to be described by the stress intensity factor (i.e. LEFM). However, these results also demonstrated the need for new modified formulations in order to characterize fracture in this class of materials which are highly tough. The fractured steel specimens showed that the crack faces had moved due to

plastic deformation, i.e. the sharp crack blunted. With this geometrical information, Wells was able to state a relation of the CTOD with the stress intensity factor. Various formulations and modifications of this relationship were established in order to capture the plastic behavior as well. An example of this work is a hinge model for estimating the CTOD from a three-point bend test, as shown in (2.14).

$$\delta = \delta_{el} + \delta_p = \frac{K_I^2}{m\sigma_{YS}E} + \frac{r_p(W-a)V_p}{r_p(W-a)+a} \ , \tag{2.14}$$

where the subscripts "*el*" and "*p*" represent the elastic and plastic part of the equation, *m* is a dimensional constant (1 for plane stress and 2 for plane strain), σ_{YS} is the yield strength, E is the Young's modulus, r_p is plastic rotational factor, V_p is the opening displacement, *W* is the uncracked ligament, and *a* is the crack (size) length.

The *J*-integral was first introduced by Rice [120] by approximating the elastic-plastic deformation with a nonlinear elastic behavior. The many applications and success of this formulation can be attributed to its valid limits which go beyond those of LEFM. Rice's work showed that the *J*-integral was closely related to the energy release rate for a nonlinear material when formulating a path independent line integral around the crack tip. This formulation in its quasi-static form can be expressed as

$$J = \int_{\Gamma} \left(w dy - T_i \frac{\partial u_i}{\partial x} ds \right), \tag{2.15}$$

where *w* is the strain energy density $\left(w = \int_0^{\varepsilon_{ij}} \sigma_{ij} d\varepsilon_{ij} \right)$, T_i are the components of the traction vector, u_i is the displacement vector components and *ds* is the length increment along the

contour Γ. In addition, the *J* contour may also be formulated to describe the singularity (also known as HRR singularity [119, 121]) field similar to its counterpart, the stress intensity factor, in LEFM. Thus, *J*-integral describes fully the conditions presented ahead of the crack tip under plastic deformation. From the relations presented by Wells between the LEFM parameters and CTOD, relationships between the *J* and the CTOD can be derived since *J* is closely related to *G*. Furthermore, resistance curves to predict unstable and stable crack growth can be developed using both *J* and CTOD and the governing conditions are virtually identical to those by LEFM parameters.

Modeling of an AE source is definitely related comprised to such concepts of fracture mechanics, which consequently define the equilibrium states of before and after crack initiation to completely characterize the source. For instance, the process of crack growth consists of a drop on the stress level at the newly formed surface area from some value σ_{frac} to zero. As a result the crack surface is deflected within a characteristic time t_{frac} and starts to oscillate until it dynamically reaches its new equilibrium state [123]. The behavior of the source can be described by the direction of the crack motion vector $\vec{b}$ (i.e. Burgers vector) and the vector normal to the crack surface $\vec{d}$ resulting in a total crack volume increase ΔV. The characteristics of crack deflection can be then essentially described by the moment tensor (M) concept [124], previously described as AE model by Rice et al. [85], which couples the crack's kinematic behavior with the elastic properties (elastic tensor C) . The relationship can be written as

$$M_{ij} = C_{ijkl} b_k d_l \Delta V \,, \tag{2.16}$$

The resulting disturbance in the form of a small elastic wave released in the surrounding medium can subsequently be described by the wave propagation and radiation patterns theories. The characteristic time for failure is also another factor that will affect the type source. Typically the orders of magnitudes associated with crack deflection are between 10^{-18} and 10^{-4} seconds which translates to ultrasonic frequencies ranges of 10 kHz to 100 MHz [125]. Along these lines, Lysak provided a calculation for the elastic wave amplitude at a distance and angle for a penny-shaped crack-through process. Others analytical works which have attempted to associate the AE source to the wave propagation include the simulation of buried AE sources, the effect of crack distribution and displacement source amplitude, as well as AE modeling during formation of a penny-shaped crack under tensile and torque loading [126-128]. Regardless to the limitations which have been the case for the models in Section 2.3, they can predict and quantify the aspects of energy and frequency spectrum of the source and associated wave released by a crack. Thus, the concept of an AE source and its energy is fundamentally related to the mechanism which in this dissertation is fracture-based for both cracked and debonded surfaces.

2.4.2 WAVE PROPAGATION DUE TO AE SOURCE

The disturbance caused by localized sources can be treated by two scales of observation, including continuum and discrete. The excitation process of an elastic wave as a result of a damage source (e.g. a crack) is described by the equation of motion of the displacement vector in the wave equation, as long as the deformation remains elastic, i.e. for small displacements. Moreover, the exact solution of the equations of motion is restricted by rate of heat generated form the deformation of a solid. However, if slower enough than

the vibrational movements within the solid, the deformation can be assumed to be adiabatic, thus the equation of motion applies [4, 90, 129]. Based on the theory of elastic waves for small initial deformations, the formulation of a traveling wave can be obtained by solving the momentum balance equation and neglecting Lagrangian inertia, as

$$\rho \frac{\partial^2 u_i}{\partial t^2} = \frac{\partial \sigma_{ij}}{\partial r_j}, \tag{2.17}$$

where ρ is the density, u is the displacement and σ is the stress tensor. Such formulation can be simplified for an isotropic material by use of the *Lamé* constants to

$$\rho \frac{\partial^2 \vec{u}}{\partial t^2} = (\kappa + \mu)\nabla\left(\vec{\nabla} \cdot \vec{u}\right) + \mu \Delta \vec{u}, \tag{2.18}$$

where κ and μ are the bulk and shear modulus. The solution of (2.18) can then be obtained for infinite media by using scalar and vector potentials which yield two independent wave equations. The two independent equations introduce two important velocities related to bulk waves. Thus, the longitudinal wave velocity c_L is defined as,

$$c_L = \sqrt{\frac{E(1-\nu)}{\rho(1+\nu)(1-2\nu)}}, \tag{2.19}$$

in terms of the Young's modulus E, and Poisson's ratio v. Similarly the shear wave velocity can be expressed as

$$c_S = \sqrt{\frac{E}{2\rho(1+\nu)}} = \sqrt{\frac{G}{\rho}}, \tag{2.20}$$

which is similar to its formulation in the 2D case, where G is the shear modulus. The resulting solution of (2.18) for infinite isotropic and homogenous media of the form of a monochromatic plane wave, $\vec{e}$, with amplitude u_o, wave number k, and angular frequency ω is:

$$\vec{u}(\vec{r},t) = u_o \cdot e^{-i(\vec{k}\vec{r}-\omega t)}\vec{e}\,, \tag{2.21}$$

A particular characteristic of (2.21) is the fact that the bulk wave velocities are equal to the phase velocities c_P of the plane waves. Consequently, the elastic wave problem can be described by using the independent longitudinal and shear wave propagation modes, shown in Figure 2.19.

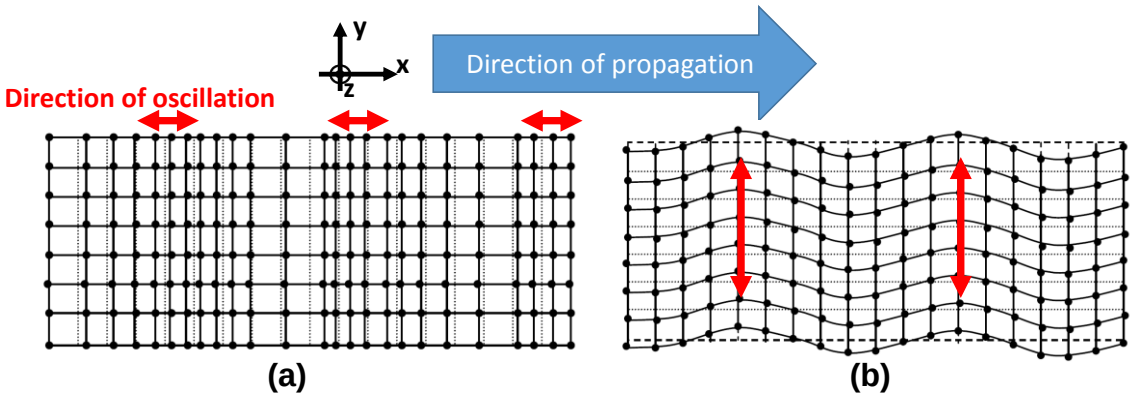

Figure 2.19: (a) Longitudinal and (b) shear elastic waves (Modified from [130])

In the case of non-monochromatic waves, anisotropic, or finite media the propagation of the velocity of the wave is defined to be the group velocity c_G, while the phase velocity is the speed at which any fixed phase of the disturbance cycle is displaced which mathematically is the ratio between circular frequency and the wave number, also known as the dispersion-relation. Both velocities can be derived in terms of the circular frequency and wave number in (2.22) and (2.23)

$$c_G = \frac{\partial \omega(k)}{\partial k}, \tag{2.22}$$

$$c_P = \frac{\omega(k)}{k}, \tag{2.23}$$

In the case that both velocities are nonequivalent, dispersion occurs which is one type of effects on the wave that has particular importance for AE. In general, some of the most important wave propagation effects include attenuation, dispersion, diffraction and scattering, among others (some illustrated in Figure 2.20). Attenuation refers to the gradual decrease of the waveform amplitude due to energy loss mechanisms from dispersion, diffraction, or scattering. Dispersion is a phenomenon caused by the frequency dependence on wave velocities. For example, sound waves comprise a range of different frequencies thus the speed of the wave will differ for different frequency contents. At interfaces, waves will reflect or refract which is known as diffraction defined as the spreading or bending of traveling waves. Moreover, scattering refers to the dispersion or deflection of the waves due to a discontinuity in the material.

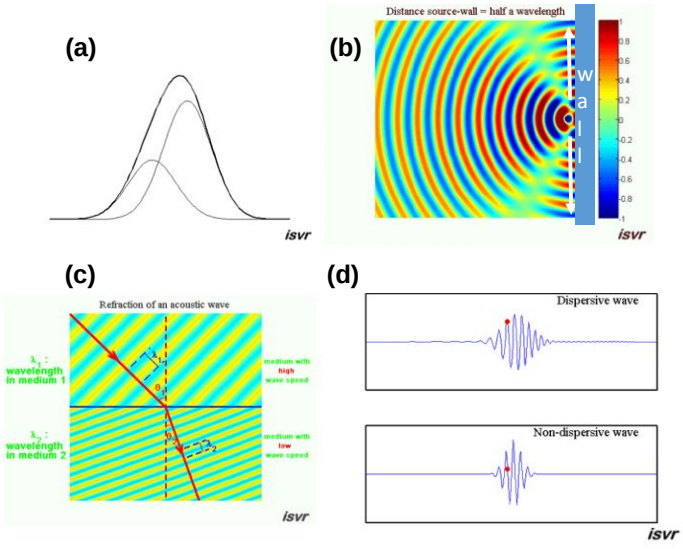

Figure 2.20: (a) Wave superposition, (b) reflection, (c) refraction, (d) dispersion (Modified from [131])

For geometries of finite media the wave equation is solved for given boundary conditions. The solutions obtained could result in so-called guided waves depending on the geometry and interface of the media. In this description, "guided" refers to the fact that the wave propagation will be guided by the geometry itselft. The most common type of guided waves are those occurring at the surface which are referred to as Rayleigh waves. In many AE studies, specifically in aerospace applications, the tested specimen tends to be of plate-like geometry [132, 133]. The guided elastic waves that propagate in this type of structures are called Lamb waves; there are two modes of propagation, extensional or symmetric (S_0) and flexural or asymmetric (A_0) mode, depicted in Figure 2.21.

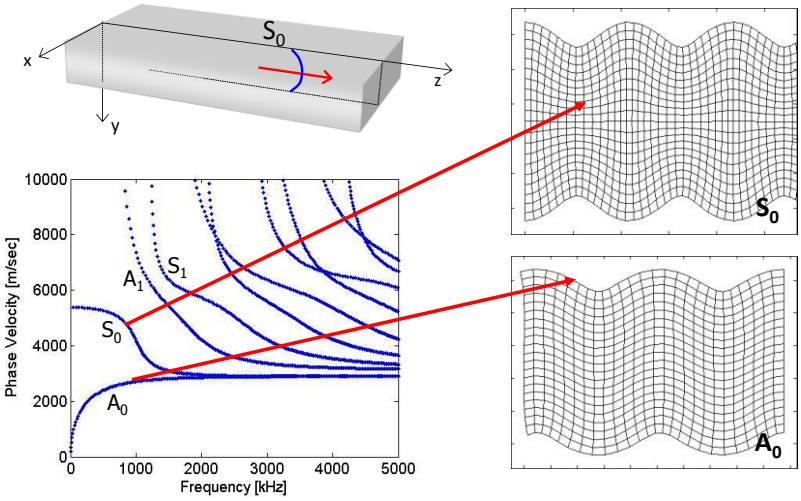

Figure 2.21: Lamb waves schematic of the wave shape and characteristics demonstrated by the dispersion curves given the phase velocity and frequency spectrum relationship [134]

The wave propagation process of an AE source is illustrated in Figure 2.22, which depicts the wave modes (i.e. type of active waves) for a given length and time scale. The time domain consists of a transient and steady-state, in which the transient period is comprised of the release of bulk waves and formation of guided waves. As the wave is emitted from AE source and its associated energy is invested in the entire volume, the bulk waves start

to propagate at the transient state. As a consequence of wave effects and depending on the characteristic of the geometry, guided waves can be created during this transient state at a distance at least tripled the thickness. Although this process can be described in the time domain, it can also be defined by the length scale. For instance, the global waves can be seen as natural modes in which the whole component is resonating after all the energy has been invested. Furthermore, these natural modes are comprised of bulk waves and depending on geometrical conditions at some locations and time instances such bulk waves can form guided waves. In general, the propagation of acoustic emission signals is subject to the boundary conditions formed by the propagation media geometry.

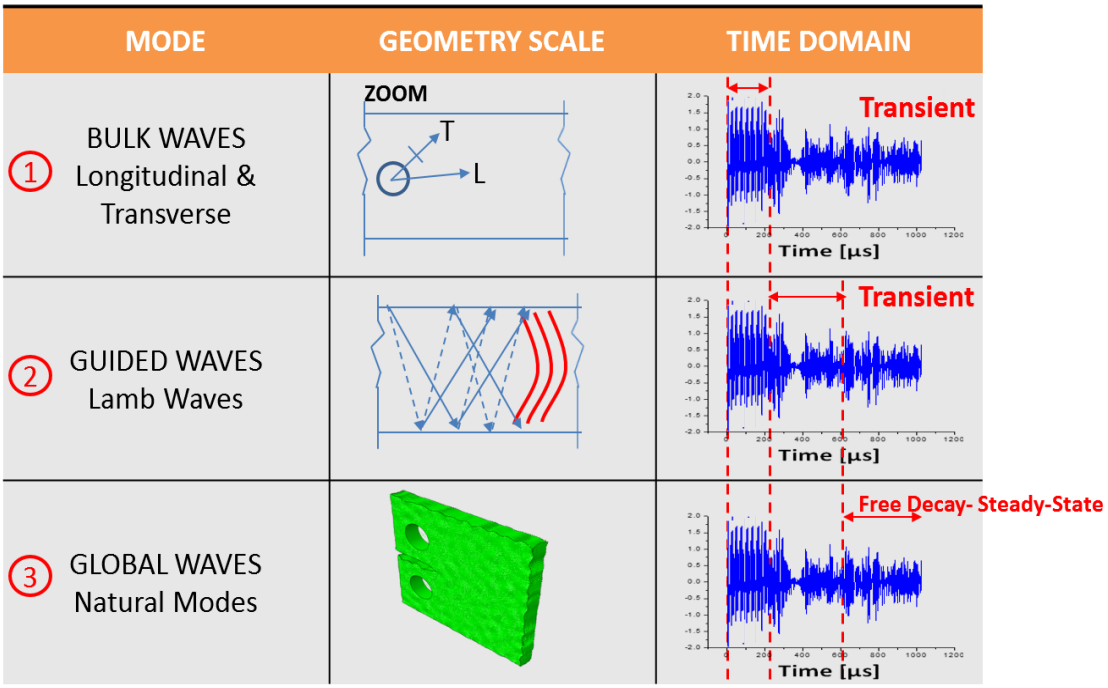

Figure 2.22: Geometry scale and time domain of wave modes [135]

Moreover, a consequence of dispersion is attenuation, which also implicates and compromises the AE signal studied. Thus, the information included in the amplitude and frequency composition of the AE signal formed from the source is altered during propagation. Ultimately, additional type of effects on wave propagation could be

associated to the actual failure mechanism such as plastic accumulation, where energy is not recovered and permanent deformation modifies the properties of the medium. In summary, it is of great importance to consider such effects in order to identify and analyze appropriately the actual AE source which may be limited to a certain distance depending on its strength and type.

CHAPTER 3: RESEARCH HYPOTHESIS & PROPOSED APPROACH

3.1 THESIS HYPOTHESIS

Acoustic emission is intimately related to wave effects caused by both the source as well as the medium of propagation. Therefore, previously reported numerical and analytical models consist of dynamic analyses that treat AE-related wave propagation as the transient response of continua to simulated sources. Although the efforts to investigate the wave propagation problem due to various damage sources have been extensive, the approaches include and rely on several limiting assumptions such that of semi- or infinite media in addition to analytically or experimentally obtained point-like sources. Accordingly, this dissertation was based on the concept that computational models could potentially capture and couple accurately damage initiation and evolution in addition to the transient dynamic effects closely related to acoustic emission and failure mechanism sources. More specifically within the Finite Element Method framework, it is attempted to link static and dynamic analyses to characterize, analyze and quantify the simulated acoustic emissions. All of these set the stage to analyze and decompose simulated AE primitive signals for better interpretation and pattern recognition from different source mechanisms. Consequently, such acquired capabilities via the proposed computational model could potentially mitigate the existing challenges in reliably using AE in SHM applications

3.2 PROPOSED APPROACH OVERVIEW

An integrated computational method is introduced herein that attempts to address the challenges in interpreting experimental AE recordings by implementing a forward computational approach [136]. The approach is called integrated as it relies on using actual testing data to construct numerical models, and forward modeling as it is capable to model AE due to crack initiation. The computational approach involves constructing damage-based models to simulate isolated dominant AE sources in specific geometries. Consequently, a coupled computational method is used to link numerically source mechanisms with AE. The overall idea of the approach is depicted in Figure 3.1.

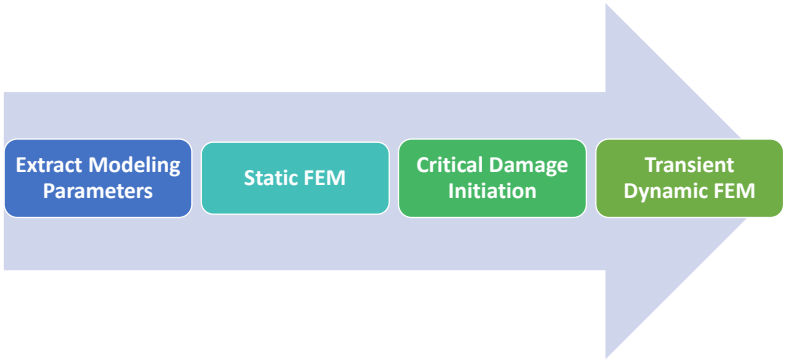

Figure 3.1: Computational process for AE modeling

Specifically, the computational model was implemented using Finite Elements (FE) tools for both fracture and wave propagation. In the case of fracture, state-of-the-art models, including a cohesive zone model and XFEM, were applied and validated with experimental results. Moreover, both fracture models were verified by comparing solutions of the static and dynamic analyses. The approach consisted in extracting all possible and accessible experimental parameters in order to calibrate the FE static computational model (i.e. neglecting inertial terms such as density and acceleration).

Once the static simulation converged and quasi-static fracture occurs at high stressed locations, it was necessary to identify the damage initiation stages and the critical time that could be used for linking it to the dynamic response. Figure 3.2 portrays the step process for a crack-induced acoustic emission computational model. The solution at this critical stage is then used to link the static with dynamic analysis by either using the displacements or the loading conditions near the damage region in a completely new model or implementing a coupled static-dynamic analysis in the entire model using all solved parameters. The transient dynamic analysis is then evaluated at different nodal locations as if the nodal acceleration, velocity and displacement were sensor locations.

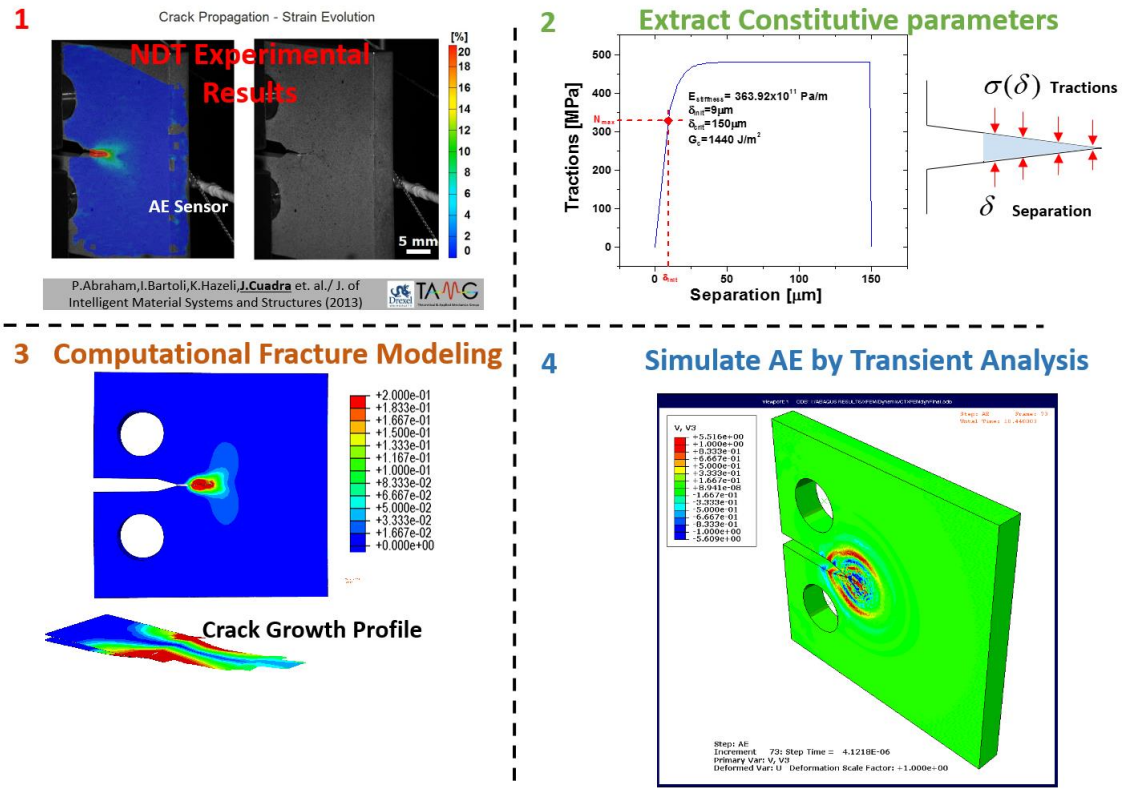

Figure 3.2: Crack-induced computational model process for AE modeling [136]

The nodal time waveforms resulting from the damage-induced wave propagation are studied and characterized in both time and frequency domain in order to differentiate the effects of geometry and damage source. For all damage and fracture methods, the wave characteristics near and far from the critical failure zone are analyzed to quantify both the so-called primitive AE content at the source, as well as to investigate the influence of the geometry and the material in the associated wave propagation.

3.3 EXPERIMENTAL PROCEDURE

The experimental part of this thesis was essential to construct, calibrate and validate the computational model presented. Specific and targeted experimental procedures were designed to extract parameters related to failure mechanisms and fracture. All experiments were conducted following the corresponding standards by the American Society for Testing and Materials (ASTM). Three types of experimental setups were implemented attempting to characterize, evaluate and simulate different failure mechanisms including a tensile test for ductile fracture, a compact tension, C(T), (Mode I fracture using two geometries), and a stiffener specimen for interface debonding failure. Aluminum 2024-T3 and similar aluminum alloys were utilized for all specimens tested. The corresponding ASTM standards are listed respectively for the tension and C(T) tests: ASTM E-8/E8M-13a [137] and ASTM E1820-13 [138]. This section mainly explains the details of the experimental setup and the extrapolated parameters for the C(T) geometry whereas the setup for the tensile and stiffener are described in Chapter 6 and Chapter 7, respectively. The mechanical tests were integrated with a hybrid NDT setup which included Digital Image Correlation (DIC) and Infrared Thermography (IRT) as visual quantifiable techniques coupled with AE for future validations with the computational

model. In the following sections we explain in detail the experimental setup in addition to the extrapolation of all accessible parameters to calibrate the initiation of crack growth in the FEM model. Moreover, the sections include background material of the techniques used.

3.3.1 MECHANICAL TEST SETUP AND STANDARD PARAMETERS

The specimens used in this thesis were mechanically loaded to failure using an MTS servohydraulic machine. Figure 3.3: illustrates a schematic of a similar model of the loading stage machine used for the tests. Some of the most important components in the machine are the load cell, actuator and the fixtures.

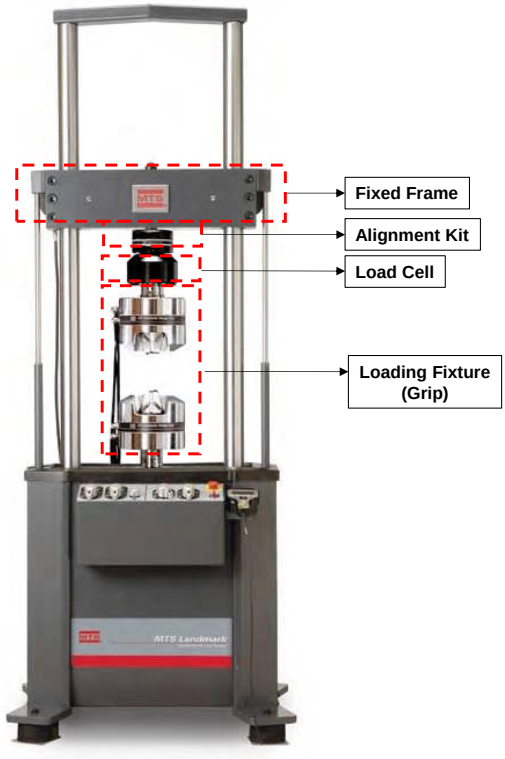

Figure 3.3: MTS servohydraulic machine

The recordable loading capacity is limited by load cell, which has a limit of 100 kN with a sensitivity ±100 N and threshold of approximately 88 kN, while the displacement controlled by the hydraulic actuator is limited to 400 mm approximately. All these mechanical parameters were considered as constraints accounted for selecting the material tested and geometry. The schematic shows important components such as the load cell, fixed frame and loading fixture (tensile grips) in which the lower grip is attached to the actuator. Depending on the type of test, the fixture is selected and attached to either both the top fixed frame and the actuator or the installed grips. Figure 3.4 shows three different experimental setups with the corresponding fixtures

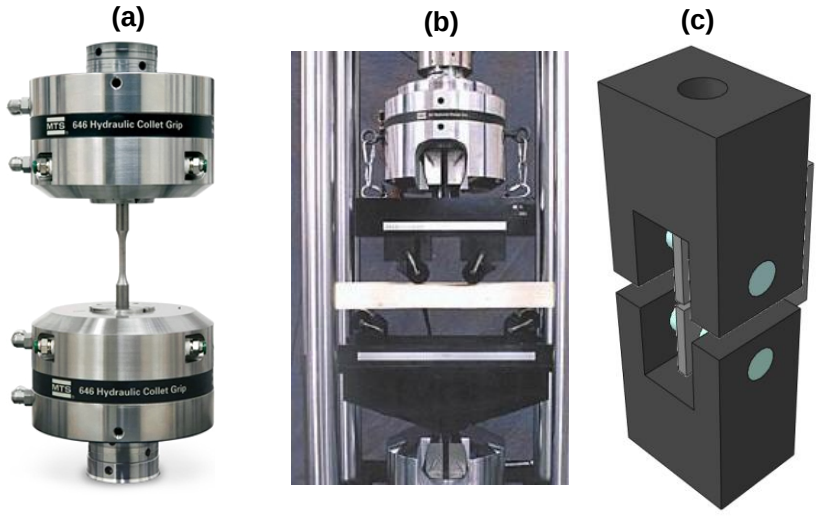

Figure 3.4: Loading machine testing fixtures for (a) tensile test, (b) 4-pt bending, and (c) Mode I compact tension

The parameters utilized for the compact tension Mode I test were determined using the standard test method for measurement of fracture toughness (ASTM 1820-13). The standard was selected since the overall goal was to obtain a force-displacement response due to crack initiation and growth in addition to evaluation of the corresponding fracture parameters. Some of these fracture parameters are the stress intensity factor, the

nonlinear energy release rate, and the crack tip opening displacement. The standards also provides guidelines for performing an accurate test, listed as follows: (i) the temperature of the specimen shall be stable and uniform during the test, (ii) alignment of the specimen should be within 0.25 mm (0.01 in) for upper and lower loading rods and the center of the specimen with respect to clevis opening should be 0.76 mm (0.03 in), (iii) the loading rate may be displacement or force control such that the rate to reach a critical force is constant and lies between 0.3 to 3 minutes, (iv) the crack size should be measured using optical methods by averaging the two near-surface measurements using the final physical crack length and subtracting the original crack to obtain the crack extension [138].

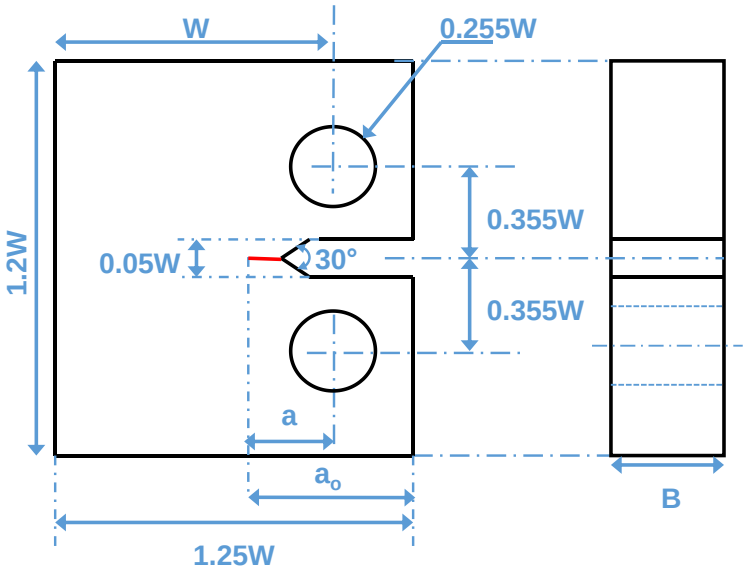

Figure 3.5: ASTM compact tension dimensions recommended for measuring fracture toughness

The standard also provides constraints to build a geometry that may produce a stable crack growth for plane stress. Figure 3.5 depicts the diagram of the compact tension sample with dimension dependent on *W*, which is defined as the distance from the loading pins to the far edge as shown. Two different geometries were selected based on a

4 mm and 6 mm thickness. Figure 3.6 shows the two C(T) geometries used in all quasi-static crack growth experiments referred as CT-A and –B throughout the following chapters and sections.

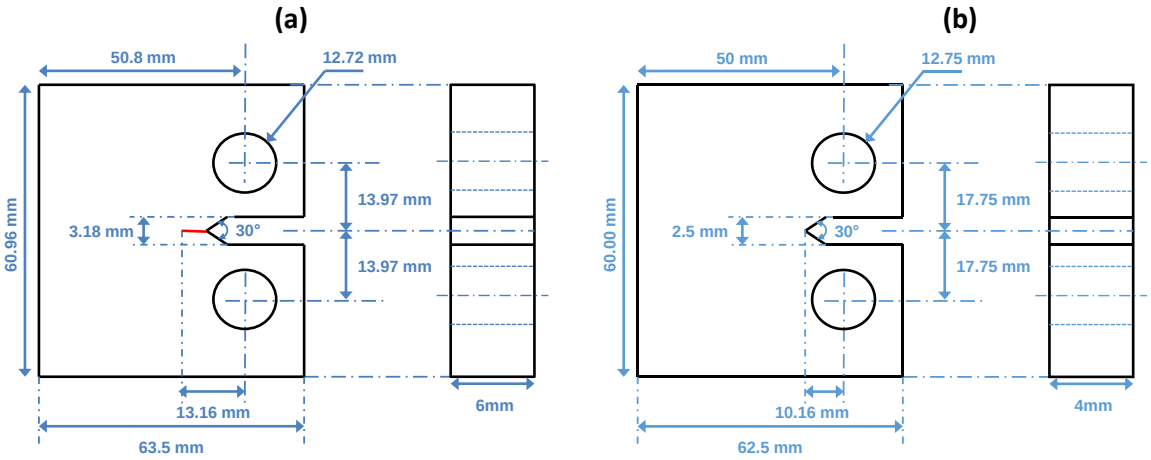

Figure 3.6: ASTM compact tension sample dimensions for (a) CT-A and (b) CT-B

Some of the major differences between the two geometries include the thickness and the pre-crack size and all other dimensions were calculated based on those as well as the loading rate. CT-A was a baseline to study fracture while CT-B was dimensioned based on aircraft component applications which are constrained by a thickness of 4mm. In addition, the CT-B did not include a pre-crack in order to compare the results to the pre-cracked baseline and evaluate the difference with a pristine unstressed sample. All derivations for determining the fracture parameters experimentally have been built under the assumption of a sharp crack. Therefore, the pristine CT-A sample must have a pre-crack extended ahead of the 30º machined notch. The ASTM standards suggest and provide parameters to create the pre-crack under fatigue loading. The parameters calculated and utilized for the given geometry of the CT-A were: 10 Hz with a maximum load of 6000N and a *R*-value of 0.1 while the pre-crack size was monitored using 5MP

cameras until the crack size was approximately 3 mm. Figure 3.7 shows the final images of the fatigued pre-crack.

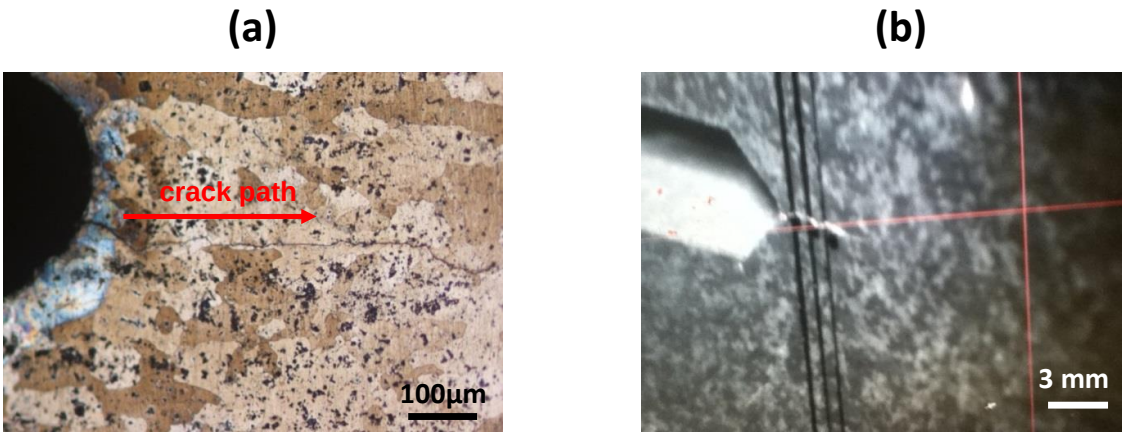

Figure 3.7: (a) Optical microscope and (b) 5M camera images of the fatigued pre-crack ahead of the machined notch

The pre-cracked CT-A specimen was then tested, using the fixture shown in Figure 3.4c, under quasi-static conditions of 0.5 mm/min for stable crack growth. This testing conditions were replicated for CT-B. Both experimental setups were repeated for various samples in order to assure data reproducibility.

TABLE 3.1: COMPACT TENSION MECHANICAL RESULTS

Sample Geometry	CT-A	CT-B
Maximum Load [kN]	14.5 ± 2	15 ± 2.5
Stiffness [MN/m]	56.39 ± 8.5	77.11 ± 9.2

Table 3.1 shows the variability of the maximum load reached for the CT samples. It is important to note that the maximum load was one of the main parameters used to calibrate validate the computational model. In addition, a variability of 7-10% for the maximum load is reported while the stiffness shows higher values. Some of the

inconsistency of the test is attributed to factors such as preload due to alignment, manufacturing process of the material, and even the machining method for cutting specimen. Therefore, the average value was used for the computational model calibration.

3.3.2 DIGITAL IMAGE CORRELATION AND HYBRID NDT SETUP

The mechanical test included three nondestructive techniques to enhance the characterization and quantification of the fracture process and eventually to provide additional validation parameters for the computational model. Chapter 2 provides all background material on AE. While, the IRT technique was used only as a complimentary technique, thus this section focuses mainly on DIC. In addition, DIC measured displacements and calculated strains were crucial to build and validate the computational model. Different combinations of the NDT hybrid setup have been successfully utilized in various experimental setups providing parameters both from the surface and volume response due to loading [139-143].

Although the AE experimental setup was not essential to construct the computational model, the experimental results are used for comparison thus the experimental parameters used for validation are described. AE was recorded using a four-channel system (AEWin DiSP, MISTRAS) and three piezoelectric sensors (PICO) mounted at various locations along the CT specimen. The three piezoelectric transducers have an operating frequency range of 200-750 kHz with a peak frequency at 500 kHz. The sensors were bonded on the surface of the specimen by means of a cyanoacrylate adhesive. Each transducer was pre-amplified by individual 40 dB gain amplifiers and the signals were sampled at a rate

of 10 MHz. The recorded signals were band-pass filtered in the frequency range of 100 kHz-2 MHz and the pick definition, hit definition and hit lockout time settings were set equal to 300, 600 and 1000 μs, respectively. A threshold of 60 dB was used in this test. The threshold used minimized the recordings of undesired noise, such as mechanical vibrations introduced by the loading frame. The wave speed in the material was estimated in accordance to ASTM E976 [1] and pencil-lead break tests were carried out to calibrate the sensitivity of the AE system. Additionally, 2D source location algorithms using triangulation were implemented, while the load and displacement parameters were directly fed into the AE system.

DIC has been successfully and widely used in experimental mechanics for determining displacements and calculating strains on the surface during deformation [144-149]. DIC has also been attributed to be successful due its robustness and computational efficiency in various experimental setups from micro to macroscale [146-148]. The principles behind DIC are intuitive and closely related mathematically to those of continuum mechanics for deformation. A speckle pattern on the surface allows the algorithm to track targets/points on the material using the pixel areas (e.g. square subsets/facets) of the recorded images. Although this pattern can be achieved using various methods, it is important to note that it needs to contain sufficient variations so that each point can be uniquely and accurately identified. Once an accurate pattern is attained, the displacement can be measured by an optimization algorithm that searches all targets in the deformed states, whose intensity pattern is of maximum similarity with the reference (undeformed) state. Figure 3.8 depicts the overall idea of DIC for obtaining the displacement field from two states.

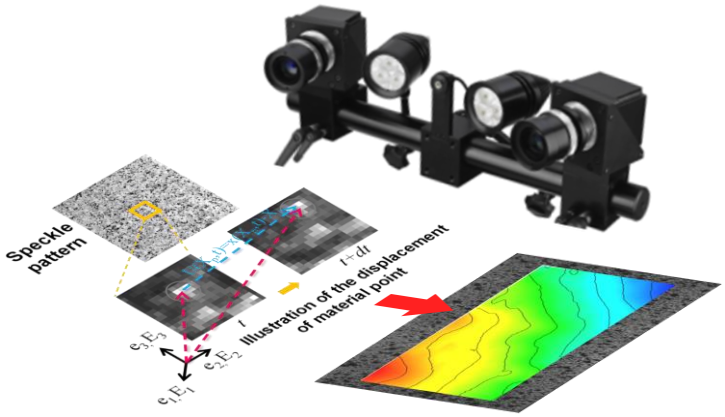

Figure 3.8: DIC concept for measuring displacement

This concept may be applied using a single camera or stereo cameras which are broadly refer as 2D and 3D DIC [147-150]. The 3D image correlation however is implemented based on stereo imaging and photogrammetry and an additional algorithm for 3D surface reconstruction via triangulation [151, 152]. The 3D reconstruction provides the in-plane displacement components in addition to out-of-plane displacements.

The mathematical derivation of the DIC concept and algorithm is described in this section. A subset centered at point "A" and a second point "B" are considered before deformation, as shown in Figure 3.9. After deformation, the subset center moves to point "a". It is important to note that a square subset is preferred rather than an individual pixel since the grayscale value (intensity) of a single pixel may be found at thousands of other pixels, causing errors to find the deformed coordinates. Using the center of the subset then the deformed state at "a" can be expressed as

$$f(a) = f\left(X + u(A), Y + v(A)\right) \tag{3.1}$$

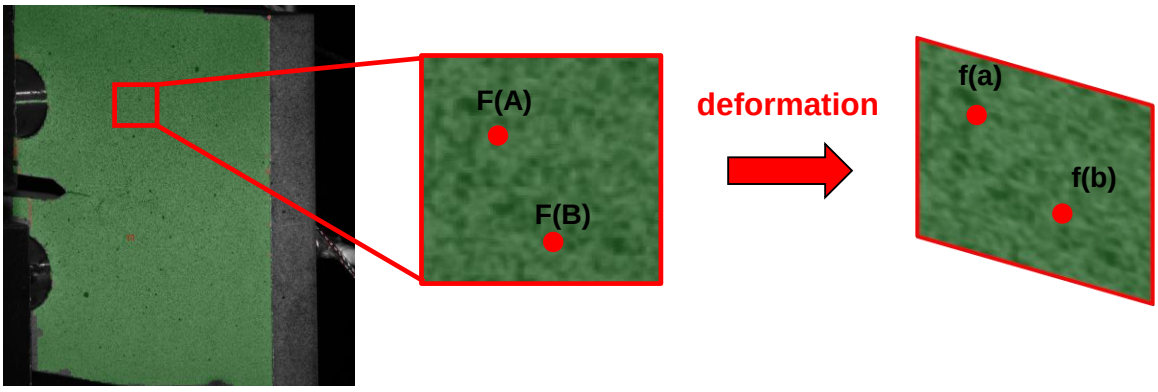

Figure 3.9: Subset (facet) pixels under deformation

where the *X* and *Y* are the reference horizontal and vertical Cartesian coordinates (lower cases of those refer to the deformed state) while *u* and *v* represent the horizontal and vertical displacement functions, respectively. Using the same definition for point B at position $(X+dX, Y+dY)$ on the surface prior to deformation, the position after deformation can be given by

$$f(b) = f\left(X + u(B) + dx,\, Y + v(B) + dy\right), \tag{3.2}$$

Under the assumption that the intensity pattern deforms without altering its local value due to deformation, then $F(B) = f(b)$ and the following relationship may be formulated

$$f\left(B\right) = f\left(X + u(B) + dx, Y + v(B) + dy\right), \tag{3.3}$$

Using (3.1) to (3.3), *f(b)* can be written

$$f(b) = f\left(X + u(A) + \frac{\partial u}{\partial x}(A)dx + \frac{\partial u}{\partial y}(A)dy + dx, Y + v(A) + \frac{\partial v}{\partial x}(A)dx + \frac{\partial v}{\partial y}(A)dy + dy\right) \tag{3.4}$$

,

It can be shown in (3.4) that by obtaining the displacements at center point "A", then $\frac{\partial u}{\partial x}(A)$ and $\frac{\partial u}{\partial y}(A)$ can be calculated. Consequently, the coordinate description of any

nearby point “a” and “b” is determined. By having the coordinates of the deformed state, the displacements at any point may be measured.

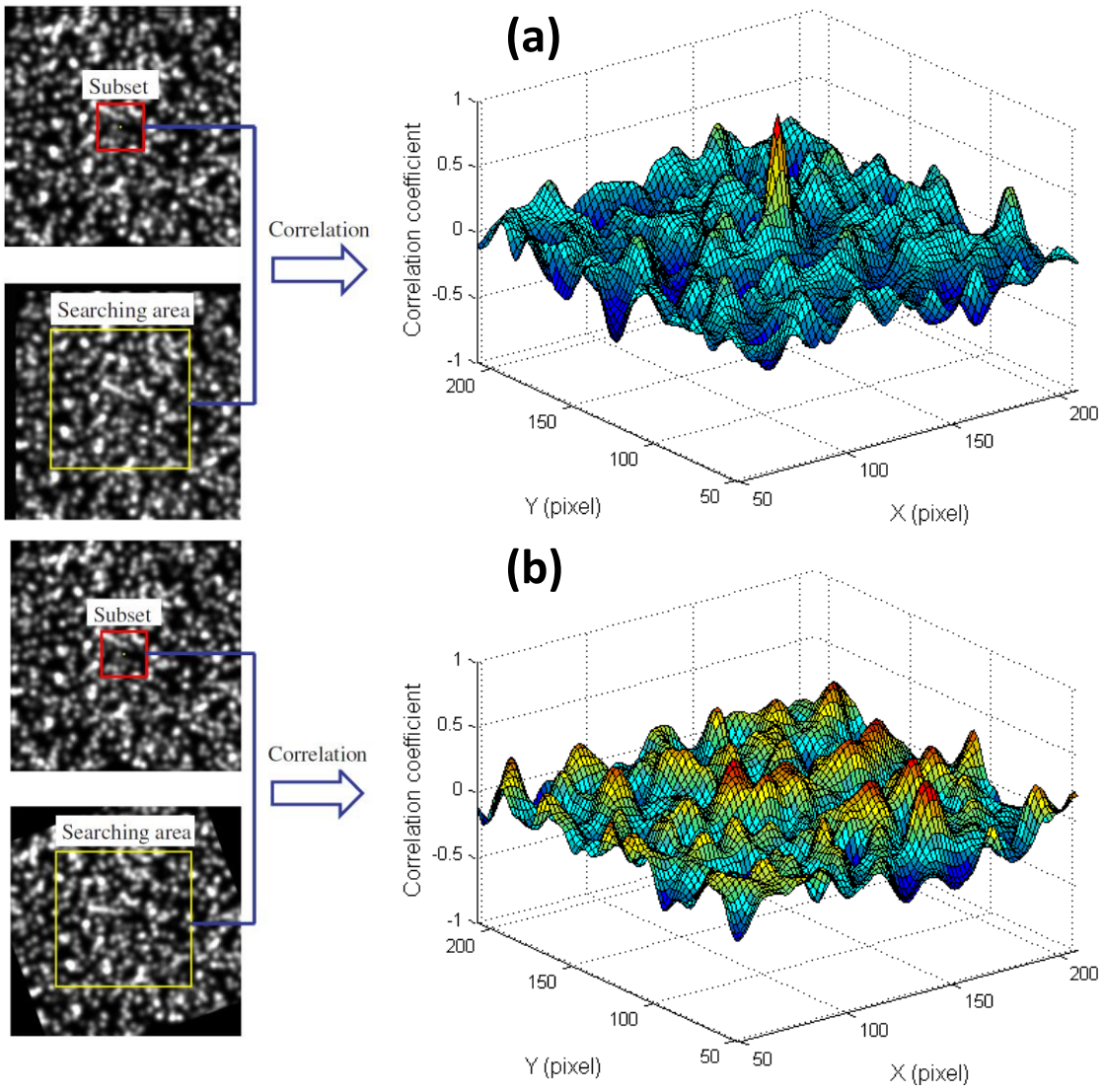

Figure 3.10: Computed whole-field cross-correlation when the deformed image is subjected to (a) rigid body motion, and (b) 20^{o} relative rotation [150] .

Although it is valid to assume that the shape of the reference subset alters in the deformed state, it is also acceptable to have a group of neighboring points in the reference state subset to remain as neighboring points in the deformed state. Therefore, it is important to quantify this dissimilarities of the reference and deformed states using the light intensity

fields of the measured points. Under the assumption that the neighboring points are stationary, sub-pixel interpolation schemes including bilinear and polynomial interpolation may be implemented [144]. Otherwise, the magnitude of the similarity may be quantified, other algorithms can be implemented such as Cross-Correlation (CC) or Sum-Squared Difference (SSD), in which the accuracy of subset domain can be evaluated by a fine pixel by pixel search routine [148, 150]. Such methods and other advanced algorithms can be applied accurately to most displacement cases but tend to be limited when large deformation distortion takes place between two subsets. In these scenarios, some pixels of the reference subset are out of bounds of the deformed subset. Figure 3.10a displays a simple case of displacement, when only rigid body motion is involved [83]. As it can be observed, if only rigid body motion exists between the reference and deformed subsets, a single peak can be found in the correlation coefficient distribution. On the contrary, a 20^{o} relative rotation occurs between the two states of deformation results in a correlation coefficient distribution map without any single dominant peak, shown in Figure 3.10b. In order to address such challenges, optimization schemes such as the SSD are implemented [153]. The objective of the scheme is to determine how far the original subset moves. It is found that the SSD motion estimation method, which is based on minimizing the grayscale value difference between a small subset from on the reference image and the deformed/displaced state, has successfully achieved great results. Some of the main assumptions of the methodology are that no lighting changes occur between two images which denotes that two states only differ by Gaussian random noise. Referring back to Figure 3.9, the reference state is represented by *F*, and the deformed

state by *f*. In order to minimize the squared difference in gray values, known as SSD, over a neighborhood [153], (3.5) is used.

$$\bar{d}_{opt} = \arg\min \sum \left| f(x+\bar{d}) - F(x) \right|^2, \tag{3.5}$$

where $\bar{d}$ represents the displacement. To solve for the optimal displacement vector, an iterative algorithm obtained by expanding the function into first-order Taylor series is suggested by [153] resulting in

$$\begin{aligned} \chi^2(\bar{d}_x + \Delta_x, \bar{d}_y + \Delta_y) &= \sum \left| f(x+\bar{d}) - \frac{\partial f}{\partial x}\Delta_x - \frac{\partial f}{\partial y}\Delta_y - F(x) \right|^2 \bar{d}_{opt} \\ &= \arg\min \sum \left| f(x+\bar{d}) - F(x) \right|^2 \end{aligned} \tag{3.6}$$

where $\bar{d}_x$ and $\bar{d}_y$ indicate the current estimates for the average motion of the subset. Here, Δ_x and Δ_y are the incremental motion updates sought in the current iteration. Taking the partials of (3.6) with respect to Δ_x, Δ_y and setting them equal to zero yields the following linear system for incremental updates of each iteration.

$$\begin{bmatrix} \Delta_x \\ \Delta_y \end{bmatrix} = \begin{bmatrix} \sum \left(\frac{\partial f}{\partial x} \right)^2 & \sum \frac{\partial f}{\partial x}\frac{\partial f}{\partial y} \\ \sum \frac{\partial f}{\partial x}\frac{\partial f}{\partial y} & \sum \left(\frac{\partial f}{\partial y} \right)^2 \end{bmatrix}^{-1} \begin{bmatrix} \sum \frac{\partial f}{\partial x}(F - f) \\ \sum \frac{\partial f}{\partial y}(F - f) \end{bmatrix}, \tag{3.7}$$

Consequently, (3.7) can be used to iteratively improve for given tolerance the estimate average motion in the p^{th} iteration using $\bar{d}^{\,p+1} = \bar{d}^{\,p} + \Delta$ until convergence to the

optimal motion vector $\bar{d}_{opt}$ is reached (e.g. Linear system solving schemes such as Newton-Raphson may be used). As previously specified, DIC is a method that is attractive since it can identify and characterize 3D-coordinates of surface points, extracting displacement fields and calculating strain distributions. Therefore, an additional algorithm is applied based on concepts of stereo vision and triangulation. The 3D DIC involves also some extra parameters in the calibration process such as the relative position and orientation between the cameras, which can be achieved through bundle adjustment.

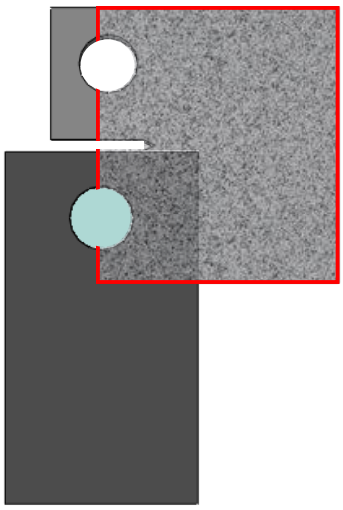

Figure 3.11: Region of interest with speckle pattern measured for CT samples

Furthermore, a computational scheme for calculating the in-plane components of the strain field from the displacement field is part of the DIC framework as an experimental mechanics technique. DIC has been implemented extensively at the laboratory scale as well as at industry level by providing quantitative understanding of material response phenomena and relating local information to global characteristics. Such phenomena include plastic instabilities, damage evolution, and highly localized strains due to

microstructural effects for various material classes [154-159]. In this thesis, the crack initiation site subjected to deformation is detected and quantified by monitoring via stereovision DIC. To this aim, DIC was applied using a stereovision 3D system (ARAMIS, GOM [160]) equipped with two 5 MP cameras.

The bundle adjustment for calibrating the 3D space was performed using a patterned panel was used for sharply focusing the camera lenses to the field of view (FOV), shown in Figure 3.11. In addition, the calibration artifact was utilized to determine the 3D stereovision parameters including the position of the cameras relative to each other, as well as their distance from the sample. The cameras had a focal length of 50 mm and were positioned 485 mm from the sample which was restricted to a separation of 176 mm for achieving a FOV 65 x 55 mm^2 and a resolution of 325 μm/pixel. A stochastic speckle pattern was placed on the surface of the CT sample and a few pretest images were taken to determine the displacement and strain field sensitivities. The system noise was calculated to be approximately ±2 μm (controlled by the correlation algorithm) and ±450 μm/m, respectively. A shutter time of 50 ms with a 5-10% open iris was used to eliminate any type of overexposure and blurring on the sample surface.

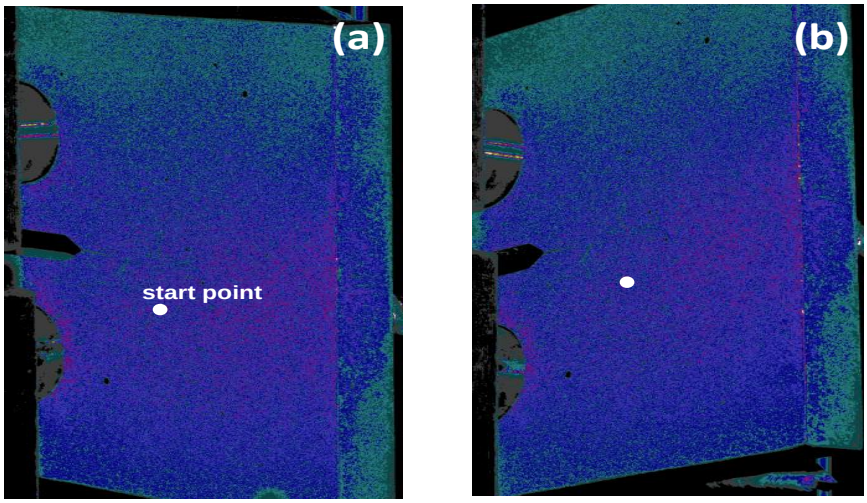

Figure 3.12: Lighting conditions for (a) left and (b) right camera image with algorithm seeding/start point

The final lighting conditions of the sample are shown in Figure 3.12. Lighting conditions can be quantified by implementing a false color method in which good lighting conditions are associated to light blue to purple colors (Figure 3.12a and b). The start point refers to the seeding point for the algorithm. A list of all other factors used and average calculated values are presented in Table 3.2. These values have been readjusted to increase resolution at the crack tip or vice-versa depending on the type of analysis. Both the subset and step control the sensitivity of the full field measurement in addition to the localization of the results for small values.

TABLE 3.2: DIC MEASUREMENT PARAMETERS

Displacement Uncertainty	± 2 μm
Strain Uncertainty	±450 μm/m
Subset size	25x25 pixels
Step Size	12 pixels
Overlap	52 % x 52 %
Computational Size	3
Validity Quote	15%

Moreover, the overlap percentage is defined as the area shared by each neighboring subset and is calculated from subset and step size. For instance, in an image of a size 40 by 40 pixels, a subset of 5 pixels and step of 2 (i.e. 60% overlap) results in 18 by 18 measuring points (i.e. 18 subset centers horizontally and vertically). The relationship for the number of center points, N_{sc}, may be written as:

$$N_{sc} = \left\lfloor \frac{L_{img} - s_{size}}{\Delta_{size}} \right\rfloor + 1, \tag{3.8}$$

where the "⌊ ⌋" symbol refers to the floor value of the argument, L_{img} is one of lengths of the image (i.e. horizontal or vertical) in pixels, s_{size} is the square subset size and Δ_{size} is the step size for a given overlap. As it can be shown by (3.8), the subset and step size refine the field when their values are small, increasing the noise but also allowing the field for localization. Although these values may be adjusted as needed, they are constrained by overlap ratio which is recommended to be close to 50% in order to avoid instabilities causing higher noise levels. Figure 3.13 displays the region of interest or calculation area, the resulting subset center points connected with a mesh, and the measured displacement field at the mesh points with linear interpolation for contour plotting for a given load increment.

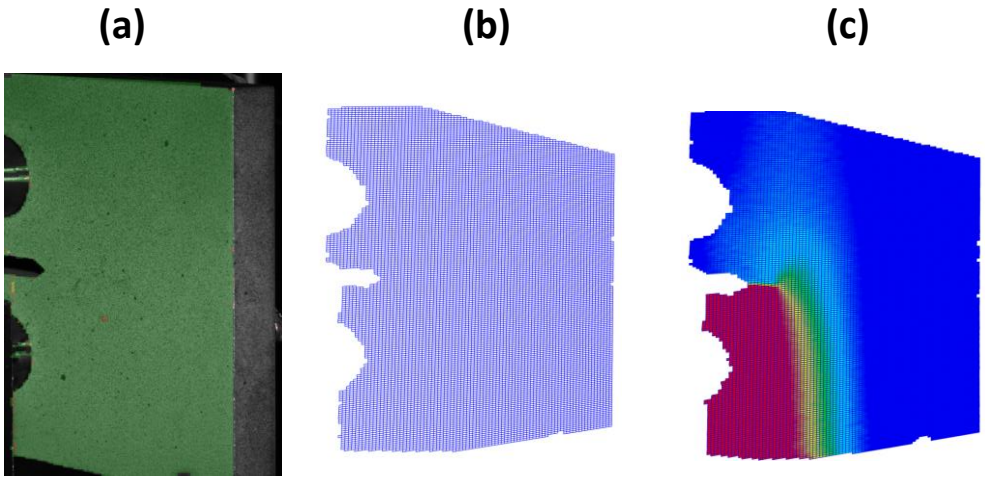

Figure 3.13: (a) DIC image with calculation field overlay map, (b) displacement mesh field, and (c) interpolated displacement contour with mesh

Other parameters such as the validity quote and computational size are more related to the linear interpolation of the displacement point values which is later used to calculate

the strain field. For instance, a computational size of 3 refers to a 3 by 3 array of displacement points to fit a plane to calculate the strain values for each array. The validity quote is a measure of the number of points necessary in the computational size array to calculate a strain value. The strain values can also be calculated from point-to-point which are referred as line strain gage. Figure 3.14 depicts the concept of using line strain gages

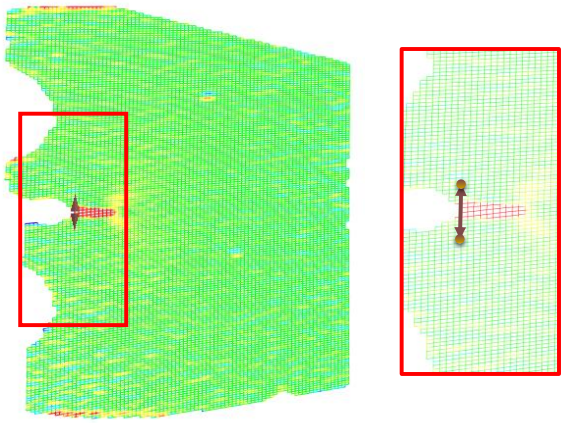

Figure 3.14: (a) DIC image with calculation field overlay map, (b) displacement mesh field, and (c) interpolated displacement contour with mesh

Similar to the strain field, the line strain gage is calculated from displacement field points but only using two points. The line strain gage measures their displacement difference and based on their distance it can provide a strain value. The various types of analyses available for a DIC measurement allow flexibility when calculating and quantifying deformation at complex sites such as a crack tip in the CT sample. All of these tools have implemented and measured to obtain critical parameters as both inputs and calibration features for the computational model.

3.4 COMPUTATIONAL METHODS

The limited and specific cases handled by analytical methods for complex geometries and boundary conditions, for instance in a fracture problem, have been the motivation for the development of several computational/numerical techniques. Although conventional finite element methods tend to be the first choice for advanced structural analysis, other alternative methods have been also developed including finite/discrete element method, the boundary element method, meshless methods, the extended finite element method, the extended isogeometric analysis, and multiscale techniques [161, 162] . This section provides background material and formulations of the computational techniques utilized for the crack initiation problem statement.

3.4.1 FINITE ELEMENT METHOD

The Finite Element Method (FEM) is widely used to solve multi-physics governing partial differential equations including structural/mechanical, heat transfer, fluid dynamics, electromagnetic, coupled analysis and many other applications. The FEM isoparametric discretization has been a great asset to handle complex geometries and complex boundary conditions resulting in its success for commercial applications in which be attributed to its simplicity [162-164]. In a structural analysis, the mechanical equilibrium in a system, as shown in Figure 3.15, can be formulated as a partial differential equation using the tractions (f^t) and inertial forces with boundary and initial conditions.

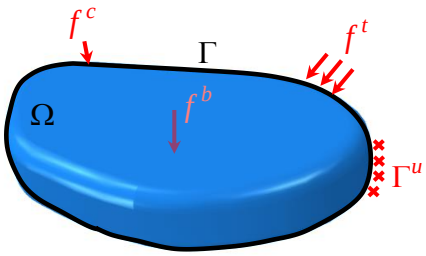

Figure 3.15: Deformable continuum body domain subjected to mechanical loading

The mathematical model of a continuum body in mechanical equilibrium subjected to external forces can be described by a system of 15 equations with 15 unknowns which include three equations from body equilibrium, six from the compatibility of strains (i.e. strain and displacement relations), and six from the material law after simplifying by tensorial symmetry. The Principle of Virtual displacement for a dynamic analysis can be formulated from Cauchy's equation of motion considering the inertial component for a deformable body in Figure 3.15,

$$\int_{\Omega} \rho_{\Omega} \ddot{u} \cdot \delta u \, d\Omega + \int_{\Omega} \sigma(\varepsilon(u)) \cdot \delta\varepsilon \, d\Omega = \int_{\Omega} f^b \cdot \delta u \, d\Omega + \int_{\Gamma} f^t \cdot \delta u \, d\Gamma + \sum f_i^c \cdot \delta u \,, \qquad (3.9)$$

where u is the displacement vector, δu is α virtual displacement, $\ddot{u}$ is the acceleration vector, σ is the Cauchy stress tensor, is ε the Eulerian strain tensor (i.e. $\varepsilon_{ij} = \left(u_{i,j} + u_{j,i} - u_{k,i} \cdot u_{k,j}\right)/2$ from compatibility), ρ is the material density, and f represents the various forces (shown Figure 3.15) for a discrete point c, surface Γ and volume Ω domains. By defining the system in terms of displacements and corresponding time derivatives for a linear elastic material, all equations can be simplified into one relation in tensorial form as

$$\int_{\Omega} \delta u^T \cdot \rho_{\Omega} \ddot{u} \cdot dV + \int_{\Omega} (\delta\varepsilon)^T \cdot C \cdot \varepsilon \cdot dV = \int_{\Omega} \delta u^T \cdot f^b \, dV + \int_{\Gamma} \delta u^T \cdot f^t \, d\Gamma + \sum \delta u^T \cdot f_i^c \,, \tag{3.10}$$

For any geometry, the system can be solved numerically by dividing the volume domain into isoparametric elements and described by a finite element formulation of the weak form of the differential equation. Thus, (3.10) can be solved uniquely at the nodal points, $\hat{u}$, and corresponding time derivatives by using shape functions *N*.

$$u = N \cdot \hat{u} \,, \tag{3.11}$$

Similarly, the strain tensor may be transformed using the compatibility relationship with displacement given as:

$$\varepsilon = B \cdot \hat{u} = D \cdot N \cdot \hat{u} \,, \tag{3.12}$$

where *D* is the derivative matrix operator for the shape functions. Using (3.9) to (3.12), the Principle of Virtual displacement for a linear elastic material assuming small deformations can re-written as

$$\int_{\Omega} (\delta\hat{u}^T) \cdot N^T \cdot \rho_{\Omega} N \cdot \ddot{\hat{u}} \cdot dV + \int_{\Omega} (\delta\hat{u})^T B^T \cdot C \cdot B \cdot \hat{u} \cdot dV = \int_{\Omega} (\delta\hat{u}^T) \cdot f^b \, dV + \int_{\Gamma} (\delta\hat{u}^T) \cdot f^t \, d\Gamma + \sum (\delta\hat{u}^T) \cdot f_i^c \tag{3.13}$$

By taking the virtual displacement as arbitrary, the final FEM formulation is

$$\left(\int_{\Omega} N^T \rho_{\Omega} N \, dV\right)\ddot{\hat{u}} + \left(\int_{\Omega} B^T C B \, dV\right)\hat{u} = \int_{\Omega} f^b \, dV + \int_{\Gamma} f^t \, d\Gamma + \sum f_i^c \,, \tag{3.14}$$

In (3.14), the nodal displacements and accelerations may be factored out from the integrals, thus for each element this formulation can be written in matrix form as

$$M^{(\mathrm{el})}\ddot{\hat{u}} + K^{(el)}\hat{u} = F^{b(el)} + F^{t(el)} + F^{c(el)} \,, \tag{3.15}$$

where $M^{(el)}$ is the mass matrix for a discretized element in the volume domain consisting of the isoparametric shape functions (i.e. basis functions) and the element density, $K^{(el)}$ is the stiffness matrix which contains the internal material tractions and includes the material constitutive law, and $F^{(\mathrm{el})}$ are the force vectors acting within the element. This formulation can be built into a global system by combining all element mass and stiffness matrices. Then, a system of equations can be constructed to solve uniquely for the nodal displacements $\hat{u}$ and accelerations $\ddot{\hat{u}}$ for each element.

FEM has been extensively used for analyzing brittle and ductile fracture of structures. FEM inherently address such cases by tackling both load conditions as well as geometry. The prominent methods within the FEM framework used to mitigate the fracture-related solutions or damage initiation include quarter point singular elements, cohesive zone modeling (CZM), virtual crack closure technique (VCCT), element deletion by damage mechanics formulations and extended finite element method (XFEM) [103-107]. Therefore, the crack initiation problem was solely solved and explained in this dissertation using both the static and dynamic structural FEM analyses. Both approaches in this dissertation to model the growth of a discontinuity are described by a traction-

separation law (TSL), which is a constitutive law based on the relationship between the cohesive opening distance and the cohesive surface tractions.

3.4.2 COHESIVE ZONE MODEL

Conventional fracture mechanics investigates the states of deformation of an existent dominant flaw in a medium which tend to be inherently challenging due to nonlinearities from geometrical factors and plasticity. The CZM is one of the methods within fracture mechanics and FEM framework that pioneered and successfully targeted the problems associated with describing mathematically the fracture process zone for crack growth, as a result of microcrack coalescence and/or plasticity [165, 166]. The cohesive approach is such that the stress singularity is nonexistent due to a relation between the work expended in the discontinuity and fields surrounding the crack tip resulting in finite stresses. From its first formulation as the fictitious crack model introduced by Hillerborg [167] based on ideas proposed by Dugdale and Barenblatt to recent formulations and analysis [104, 168, 169], the CZM has been implemented in various materials where crack growth, delamination, debonding, adhesive failure were among the failure mechanisms studied [165, 169, 170]. The CZM may be implemented as a material interface (i.e. with interaction properties) or as a continuum in which voids grow as a function of loading.

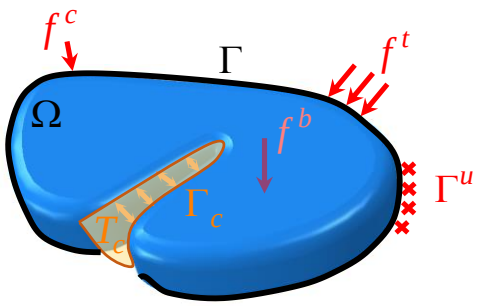

Figure 3.16: Fractured continuum body subjected to deformation with cohesive tractions

The cohesive formulation includes both the bulk material and cohesive constitutive relations specified independently, in which the cohesive relation embodies the failure characteristics of the material in addition to the separation process. Thus, failure is achieved (at the critical state of stress) naturally from the balance laws and corresponding boundary and initial conditions without any additional failure criterion other than the stiffness degradation (softening) initiation. Various type of shapes and functions have been proposed to construct the CZM traction-separation law, which can be obtained by experimental extraction of parameters or optimization/calibration processes using experimental results [171, 172]. The simplest form is the one having the cohesive surface tractions as a function (bilinear or coupled linear-nonlinear) of the displacement jump across a discontinuity. The TSL consists of at least two stages in its simplest form an elastic (small opening) and a softening (large opening) region in which the tractions reduce to allow complete surface separation. The finite element formulation of the CZM can be derived from the principle of virtual work by balancing the bulk, cohesive and external tractions [104, 105, 173] as it was formulated in (3.15). The CZM FEM formulation for the fracture process zone (i.e. finite elements at the discontinuity) within the continuum body with a given TSL in Figure 3.16 can be derived in terms of its internal and external work as,

$$M^{(\mathrm{el})}\hat{\ddot{u}} + K_{coh}^{(el)}\hat{u} = F^{T_c(el)}, \tag{3.16}$$

where $M^{(el)}$ is the mass matrix, $K_{coh}^{(el)}$ is the cohesive stiffness matrix and $F^{T_c(el)}$ represents the tractions related to the fracture process zone. The global stiffness however includes also the bulk stiffness matrix. It is important to note that the stiffness matrix is

expressed in terms of traction derivatives with respect to the opening displacement, thus the TSL local derivative is crucial for the stability of the CZM solution. One fundamental limitation and assumption of cohesive elements and surfaces is that the separation process is confined to a set of discrete imposed interfaces (i.e. lines for 2D or planes for 3D). Regardless of the challenges of the cohesive method that limit the type of model, the method has demonstrated accurate predictions and agreement with experimental results in instances where the path is known or in lamellar solids where the cohesive surface is apparent.

To this aim, the CZM presented in this dissertation was built by implementing user-defined elements to a standard finite element code in order to improve the efficiency and accuracy of the cohesive property for ductile fracture. The CZM TSL was extracted using the displacement and strain fields acquired by DIC during the CT sample experiment, as it's further explained in Section 3.5. Expanding (3.16), the cohesive tractions, T_c, and the traction stiffness, $\partial T_c / \partial D$, can be calculated using a TSL curve. The element stiffness matrix K and nodal forces f_N for local coordinates ζ and η can be expressed as,

$$K_N^{el} = \int_{-1}^{1}\int_{-1}^{1} N^T \Theta^T \frac{\partial t_{loc}}{\partial \Delta u_{loc}} \Theta N d\zeta d\eta \ , \tag{3.17}$$

$$f_N^{el} = \int_{-1}^{1}\int_{-1}^{1} N^T \Theta^T t_{loc} \det J N d\zeta d\eta \tag{3.18}$$

where N **is** the shape function matrix, Θ is a relevant transformation matrix, J is the Jacobian matrix associated with the transformation between the local (ζ, η) and global (x

, y) coordinates, t_{loc} is the local traction's vector and Δu_{loc} is the local opening displacement vector. A complete derivation of the implementation is presented in the user subroutine defined in Appendix A. The relative opening displacements between top and bottom nodes, Δu_{loc}, was passed to a subroutine that computes the corresponding stress/traction values based upon the defined TSL. These tractions t_{loc} are computed in the local coordinate system, and then transformed to the global coordinate system using the transformation matrix Θ. To compute element stiffness matrices and nodal forces and to ultimately solve the static problem, an appropriate Fortran subroutine for the cohesive user elements was implemented [174]. The cohesive elements are composed of zero-thickness quadratic 16-node brick element with 48 degrees-of-freedom coupled to quadratic 20-node brick elements with 60 degrees-of-freedom used to discretize the half CT sample model. It is important to mention that although all the advantages of CZM to relax the singularity problem, this approach has some disadvantages including *a priori* knowledge of the crack and the hurdle of adding additional elements on the crack path interface. Consequently, the CZM served as a verification method for XFEM model presented in Section 3.4.3 [106].

3.4.3 XFEM MODEL

A comparable method to mitigate the mathematical singularities introduced by discontinuities, such as cracks or other types of flows at the continuum level, is the XFEM. This modeling technique treats material flaws as enriched features numerically. XFEM approach uses enrichment functions within the conventional formulation of FEM and has become attractive since the crack propagation is not defined *a priori*. Complex

stress singularities in addition to crack nucleation, growth and coalescence indicative of the nature and physics of cracks in materials are far beyond the capabilities of smeared (cohesive zone) methods dependent on the topology of the finite element mesh.

XFEM is based on the concept of enriched finite element models and partition of unity finite element method who were first proposed and introduced by Benzley (1974) for refining the asymptotic solution of the static fracture problems. The extended finite element methodology was firstly introduced by Belytschko and Black [175, 176] in 1999.

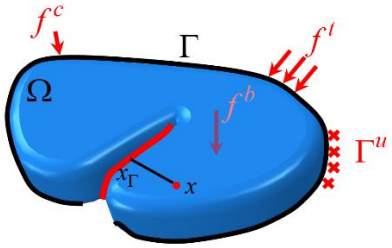

Figure 3.17: Continuum body subjected to loading conditions containing enriched XFEM crack

The XFEM methodology has been rapidly extended to various applications in which cracks are present and the need to know the carrying loads or even the evolution is needed. Some of the advantages, added to those of conventional FEM, include the capability to reproduce the stress singularity at the crack tip and allow unrestrained crack propagation paths within an unmodified FEM mesh. Figure 3.17 depicts a stressed continuum body with an existing crack. The singular stress at the tip in fact is estimated via the XFEM by implementing enriched shape functions which contain the following asymptotic analytical solution

$$f_\alpha(x) = \left[\sqrt{r}\sin\frac{\theta}{2}, \sqrt{r}\cos\frac{\theta}{2}, \sqrt{r}\sin\theta\sin\frac{\theta}{2}, \sqrt{r}\cos\theta\cos\frac{\theta}{2} \right] \tag{3.19}$$

where r and θ are the polar coordinates around the crack tip. A second enrichment term may be introduced for nonstationary cracks. The full enrichment formulation is presented as,

$$u^h(\mathrm{x}) = \sum_{I\in N} N(x) \left[\hat{u} + \underbrace{H(x)a_I}_{I\in N_\Gamma} + \underbrace{\sum_{\alpha=1}^{4} f_\alpha(x) b_I^\alpha}_{I\in N_\Lambda} \right] \tag{3.20}$$

where $\hat{u}$ and $N(x)$ are part of the conventional FEM nodal shape functions, $H(x)$ is a Heaviside enrichment function for crack separation, a_I is the corresponding nodal solution to H in nodes N_Γ in an element with a discontinuity , $f_a(x)$ is given in (3.19), and b_I is the corresponding nodal degrees of freedom at nodes N_Λ at the crack tip.

Some of the differences of XFEM compared to other enrichment methods is the fact that XFEM implements the enrichment at a local level rather than a global one. XFEM can be treated based on the concepts of LEFM following in virtual crack closure technique or a nonlinear fracture zone which follows CZM approach.

The XFEM modality may be applied using a cohesive based or LEFM based approach. Within the practical use procedures of XFEM based on a cohesive formulation include a damage initiation criteria and evolution. The damage initiation criteria include maximum principal stress/strain, quadratic nominal stress/strain, and maximum nominal

stress/strain. The concept of damage initiation criteria and damage evolution for a TSL is depicted in Figure 3.18.

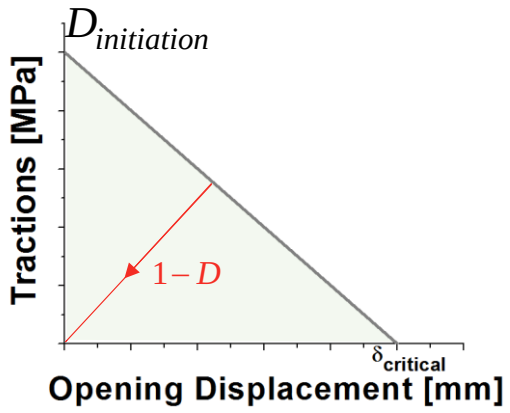

Figure 3.18: XFEM TSL (softening linear law)

The damage evolution is based on a softening curve (i.e. decreasing traction vs. separation) which can be formulated using the displacements or energy. In an energy-based softening, the area under the TSL curve is the energy per unit area (in S.I. units J/m^2) which can be associated to the energy release rate. The parameters for XFEM fracture criteria could be directly extracted from targeted experiments in order to calibrate the crack-initiation model. Part of the calibration process pertain to choosing a damage initiation criteria. The criteria is briefly described in this section for the maximum principal and maximum nominal criteria. The maximum nomimal criterion can be expressed as

$$\max\left\{\frac{\langle\sigma_n\rangle}{N_{\max}}, \frac{\sigma_t}{T_{\max}}, \frac{\sigma_s}{S_{\max}}\right\} = f \tag{3.21}$$

where N_{max}, T_{max}, and S_{max} are the maximum allowable values assigned for the different stress components (i.e. normal σ_n, and two transversal σ_t and σ_s) and f represents the ratio (the criterion is met when f =1). The tolerance is also assigned as a model parameter and can be formulated as:

$$1.0 \leq f \leq 1.0 + f_{tol} \tag{3.22}$$

The symbol <> represents the Macaulay bracket implying that a purely compressive stress state does not initiate damage which can also be defined as

$$\langle \sigma_n \rangle = \begin{cases} \sigma_n \text{ for } \sigma_n > 0 \\ 0 \text{ for } \sigma_n < 0 \end{cases} \tag{3.23}$$

Similarly, the strength-based criterion in (3.21) can be formulated as a strain-based criterion by using nominal components of the strain tensor for a given state of deformation. Furthermore, a second damage initiation criterion can be used in terms of the maximum principal stresses or strains. (3.24) shows this criterion for stresses as:

$$\frac{\langle \sigma_{\max} \rangle}{\sigma^o_{\max}} = f \tag{3.24}$$

where $\sigma^o_{\max}$ is the maximum allowable principal stress. Similar to the nominal stress criterion, damage is assumed to initiate when the maximum principal stress ratio reaches a value of one. When the maximum principal stress or the maximum principal strain criterion is specified, the newly introduced crack is always orthogonal to the maximum principal stress/strain direction when the fracture criterion is satisfied. On the contrary, in the nominal criterion, the crack is parallel to the local direction assigned and goes

through the evaluated element centroid. In contrast with the CZM, the XFEM was implemented using 8-noded linear elements. The model had no symmetries since the crack growth was directional and mesh independent crack growth. Moreover, all the formulations were applied without building additional user subroutines. In addition, the XFEM was solved using an implicit numerical scheme which coupled the static and dynamic solutions into a single computational model with two step analysis. Due to all these advantages and robustness, the XFEM model in this dissertation is presented as the main computational model for linking crack initiation with the release of stress waves.

3.5 COMPUTATIONAL MODEL CALIBRATION, IMPLEMENTATION AND VALIDATION

The integrated method presented in this dissertation attempts to implement phenomenological laws extracted from experimental parameters to build a crack initiation fracture model for AE. The approach followed herein therefore, attempts a departure from both prior analytical and computational approaches in the area of AE modeling, described in Chapter 2. Both a CZM and XFEM framework in ABAQUS was adopted to model the crack initiation and its dynamic response in terms the emission of stress waves. The CZM was used mainly to compare and verify the computational results of fracture and AE generation from a full 3D CT model with the ABAQUS XFEM library for enriched continuum discontinuity onset and growth. The CZM that required two independent models (i.e. Standard and Explicit) to model first crack initiation and then stress wave propagation. In contrast, the ABAQUS implicit solver was solely used in the XFEM approach to model the onset of cracking and the concomitant AE, achieving in this way the use of a single computational model.

The main parameters to calibrate were: (i) the cohesive constitutive law (i.e. TSL) in the case of the CZM, (ii) XFEM damage initiation criterion, and (iii) XFEM damage evolution softening curve for crack growth. All of these tuned model inputs were adjusted by comparing: (i) numerical reaction forces the carrying load obtained from the experiments, (ii) DIC full-field and FEM nodal displacement close to the pins, and (iii) the crack initiation stress state and site. Therefore, the initial step consisted to build a phenomenological TSL using the DIC full-fields as previously implemented in other similar works via inverse or optimization methods [104, 177, 178]. Such earlier approaches directly extracted or optimized displacements and/or strains from DIC and in others the overall tractions from the energy release rate claiming instabilities from the sensitivity of the strain fields. The methodology applied herein is direct extraction of the TSL parameters, including both tractions and opening displacements, using DIC displacement and strain fields close to the crack tip assuring low inconsistency. The selected power law (obtained from [174]) for the TSL can be written as

$$T(\delta)=\begin{cases}\left[1-\left(\dfrac{\delta_c-\delta}{\delta_c}\right)^{\alpha}\right]\sigma_{\max}, & 0\le\delta<\delta_c\\ 0, & \delta=\delta_c\end{cases} \tag{3.25}$$

where δ represents the separation or opening displacement and the curve fitting constraints are σ_{max} , δ_c , and α. In order to construct the TSL, a stress-strain relationship was necessary. Consequently, a tension test was performed to obtain the stress-strain curve for a wrought aluminum 2024 alloy and then confirmed by [179]. A continuous piecewise function was then defined using the logarithmic/true strain and stress

$$\sigma(\varepsilon)=\begin{cases} 73.1x10^{3}\varepsilon & 0<\varepsilon\le 0.0036 \\ 52.61\ln(\varepsilon)+568.42 & 0.0036<\varepsilon\le 0.21 \end{cases} \tag{3.26}$$

where the stress σ is in MPa units and the strain in m/m. The corresponding curve with both logarithmic and nominal values is shown in Figure 3.19. The Young's Modulus was calculated from the linear fit while the Poisson's ratio was obtained from ratio of the experimentally calculated full-field average transversal and longitudinal strains.

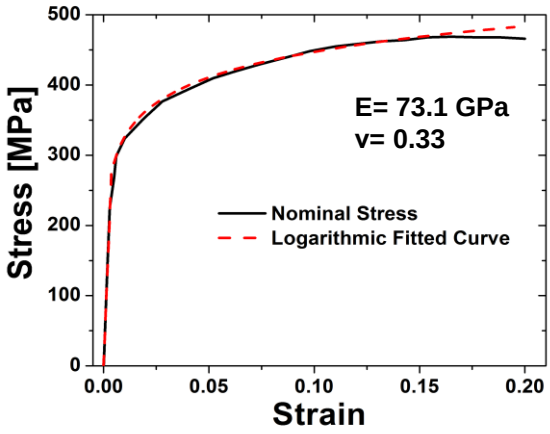

Figure 3.19: Experimentally obtained stress-strain curves for the aluminum alloy 2024 T-3 with mechanical properties

The stress-strain relationship was essential to both create the TSL for the cohesive elements and assign the material law, including elastic and plastic regimes, of the CT FEM model. In the case of the TSL, an array of measuring points close and ahead of the crack tip were extracted.The strain component in loading direction (Mode I) at these sites were then converted to stresses, which can be defined as tractions assuming a small area and neglecting all shear components. The array of points were extracted at different time instances in order to understand the state of deformation related to crack initiation.

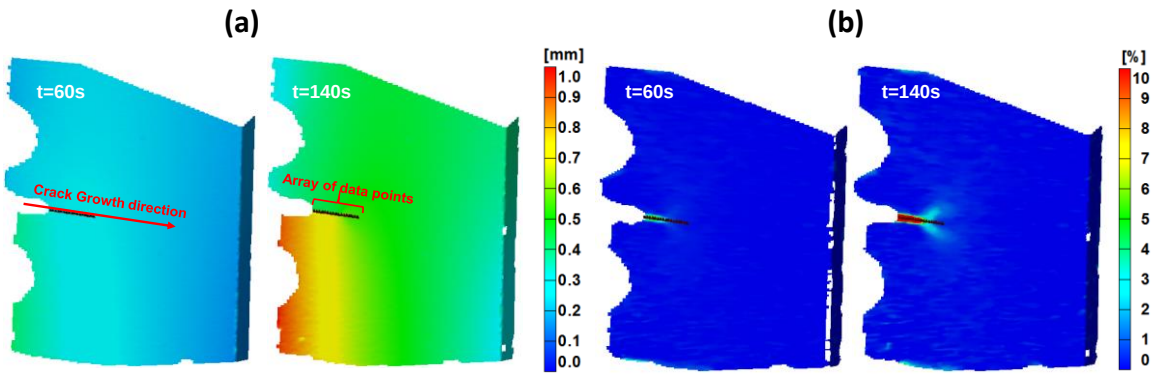

Figure 3.20: (a) DIC displacement field with selected array of data points ahead of the crack tip. (b) Associated full field strain fields in the load direction at 60s and 140s.

Specifically, an array of fifteen experimentally obtained DIC measurement points ahead of the crack tip (i.e. pre-crack region) were used to obtain crack opening displacement and strain values. Figure 3.20 illustrates this process from the DIC full-field displacements and strains at two time instances. After identifying, the critical stage for crack initiation, five time instances and two to three out of the fifteen array points were chosen in order to avoid saturated values from the plastic wake or false data at the discontinuity.

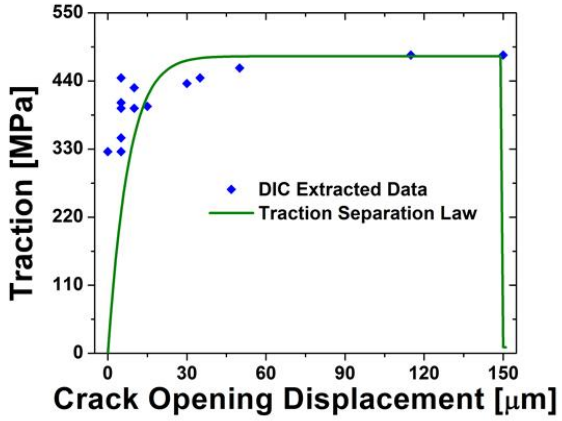

Figure 3.21: (a) Tractions to crack opening displacement values obtained from DIC strains and opening displacements ahead of the crack tip fitted with energy-based TSL

In addition, displacement values directly above and below the crack were measured for each point in the selected DIC stages in order to calculate the crack opening displacements. These experimental data points were used to fit a three-parameter power law function, shown in (3.25) [174], formulated based on the requirement to preserve the fracture energy, as shown in Figure 3.21. Note that based on the procedure described herein, the critical displacement value was determined at fracture initiation with a value of 150 μm, and corresponds to a measurement point in the plastic region of the material behavior described in Figure 3.21. Accordingly, the power law fitting function yielded a tensile strength value of σ_{max} = 480 MPa, while the parameters α was defined to be equal to 19 for a fracture energy estimate G_o=1490.7 J/m.

Before implementing the CZM, the nonlinear cohesive constitutive law in Figure 3.21 was adjusted for a quasi-static half model by reducing the displacements with a factor of two. As mentioned in the previous section, the model consisted of quadratic 20-node brick elements and 16 node zero thickness elements. The brick elements had an elastoplastic material law governed by (3.26) whereas the zero-thickness elements followed the power TSL in (3.25). Additional steps were needed to complete the cohesive part of the model since an ABAQUS user subroutine (UEL) was necessary to build the cohesive elements. All details about this implementation are specified in the user subroutine created and presented in Appendix A. In order to validate the quasi-static model for finding crack initiation state, the half CT model with a UEL was compared to experimental results including the force and load line displacement at the pins. The boundary conditions for the CZM are shown in Figure 3.22.

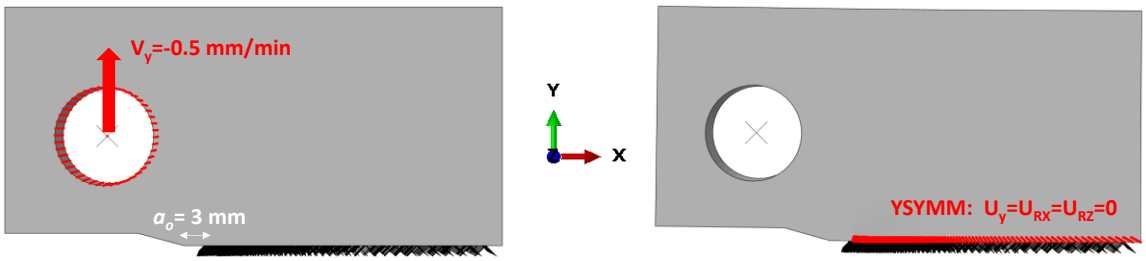

Figure 3.22: (a) Half CT model comparable boundary conditions

Similar to the CT experiment, the model has a loading displacement rate of 0.5 mm/min and a 3 mm pre-crack. This loading rate was implemented at the pin section with a rigid constraint (i.e. assuming the fixture steel pins are rigid in Figure 3.4). The rigid constraint is represented by a center point at the pins constraint with surface around the pins. Before comparing the FEM results with the experiments, the influence of the mesh needed to be analyzed. Two meshes were selected: one having a refined mesh around the crack tip and second one uniform throughout the volume. The FEM results for these two cases are shown in Figure 3.23. The local refinement case had 1200747 degrees of freedom while the uniform global size mesh had 1190250. It is important to note that the uniform mesh is crucial to evaluate since it is used in the subsequent dynamic analysis, thus yielding good results will confirm the global mesh that needs to be used. Both cases showed good agreement throughout the whole volume and close to the crack tip. Figure 3.23 displays the meshes and FEM results for both cases.

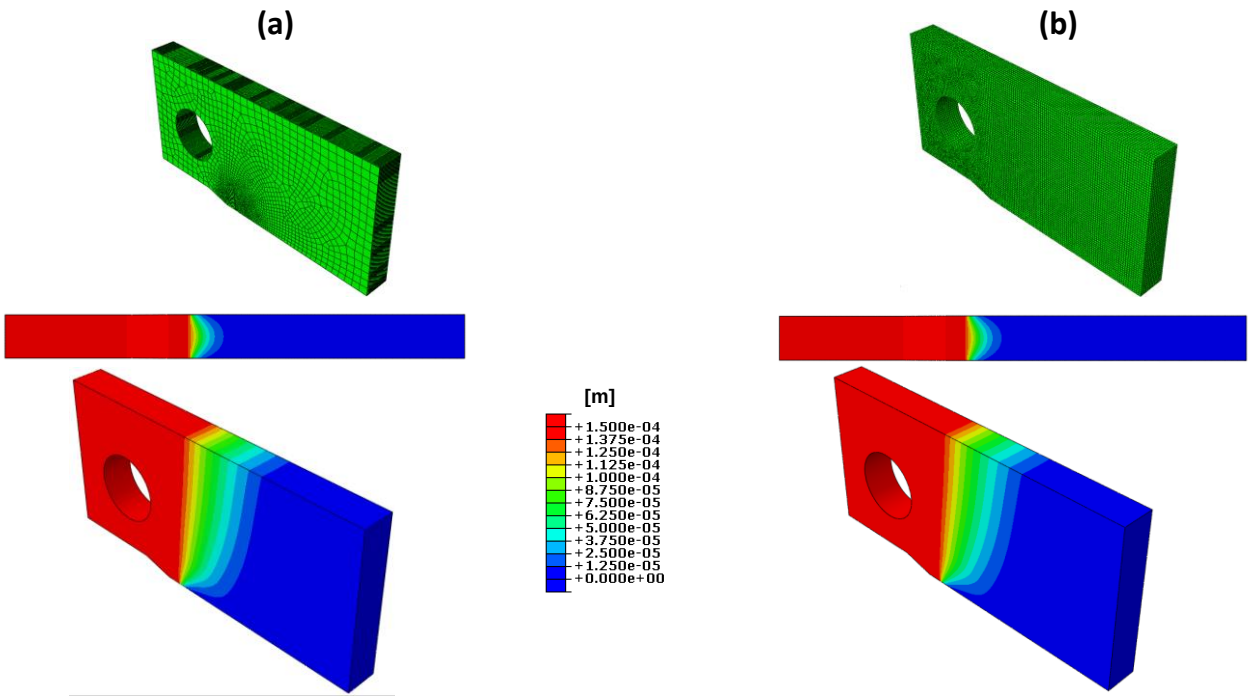

Figure 3.23: (a) Locally adaptive/refined mesh and (b) uniform global size mesh with corresponding displacement contour

As it can be seen in Figure 3.23, the top contour is the crack interface or symmetry interface where the cohesive elements and the precrack are located. The accuracy of the FEM solution, both displacements and stresses, at this interface is essential to quantify and identify the crack initiation stage.

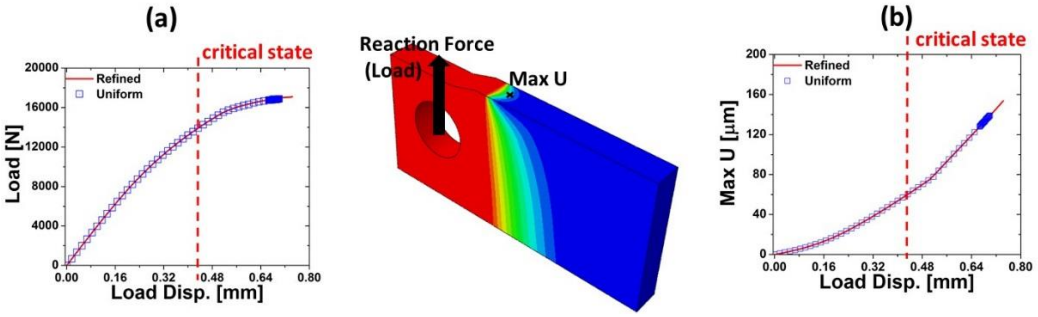

Figure 3.24: (a) Pin reaction force (Load in Newtons) and (b) maximum displacement curves as a function of load displacement at the pins for both mesh cases

The two models were compare using their reaction forces, plotted as Load in N, and maximum displacement at the center of the crack tip, as shown in Figure 3.24. The critical stage is also illustrated which refers to the crack initiation stage, i.e. when the displacement y-component at the interface is 75 μm.

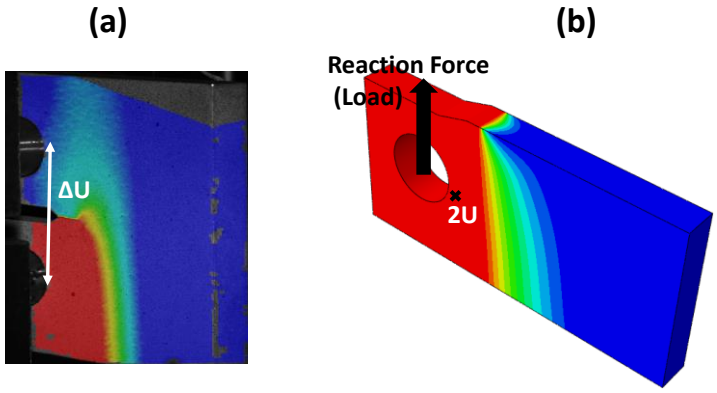

Figure 3.25: (a) DIC and (b) CZM displacement contours with load displacement defined as ΔU and 2U, respectively

Subsequently, the model was compared to experimental values. The load-displacement curve using the reaction force and the difference of surface displacements at the pins was utilized for this comparison. Figure displays the parameters used for comparison and validation of the CZM. For an accurate contrast of the two type of displacements, the surface displacements close to the pins from DIC and FEM were used as load displacements. The difference between using surface displacements and displacements at the pins are depicted in Figure 3.26. It is clearly shown that the surface displacements compared to those from the DIC have a better agreement. This inconsistency may be associated to the machine compliance and/or the rigid pin and fixture clearing which causes additional measured experimental displacements. Furthermore, the results presented in Figure 3.26 showed in a good agreement of the load displacement of the critical. Although the load does not match perfectly the experimental value, the

difference is not as unreliable since the load machine has a sensitivity and a variability with repetitions, as provided by Table 3.1.

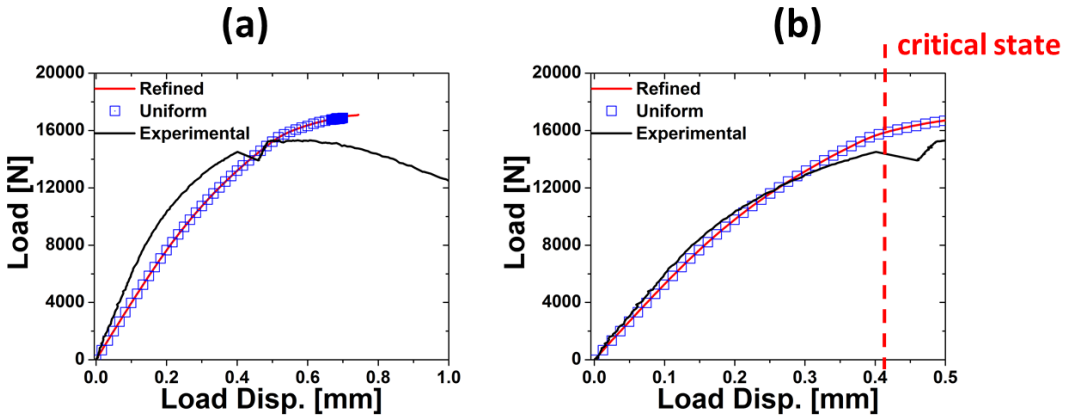

Figure 3.26: Load vs load displacement curves using (a) pin and (b) surface displacements as load displacement

The CZM was successfully validated with experimental results for the static and succeeding dynamic FEM. However, the CZM served also as verification method for the XFEM. Therefore, the XFEM model was initially built using a cohesive-based (explained in Section 3.4.3) approach and the CZM TSL, accordingly. Furthermore, damage initiation and evolution were included in the XFEM model based on cohesive damage parameters including: (i) a maximum principal stress criterion, which was defined to be equal to 480 MPa based on the mechanical behavior shown in Figure 3.21, and (ii) a damage evolution (i.e. softening) parameter which consisted of a sudden stress drop similar to the one in the CZM defined by the energy (i.e. 1490.7 J/m^2) of the TSL curve. The results of this model underestimated the reaction forces, thus the state of stress. However, the results were promising for a crack-induced wave propagation since the hypothesis of linking crack initiation to the dynamic response was achieve. Such results are partially shown in Chapter 4. Essentially, the simulation of wave propagation

with the XFEM model captured the transient process of AE generation exactly at the time instance of crack initiation and prior to the establishment of a new crack increment (i.e. a subsequent equilibrium state).

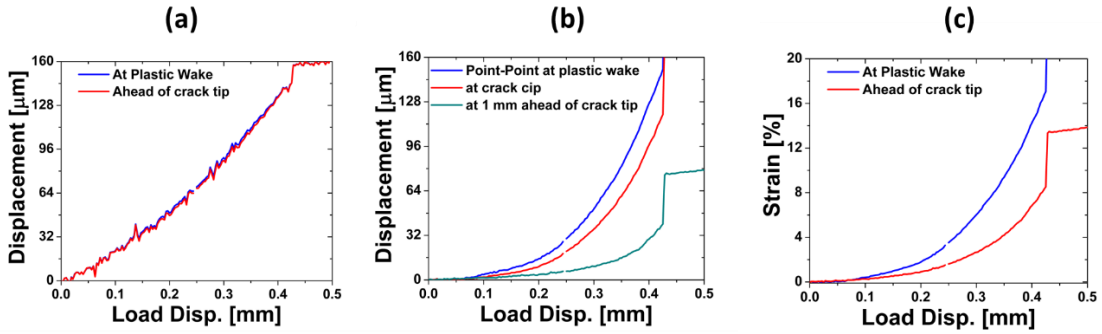

Figure 3.27: (a) DIC point and (b) two-point displacements, (c) strain point values near the crack tip region

In order to optimize the state of stress at crack initiation, it was necessary to calibrate the XFEM disregarding the CZM TSL. Consequently, further DIC analysis and evaluation of the FEM boundary conditions were required. As it can be seen in Figure 3.27, all DIC measured and calculated values close to the crack tip show a high increase at the critical stage. However, in the case of the point displacement, the plastic wake (referring to the false strain or accumulated strain behind the crack tip) site cannot be distinguished from the one at the crack tip which can lead to overestimating or underestimating the displacements. Therefore, two point calculations were performed and averaged using neighboring points at the plastic wake and at the crack tip. The results show a distinction between each location. Notice that the average critical value of opening displacement is close to 150 μm which is similar to the value obtained from the TSL. Although the displacement values were identified, the failure initiation criterion was based on the maximum nominal strain. Hence, a strain analysis was also necessary and was obtained from Figure 3.27c. Strain evolution provided information about the levels of strain

concentrated; however, they were not sufficient to establish the damage parameter. It was shown previously in Figure 3.26 that the boundary conditions dominantly control the load-displacement response, regardless of the mesh density. Therefore, it is crucial to confirm that these results are also applicable for the XFEM model. Two boundary conditions types were used to ratify the results, shown in Figure 3.28.

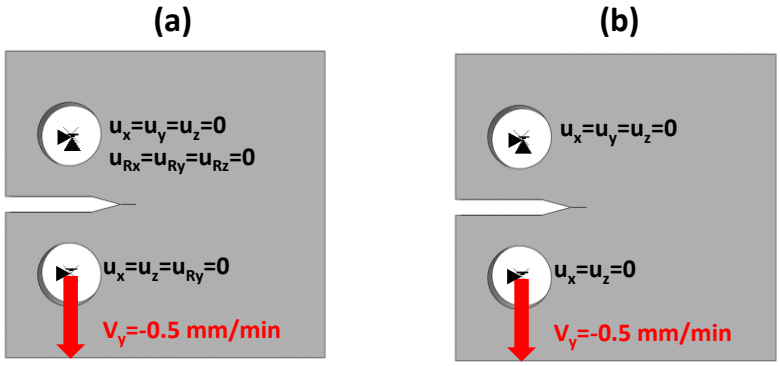

Figure 3.28: (a) Boundary condition (BC1) and (b) BC2

Furthermore, to alleviate the number of degrees of freedom, thus the computational time to test both the criterion and boundary conditions, a local adaptive refining of 400 μm size was applied in volume around and including the crack tip region (shown as S2 in Figure 3.29).

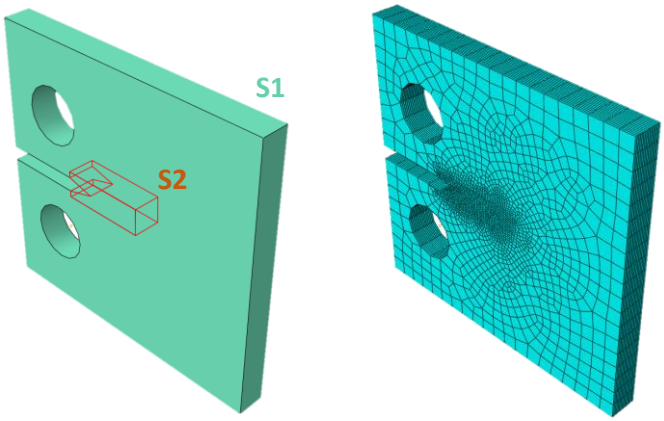

Figure 3.29: CT-A sectioning for refining mesh around crack tip

The effect of the global mesh size of the rest of the volume was studied using three different sizes which are displayed in Figure 3.30. The resulting crack profiles showed good agreement for a given damage criterion.

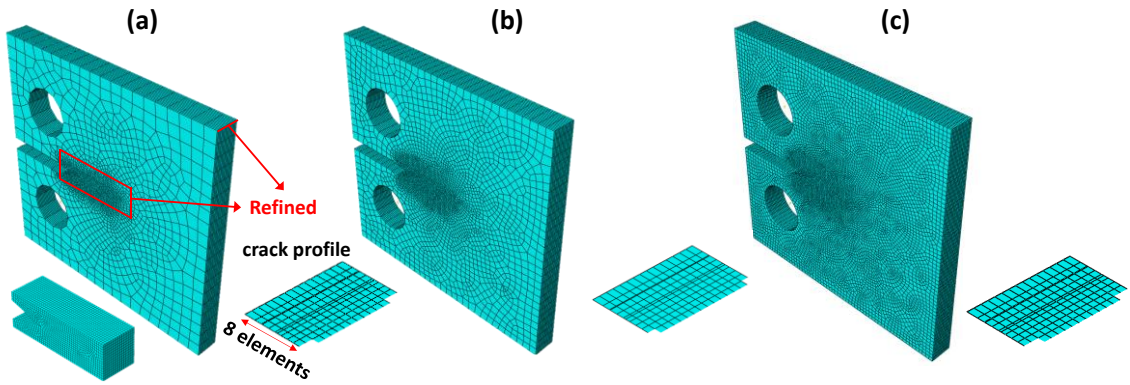

Figure 3.30: Three global size meshes in S2 using (a) 3 mm, (b) 2 mm, and 1mm along with final crack profile and extracted S2

Furthermore, the load-displacement curves for the three cases were compare to quantitatively assure that the global size did not affect the FEM results as long as the S2 partition was created. This comparison is illustrated in Figure 3.31.

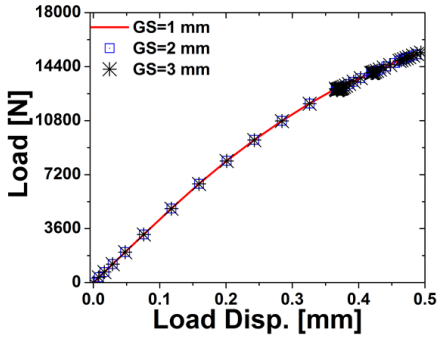

Figure 3.31: Converging load-displacement curves for the three mesh cases in Figure 3.30

The FEM contour results were also compared for the three mesh cases. Figure 3.32 shows equivalent von Mises contours for the three cases with some discrepancies outside

the S2 region. All of these results assure that the model for the optimization can be reduced to the mesh case in Figure 3.30a.

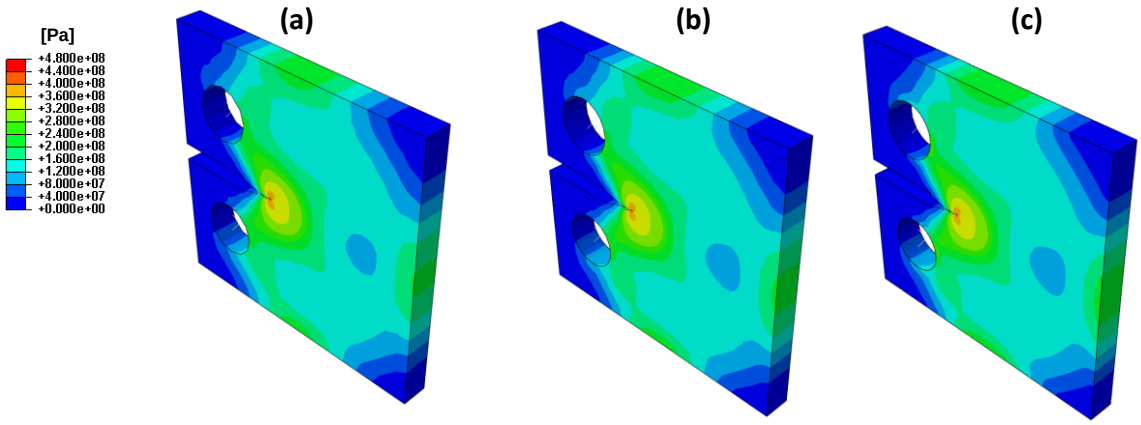

Figure 3.32: Stress contour for the three mesh cases in Figure 3.30

By reducing the computational time, the model was then optimized by adjusting the maximum nominal strain. Moreover, since the shape of the load-displacement curve was consistent regardless of the global size, the second parameter taken into account to calibrate the model was the load drops due to crack growth which occurred approximately at the same state that the crack tunnels to the surface. The boundary condition effects in the load-displacement response of the XFEM model are shown and compared to experiments in Figure 3.33.

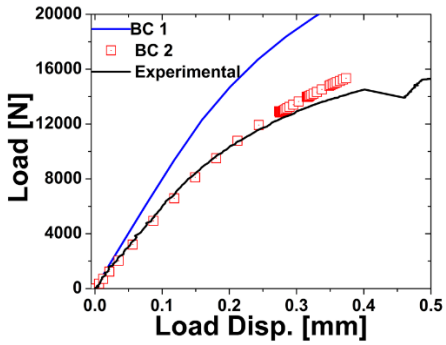

Figure 3.33: Load-displacements curves for both type of boundary conditions compared with experimentally obtained one

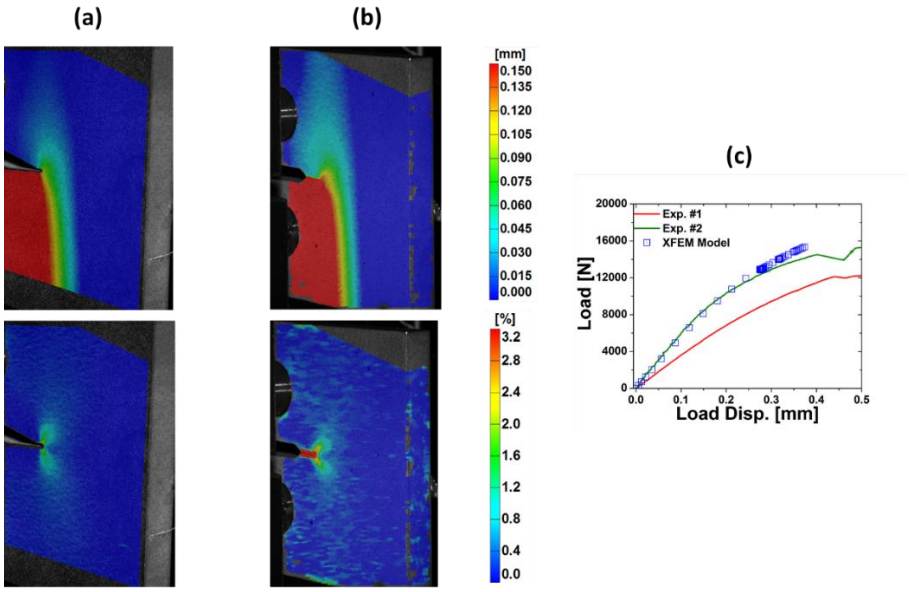

Figure 3.34: CT-A (a) experiment 1 and (b) 2 comparison of DIC displacement and strain full-fields. (c) Calibrated XFEM model resulting load-displacement relationship compared to two different experiments

The results depict similar differences to those obtained for the CZM. These can be correspondingly attributed to the variability from experiment to experiment in addition to the loading fixture which can over or under measured the load in the pins. Figure 3.34 demonstrates this experimental variability comparing the FEM results.

TABLE 3.3: XFEM MODEL INPUTS

Parameter	Optimized Value
Normal strain, $\varepsilon_n^{\max}$	3.2 %
Tangential strain, $\varepsilon_t^{\max}$	10 %
Shear strain, $\varepsilon_s^{\max}$	10 %
δ_{critical}	80 μm

The optimization process then consisted of implementing the appropriate boundary conditions and adjusting the maximum nominal strain for crack initiation. The final

results are listed in Table 3.3. Ultimately, the same process was applied to the CT-B. The boundary condition effects are illustrated in Figure 3.35. Consequently, BC 1 (over-constraint) was selected for the XFEM model.

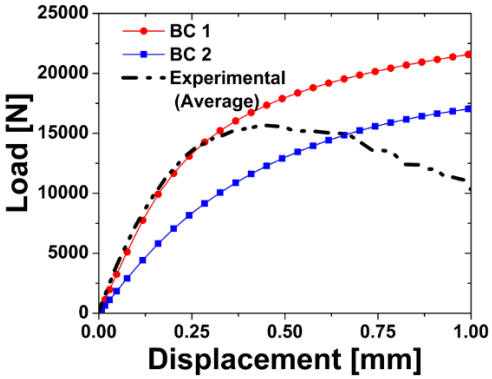

Figure 3.35: Load-displacement curve for the two type of FEM boundary conditions compared to experimental results

In addition, after obtaining the suitable boundary conditions, the same calibration process was implemented using DIC parameters and then comparing the load at first crack initiation and corresponding location. The optimized values for the CT-B were equivalent to those from CT-A except for the normal strain which was 3 %.

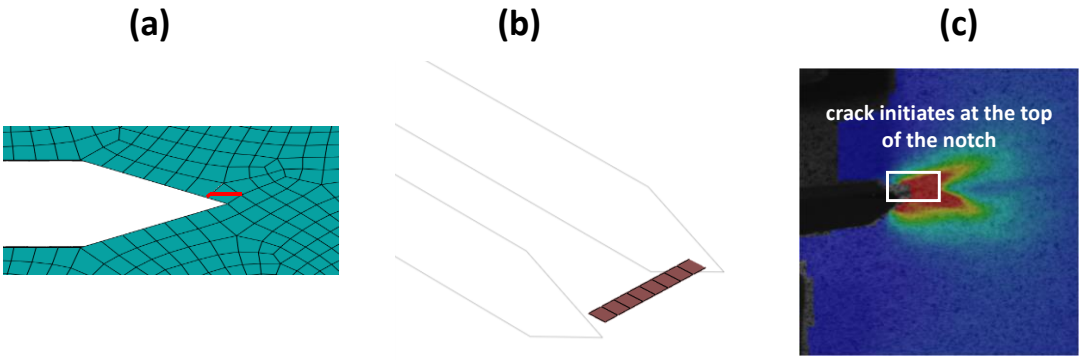

Figure 3.36: Crack formation at the top of the machined notch shown (a) on the XFEM mesh, (b) in the wireframe view through the volume, and (c) in the DIC optical image overlay with the strain

The optimization provided two accurate XFEM models for the crack initiation problem and subsequent dynamic response. The XFEM were validated using experimental parameters from both the mechanical frame and the DIC system. The results of these two models is presented in Chapter 4 for both the static and dynamic simulations. In addition, the dynamic wave propagation results are then compared to the calibrated CZM dynamic for verification.

CHAPTER 4: DATA-DRIVEN COMPUTATIONAL FRACTURE METHOD FOR AE SOURCE MODELING

4.1 INTRODUCTION

Solids when subjected to a disturbance from mechanical, acoustic, thermal, electrical, or chemical sources produce an AE event that travels with a wavefront similar to that of seismic waves [180]. Depending on the source and geometry, the elastic wave generated assumes certain intrinsic features, some of which are affected as it propagates along the medium thus resulting in complexities in identification and classification of the source. These altered traveling elastic waves can be detected by a variety of sensors that are typically mounted on the surface. However, the primitive nature of a wave emanating from an AE source is greatly influenced and affected both by the medium of propagation and type of the sensing, and this process is referred to as the signal shaping effect [181]. As a result, the use of signal inversion techniques used to identify AE sources frequently encounter several challenges, thus it is beneficial to undertake a forward approach of simulating AE from a specific source in the medium in order to better understand the AE process[19, 29, 95, 97, 136]. In addition, a major hurdle associated with acoustics based NDT testing is that of wave propagation in waveguide geometries. High frequencies tend to attenuate significantly as they propagate in materials and structures due to factors such as geometric spreading, dispersion, etc. Therefore, the true "signature" of the source mechanisms difficult to be detected and hence reliable information regarding the state of structural integrity and associated health condition is not effectively attained. The reflections at the geometrical boundaries can greatly

influence the wave signature and could potentially raise false conclusions in SHM applications. In this context, the type, characteristics, reliability, accuracy and use of sensors and their role in decoupling effects that are related to the core of the AE method still need to be quantitatively considered so that both research and development of NDT and SHM applications based on AE is attainable and efficient. In addition to primary AE sources, secondary sources such as fretting, friction, dislocation movement, mechanical and electromagnetic noise etc, can be present and certainly affect the characteristics of what the actual AE user is called to analyze. Similarly, AE signals can be continuous or intermittent and their analysis can greatly influence the reliability of their interpretation. In addition, unwanted signals can also trigger false sources and mask the primary AE sources creating difficulties in actual inspection scenarios.

AE faces limitations and challenge many of which were introduced in Section 1.1 and Section 2.2. To mitigate critical challenges of AE and aid the process of interpreting experimental AE recordings for crack-induced sources, this Chapter presents the results of an integrated computational method, previously verified, validated and optimized by targeted experiments. The presented approach is capable to model the AE source due to crack initiation in a metallic alloy specimen with the assumptions of isotropy and continuity. Such forward approaches for AE source modeling have been suggested using both analytical [80, 82, 126, 182] and computational techniques [24, 30, 81, 183-186], briefly described in Section 2.3,which produced wave content that was used to investigate interactions with the materials' constitutive behavior, geometry, as well as with defects. In general, forward modeling approaches that simulate primitive AE sources could be beneficial in: (i) optimizing sensor placement and spacing allowing more effective NDT

and SHM applications, (ii) quantifying the scattering effect at various structural features, and (iii) filtering recorded spurious signals (i.e. noise) [30, 31].

4.2 FRACTURE MODELING CHARACTERIZATION AND FRACTURE-INDUCED RELEASE OF EMISSIONS

The results included an analytical and computational analysis of the static crack initiation and the subsequent dynamic response of in Compact-Tension (CT) type sample geometries. To this aim, data from crack initiation experiments, as presented in Section 3.5, was used to obtain full field deformation measurements ahead of the crack tip which assisted in defining fracture mechanics parameters and to construct a traction-separation law for a 3D CZM which was subsequently extended to a XFEM-type model. Computational results obtained for both the static (crack initiation/growth) and dynamic cases (transient wave propagation) using the CZM were utilized to validate and verify the results obtained by the XFEM computational approach.

4.2.1 STATIC SIMULATIONS

As it was introduced in Section 3.5, a 3D half-symmetry computational CZM was utilized taking the advantage of symmetries in the CT specimen. In contrast and due to the asymmetric crack growth in the XFEM, a full model simulation was implemented. The corresponding results of both models (including the optimized models) are presented in this section. All boundary conditions were replicated from the experimental setup (all details described in Section 3.5)

The CZM was solved statically to the first increment of crack growth. Specifically, the time needed for crack initiation was found using a critical crack opening displacement

value of 150 μm for the full model and 75 μm for the half symmetric model, based on the TSL defined experimentally. In addition, the stress relaxation, observed at the crack front, was another indication of crack initiation at the cohesive elements. By using these two parameters, the critical time for crack initiation was found to be ~31sec, which corresponds to an approximate value of 0.25 mm of total displacement in the loading direction. The pertinent opening displacement results are shown in Figure 4.1.

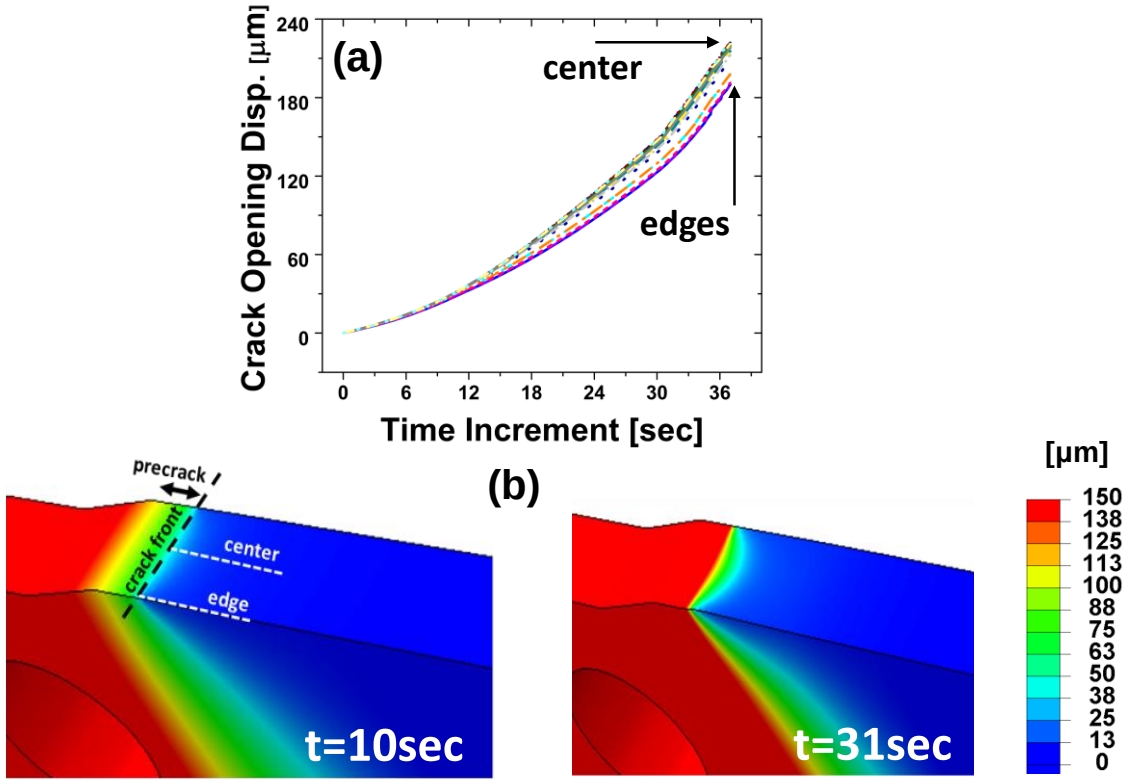

Figure 4.1: (a) CZM nodal displacement histories at the crack front defined in (b), as shown in (b); (b) displacement contour in the loading direction at initial (t=10sec) and critical crack growth time increments (t=31sec)

Figure 4.2 presents the displacement profiles in several nodes along the crack interface (i.e. ahead of the crack front) at the center through the thickness, which is where the point of maximum displacement occurs as shown in Figure 4.1. The horizontal darker line in Figure 4.2 was used to mark the critical crack opening displacement value in the half

symmetry model (defined previously to be 75 μm and 150 μm for the full model denoted as an insert in Figure 4.2) to visually show that for time instances greater than ~31 sec, the opening displacement values computed begin to exceed the critical value and therefore crack initiates according to the CZM. At exactly a time instance of 31 seconds, for example, a crack length, orthogonal to the loading direction and equal to 220 μm, can be defined by the distance along the half symmetry line at the center of the crack front; and for which the calculated opening displacement was greater than the critical value. It can also be seen that as time increases, the crack opening displacement values were always higher near the crack tip and decrease nonlinearly for increasing distance from the crack tip (denoted as distance from the crack front in Figure 4.1b).

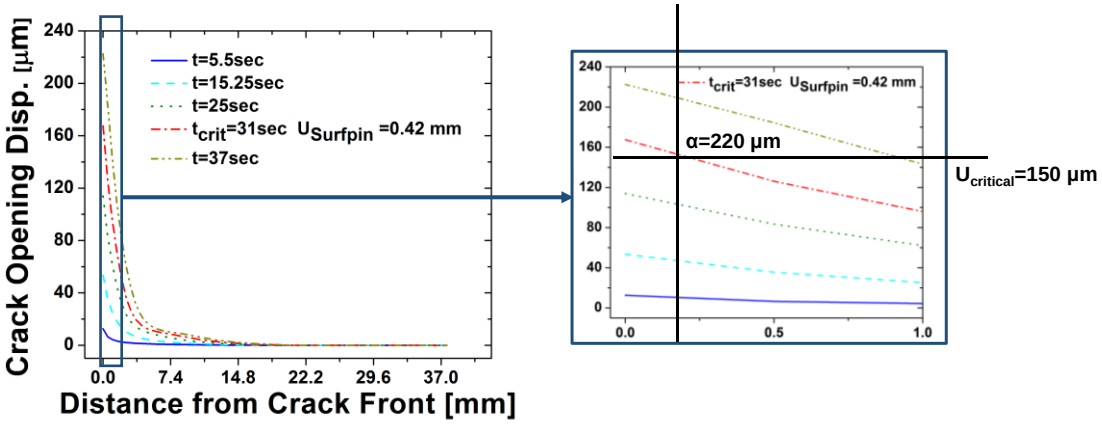

Figure 4.2: Crack opening displacement profile evolution as a function of the distance from the crack front at various time instances and for the central nodes that have the maximum displacement in the parabolic profile through the thickness

Furthermore, opening displacement values for several points along the crack front are plotted as a function of time increments are shown in Figure 4.1a. A linear increase of crack opening displacement up to approximately 10-12 seconds, followed by a nonlinear increase due to the development of the plastic region near the crack tip is observed in Figure 4.1a. This behavior was characteristic for all nodes along the thickness, with

higher values at the center of the cross section (i.e. at the middle point through the thickness) forming the parabolic profile shown in Figure 4.1a. Similarly, the XFEM model was run until the first crack increment was observed according to the defined damage criteria mentioned earlier. Figure 4.3 shows the computed stress (Figure 4.3a) and displacement (Figure 4.3b) contours, which provided information about the crack process observed at the crack surfaces beyond the pre-crack. The maximum value of 480 MPa was reached near the center of the interface thickness, as shown in Figure 4.3a, which agrees with the CZM results in Figure 4.1c, which furthermore validated the use of a half model in the case of CZM.

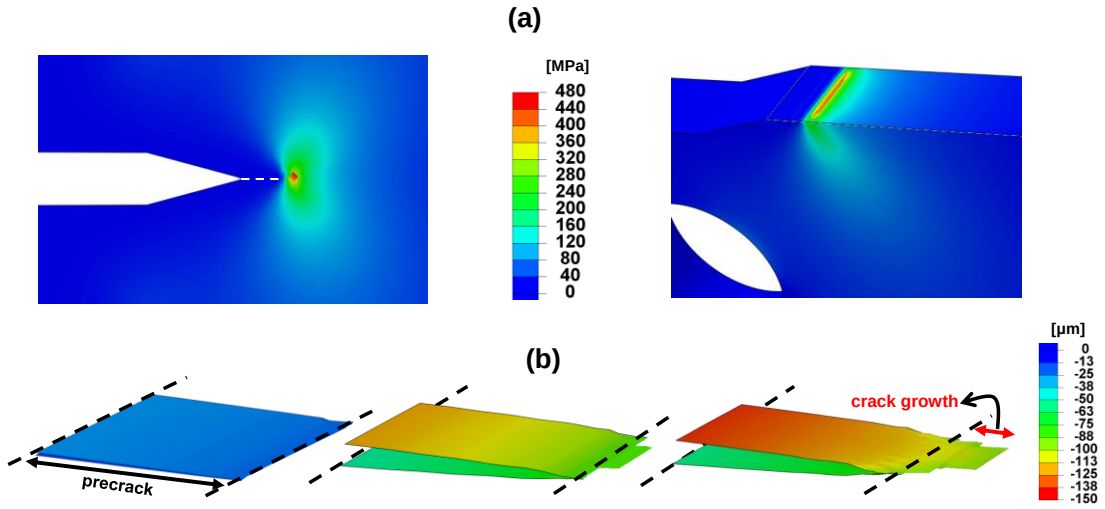

Figure 4.3: Loading direction stress contour at the onset of crack growth for two sections: near the crack tip (Left) and through the thickness (Right). (b) Displacement contours at the crack surfaces and associated growth

Moreover, Figure 4.3b depicts the crack growth in terms of the displacement contour for an extracted "cut view" of the crack surfaces. Specifically, the crack initiates and grows at the center as computed by both the CZM and XFEM models. Based on the results in Figure 4.3b, a crack increment of ~400 μm in the direction parallel to the pre-crack and

an average 600 μm through thickness was computed for the first crack increment. In addition, the displacement and stress results from the optimized XFEM model, which was implemented the maximum nominal strain criterion, are presented and show some similarities. The corresponding contours of three views at the critical time instance are illustrated in Figure 4.4.

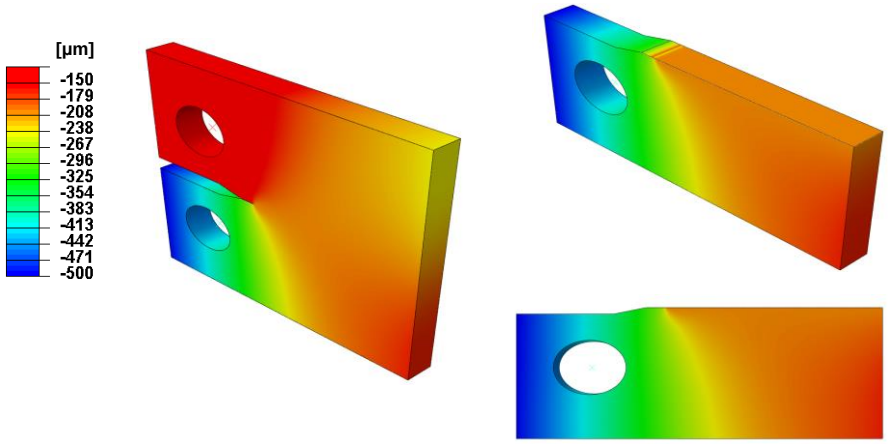

Figure 4.4: (a) Optimized XFEM displacement contours in the loading direction for three different cut views at critical stage time instance

The displacement contour at the surface depicted a gradient across the crack tip and a rather linear gradient around the displacement controlled pin. One difference was observed at the crack interface where the displacements showed a flat distribution in addition to displacement value jumps close to the crack tip and through the volume.

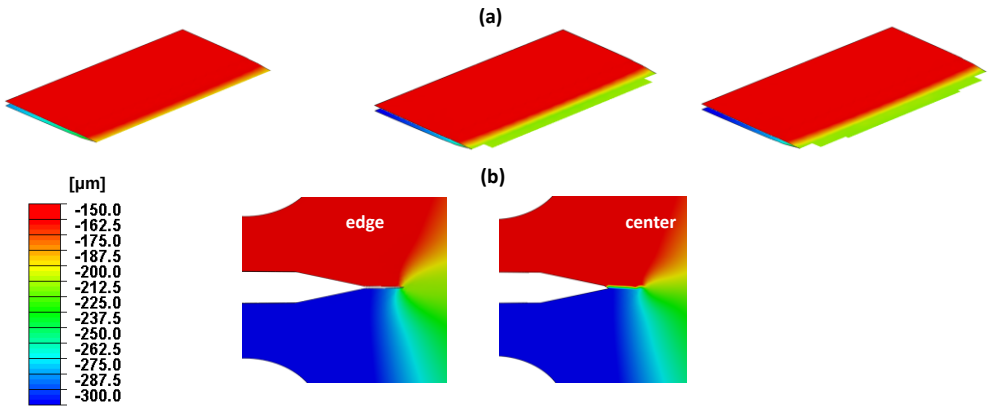

Figure 4.5: (a) Crack profile as it grows with displacement contour plot. (b) Displacement at the surface and at the center (cut view) through the volume close to the crack tip

This can be attributed to the linear elements, as well as the type of symmetrical cut used to expose the through volume results and the non-structure elements around the crack tip. It is important to note that the contours are not symmetric due to the imposed boundary conditions. The displacement close to the crack tip can be obtained from the model. Figure 4.5 illustrates the evolution of the displacement map close to the crack tip as the crack nucleates. Moreover, the optimized model load-displacement response is shown in Figure 4.6.

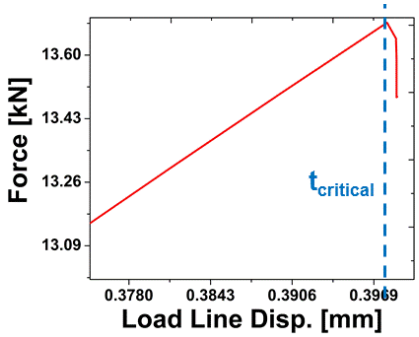

Figure 4.6: Load-displacement at pins relationship close to the crack initiation stage

The load-displacement relationship clearly depicted the start of a critical for a given crack growth increment with a drop in the load. Identifying the critical stage is necessary for the dynamic problem as well as to study the state before crack initiation. The stress contours at this stage are illustrated in Figure 4.7.

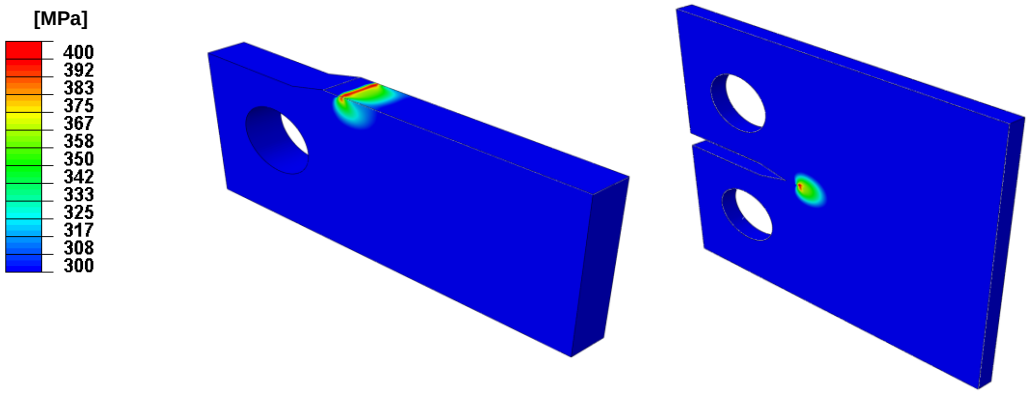

Figure 4.7: Stress contour in the loading direction at the critical stage of crack initiation presented in two symmetrical cuts of the optimized XFEM model

The stress distributions show the concentration close to the crack tip and corresponding nonlinear fields due to accumulated plasticity. Notice that the "kidney" is more pronounced compared to the results presented in Figure 4.3. Similarly, the strain distributions are plotted in order to obtain an idea of critical sites in Figure 4.8. The maximum value in the legend was chosen to be 3.2 % since this is the damage initiation value for the nominal strain-based damage initiation criterion utilized for the optimized model. The through thickness cut view clearly shows where the crack could potentially confirmed by Figure 4.5.

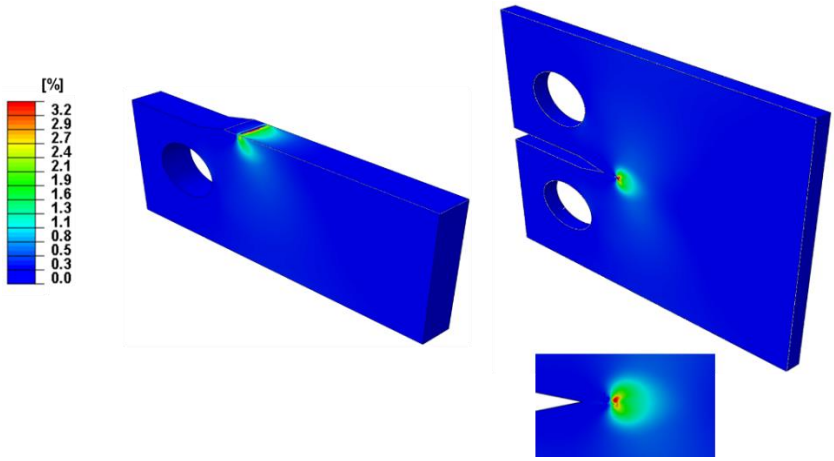

Figure 4.8: CT-A Strain contour in the loading direction at the critical stage of crack initiation presented in two symmetrical cut views

Similar results were obtained for the CT-B; however, the fact that the sample was not precracked complicated the fracture model. After CT-B model was calibrated, the strain-based criterion had many similarities to the CT-A, indicating that the damage criterion was not geometry dependent but material dependent. The XFEM model with nominal strain criterion with maximum allowable value of 3% resulted in crack growth before reaching the maximum load value attained in the experiment (shown in Figure 4.9). Although this could be indicative the model was underestimating the load response, the

crack growth attained by the model occurs through the thickness at this critical time instance.

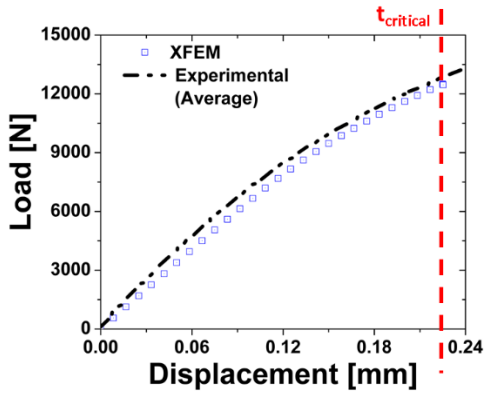

Figure 4.9: CT-B (4 mm thick) load-displacement response showing $t_{critical}$

The maximum load reached by the XFEM model before crack initiation is close to 12,000 N, while its corresponding displacement is approximately 0.23 mm. These results show lower values compared to CT-A which are reasonable since this sample is thinner and does not include a precrack.

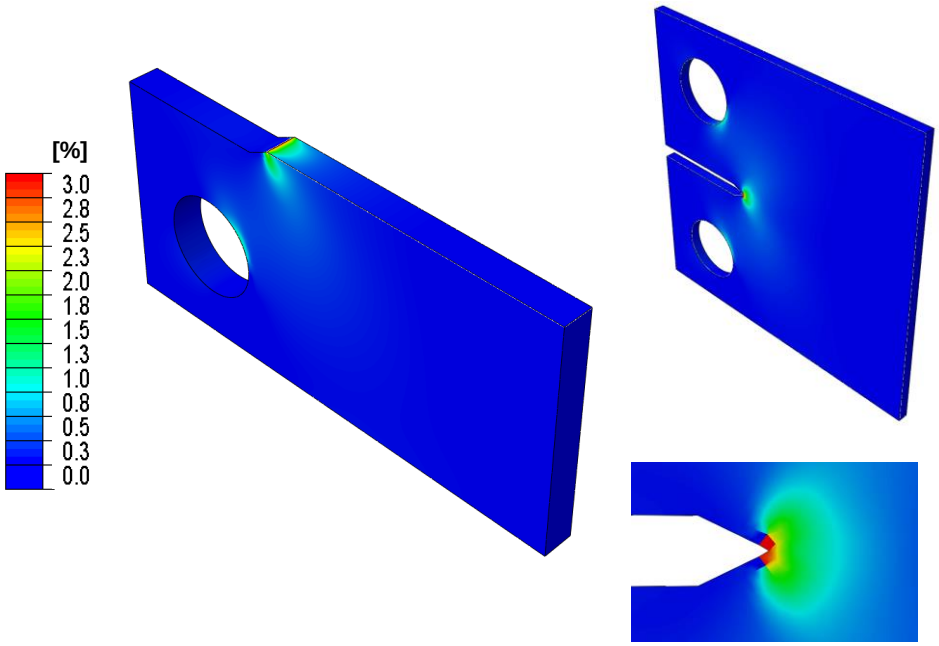

Figure 4.10: CT-B Strain contour in the loading direction at the critical stage of crack initiation presented in two symmetrical cut views

Figure 4.10 illustrates three cut views of the CT-B with strain contours at the time right before crack initiation. The results show two elements with strain concentration as high as 3%, being the top element the highest one. Consequently, as it was shown in Figure 3.36, the crack initiated on the top through the element with a surface perpendicular to the loading direction. The static simulations for both models quantified the transition from an undamaged to a damaged stage based on the determined criteria for crack initiation. The results presented in this section were subsequently used in dynamic simulations in order to model the emission of waves due to the crack initiation.

4.2.2 DYNAMIC SIMULATIONS

To simulate wave propagation at early stages of cohesive crack growth a full as opposed to a half dynamic model was utilized in ABAQUS/Explicit. The model was meshed using an element size of 400 μm, with 8-noded linear and reduced integration brick elements (C3D8R). A displacement excitation was applied in the form of a Dirac delta function $\delta(t)$ (formulated similar to the probability density function of the Gaussian distribution plotted in Figure 4.11),

$$\delta(t) = \frac{C}{a\sqrt{\pi}} e^{-(t-1/2a)^2} \tag{4.1}$$

with 1 μs duration along the entire crack interface (i.e. from the crack front to the far edge). In Eq. (4.1), α is a constant which adjusts the period of the Dirac delta function and C is a constant used to achieve the desired displacement magnitude jump obtained from the static CZM simulations. It should be noted that the integration time step of 0.1 μs, whichwas used in the dynamic simulations, allowed a sampling frequency within a

range of values as suggested by the Nyquist criterion for an AE sensor with 1 MHz bandwidth. Different from the CZM which required two independent models (i.e. Standard and Explicit) to model crack initiation first and then stress wave propagation, the ABAQUS implicit solver was the only one used in the XFEM approach to model the onset of cracking and the concomitant AE, achieving in this way the use of a single computational model. The emission of waves due to the onset of cracking was investigated using both the CZM and XFEM static results, described previously.

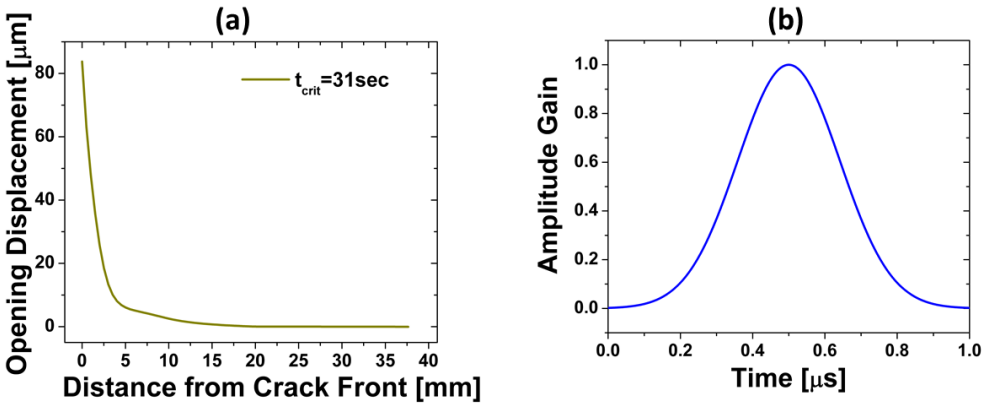

Figure 4.11: (a) Nodal displacement profile at critical time for crack initiation for the CZM and loading function time history defined for wave propagation studies

Specifically, for the CZM results shown in Figure 4.1, the computed crack opening displacement profile at the critical time for crack initiation (~31 μs) was used to determine an initial displacement boundary condition along the crack interface in a corresponding full CT model intended to model the transient wave propagation process, i.e. AE generation at the crack site. To accomplish this, the displacement profile shown in Figure 4.1b at the critical time was fitted by an exponential function, from which a first crack increment of length equal to 220 μm was determined, as shown previously in Figure 4.2. Based on this calculation and to appropriately model the rapid release of

energy due to crack initiation, a Dirac delta function illustrated by Figure 4.11b with duration equal to 1 μs was imposed.

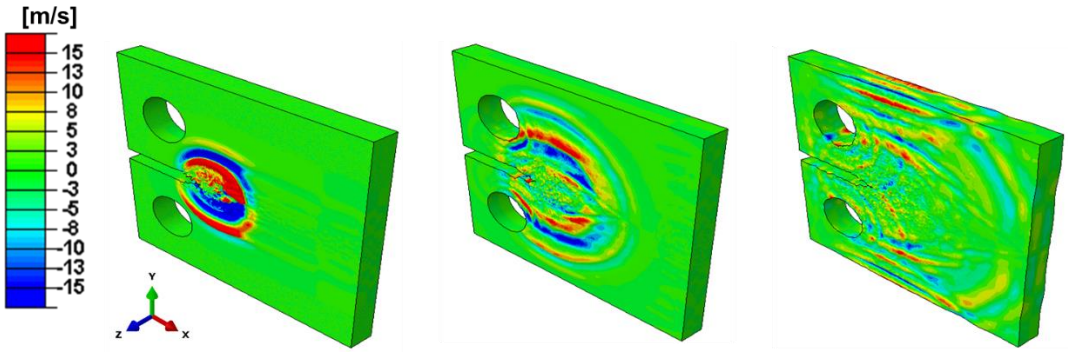

Figure 4.12: Velocity contours at three different stages showing wave propagation

Figure 4.12 illustrates three snapshots of the full field wave propagation process. These contour plots showed symmetric propagation around the crack source location and result in out-of-plane velocity values as high as ± 15 m/s. In order to further understand and validate the computed stress wave emission and propagation in the CT specimen and to potentially identify the characteristics of the primary AE waves associated with crack initiation, the out-of-plane velocity was obtained also using the XFEM approach and was compared with the Dirac excitation method at various simulated sensor locations, as shown in Figure 4.13a. The waveforms calculated near the crack (referred to as "close" in Figure 4.13a) for both models are shown in Figure 4.13b. The main differences, such as (mainly) in amplitude and (secondarily) in waveform profiles between the two methods, may be attributed to their computational implementation. In fact, and as explained in the computational modeling section, XFEM uses the same model for both static and dynamic simulations, which allows to intrinsically grow the crack according to the specified criteria. However, in the case of the cohesive modeling approach, two

separate models were used; one to statically compute the crack opening displacement profile at crack initiation and another to study the wave emission and propagation.

The calculated numerical waveforms near the crack source provided a valuable insight on both the signature of the AE source as well as the concomitant wave propagation along with related effects due to geometry. Specifically, in the CZM both the amplitude and the shape of the waveforms are found to decrease upon the interaction of the waves with the holes. Furthermore, the amplitude was noted to decrease upon the interaction of the waves with the boundaries. Subsequently, the waves were observed to reflect at the multiple boundaries and continue to propagate in the medium. Similar effects were observed in waveforms extracted from the XFEM model. The waveforms in Figure 4.13b contain two pertinent highlighted regions one for the portion found to be related to the time interval between initiation and right before the interaction with the pin/holes and the other one with corresponding time interval before arriving and reflecting on the boundaries. It is important to note that all of the waveforms in this dissertation were analyzed using a customized code, which is described and provided in Appendix B.

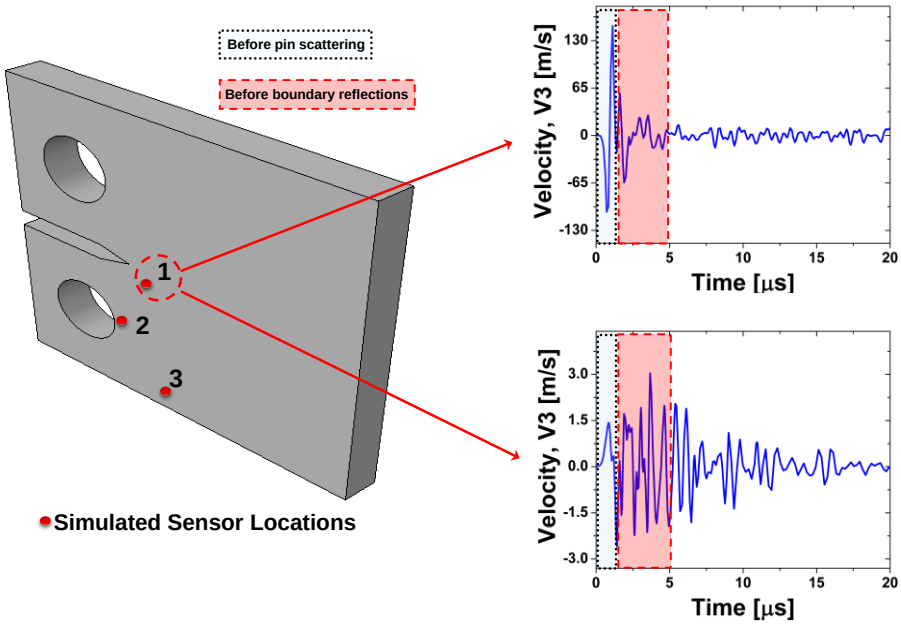

Figure 4.13: (a) Simulated sensor locations for wave propagation investigation. (b) CZM (top) and XFEM waveforms (bottom)

The spectral characteristics of the extracted waveforms were also analyzed extensively. Specifically, for the waveforms in Figure 4.13b, which were computed using the CZM and XFEM approach are shown in Figure 4.14a-b with their spectral analysis using FFT and STFT. Based on these results, then main wave energy is centered in the region between 1500-2000 kHz, and a peak frequency appears in the 1500-1700 kHz region. The STFT distribution revealed that both the low and high frequency wave components have comparable speeds. However, it was also found that the higher dominant frequencies attenuate significantly after the interaction of the stress waves with the holes. A noticeable difference between the CZM and XFEM models (besides their peak amplitude) is the dispersion observed with increasing time to lower frequencies. These discrepancies can be attributed to the difference in amplitude in the captured waves and to the fact that the CZM uses a pulse with a single dominant component of displacement applied in the loading direction.

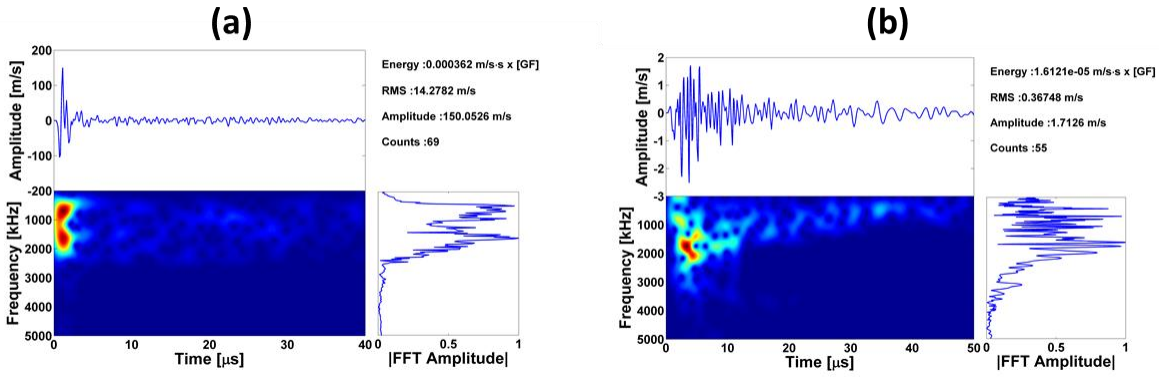

Figure 4.14: FFT results of simulated waveform with corresponding frequency distributions analysis using STFT corresponding to initial part of the wave near the crack tip for both (a) CZM and (b) XFEM

A further investigation of wave propagation as a function of distance from the crack source shows that waveforms extracted from the location labeled as 2 reveal differences in both time and frequency domains (Figure 4.15a and b) compared to the ones obtained in location 1 (i.e. close to the source). Specifically, only low frequency components are seen to be present in the waveforms' first arrival shown in Figure 4.15, with a peak frequency centered around 500-1000 kHz, as confirmed by both CZM and XFEM.

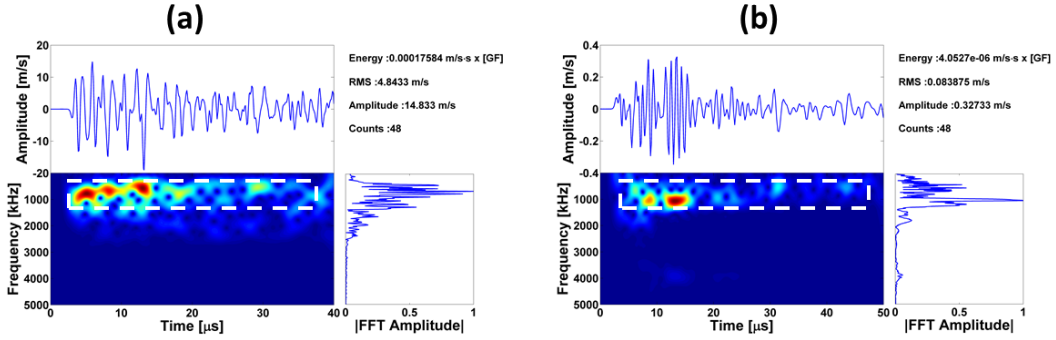

Figure 4.15: Simulated waveforms at locations far from source (i.e. labeled as 3 in Figure 4.13a) and wavelet transforms obtained using (a) the XFEM and (b) CZM. The highlighted regions show the dominant frequencies in each case, which are found lower than the corresponding peak frequencies of location 1 waveforms in Figure 4.14

Furthermore, the waveform amplitude decreases significantly compared to those waveforms extracted close to the crack tip. An overview of the waveform time-

frequency analysis of all three locations marked in Figure 4.13a is provided in Figure 4.18 and Figure 4.19. In summary, the presented simulation results suggest a shift in the dominant frequencies as the wave propagates from the source towards the geometrical boundaries. In addition, the XFEM results revealed significant attenuation of the high frequencies as a function of time. These are direct indications that the characteristics of the so-called "primitive" AE, which is frequently defined as the waveform near the AE source (both in distance and in time) [34], were affected by the acquisition setup. Such "primitive" AE waves carry spectral information that is evolving due to several convolving effects, such as their interactions with the geometry. Waveforms were also extracted along a straight line shown in Figure 4.16, to further investigate the characteristics of the wave propagation in the specimen. At this point, it should be stated again that the assumption was made that wavefronts (as shown in Figure 4.12) are circular and symmetric, thus only waveforms along the lower section of the model were analyzed.

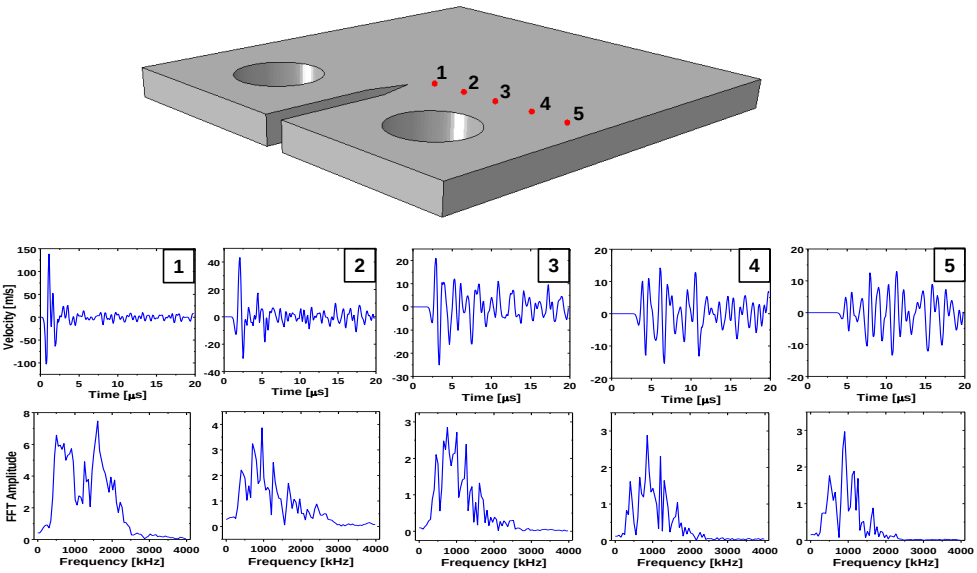

Figure 4.16: (a) Sensor Locations (b) Attenuation plot computed by calculating the amplitude of the out-of-plane velocity waveforms computed using the CZM approach along sensor locations. (c) Out-of-plane velocity waveforms and corresponding FFT results

As the waves travel from the middle to the bottom of the 3D specimen, both the out-of-plane velocity amplitude and frequency content were found to change, in agreement with the results in Figure 4.15.

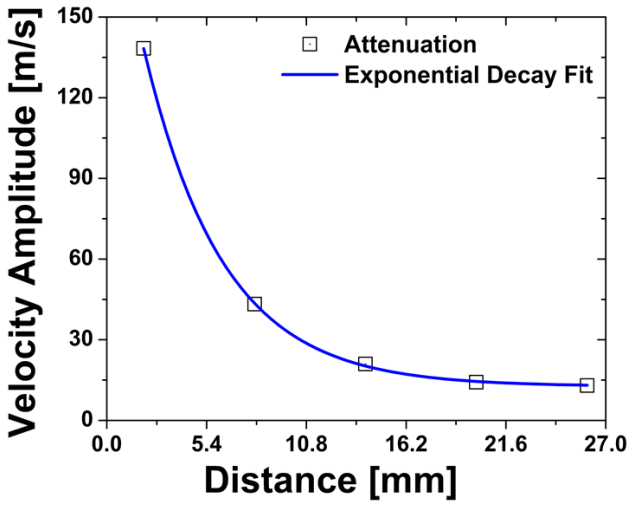

Figure 4.17: Attenuation plot computed by calculating the amplitude of the out-of-plane velocity waveforms computed using the CZM approach for several nodal points

This shift in frequency from ~1700 kHz to 800 kHz and decay in amplitude from 140 m/s to 15 m/s, was prominent in the first three nodes, after which the peak frequency remains nearly constant. A plausible explanation for the shift in the frequency could be found by considering the possibility of geometric spreading of the amplitude and reflections at the pins which is located between the 1st and the 4th node. The decaying in the amplitude could be attributed to reflections and scattering of the waves due to geometry features. Furthermore, a practical physical parameter that affects the experimental application of the AE method is the attenuation resulting from geometrical factors, which is essentially the spreading and wave dispersion that ultimately cause a decrease of the amplitude of the recorded waveforms. As far as attenuation quantification is concerned, several waveforms along a straight line similar to Figure 4.18 were used to compute the

amplitude of the out-of-plane velocity as a function of distance from the crack source. The corresponding results are shown in Figure 4.17 . The evaluated results evidently showed an exponential decay of the amplitude that can be explained to be a consequence of scattering, as explained earlier, in addition to be due to the use of a Rayleigh mass proportional damping coefficient of 0.05 in the dynamic FEM model. This type of attenuation further agrees with experimental AE results, demonstrating the potential of this computational approach to quantify AE effects. Figure 4.18 and Figure 4.19 show results obtained using waveforms extracted in three locations away from the AE source for both methods, as denoted in Figure 4.13a. Based on the results in Figure 4.20 it can be immediately observed that the waveform near the crack has the highest frequency and the greatest time decay among the three groups of waveforms. In addition and in agreement between the results in Figure 4.18 and Figure 4.19, the dominant frequencies appear to decrease when the wave reaches the pin. Finally, mainly the lower frequency components (500-750 kHz) appear far from the crack.

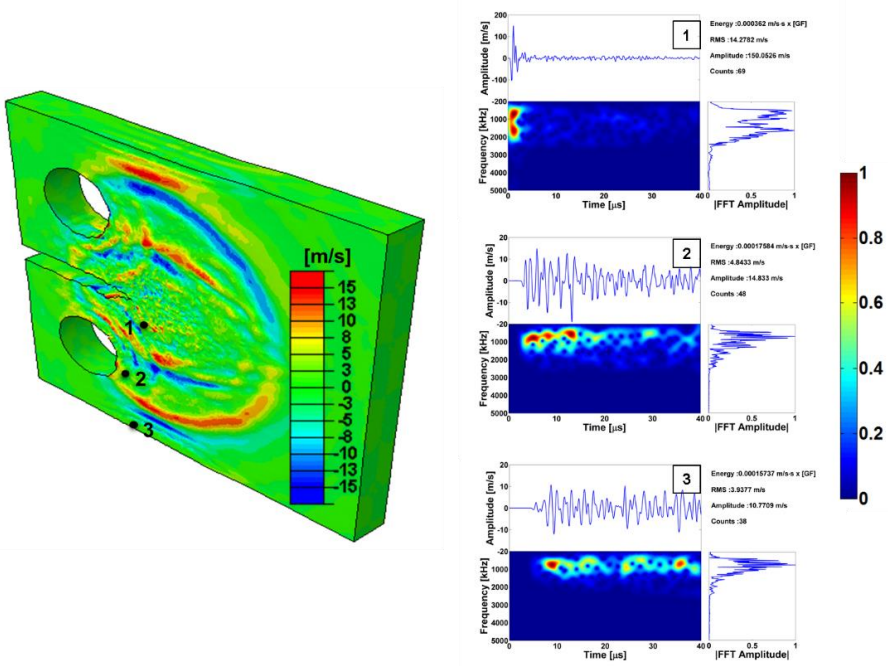

Figure 4.18: Summary of results of the waveform analysis at different locations including near crack tip, near the pin, and far from the source for CZM

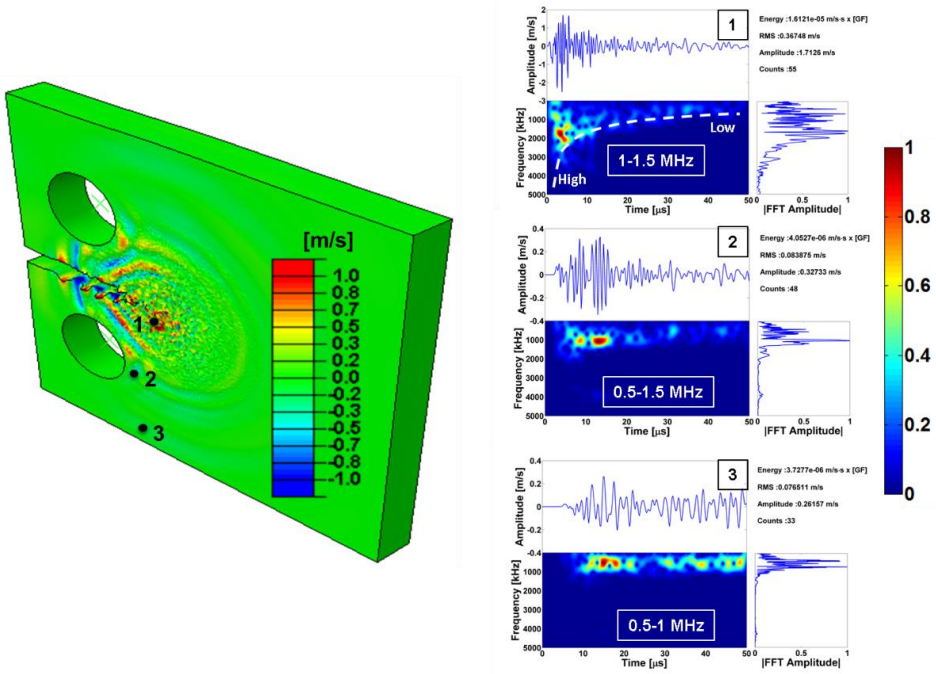

Figure 4.19: Summary of results of the waveform analysis at different locations including near crack tip, near the pin, and far from the source for XFEM

Specifically, it is generally true that the response of a sensor mounted on the surface of a continuum will be the combined effect of either displacement, velocity or acceleration

components depending on the type of sensor. To investigate this aspect of the AE phenomenon, Figure 4.20 shows all three directions acceleration and velocity waveforms close to the crack source location and computed using the CZM approach, along with their corresponding FFT plots. Although loading is applied along the vertical (y-axis) direction and the crack is Mode I, it is interesting to indicate that the magnitude of the out-of-plane velocity (i.e. coincident to the z-axis in Figure 4.20) is higher and more dominant than the other components on the surface.

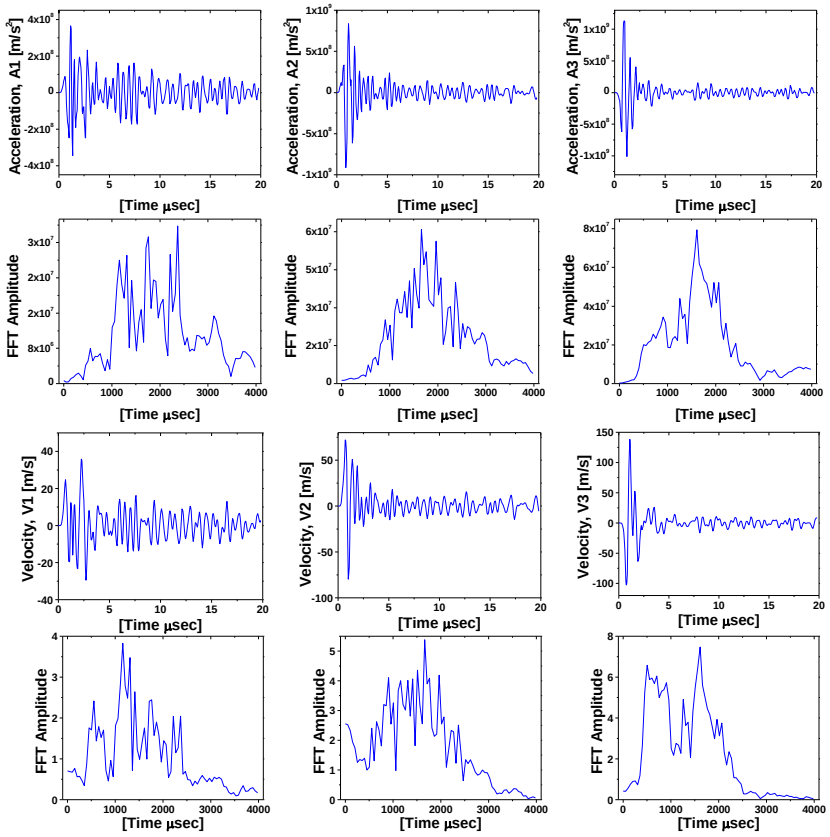

Figure 4.20: Three component of acceleration and velocity waveforms computed using the CZM approach along with corresponding FFT results

Moreover, it is interesting to observe that the three components of both velocity and acceleration data appear to have differences in their frequency response, which clearly shows that a direct quantitative comparison between simulation and experimental results

can only be made in the case that the sensor response is properly understood and tested. Although the dynamic results showed were validated by the results obtained for the CZM, the static solution was not calibrated for the XFEM model. The following results provide the dynamic analysis for the optimized XFEM which has similarities. An important analysis is identifying or quantifying the AE source is to study the displacement close to the source. Figure 4.21 quantifies the displacement related to the crack-induced disturbance for the uncalibrated XFEM model. Notice that the displacement jump, extracted at a nodal point close to the crack tip and at the center through the thickness, was approximately 5 μm and then oscillates around its equilibrium.

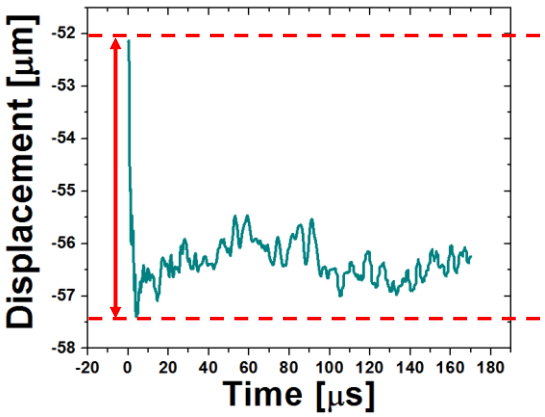

Figure 4.21: Displacement jump of a nodal point close to the crack growth increment (the component measured is in the direction of loading)

Similarly, the same type of analysis was performed in the calibrated and validated XFEM. Figure 4.22 illustrates such analysis as well as the wave propagation visualization at three time instances. However, in addition to utilizing only one point as shown in Figure 4.22a, the same measurement was calculated for two points top and bottom close to the source. It can be observed that the displacement jump is one order magnitude lower than the uncalibrated model, which is approximately 540 nm. Compared to these values the two point analysis showed a value close to double, i.e.

approximately 800 nm. Although the values for the optimized XFEM model seemed lower, the corresponding velocities by observation of the out-of-plane velocity contour have higher values in contrast.

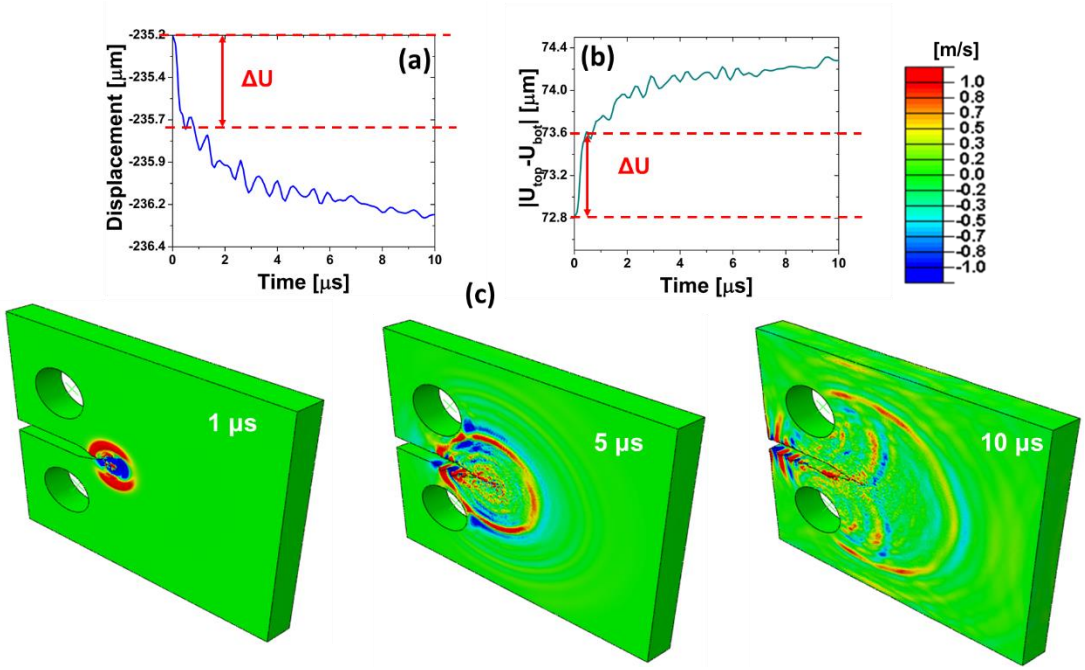

Figure 4.22: (a) Single nodal point displacement jump close to the crack tip. (b) Two point displacement for top and bottom (the components measured are in the direction of loading). Out-plane-velocity contour at different time instance of the wave propagating

Similarly, using the same point in Figure 4.22a, the two other components of the displacement were analyzed which include the *x*- and *z*-component. Although the *y*-component (i.e. in the loading direction) should be dominant, the crack-growth process is three dimensional causing the disturbance to have three non-zero components as well. The plots showed that the z-component has the lowest displacement jump having only 45 nm compared to 435 nm of the x-component.

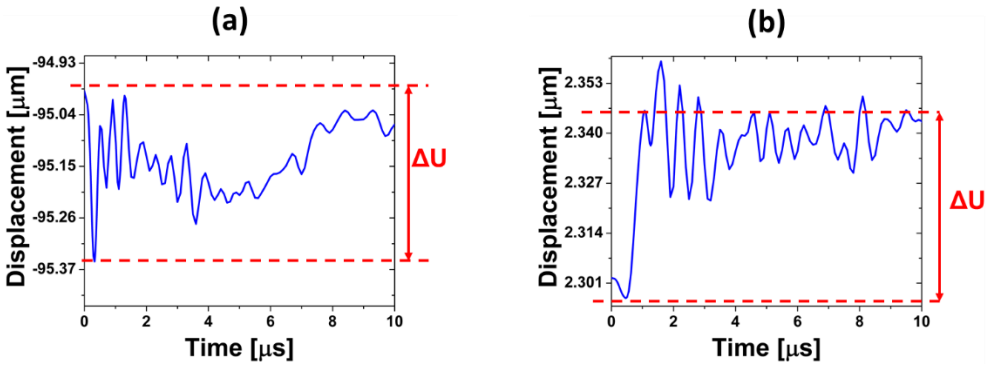

Figure 4.23: Displacement disturbance at the same point as Figure 4.22a for (a) x-component and (b) z-component

This three dimensional concept is visualized in Figure 4.24 by having different cut views and plotting the velocity magnitude with a deformed shape using the velocity component (instead of using the displacement, which is commonly used to visualize deflection). It was clearly shown that the disturbance caused by the crack initiating has three components, with the one in the loading direction being the most dominant.

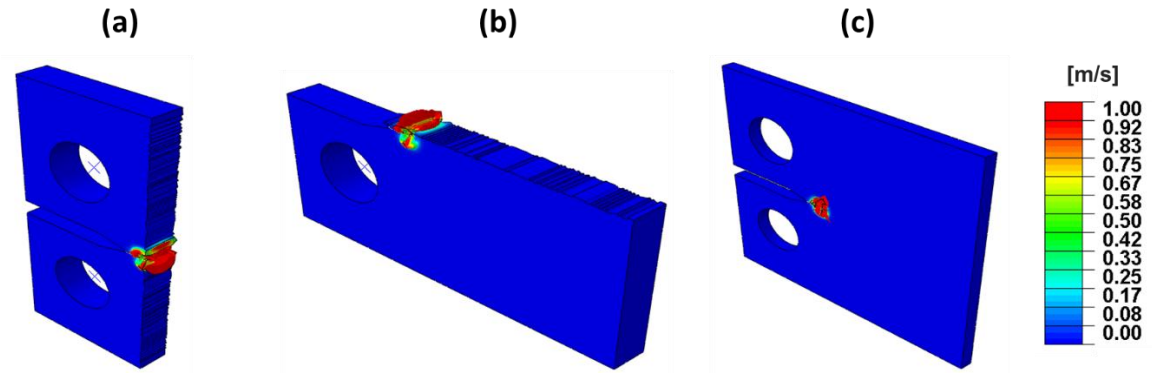

Figure 4.24: Velocity magnitude contour with different cut views to visualize the AE source for the (a) x-, (b) y- and (c) z-component

In order to contrast the results obtained in the optimized XFEM model, a waveform analysis was performed. The extracted waveforms on the free surface of the model and corresponding waveform analysis are shown in Figure 4.25. Similar to previous results,

the frequencies shift tow lower frequencies as function of time and distance. In addition, the same dominant frequency ranges are present in the spectral analysis.

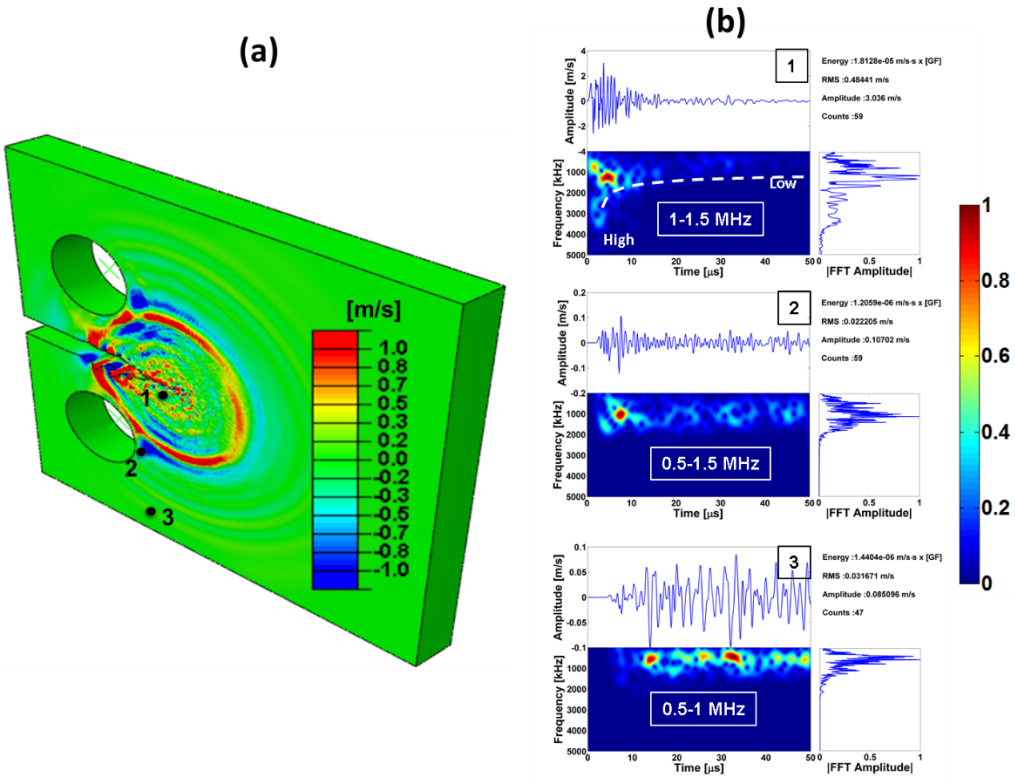

Figure 4.25: (a) Simulated sensors locations for primitive AE waveforms shown on top of the out-of-plane velocity contour. (b) Out-of-plane velocity waveform analysis at the three marked locations

To further study the effects of the wave on this optimized model, the waveforms were also extracted along the horizontal direction, where they did not face any geometrical factors. Therefore, the wave front cleanly passes through the points marked in Figure 4.26. The wave did not encounter any possible alterations at least for approximately 10 μs which is the time it takes to reach the far edge ahead of the crack (marked as point 3). It can be observed that the dispersion to lower frequencies mostly occurs as function of distance. Therefore, it can be concluded that geometrical features, such as the pin along the vertical, play a major role in attenuation and dispersion.

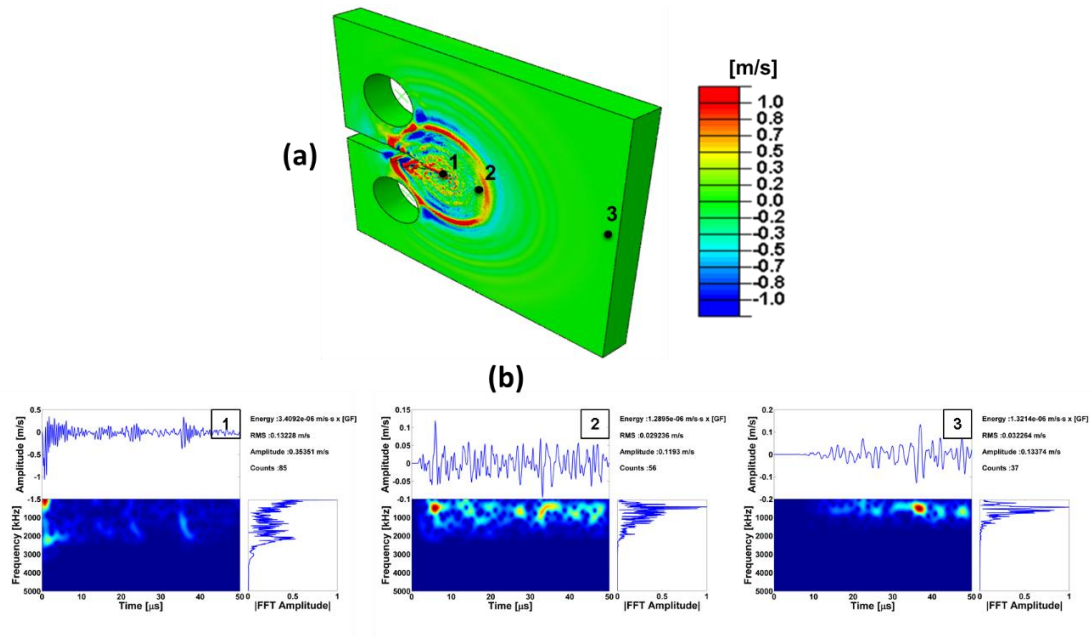

Figure 4.26: (a) Simulated sensors locations along the horizontal to capture cleanly wave front. (b) Out-of-plane velocity waveform analysis at the three marked locations

Similar to previous analysis performed, the role of attenuation and dispersion was performed using a series of evenly distributed point along the vertical. Figure 4.27 clearly illustrates a shift in the frequencies in addition to a decay in the waveform amplitudes.

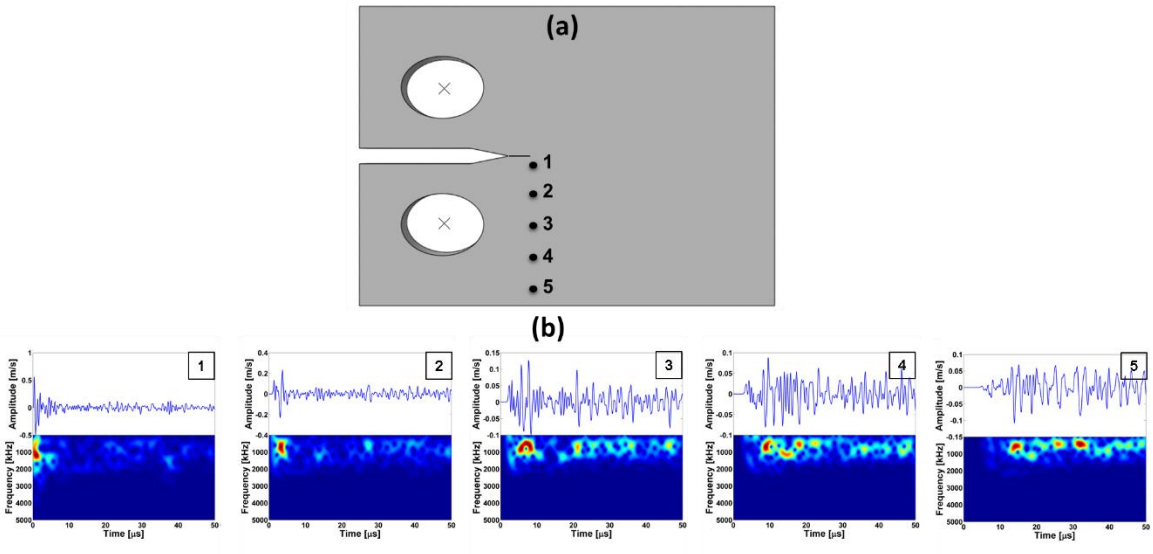

Figure 4.27: (a) Evenly distributed locations for waveform extraction. (b) Waveform analysis at 5 locations in order to quantify dispersion and attenuation

The attenuation was quantified using the peak amplitudes for each waveform marked spatially in Figure 4.27a. It can be seen in Figure 4.28 that similarly to the results for the CZM, the amplitude fit closely to an exponential decay as a function of distance.

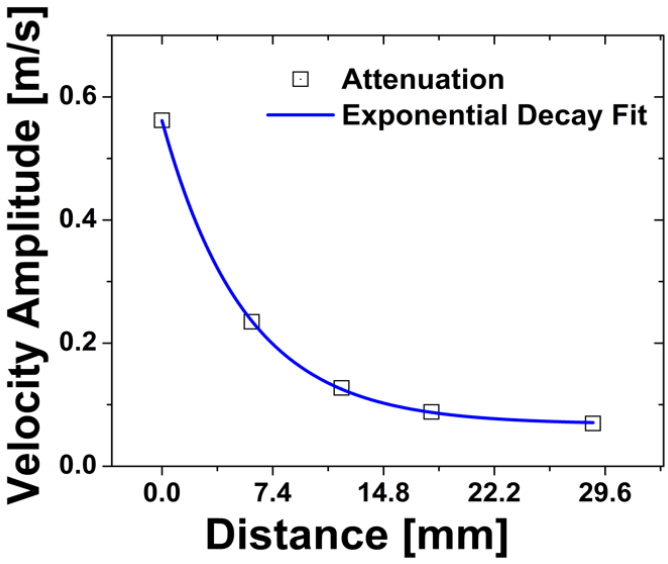

Figure 4.28: Peak amplitude of the waveforms in Figure 4.27 fitted with an exponential decay function

It was also important to assure that the results extracted in one of the faces and lower section of the CT-A were representative of the crack-induced source.

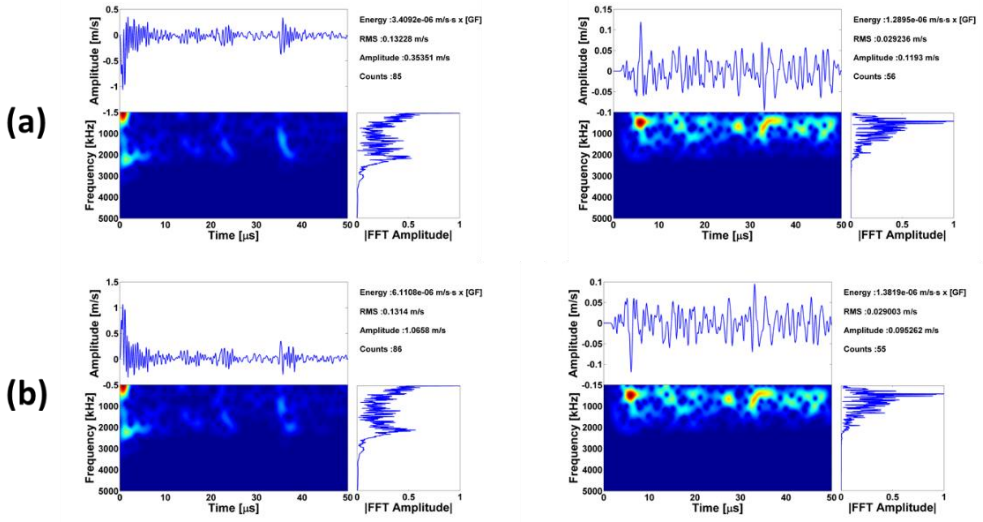

Figure 4.29: Two extracted waveforms at two nodal locations along the horizontal ahead of the crack tip for (a) the front and (b) back face of the CT-A sample model

Figure 4.29 illustrates this for two extracted waveforms along the horizontal for the front and back face. The waveforms are clearly anti-symmetrical; however, their frequency is identical in addition to their peak amplitudes. The same process was performed for other sections of the CT-A model. For instance, it was expected that the top and bottom waveforms are not similar since the boundary conditions across that symmetry plane are not symmetrical, in which the lower section has more displacement. This analysis is depicted in Figure 4.30.

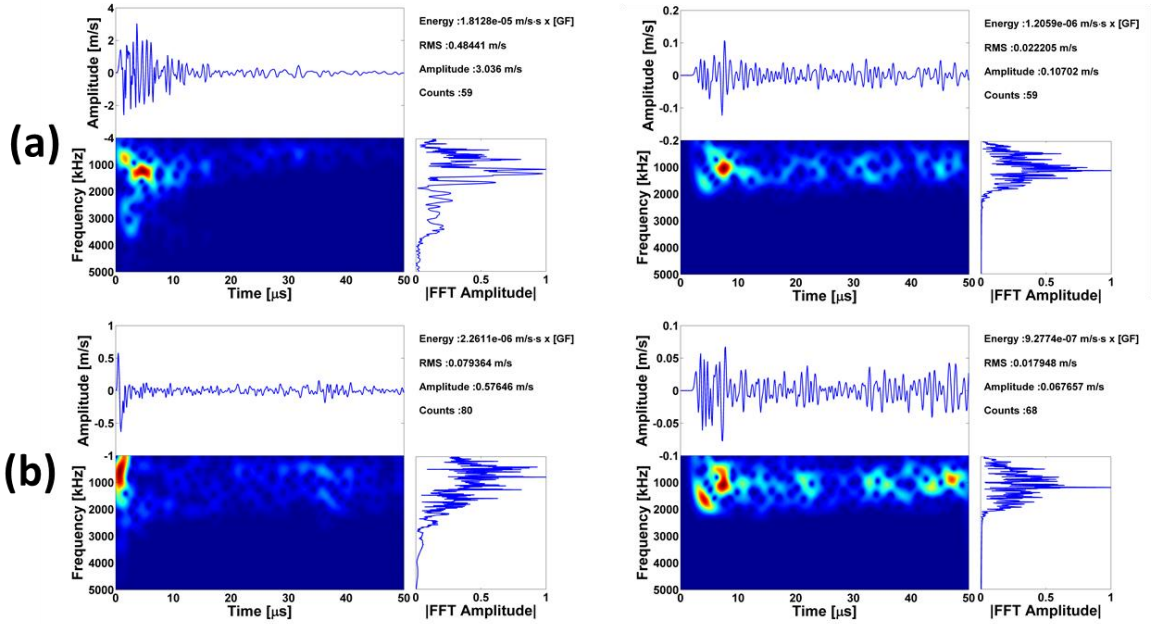

Figure 4.30: Two extracted waveforms at nodal locations along the vertical on the front face at locations (a) top and (b) bottom with respect to the AE source

Furthermore, since the model provides the solution at thousands of nodal points from the FEM mesh, it was necessary to understand better other inaccessible region to actual AE sensors. For instance, from the static simulation results it was observed that fracture initiates through the thickness at the center. Therefore, the waveforms at particular locations through the model's thickness were analyzed. Before comparing different locations, it was necessary to understand which component of the velocity is dominant

and active through material. Figure 4.31 shows that the *x*- and *y*-component have the highest amplitudes and similar frequency. It can also be observed that the waveform was higher frequencies than the ones observed at the surface. This is key to understand dispersion from source to signal detected. Moreover, the waveforms through the material clearly show other wave effects such as superposition (marked with the boxes) at 10 μs and 35 μs.

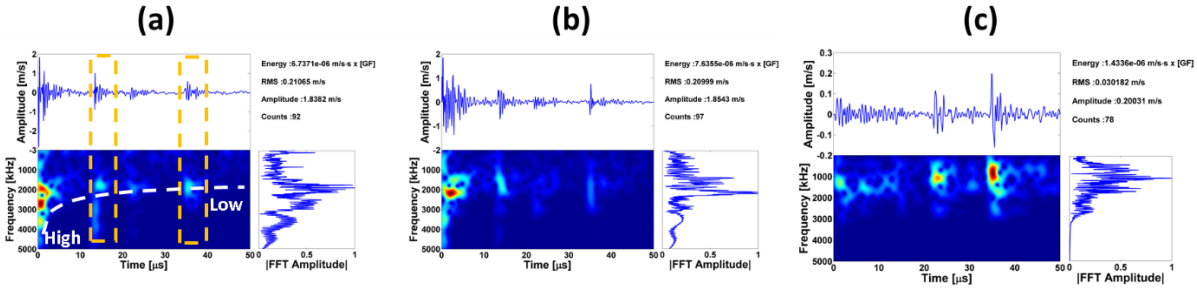

Figure 4.31: Velocity waveforms at a point close to the AE source at the center through thickness. (a) *x*- , (b) *y*-, and (c) *z*-component.

Ultimately, to finalize the wave propagation analysis of the CT-A model, the through-thickness waveforms were compared to those extracted on the surface at similar in-plane locations, by taking advantage of the structured mesh used.

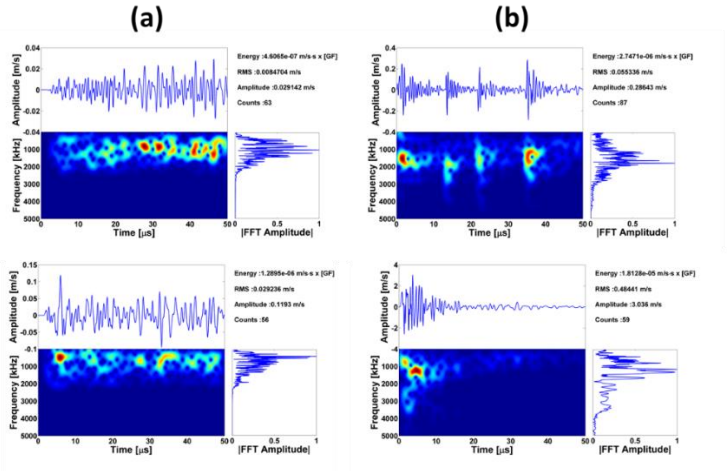

Figure 4.32: Out-of-plane velocity waveforms (*z*-component) at two locations from the source along (a) the horizontal ahead of the crack tip and (b) bottom with respect to the AE source (waveforms at the top of the figure are at the center through the thickness and those at the bottom are at the surface)

Figure 4.32 illustrates through-thickness waveforms at the top and on the surface at the bottom of the figure for two nodal locations. Both waveforms have the same frequency content for the two locations; however, they differ in amplitude in addition dispersion as function does not occur. The second calibrated model was the CT-B which as major difference has a thickness of 4 mm compared to 6 mm of the CT-A. In order to study the effect of thickness in addition to the precrack, the CT-B was analyzed according to the procedure followed for the CT-A. Figure 4.33 visualizes the wave propagating from the crack source with the aid of the out-of-plane velocity contour.

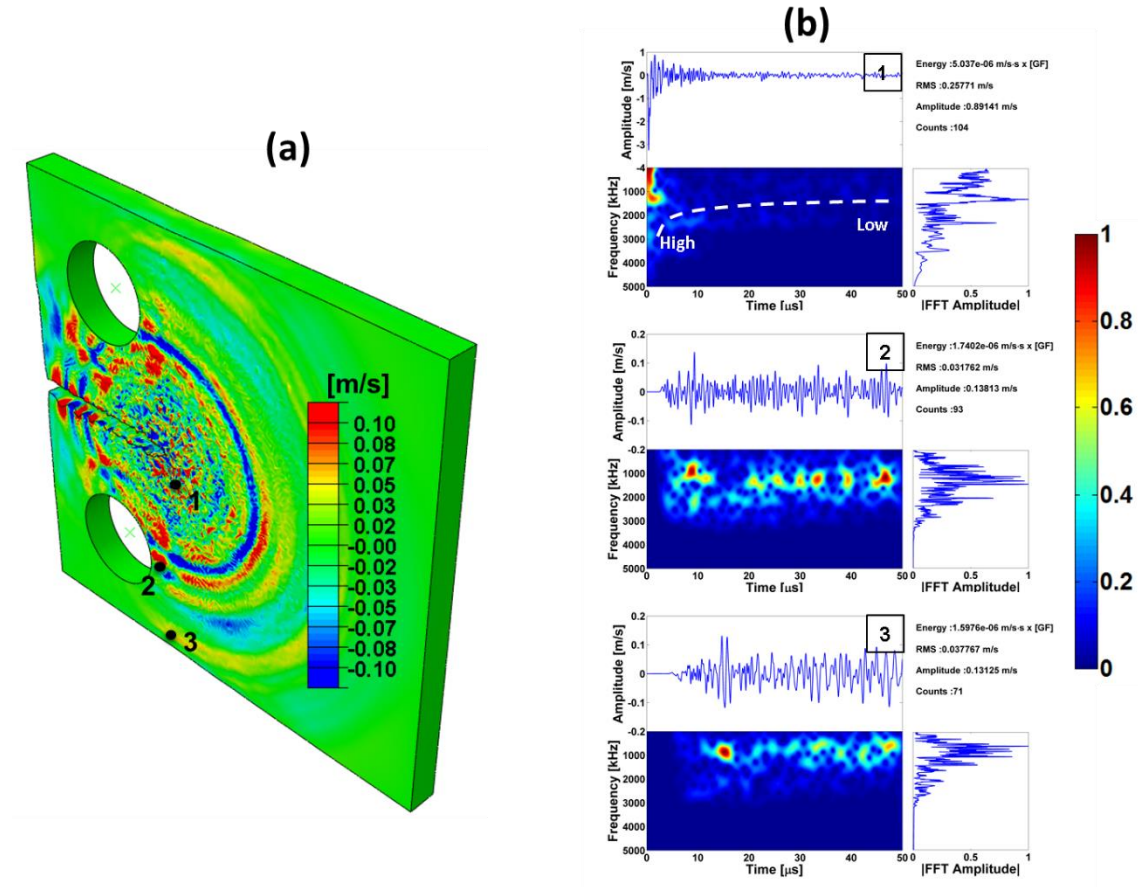

Figure 4.33: (a) Simulated sensors locations for primitive AE waveforms shown on the out-of-plane velocity contour. (b) Out-of-plane velocity waveform analysis at the three marked locations for CT-B (4 mm thick)

Three similar sites were selected in order to be comparable to the previous results. The results from the STFT distributions showed a shift in dominant frequencies mainly as function of distance without any significant shift as a function of time. Therefore, this one major difference, as opposed to the 6 mm-thick model, could be potentially attributed to the fact that the AE source (i.e. the crack initiation) is on the top section of the model. Although along the vertical the observed dominant high frequencies did not shift as a function of time, it was clearly shown that along the horizontal the frequencies are transitioning from high to lower frequencies as a function of time and distance while keeping the peak frequencies constant.

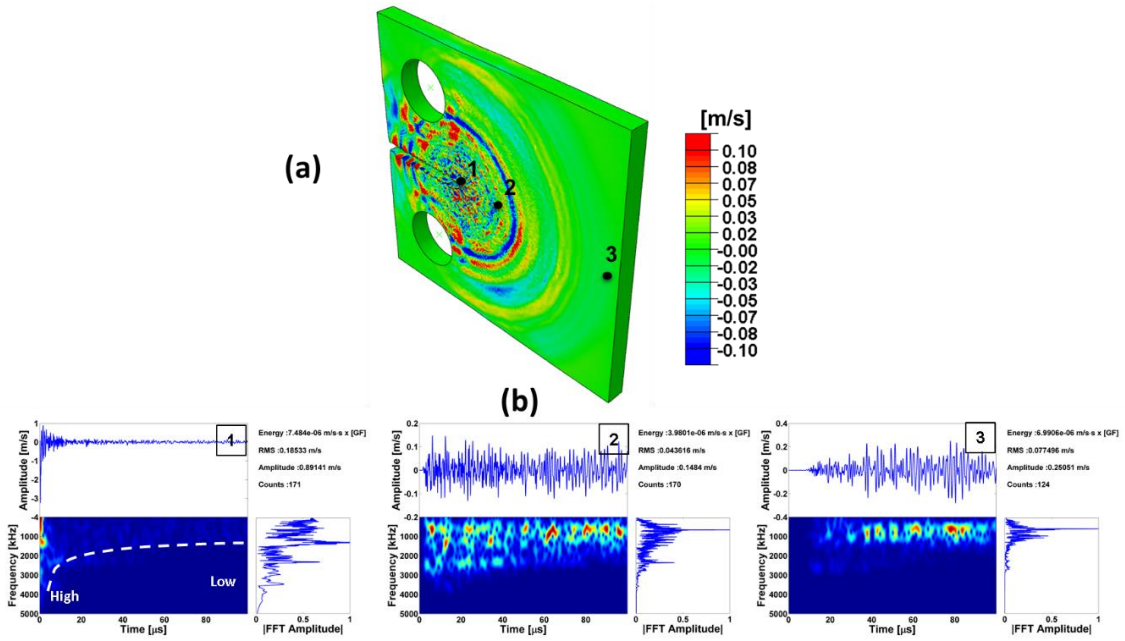

Figure 4.34: (a) Simulated sensors locations along the horizontal to capture wave front. (b) Out-of-plane velocity waveform analysis at the three marked locations

To further analyze dispersion, two waveforms were extracted from the surface and through the thickness. It can be observed that the waveforms are very different in both time and frequency domain. However, the range of dominant frequencies (0-1.5 MHz) is similar.

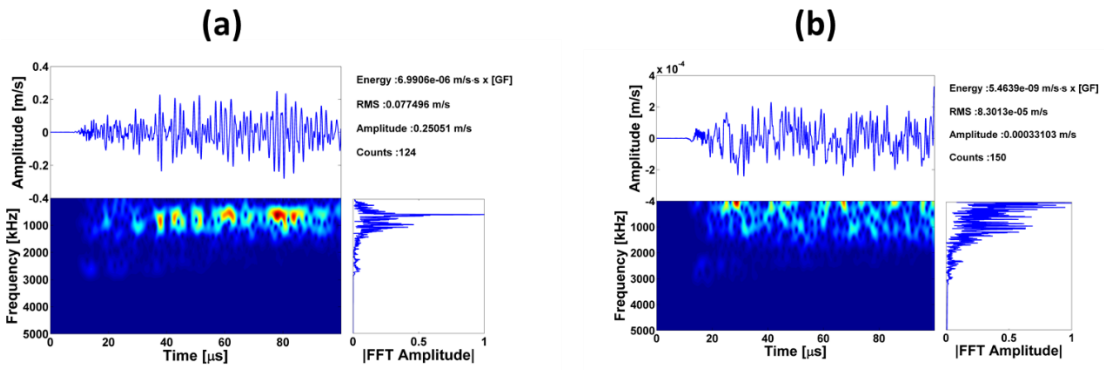

Figure 4.35: Out-of-plane velocity waveforms at a far location with respect to the source on (a) the surface and (b) at the center through the thickness

Ultimately, the waveforms from the top and bottom section of the model were analyzed to determine if there was any effect due to the fact that the crack initiated on the top of the machined notch. The waveforms, shown in Figure 4.36, are comparable in both time and frequency domain. In addition, although there is some differences at the beginning of the signal, both velocity waveforms shift to lower frequencies.

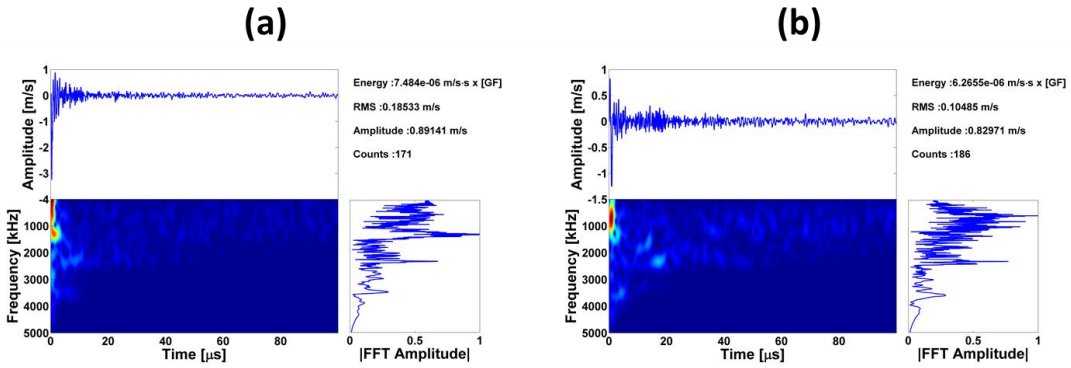

Figure 4.36: Out-of-plane velocity waveforms at a close location (a) top and (b) bottom with respect to the source for CT-B

In total, four computational models were studied in order to validate and better understand both the AE source and associated wave propagation. There were definitely some similarities from model to model but definitely the models provided enough information on how to quantify all different wave effects. A recent published

experimental work [159] on crack initiation for the CT-B has shown some similar results to those presented in this Chapter. Figure 4.37 shows a one-to-one comparison of the numerical and experimental waveforms. Although the dominant frequencies are different, the range of frequencies are similar. This could be attributed to the fact that the piezoelectric AE sensor is sensitive to certain frequencies. Consequently, the primitive peak frequencies are narrow into smaller frequencies ranges.

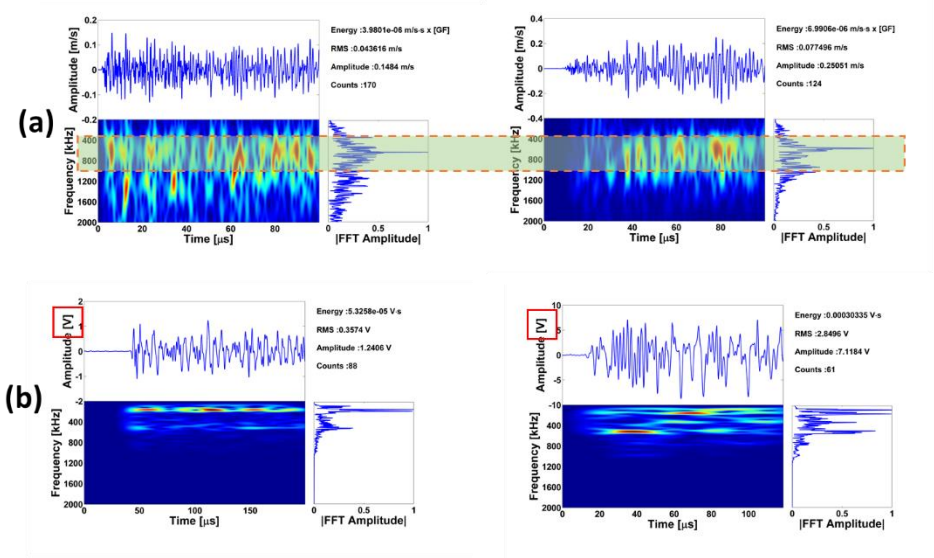

Figure 4.37: (a) Numerical waveforms at two comparable locations to those chosen in the experiment, (b) AE experimental signal at two different time instances associated to crack growth

4.3 CONCLUSION

The proposed forward AE model successfully linked an experimentally-constructed static FEM analysis for damage initiation to a computational wave propagation simulation. The simulated AE wave propagation provided additional information about the primitive AE emissions and possible characteristics that could be beneficial for an optimized AE experimental setup and signal analysis. The results of the model showed a shift of the peak frequency of the simulated waveforms as a function of distance and time from the crack source which can improve the sensor-type selection. Furthermore, the analysis of

the AE simulated wave propagation displays the scattering role of geometrical features and parameters in the computational models, such as the pin holes in the simulated compact tension specimens providing additional data for sensor location. An exponential decay-type attenuation was also observed due to dispersion. Ultimately, the results at different nodal locations were used for calculating attenuation of the calculated waveforms which are useful in the analysis of the experimental waveforms for signal processing. In regards to the AE source, the model also allowed to extract associated displacement jumps in the three directions, suggesting that the AE source was complex. The proposed technical approach also shows excellent agreement with experimental results and has great potential assisting to optimize the AE experimental signal analysis and AE sensor location and selection. Therefore, the results successfully demonstrate material and geometry effects in fracture-induced wave propagation simulations and create a pathway for the quantitative comparison between experimental and theoretical predictions of AE information.

CHAPTER 5: ENERGY RELEASE DUE TO FRACTURE-INDUCED ACOUSTIC EMISSION

5.1 INTRODUCTION

Acoustic emission is defined as a process of sudden redistribution of energy in a solid caused by the activation and/or development of one or more localized sources. Such energy redistribution is directly associated with the potential energy stored in a system before, for example, damage occurs; subsequently a portion of this energy is released and travels in a transient manner within the material/structure solid medium accompanied by a transfer energy in the form of vibrations/emissions. Therefore, characterization of an AE source in terms of its energy release can be described by time related considerations including: time instances before and after the localized source, has been activated as well as a transient period related to the release of emissions.

In the case of the onset of crack growth, which as explained previously it is a dominant/primary AE source, a large amount of potential energy is stored in the region near the crack tip and is related to both elastic and plastic contributions. The high concentration of stresses at the crack tip, eventually causes separation of atomic bonds, which is manifested macroscopically by the creation of new surfaces as the crack front advances. Overall, the stored energy at such localized regions can excite motion (i.e. emissions – partially in the form of kinetic energy) as well as plastic dissipation among other forms of multispectral (e.g. thermal) of energy redistributions. Such irreversible changes within the medium due to crack growth are responsible for what is defined as acoustic emissions, which are therefore just a piece of the total energy redistribution, including small scale motion, plastic dissipation and heat generation among other forms

around the crack surfaces [187-190]. For instance, in ductile metals most of the energy invested on fracture processes results in plastic dissipation, which is a reason that AE is capable to detect early signs of plastic deformation. In addition, the experimental work by Doll, Gross et al. suggested that most of the stored energy is expended as heat and that only a fraction, approximately 3%, of the total fracture energy yields acoustic emission [187, 189, 191]. In other investigations, these concepts have been applied experimentally to detect the fracture process zone by using energy measures and density of AE events which resulted to providing two critical regions for crack detection [192]. Other research efforts which relied on the use of the AE experimental methodology to characterize the energy released showed some quantitative limitations due to inherent restrictions placed by the sensors. Nevertheless, such efforts provided empirical relations which predict damage initiation and severity by using AE features [193-197], as shown previously in Figure 2.18. The generation of AE from the fracture process can also be described based on the different types of produced waves. For example, in semi-infinite media, Rayleigh waves have been estimated to carry about 67% of the total energy transiently released in perfectly isotropic materials, while the shear and longitudinal waves contain 26% and 7%, respectively [83, 198]. Furthermore, Rayleigh waves tend to decay much slower than the other bulk waves, a rate equal to $1/\sqrt{r}$, which is when $\boldsymbol{r}$ is the distance from the source.

In the context of fracture mechanics, the early studies related to fracture were also based on associated energy concepts. Specifically, the pioneering work by Griffith aimed at describing the energy release rate, which in its simplest form may be associated with the rate of change in potential energy near the crack and provided a way to characterize and

quantify crack formation. Griffith's criterion basically was built upon the condition that sufficiently high applied loads at the continuum scale are related to similar ones at the microscale in order to predict fracture initiation [113]. Various works followed his studies including the work by Rice [199], in which an energy balance for the fracture process was derived for both linear elastic and plastic materials. Rice's investigations were not only an extension to Griffith's work but provided a broader overview of the energy quantities associated with crack formation by defining two concomitant equilibrium states. Furthermore, this energy balance was not imposed; instead it was derived using continuum formulations of the energy at each state, disregarding microstructural effects at the atomic or mesoscale which are not adequately described by continuum mechanics theories. In addition to the energy balance formulation, Rice developed a path independent integral, *J*-integral, to characterize fracture. The work was later used to construct the so-called HRR singularity [200, 201] by deriving a formulation for the singular stress and strain field at the crack for a power law hardening material. The *J*-integral is not only a measure of the stress intensity in ductile materials but it can also be used as a criterion for crack initiation and to some extent for crack growth. Although the *J*-integral has been widely accepted, the requirements and limitation for a valid *J*-integral are somewhat severe. For instance, the application of the *J*-integral for crack growth implies an extrapolation of a reversible nonlinear elastic material behavior to an elasto-plastic behavior. In addition, for large crack extensions the *J*-integral's validity causes inconsistencies in the tearing resistance since it is no longer the true driving force. Such limitations and restrictions of the *J*-integral to describe and characterize fracture have inhibited in some cases its application to materials/structures.

Given this background, this Chapter attempts to quantity the energy associated with acoustic emission by using both Rice's energy balance approach as well as an energy flux approach (similar to the *J*-integral) for the fracture-induced AE model, described in Chapter 3and 4. Regardless of the limitations encountered when applying the *J*-integral, this parameter is used herein as a way to quantify the energy flux in a confined area near the fracture process zone.

5.2 BACKGROUND AND MODEL SPECIFICATIONS

The fracture-induced AE model introduced in Chapter 3 and used for both static and dynamic simulations in Chapter 4 is further used in this Chapter to quantify the energy associated with the onset of crack growth.

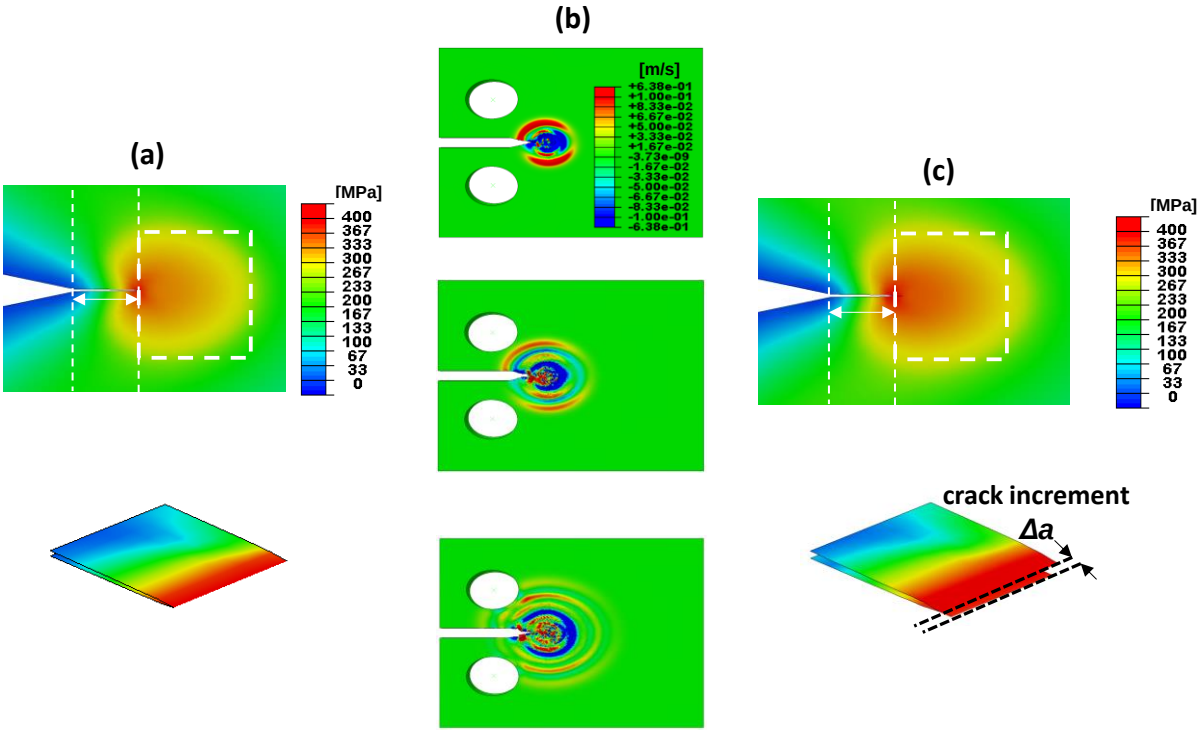

Figure 5.1: Quasi-static equilibrium state (a) before and (c) after crack growth. (b) Wave propagation due to sudden release of energy associated to crack initiation (illustrated here by out-of-plane velocity contours)

The adopted methodology consisted of using two equilibrium states corresponding to before and after crack initiation to calculate their corresponding energy states and any differences caused by the fracture process. This approach and related formulation had been introduced, as mentioned previously, by Rice [199] as an extension to the work proposed by Griffith [202]. Basically, the work by Rice included the energy balance for crack extension for elastic and ductile materials, while also interpreting the role of surface energy and work hardening. This concept is illustrated in Figure 5.1, in which the states before (Figure 5.1a) and after crack initiation (Figure 5.1c) are displayed in addition to the release of wave propagation (Figure 5.1b).The energy related to each state is assumed to be composed of the internal (stored) energy which is typically equal to the external work before crack initiation. The subsequent equilibrium state (shown in Figure 5.1c) comprises an additional energy constituent due to the crack extension. The final energy balance for a state without fracture can be written as

$$\int_{\Gamma} f_i^c u_i dA = \int_V \sigma d\varepsilon_{ij}^{el}\, dV + \int_V \sigma d\varepsilon_{ij}^{pl}\, dV \tag{5.1}$$

where Γ is the surface area (in specific at the pins) where external(Mode I type) loading is applied and V is the volume, while f represents the tractions associated to externally imposed displacement. The right hand side is composed of the elastic strain energy and plastic dissipation terms where the assumed strain decomposition is denoted by the subscripts "*el*" and "*pl*." Following Ref. [199], a derivation which ignores any thermal-mechanical coupling, and consequently the energy balance related to the fracture process is simply the difference in the energy description in Equation (5.1) between the two

states. Therefore, the energy associated to the crack formation, called E_{crack}, is obtained using the Green's theorem and applying the corresponding boundary conditions, i.e.

$$E_{crack} = \int_V \left(\int_a^b \sigma_{ij} d\varepsilon_{ij}^{el} \right) dV + \int_V \left(\int_a^b \sigma_{ij} d\varepsilon_{ij}^{pl} \right) dV - \int_\Gamma \Delta f_i^c \Delta u_i \, dA \,. \tag{5.2}$$

In (5.2), "*a*" and "*b*" denote the state before and after energy release due to crack growth and "*Δ*" refers to the change in imposed tractions or displacements between the two states. Essentially, (5.2) represents the difference in the total (mechanical) energy, which refers to the internal energy minus the external work for the two equilibrium states involved in these formulations. Thus, the energy at each state can be reformulated as the sum of the total energy in all elements of an assumed FE representation. By calculating the difference between the two states, it can be found that

$$E_{crack} = \sum_{elems} \left[\int_{V_{elem}} \left(\int_a^b \sigma_{ij} d\varepsilon_{ij}^{el} \right) dV_{elem} + \int_{V_{elem}} \left(\int_a^b \sigma_{ij} d\varepsilon_{ij}^{pl} \right) dV_{elem} \right] - \Delta E_{ext} \,, \tag{5.3}$$

where "*elem(s)*" refers to the FE model elements so that the internal energy is the sum of the elastic strain energy and plastic dissipation in all element, while ΔE_{ext} is the change in external work done in the system calculated from the imposed force/displacement boundary conditions. It can be observed that (5.3) is only valid for two states associated with a single crack growth increment. Consequently, E_{crack} is simply the dissipated energy in the system. Therefore, the energy associated with crack initiation can be calculated in a quasi-static manner by using (5.3) which involves two states before and after the occurrence of a crack increment.

The energy from the crack source is released in the form of transient stress waves which transiently (due to dissipation and attenuation) spread through the entire volume. Hence, although the total energy attenuates in the volume, it would be equal to that of the source if there were no dissipation. The associated concept of quantifying the radiated energy from a source has been extensively studied in the fields of electromagnetism and acoustics (mostly ultrasonics) and is often characterized by deriving the related power (i.e. the energy rate) from Maxwell's or Cauchy's equations, respectively [83, 129]. This derivation is referred to as the Poynting vector [129] and it could be formulated in the context of solid mechanics from the equilibrium equations considering the mass inertial terms (i.e. by using Cauchy's equation of motion).

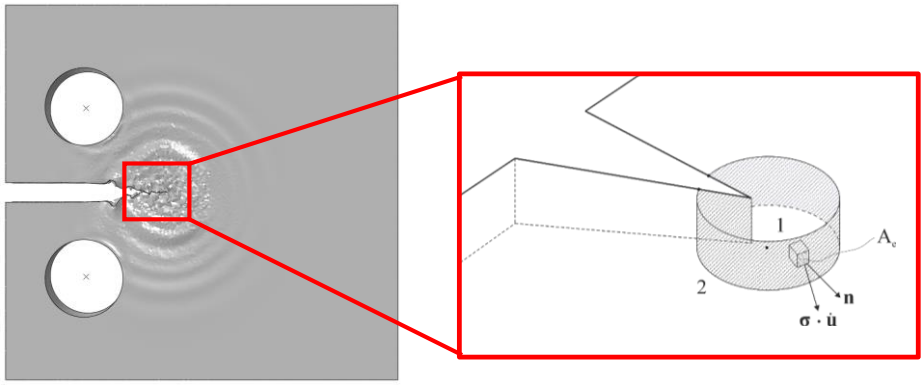

Figure 5.2: Schematic of a confined cylindrical volume close to the crack tip (AE source) with representation of the pointing vector on surface A_c

The Poynting vector is illustrated on the model in Figure 5.2 in which the energy radiates from region "1" (inside) to "2" (outside a cylindrical surface enclosing the crack tip). Furthermore, the Poynting vector is represented by the product of $\boldsymbol{\sigma} \cdot \dot{\boldsymbol{u}}$ which can be considered radiating out all possible directions defined through the cylindrical surface and quantified by the normal vector, $\boldsymbol{n}$, on the surface area A_c of this surface. Essentially,

the energy radiated is associated to the tractions (i.e. $\boldsymbol{\sigma}\cdot\boldsymbol{n}$) and corresponding velocity vectors, $\dot{\boldsymbol{u}}$, evolving over time, for which the Cauchy's equation of motion becomes

$$-\frac{\partial\left(\sigma_{ji}\dot{u}_i\right)}{\partial x_j}=\rho\ddot{u}_i\,\dot{u}_i+\sigma_{ji}\frac{\partial\left(\dot{u}_i\right)}{\partial x_j}+\dot{u}_i\cdot f_i^{AE}, \tag{5.4}$$

where f_i^{AE} are the tractions related to the AE source and $\ddot{u}$ denotes acceleration. Therefore, the energy radiated, E_R, by using the velocity vector, and by applying the Divergence Theorem and ultimately integrating over time can be written as

$$\begin{aligned}E_R=\int_0^t\iint_{A_c}\left(-\dot{u}\cdot\sigma\right)\cdot\hat{n}\,dA_c=&-\int_0^t\left(\int_V\sigma:\dot{\varepsilon}^{el}\,dV\right)d\tau-\int_0^t\left(\int_V\sigma:\dot{\varepsilon}^{pl}\,dV\right)d\tau\\&-\int_0^t\left(\int_V\rho\ddot{u}_i\,\dot{u}_i dV\right)d\tau+E_{external}\end{aligned}, \tag{5.5}$$

i.e. the radiated energy is simply the surface integral over A_c and over time of the Poynting vector, which is equal to the difference of the total energy over time including the kinetic energy (which was ignored in (5.2)). Equation in (5.5) can then be expressed in terms of the finite elements approximation, while if it is e.g. also integrated by discretely using the trapezoidal rule; it becomes

$$E_R=\sum_{i=1}^{N}\frac{t_{i+1}-t_i}{2}A_{eff}^{j}\left[\left(\sum_{j=1}^{M}\left(-\dot{u}^j\cdot\sigma^j\right)\cdot\hat{n}^j\right)_{i+1}+\left(\sum_{j=1}^{M}\left(-\dot{u}^j\cdot\sigma^j\right)\cdot\hat{n}^j\right)_i\right], \tag{5.6}$$

where "*i*" represents the number of energy rate data points (related to number of time increments in the FEM) and "*j*" is the number of nodes belonging to the effective surface areas of each node, A_{eff}. Hence, energy "exits" from the confined area defined by the cylindrical region and is approximated to be equal to the area defined by each finite

element (i.e. for a 400 μm size a 2D area of 0.16 mm^2 is obtained). In summary, (5.5) and (5.6) provide a method to quantify the energy from the source which is radiated in a transient period of duration, *t*, as the stress waves propagate through the volume.

An alternative method to estimate the energy associated with acoustic emission could be formed by using the energy flux in a confined volume close to the crack tip. The formulation of such quantity is similarly derived from Cauchy's equation of motion to obtain the energy rate, presented in Equation (5.4). In contrast to the Poynting vector, both the Transport and Divergence Theorem are applied for a fixed contour with a given area, *A*, and a moving contour, *Γ*, with a fixed size which moves with the crack. A 2D representation of the constituents for obtaining in this way the energy flux is depicted in Figure 5.3.

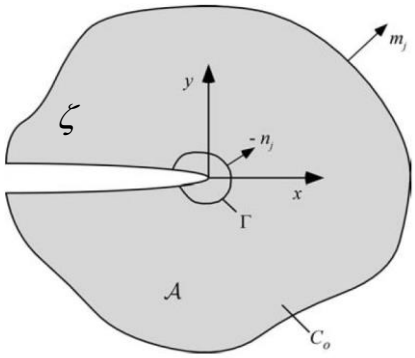

Figure 5.3: Illustration of contours and terms associated with the energy flux of a propagating crack [113]

The energy flux, Φ_E, is comparable to the generalized energy release rate, defined by the *J* integral (presented in Section 2.4.1), which can be formulated for a 2D case and a crack increment along the horizontal (*x*-direction) as

$$J = \lim_{\Gamma \to 0} \int_{\Gamma} \left[w\delta_{1j} + \sigma_{ji} \frac{\partial u_i}{\partial x} \right] n_j d\Gamma , \tag{5.7}$$

i.e. it consists of the internal energy *w*, the normal vector $\vec{n}$ to the contour Γ, while the Kronecker delta (δ) represents the direction of the crack [120, 203]. The energy flux is evaluated herein for an elastoplastic constitutive model with incremental plasticity in contrast to an idealized nonlinear material law which is the case for the generalized energy release rate, *J*. It is important to note that (5.7) assumes a linear unloading path based on the deformation theory of plasticity, steady state conditions and negligible kinetic energy. Furthermore, the limit of Γ to zero allows for the line integral to be independent of the shape of the contour itself. Equation (5.7) has also been introduced as a surface integral and subsequently derived for the FEM framework by using a smooth function, *q*. In this case, the energy flux can be expressed as [113, 204]:

$$\Phi_E = \sum_V \sum_{p=1}^{m} \left\{ \left[\left(\sigma_{ij} \frac{\partial u_j}{\partial x_1} - w\delta_{1i} \right) \frac{\partial q}{\partial x_i} \right] \det\left(\frac{\partial x_j}{\partial \xi_k} \right) \right\}_p \omega_p - \sum_{crack\ faces} \left(\sigma_{2j} \frac{\partial u_j}{\partial x_1} q \right) \omega , \tag{5.8}$$

where $\{\ \}_p$ and subscript "*p*" represent the quantities evaluated at the Gaussian points, ω is the Gaussian weighting factors, *m* is the number of Gaussian points per element, and ξ are the natural coordinates (i.e. FEM isoparametric coordinates). Moreover, the smooth function, *q*, can be represented in terms of the shape functions N_I by interpolating within an element, such that

$$q(x_i) = \sum_{I=1}^{n} N_I q_I , \tag{5.9}$$

where n is the number of nodes per finite element. Consequently, the energy flux is calculated in this Chapter by using Equation (5.8) for the computational model in order to characterize and quantify its energy state before and after the onset of crack growth under both equilibrium and transient dynamic conditions.

In addition to the integral formulation of the energy flux in the direction of crack propagation, the energy flux can be formulated by the J integral (for the Mode I loading assumed in this thesis) by conveniently separating the elastic and plastic displacement, which is valid if unloading does not occur. Thus, in a load-controlled formulation

$$J = J_{el} + J_{pl} = \int_0^P \left.\frac{\partial \delta}{\partial a}\right|_P dP = \int_0^P \left.\frac{\partial \delta_{el}}{\partial a}\right|_P dP + \int_0^P \left.\frac{\partial \delta_{pl}}{\partial a}\right|_P dP , \tag{5.10}$$

where δ_{el} and δ_{pl} are the elastic and plastic components of the displacement, δ, which are assumed to follow an additive decomposition. Intuitively, the elastic part can be related to LEFM using Griffith's formulation of the energy release rate, where $J_{el}=G$. The plastic part can be then derived by dimensional analysis assuming that the plasticity is confined to the characteristic length of the uncracked ligament, b, for any medium containing a crack. A second assumption regarding the dimensional integrand states that separation variables can be applied. Then the analytical J-integral formulation can be written as

$$J_{pl} = \frac{2}{b}\int_0^{\delta_{pl}} P d\delta_{pl} - \frac{b^2}{W^2}\int_0^{\delta_{pl}} \frac{\partial F}{\partial\left(\frac{a}{W}\right)} d\delta_{pl} , \tag{5.11}$$

which includes geometrical parameters such as the force per unit of length (thickness) P, crack size a, characteristic length W, and the dimensional parameter F [188, 205]. Equation (5.11) featurs two terms referred to as the Rice's and the Merkle-Corten terms, respectively. It was later shown that the second monomial can be estimated empirically for a compact tension specimen [206]. Thus, the plastic part of the J-integral can be written as a function of the plastic work A_{pl} (i.e. the area under the nonlinear part of the load-displacement curve), in which case Equation (5.11) can be reformulated as follows

$$J_{pl} = \frac{2A_{pl}}{Bb} + \frac{0.522A_{pl}}{BW}, \tag{5.12}$$

Using (5.10) and (5.12), J-integral can be analytically derived to be:

$$J = \Phi_E = \frac{K^2(1-\nu^2)}{E} + \frac{2A_{pl}}{Bb} + \frac{0.522A_{pl}}{BW}, \tag{5.13}$$

This convenient form of J-integral is equal to the energy flux as long as there is no load drop and can be used to validate the contour integral formulation presented in (5.8). This convenient formulation is part of the ASTM E1820 standard, which is used for experimentally measuring fracture toughness [138]. This calculation relies on an experimental record of the load and displacement for a specific crack size with the expectation that no unloading occurs. In summary, once the energy flux is validated for a stationary crack with Equation (5.13), then the energy difference between the two states before and after crack growth can be defined. From such difference, the associated energy radiated due to crack initiation can be calculated for a given crack increment area, since the energy flux is expressed in terms of energy per unit of area. Similarly, the J-

integral in any steady-state can be calculated using the computational found dynamic solution of the crack-induced wave propagation model, defined in this dissertation.

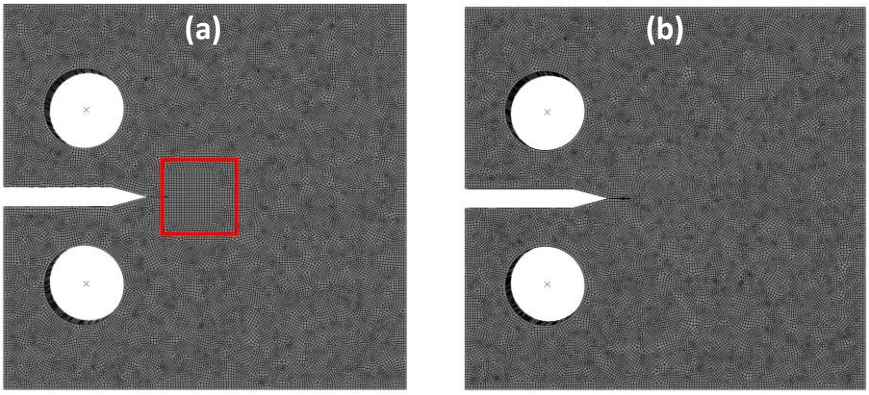

Figure 5.4: (a) Partitioned and (b) uniform mesh for Poynting vector and energy flux calculations, respectively

The two methods, i.e. using either the energy based balance or energy flux, were implemented in this Chapter to quantify the energy associated with crack initiation using the fracture-induced AE model. As a result, two CT models with the same properties and material law, but with different meshes features were utilized for the energy balance and flux methods, respectively. The additional feature in the mesh was a 3D rectangular partitioning surrounding the crack tip in order to calculate the surface integral discretely for the Poynting vector case. The two mesh are shown in Figure 5.4. Furthermore, a CT model with a different thickness was utilized to evaluate and study the effects of geometry on the energy quantities.

5.3 RESULTS AND DISCUSSION

The results are presented based on the two methodologies used to quantify the energy released due to crack growth from the fracture-induced computational model described previously. The first part focuses on using the energy balance in the system at two specific static equilibrium states before and after crack initiation. In this case, the

radiated energy from the source is quantified by using a confined volume close to the crack tip using the Poynting vector formulation. The second methodology used to determine the energy related to acoustic emission in this model consists of using the change in energy flux and crack size for both the static and dynamic solution.

5.3.1 ENERGY BALANCE AND POYNTING VECTOR APPROACH

The critical stage for onset of crack growth was necessary to be defined in Chapter 4 to link the static to the dynamic model in order to accurately simulate the AE source generation and propagation. In addition to providing the conditions for the AE source, such critical stage serves as the equilibrium state before crack initiation in a corresponding energy balance approach. Consequently, the static equilibrium solution right after crack initiation is key to calculate the energy total differential related to a specific crack increment.

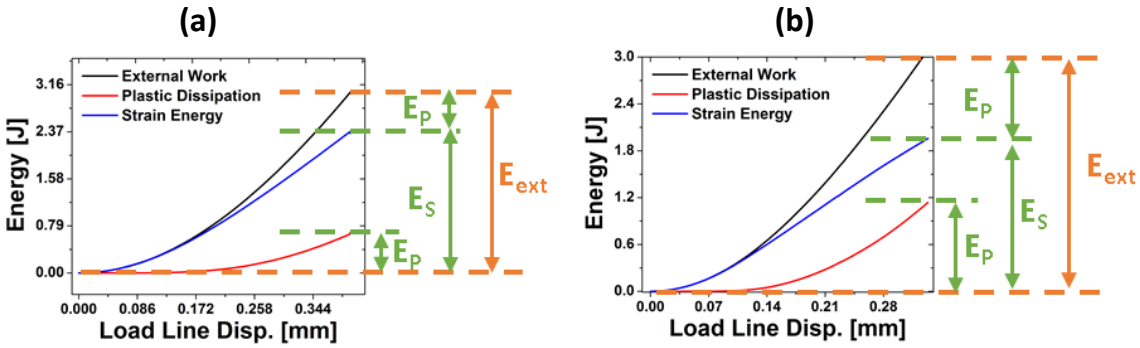

Figure 5.5: Energy balance including external work, plastic dissipation and elastic strain energy for (a) CT-A model (6 mm thickness) and (b) CT-B (4 mm thickness)

Typically, for equilibrium the external energy (i.e. work) is equal to the internal energy (i.e. stored energy) used for deformation. Figure 5.5 illustrates the evolution of such energy balance as a function of loading. However, instabilities in the dissipated energy among other reasons result in excess of energy or sudden energy redistributions

quantities. Although the total energy, which is the difference between the external work and internal energy, is nonzero in some cases, the equilibrium state is still valid since the FEM formulation solves for the first energy differential to be zero.

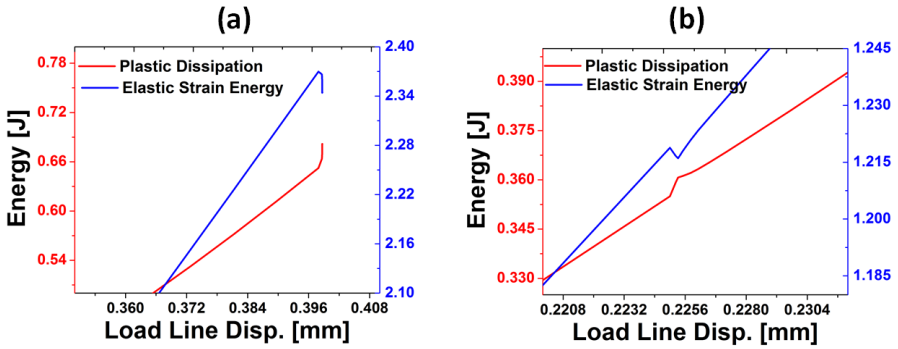

Figure 5.6: Plastic dissipation and strain energy close to critical stage for (a) CT-A and (b) CT-B model as function of applied displacement

The fracture-induced model contains two mechanisms that could create nonzero energy states which are incremental plasticity and crack growth (i.e. stress relaxation due to newly created surfaces). Taking a closer look at the plastic dissipation and strain energy, the onset of crack growth can be identified, as shown in Figure 5.6. It can also be observed that a sudden redistribution occurs close to the critical equilibrium state right before crack initiaion. Furthermore, in the case of the CT-B model, the energy rapidly increases and then stabilizes as the displacement continues to be applied.

In addition to evaluating the energy in the entire model, the energy can be quantified for a confined area surrounding the crack. In this region of interest, the energy dissipated by plasticity is higher than the elastic strain energy due to the high localized strains close to the crack tip. Figure 5.7 confirms that the instability of energy is originated from the crack.

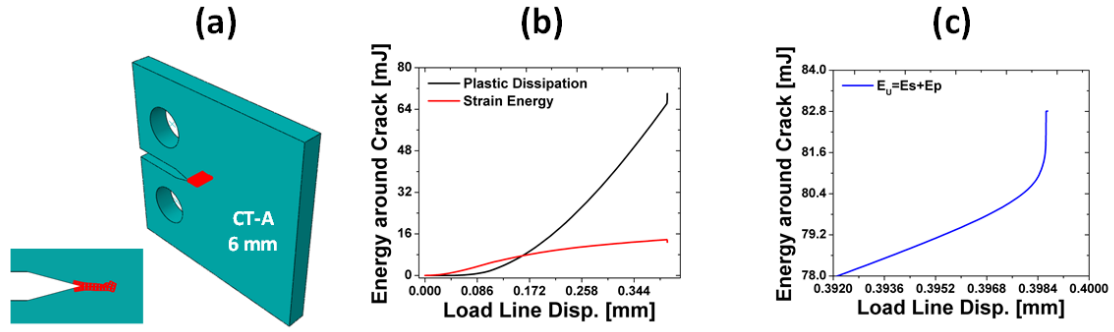

Figure 5.7: (a) CT-A model selected elements for energy calculation, (b) dissipated and strain energy plotted separately and (c) combined energy evolution, E_U, for (a)

As it can be observed, similarly to Figure 5.6, the energy increases suddenly at the critical stage. Moreover, Figure 5.7c shows the evolution of the sum of the dissipated and strain energy (i.e. E_U). The jump in the combined energy is approximately 2.4 mJ for a crack increment with an area approximately equal to 2.32 mm^2, which confirms that there is a redistribution of the energy produced by crack growth. Similarly, the same analysis was performed for the CT-B model and the results are shown in Figure 5.8.

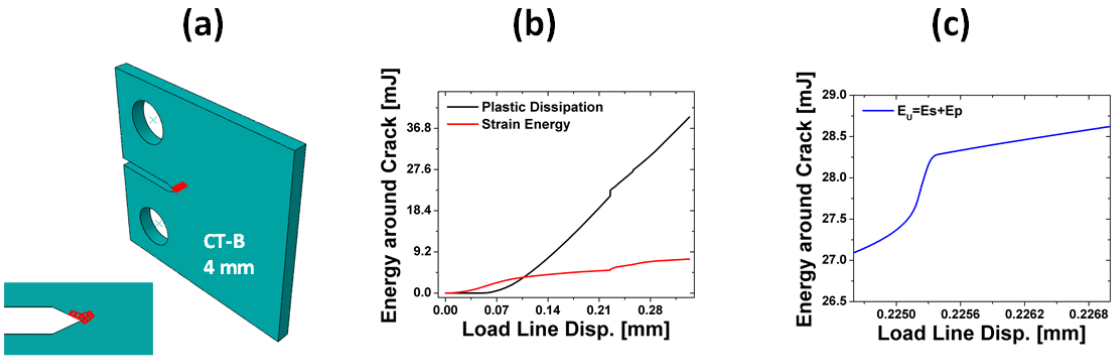

Figure 5.8: (a) CT-B selected elements for energy calculation, (b) dissipated and strain energy plotted separately and (c) combined energy evolution, E_U, for (a)

CT-B also exhibits a sudden change in the energy evolution due to crack growth for a confined region close to the crack increment. However, the combined energy is close to 1 mJ for a crack increment of 1.28 mm^2, which are lower than the respective values

obtained for CT-A. In order to further analyze all instabilities and quantify the two energy states in the fracture-induced model, the total energy is evaluated. A load drop of 200 N for a crack surface area increment, Δa, of 2.32 mm^2 is characteristic of the critical stage in CT-A, as shown in Figure 5.9a.

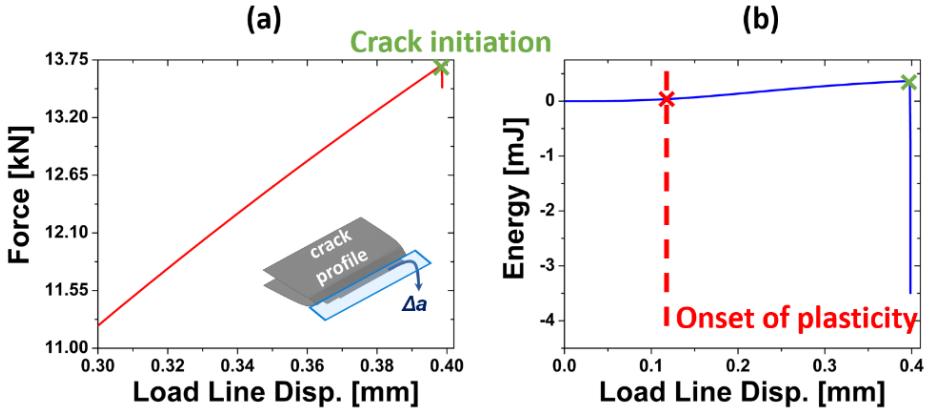

Figure 5.9: (a) Load drop response due crack growth. (b) CT energy balance as it is loaded in displacement control with onset of plasticity and crack growth

Moreover, the total energy in the system (plotted in Figure 5.9b) clearly shows the onset of plasticity as excess of energy or energy that has been dissipated (not recoverable), plotted as positive in Figure 5.9b. The total energy evolution also denotes the onset of crack growth, which involves a sudden drop in the negative *y*-axis (a negative in the energy plot represents the external work being higher than the internal energy due to instability). The drop in energy and difference between the two equilibrium states was calculated to be approximately 3.86 mJ. It can be stated then that this difference in the total energy in these two static equilibrium states is equal to the energy associated with the crack, E_{crack} as represented by Equation (5.3). Such energy is closely related to the energy of the AE damage source since it is the energy used to create the new crack surface.

The energy balance using the dynamic solution approach of the fracture-induced model was also utilized to quantify the energy associated to the crack AE source. In order to make the proper calculations in the transient period of the wave propagating due to crack growth, the Poynting vector formulation was implemented, as shown in Equation (5.6). The first attempt to calculate the radiated power and associated energy was performed using the non-partitioned mesh shown in Figure 5.4b. Two irregular volumes (i.e. extracted volume from uniform global sized mesh) were used. These elements in two confined volumes, i.e. 227 mm^3 and 1683.3 mm^3 are shown in Figure 5.10; they were selected to extract both the stress tensor and velocity vector components at the nodes to quantify the surface integral in Equation (5.6).

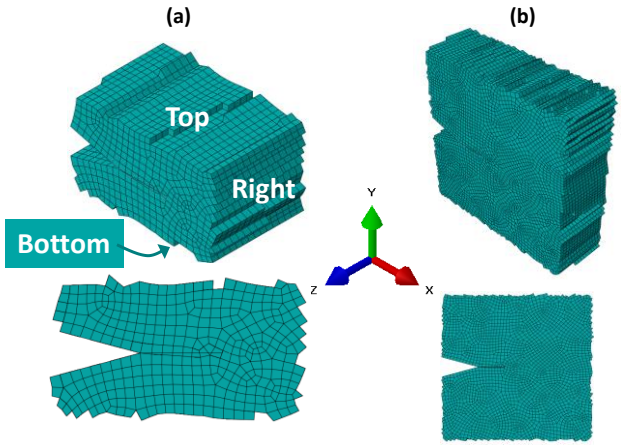

Figure 5.10: Extracted elements close to the crack tip for power and energy radiated calculations with a volume of (a) 227 mm^3 and (b) 1683.3 mm^3

Three main surfaces for both volumes had nonzero values for the corresponding surface integrals, marked as top, bottom, and right in Figure 5.10. In order to calculate the integral, the normal vector corresponding to each surface was approximated to be in the direction of the standard basis vectors of the global coordinate system, e.g. for example the top surface elements have a [0 1 0] direction(i.e. they lie in the direction of the *y*-axis) quantified by their normal vector. Regardless of the irregularity of the mesh, the power

and energy radiated using the Poynting vector formulation were implemented plotted in Figure 5.11b and c, respectively.

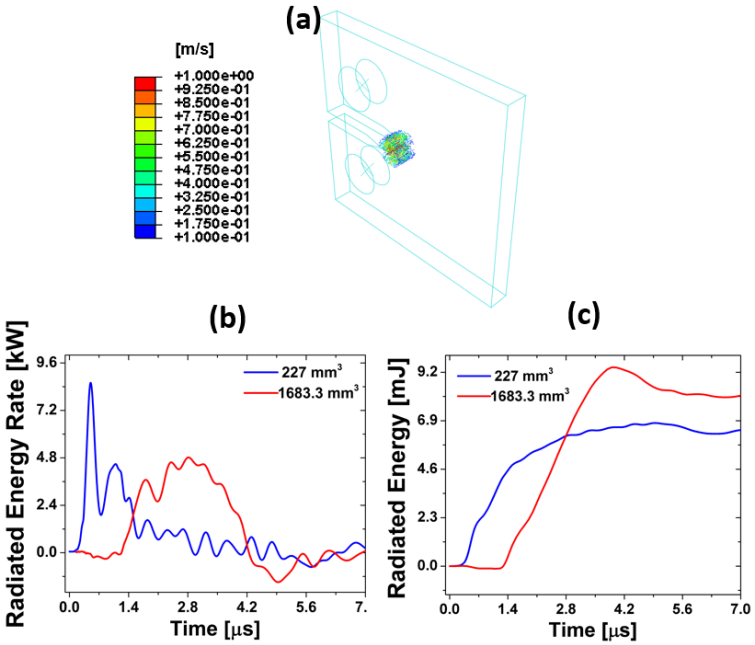

Figure 5.11: (a) Velocity resultant vector quiver plot as energy source is invested in the volume. Calculated (b) power and (c) energy radiated for two confined volumes for CT-A

Figure 5.11a illustrates the release of energy from the AE damage source as it is invested in the CT volume. Moreover, the power, referred to as 'energy rate' in the plot, exhibits a characteristic transient and steady-state behavior since the energy exits and reenters the confined volume due to geometrical reflections. The smaller the volume, the shorter the transient time period for power to accumulate and reach steady-state. Figure 5.11 shows that this time periods is close to 1.5 μs for a value of 227 mm^3 to reach a maximum value of 8.4 kW, and from 1.5 to 4.2 μs (i.e a 2.7 μs period) for a value of 1683.3 mm^3 reaching a maximum value of 4.8 kW. These results are crucial since the energy is the time integral of the power and the calculated results are shown in mJ in Figure 5.11c. Similar to the power evolution with time, the energy reaches steady-state around 4 μs reaching

from 6.9 to 9.2 mJ for the two volumes. The same type of analysis was performed for the CT-B model making the same assumptions about the mesh irregularity and calculation parameters including the effective area and surface normal vectors in addition to averaging the stress values at the nodal points. The results for CT-B model are depicted in Figure 5.12.

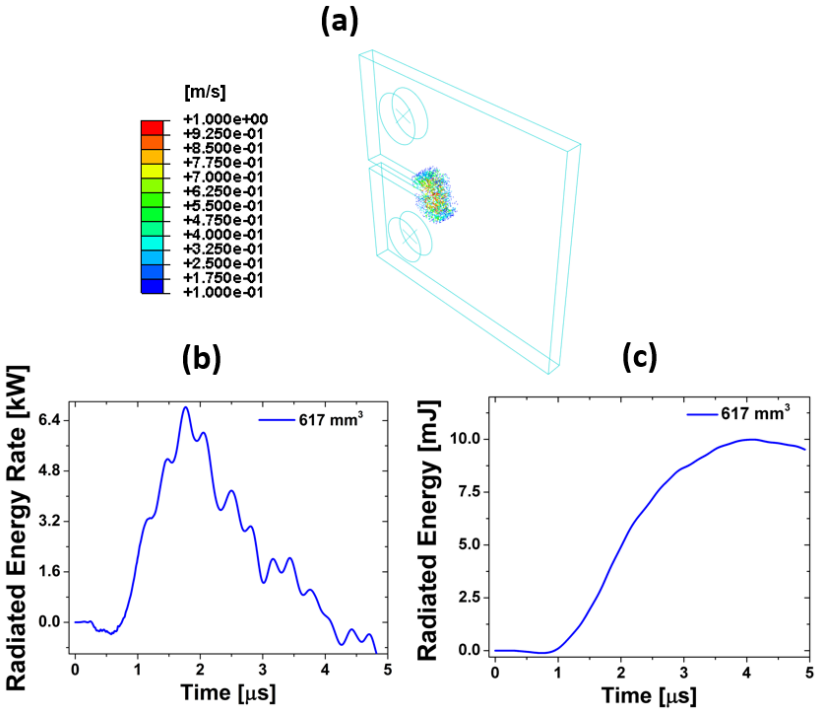

Figure 5.12: (a) Velocity resultant vector quiver plot as energy source is invested in volume. Calculated (b) power and (c) energy radiated for two confined volumes for CT-B

A volume size of 617 mm^3, which is in between the range of the values selected for the CT-A, was extracted for the CT-B. The power radiated shows that the transient evolution is close to 4 μs with a maximum value of 6.4 kW which results in an energy accumulation of 10 mJ. These results of a thinner sample with a smaller crack size compared to the CT- A led to the conclusion that the assumptions made, resulted to inaccurate calculations of the radiated energy from the AE source. Some of these assumptions included the irregular mesh with approximated normal vectors and

associated effective areas, as well as adding the residual static stress in the Poynting vector calculation. Therefore, a second model with a partitioned mesh surrounding the crack tip for the CT-A which excluded the residual stresses was utilized to recalculate the radiated energy from the AE source. The mesh of the second model was shown in Figure 5.4a and the two selected volumes are shown in Figure 5.13 .

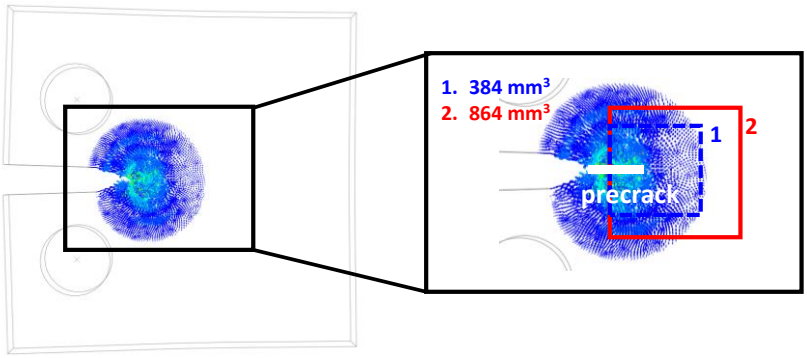

Figure 5.13: Crack-induced emission of energy illustrated by velocity vector plot with zoomed box displaying two calculation volumes denoted as “1” and “2”.

The two volume sizes were 384 and 864 mm^3 which were sufficiently large to include the crack tip and plastic zone. Similar to the methodology used in the first model, the power and energy radiated was calculated.

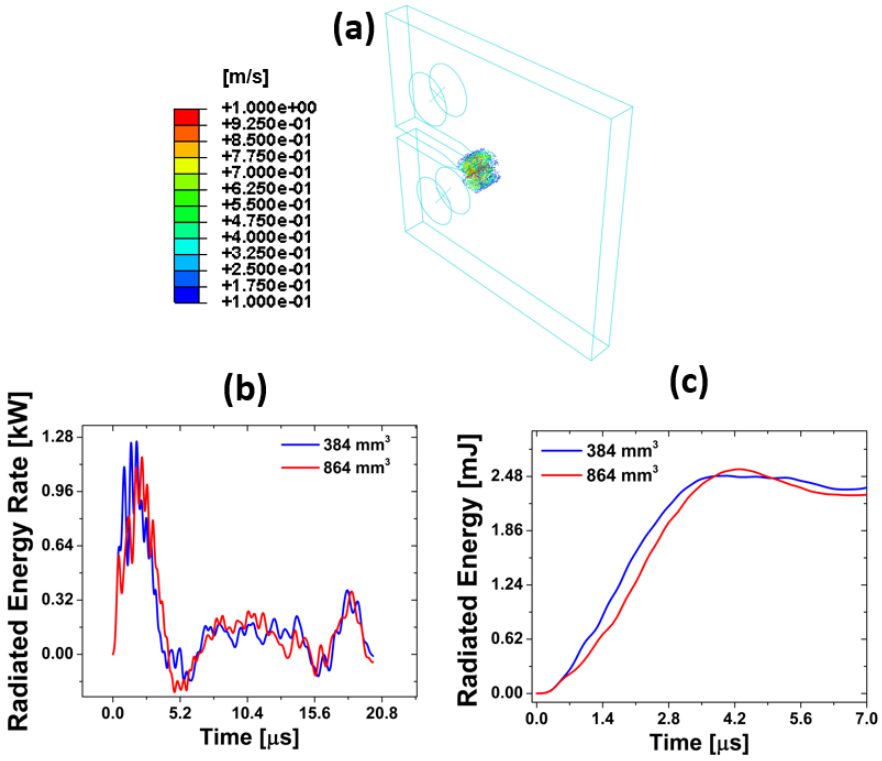

Figure 5.14: (a) Velocity resultant vector quiver plot. Calculated and convergent (b) power and (c) energy radiated for two confined volumes for CT-A model with partitioned mesh.

The results of the second model show convergence regardless of the volume size, suggesting better accuracy in the calculation, as shown in Figure 5.14. The maximum power value is close to 1.28 kW and 2.48 mJ for the energy, which are much lower than what it was previously calculated for CT-A. Moreover, the transient time period before the energy reflects back into the volumes is close to 5.2 μs. A plausible factor that could attribute to the convergent results is the fact that the smaller volume selected in this case was included into the large one. The stresses accumulated from the static solution, however, they were still included in this calculation while the velocity values used included those from the dynamic solution. The energy radiated was recalculated therefore using the dynamic stresses to account only for the energy associated to the

transient stress waves. The results of the recalculated radiated energy along with the energy from the AE source are shown in Figure 5.15.

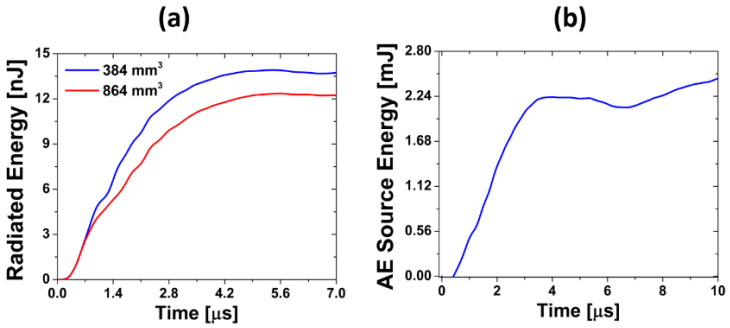

Figure 5.15: (a) Radiated energy and (b) AE source energy associated to the transient dynamic effects of quasi-static crack growth

By removing the accumulated static stress from the calculation the radiated energy is reduced from the mJ to the nJ scale. It can be seen that the radiated energy reaches a plateau to a value between 12 to 14 nJ at around 5 μs. Furthermore, the energy from the AE source is calculated by adding the elastic strain energy, plastic dissipation and kinetic energy to the radiated energy as derived in Equation (5.5). The AE source energy also reaches a plateau at around 5 μs to a value of 2.24 mJ. In summary, two energy quantities associated to the crack source and wave generation were obtained for the dynamic solution of the fracture-induced model disregarding accumulated parameters from the static solution. It is important to note that the radiated energy is a more comparable parameter to what the AE sensor captures experimentally since most of the energy is recorded after the AE source has formed and therefore corresponds to the radiated portion only calculated herein by the Poynting vector.

5.3.2 ENERGY FLUX CHARACTERIZATION

The AE source related to crack formation is closely related to the energy flux since this process involves a change of total energy due to the formation of a finite crack surface area. The method implemented herein to calculate the energy flux was based on the generalized formulation of the *J*-integral for a static analysis, as derived in Equation (5.8).

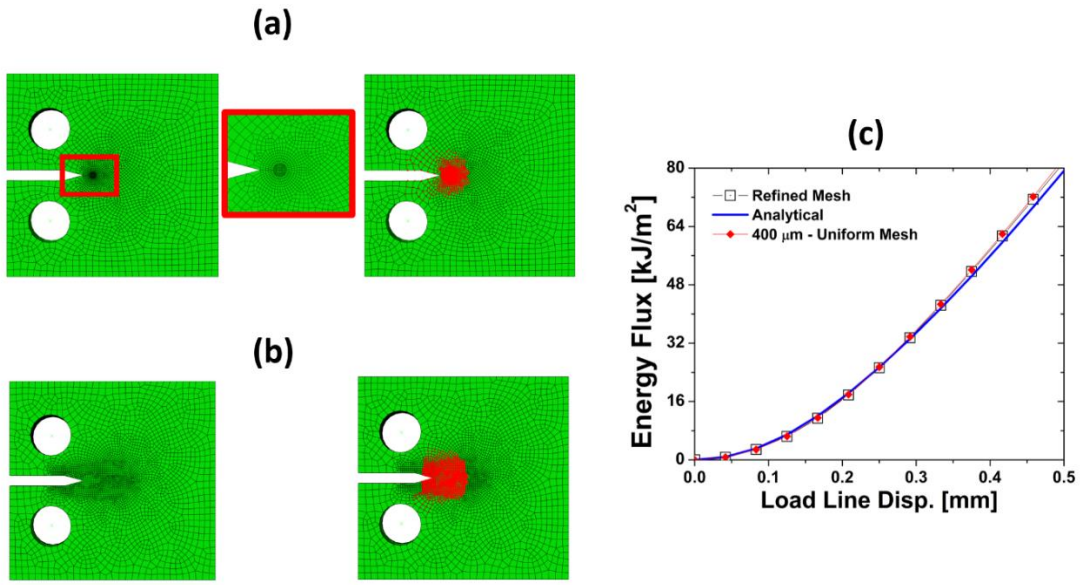

Figure 5.16: CT-A (a) refined (focused wedge-like mesh) and (b) uniform mesh surrounding crack tip and precrack. (c) Calculated energy flux evolution for (a), (b) using contour formulation and the convenient analytical formulation of Φ_E using (5.13)

Regardless of the validity of such parameter for elasto-plastic materials (as compared to nonlinear elastic materials) when a stress relaxation occurs due to the creation of new surfaces, the energy flux is calculated at different loading increments as long as they meet statically and dynamically the requirements for an equilibrium state. Before evaluating the energy flux during crack growth, these parameters were analyzed using a stationary crack. The first analysis consisted in studying the mesh sensitivity, as shown in Figure 5.16. Two meshes were evaluated for the same contour calculation size and compared to

the analytical formulation. The results showed excellent agreement for both methods and different mesh sizes. An additional analysis was needed in order to confirm that the contour calculation was convergent. Therefore, various contour sizes (shown in Figure 5.17) were utilized to calculate the energy flux and to study convergence.

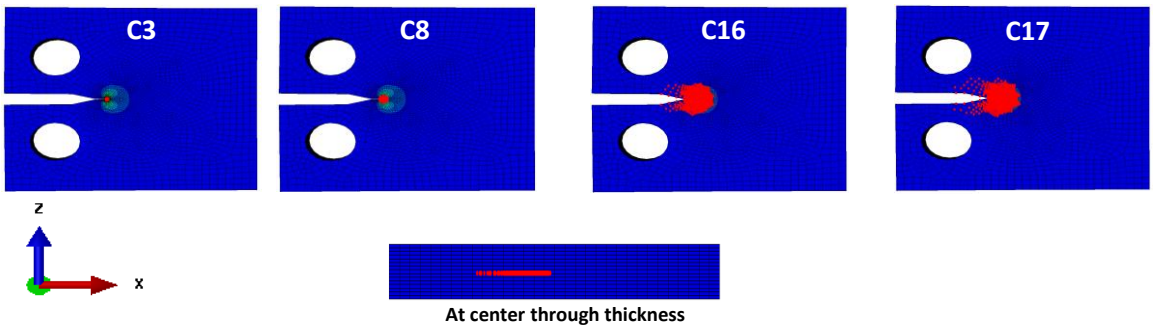

Figure 5.17: Four different contour sizes (area of group of nodes), at the center of model through thickness, shown on the plastic strain accumulation color plot

The integral involved in this approach was transformed from a line integral to a surface integral formulation, thus the contour area size was found to be key parameter to accurately obtain the energy flux. However, there was a limit to its size that could be used since other geometrical features, such as the CT model pins, cause divergence of the integral calculation. Another important factor about the size of the contour was to assure that the plastic process zone is completely included in order to account for all dissipation around the crack tip. The energy flux calculations for contours C3, C8, C16 and C17 are shown in Figure 5.18.

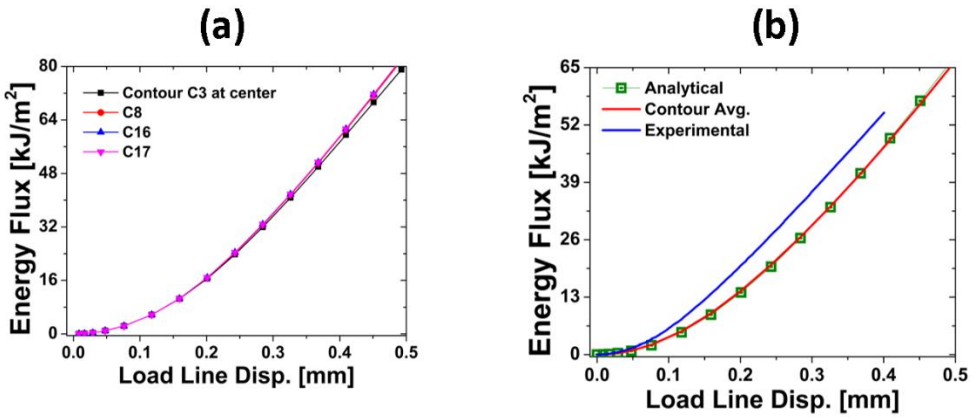

Figure 5.18: (a) Contour size convergence for integral calculation. (b) Contour calculation using integral and analytical form compared to experimental results.

The corresponding results for all contour sizes at the center shows that at C8 the energy flux calculation converges. This result suggested that C8 comprised most of the plastic zone and can be used to accurately determine the energy flux as function of loading increments. In order to confirm this convergent result, the integral calculation was compared to that of the convenient analytical form using the load-displacement response of the model. Since a single value is needed and the integral values were calculated throughout the thickness (i.e. 16 contour values for the 16 nodes through thickness in the case of the CT-A model), the contour values through thickness were averaged. The results show excellent agreement between the two formulations for the CT-A model. In addition, the same convenient form was utilized to calculate the energy flux for the experimental data. Although there are some differences in the magnitude of the energy flux, such discrepancies can be attributed to the fact that the experimentally determined displacement values at the pins could contain compliance from the machine (i.e. fictitious additional values). All of the integral calculations have been performed for the CT-A using a stationary seam as precrack in order to verify and validate that energy flux calculation. However, the fracture-induced model uses an enriched-type crack in contrast

to the seam crack, which depends on the mesh and duplicates nodes on top and bottom crack surfaces. This difference between the two types of numerical cracks is illustrated in Figure 5.19.

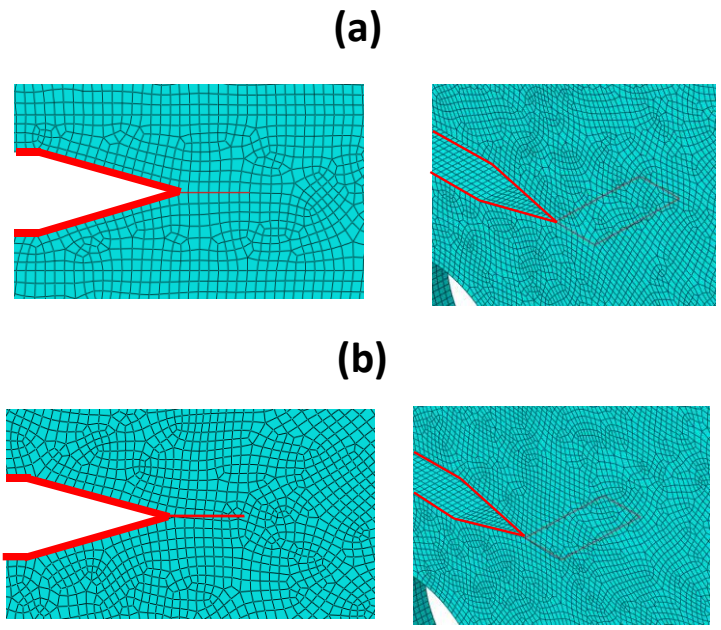

Figure 5.19: (a) Seam and (d) enriched XFEM precrack with corresponding mesh

The XFEM model relies on a Heaviside step function and a search algorithm to determine if an element is separated, while the location of such separation can be found without the need to explicitly create nodes on the mesh. In contrast, the seam methodology uses a stationary crack which needs to be predefined before running the FEM analysis. Therefore, a hybrid methodology which takes under consideration the contour integral for a growing enriched crack was necessary to quantify the energy flux as a function of loading increments. Figure 5.20 shows a comparison between different analyses using the seam and XFEM crack.

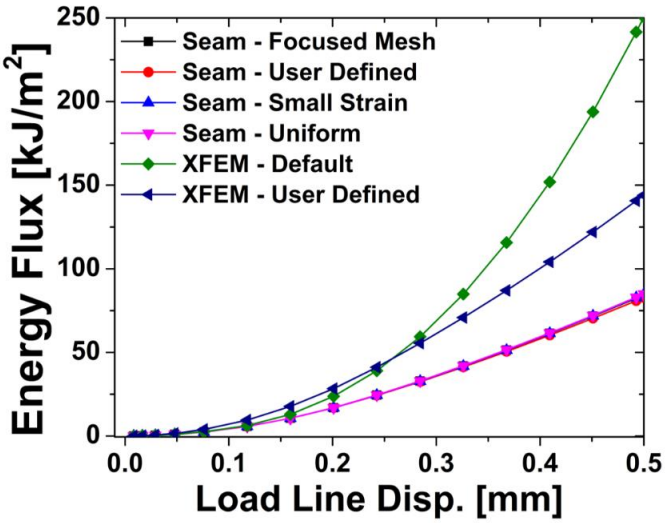

Figure 5.20: (a) Contour integral results calculated using various seam crack methodologies and compared with two XFEM crack methodologies

All seam crack methods agreed regardless of the analysis type in the FEM formulation. However, the XFEM crack results differ from each other; in addition, the XFEM default method is also limited to a stationary crack with small strain (i.e. infinitesimal FEM formulation) and overestimates the energy flux compared to the seam crack. Consequently, a user-defined hybrid methodology to calculate the energy flux is necessary. Such methodology relied in manually defining the crack front by specifying nodes close to the enriched crack tip, which were within an element as shown in Figure 5.19. The second step was to set the direction of the flux using the global coordinates. This methodology definitely has limitations and as seen in the results of Figure 5.20, from which it could be stated that it still overestimates the energy flux, nevertheless less than the XFEM default method. However, the XFEM user-defined approach can be used to characterize and quantify the energy flux in the fracture-induced model for a growing crack. Using the XFEM user-defined approach, the energy flux formulation was applied

for two crack fronts and two corresponding normal directions. These results along with the schematic of the crack fronts are depicted in Figure 5.21.

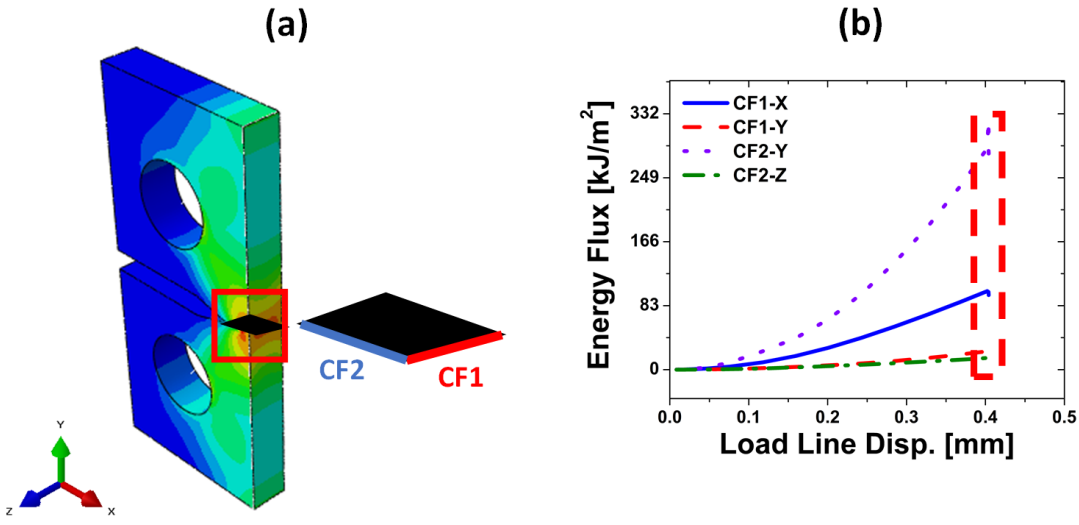

Figure 5.21: (a) Crack fronts utilized for energy flux calculation marked as CF1 and CF2. Energy flux for various two perpendicular directions to each of the two crack fronts

After performing a contour size convergence study for each of the four calculations, the final evolution of the energy flux shows a sudden drop at the critical stage when the crack initiates. This particular behavior had been previously seen in the energy distribution and it is supported by Griffith's formulation of the energy release rate (i.e. similar to the energy flux) for two different crack sizes. This concept is illustrated using the CT-A model with seam crack sizes in Figure 5.22.

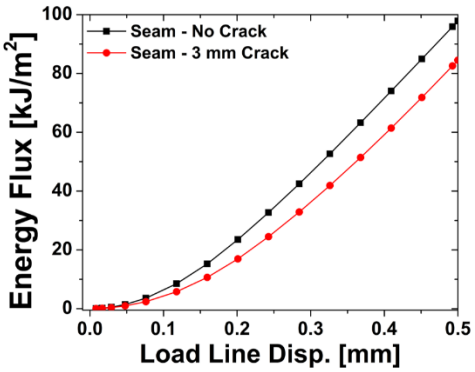

Figure 5.22: Contour integral results calculated using a seam crack for two crack sizes

The drop in energy flux is close to 20 kJ/m^2, which is equal to 20 mJ/mm^2 for a crack surface area of 18 mm^2 (from 3 mm crack growth). The results in Figure 5.21 also show that the energy flux for the crack CF1 in the direction of the global *y*-axis has the highest values compared to all the other calculations. However, this direction of the energy flux was very sensitive to the contour size chosen in addition due to the precrack the crack growth occurs in the *x*-direction. In order to compare such results, the same type of analysis was applied to the CT-B model and the results are shown in Figure 5.23.

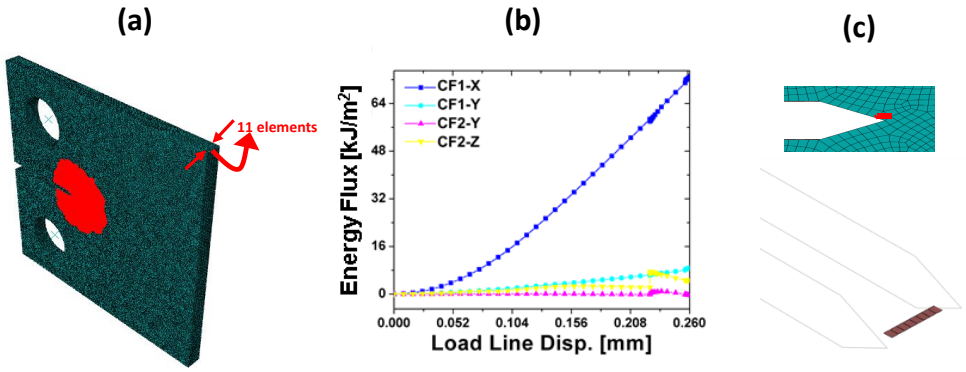

Figure 5.23: (a) Convergent contour size. (b) Energy flux for different crack fronts and directions. (c) Resulting crack profile at 0.21 mm of loading displacement

The CT-B results showed that the *x*-direction was dominant to all the other fluxes but similarly it showed that an instability occurs when there is a crack increment (shown in Figure 5.23c). It can be observed that the energy flux during crack growth is also characterized by an instability (i.e. sudden redistribution denoted by a drop or increase), which denotes behavior similar to that found by using the energy balance approach. Therefore, the change in energy flux during these stages before and after crack growth is calculated and then multiplied by the newly created crack surface in order ultimately obtain the crack energy.

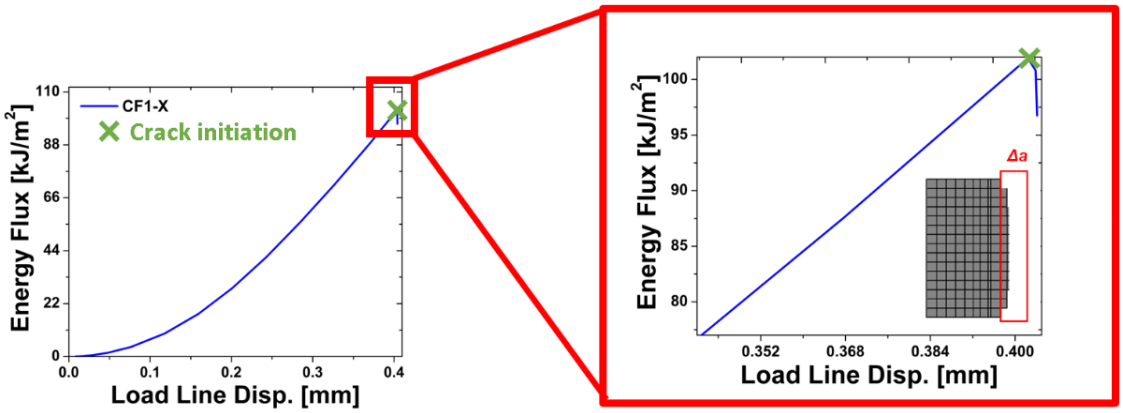

Figure 5.24: Energy flux evolution as displacement-controlled loading is increasing with zoomed region close to drop instability

The results for the energy flux in CF1 in the *x*-direction are plotted again in Figure 5.24 in order to further study the instability due to the onset of crack growth. The energy flux's first drop is equal to 1.11 kJ/m^2 for a crack surface extension of 2.24 mm^2 which results in a 2.48 mJ energy release. The energy associated to static crack growth calculated from the energy flux is in the same scale as the one obtained using the total energy in the system. Although the difference between the methods is within 35% (i.e. 1.38 mJ of the 3.86 mJ obtained using the energy balance), both methods produce results of the same order of magnitude which validates the approach followed.

In addition to using the static solution, the same energy flux formulation can be used for the dynamic model. Hence, by using the same contour size, crack front, and direction, the energy flux results were calculated, and the corresponding results are shown in Figure 5.25. The transient response of the energy flux depicts a sudden increase from 100 to 112.1 kJ/m^2 in addition to fluctuations as it reaches a steady-state around 50-75 μs, which is a much longer time period (5μs) than the respective one in the Poynting vector formulation. The difference between the energy fluxes at the initial jump at 0μs and at

the steady-state at ~60 μs is approximately 3.88 kJ/m^2. This change in energy flux is again for a crack surface increment of 2.24 mm^2 which yields a difference equal to8.69 mJ, which although higher (possibly also because it does not include the kinetic energy contribution) is found again to be at the same order of magnitude (mJ).

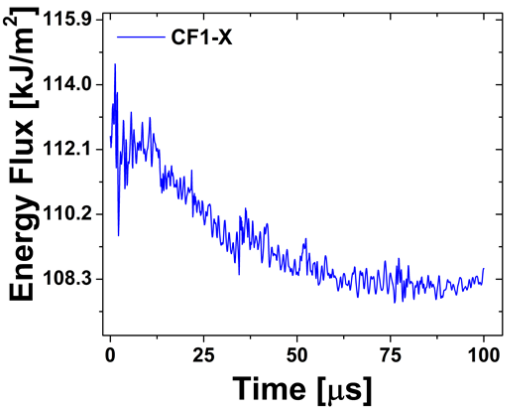

Figure 5.25: Energy flux calculation calculated using the dynamic solution

In Table 5.1 all the results obtained by two methodologies are summarized in addition to the calculations of the energy radiated which is the quantity more closely related to that of the AE energy captured experimentally. It can be seen that although there are discrepancies between all values, they are all in the milli-Joule regime.

TABLE 5.1: AE SOURCE ENERGY SUMMARY FOR CT-A

Method/Parameter	Static	Dynamic
Energy Balance	3.86 mJ	2.2 mJ
Energy Flux	2.48 mJ	8.69 mJ
Energy Radiated	-	14 nJ

Furthermore, the overestimation of the energy flux in the dynamic analysis can be attributed to the fact that the kinetic energy was neglected in static type calculations and

that then all parameters calculated (i.e. stresses, strains, and displacements) contained the residual values from the static analysis only. The removal of such residual values was actually performed for the Poynting vector results in order to accurately obtain the radiated energy from the energy associated with the formation of a crack increment.

5.4 CONCLUSION

The energy considerations for the fracture-induced model, presented in Chapter 3 and 4, were successfully implemented and studied using two different methods for verification purposes. The results propose an upper bound for the amount of energy redistribution due to crack growth. Both methods were evaluated using both static and dynamic considerations based on the developed fracture-induced AE model, providing two different approaches. Specifically, the energy balance approach was based on the difference of the total energy between two equilibrium states, while the Poynting vector formulation for the dynamic part was used to compute the energy radiation through a fixed volume around the crack. In addition, the energy flux approach was applied using the same formulation for both static and dynamic analyses. Even though this model excludes parameters such as heat dissipation, the energy quantification presented herein effectively quantifies the energy due to crack formation, where energy is dissipated due to plastic accumulation. In conclusion, the framework for quantifying the energy associated with AE not only aids in the better understanding of the AE sources and concomitant wave generation, but it also provides a benchmark for applications such as the manufacturing of new innovative AE sensors with improved and tailored design to more effectively identify and evaluate e.g. crack formation in materials/structures.

CHAPTER 6: PLASTICITY EFFECTS IN ACOUSTIC EMISSION-RELATED WAVE PROPAGATION

6.1 INTRODUCTION

The AE process can be generally described by one or more sources that due to their activation they generate bulk pressure waves that propagate in a material. Independently of the content and features of the AE source, the traveling waves are affected by the surrounding medium before being recorded by an appropriate sensor. Therefore, the interactions of the AE-related waves with the medium, in which propagation occurs, are necessary to be understood in order to quantify the effects that occur in the trajectory defined from the source (thought as a "material point" in this description) to the location of the known sensors. Fundamentally, the wave propagation associated with the AE process is subjected to wave effects within a continuum, including attenuation, dispersion, geometric spreading, etc. In addition to the boundary conditions imposed by the continuum itself due to its geometry, its state of deformation is an additional factor that could potentially affect the wave characteristics, e.g. in the case of a solid with plasticity.

In this context, it has been reported that an excitation/vibration with a given frequency and a sufficiently large amplitude, is affected when it travels through a nonlinear solid [1-3]. Essentially, the fundamental wave is distorted as it propagates and consequently second and higher harmonics are generated [2]. In essence, plastic deformation softens locally the material by reducing its load carrying capacity and creating zones with different material properties [4, 5]. This concept could be better understood by

considering the case of wave propagation in a soft material attached to a stiffer one. The soft material for a given perturbation would tend to vibrate more than the stiffer region causing changes in the traveling waves, above and beyond the effects that also occur at their interface. Based on this explanation, this Chapter attempts to capture, analyze and quantify effects caused by plasticity near simulated AE sources. Specifically, numerical results of the compact tension model, implemented earlier in Chapter 3, 4, and 5, are firstly validated based on previously reported investigations and then linked to AE by applying an appropriate source model. These analyses provide a benchmark for understanding the influence of plasticity on AE by deconvolving the AE process into its source and wave traveling components, which could potentially assist in the practical detection and identification of AE sources.

6.2 MOTIVATION AND OBJECTIVE

The concept of generation of higher harmonics has been extensively studied with the main objective of developing NDT tools to detect and identify plastically deformed regions where critical damage could initiate. Such investigations, typically in the field of ultrasonic techniques, had led to the definition of parameters to not only detect but to also characterize the evolution of plasticity in several materials [4-7]. However, most of these investigations focused on generating appropriate sources with second/higher harmonics that could potentially interact with existing flaws in order to detect them. Figure 6.1 shows some related experimental results, among several others [3, 8, 9], which were recently obtained by Liu et al. [10]. The development of higher harmonics can be observed in this figure, as well as fact that these frequencies are proportional to the

fundamental (i.e. primary, denoted as f_0) harmonic due to Rayleigh-Lamb (RL) and Shear-Horizontal (SH) ultrasonic wave modes.

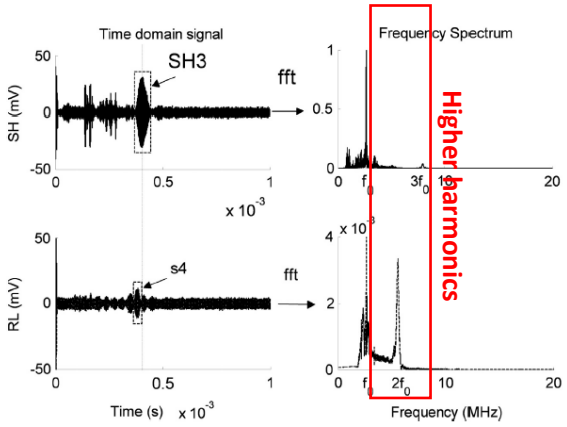

Figure 6.1: Received SH and RL signals (Modified from [10])

The fundamental idea explored herein refers to the fact that large deformation inside a plastic region and the resulting softening of a solid due to plasticity could distort traveling waves. This concept is visualized in Figure 6.2 using plastic equivalent strain contours near the simulated notch tip of the CT model developed in this dissertation to show the process zone and the associated wave propagation within and beyond the plasticity area.

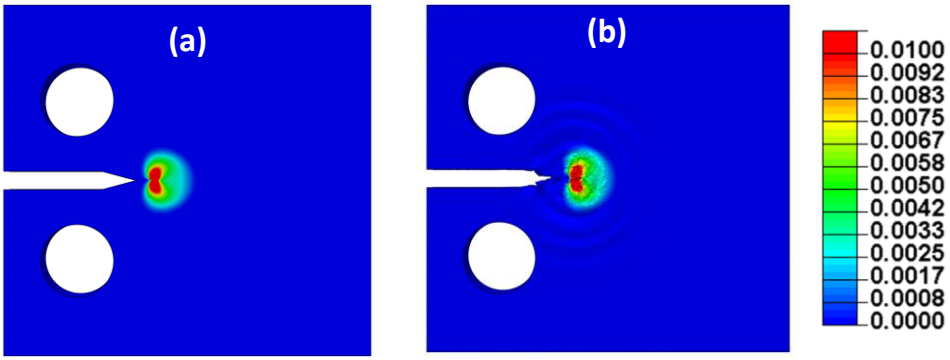

Figure 6.2: Equivalent plastic strain contour $\left(\sqrt{2/3}\left\|\varepsilon^{p}\right\|\right)$ for the CT-A model (a) at static equilibrium and (b) at transient dynamic release of stress waves due to AE source

In order to develop such a plasticity zone, the CT model was loaded to a specific displacement (shown in Figure 6.2a), and then an imposed pulse was used as a source that generates waves, similar to what occurs in the AE process.

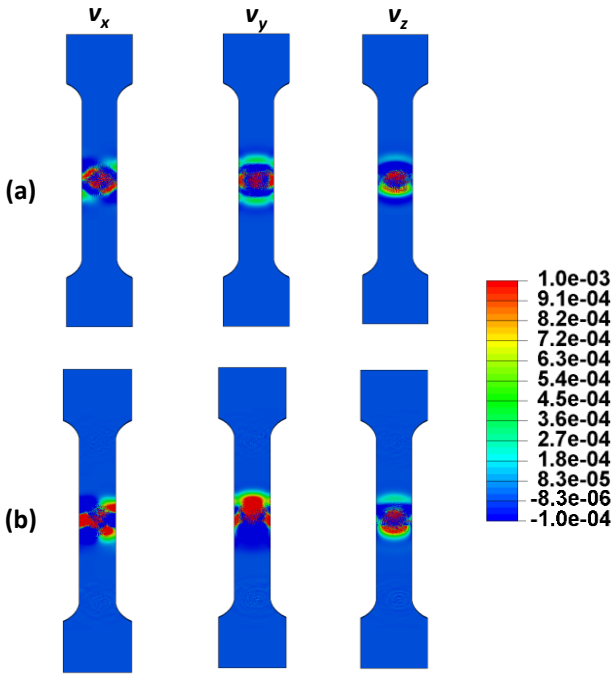

Figure 6.3: Velocity vector contour plots illustrating wave propagation on a tensile coupon geometry under (a) elastic and (b) plastic conditions

In addition, the same idea was implemented and illustrated for a tensile coupon geometry. Specifically, the velocity contours for each component with a fixed legend in Figure 6.3 illustrate wave propagation for an undeformed (shown in Figure 6.3a) and plastically deformed (shown in Figure 6.3b) solid. It can be seen clearly that the wavefront was affected by the permanent large deformation caused by plasticity. Moreover, it was also observed that the most affected velocity components are the *y*- and *z* (i.e. loading direction and out-of-plane, respectively), which could be explained by the fact that such contours are plotted on the surface, where such components have the highest amplitudes.

6.3 COMPUTATIONAL MODEL BACKGROUND AND DESCRIPTION

The computational model was built using an incremental plasticity approach with an isotropic hardening law. In addition and in comparison to the CT models presented in Chapter 3, 4, and 5, the models employed in this Chapter did not include the XFEM formulation or any discontinuities. Therefore, the models presented herein are solely built using the standard FEM formulation and are used for both quasi-static and dynamic conditions. The analysis focused mainly in two CT models with two different values of thickness (similar to CT-A and CT-B from Chapter 4 and 5). An additional geometry of a tensile dog-bone specimen was utilized as a supplementary case to confirm the results obtained from the CT models.

The computational model includes a nonlinear material law obtained experimentally by tensile tests. It further uses a mathematical description of plasticity that consists of an isotropic yield function, *f*, which for the applied plasticity law can be written as follows

$$f = \sqrt{S_{ij} S_{ij}} - \kappa = 0\,, \tag{6.1}$$

where S_{ij} is the deviatoric component of the stress tensor σ, and κ is the maximum yield stress which can be obtained from a tension test by,

$$\kappa = \sqrt{\frac{2}{3}}\sigma_y\,, \tag{6.2}$$

where σ_y represents the computed yield stress from the tension test. The first term in the yield function in Eq. (1.1), is often set equal to $\sqrt{2J_2}$, where J_2 is the second invariant of the deviatoric stress and therefore this formulation is also referred to as J_2 plasticity.

Moreover, this term is also equal to the Von Mises stress. The mathematical description of the yield function is defined by an elastic region Ξ which can be written as

$$\Xi = \left\{ \sigma_{ij} \in \mathbb{R} \,|\, \sigma_{ij} = \sigma_{ji} \;,\; f\left(\sigma_{ij}, \kappa\right) < 0 \right\}, \tag{6.3}$$

while the yield surface is defined in a 6-dimensional space as follows

$$\partial\Xi = \left\{ \sigma_{ij} \in \mathbb{R} \,|\, \sigma_{ij} = \sigma_{ji} \;,\; f\left(\sigma_{ij}, \kappa\right) = 0 \right\}. \tag{6.4}$$

The formulations, from (6.1) to (6.4), for the incremental plasticity methodology are fundamentally based on the additive decomposition of the strain tensor. Figure 6.4 graphically depicts a 2D representation of this formulation.

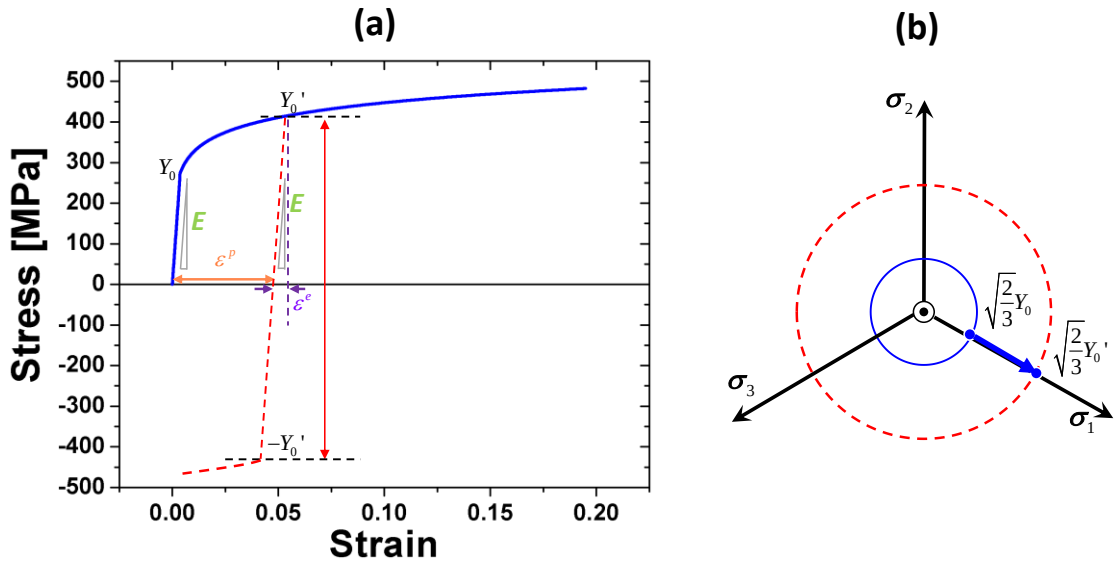

Figure 6.4: Graphical representation using the computational model's aluminum alloy constitutive law, which defines the elastic and plastic (denoted as ε^e and ε^p) component of strain at and portrays the isotropic hardening law when linear unloading occurs. (b) Schematic of the isotropic hardening law in the deviatoric plane (i.e. the three axes are the three principal stresses of the state of stress denoted as $\boldsymbol{\sigma_1}$, $\boldsymbol{\sigma_2}$, and $\boldsymbol{\sigma_3}$) for a 3D state of stress

The constitutive law for an aluminum alloy, shown in Figure 6.4a, was described in detail in Section 3.5 as a piecewise function which had a logarithmic function for the plastic nonlinear part, as written in Equation (3.26)(3.26). The formulation for yield stress as function of plastic strain (i.e. the hardening law) shows nonlinear behavior which can also be described by a power law defined in terms of the plastic strain (ε_{pl}) as follows

$$Y = Y_o + H\varepsilon_{pl}^{\,1/m}, \tag{6.5}$$

where Y_0 is the initial yield stress, H is plastic modulus and m is exponent coefficient of the power law. Table 7.1 lists all the fitting parameters calculated for the function in (6.5).

TABLE 6.1: ISOTROPIC POWER LAW FITTING PARAMETERS

Fitting Parameter	Values
Initial yield stress, Y_0	289.7 MPa
Plastic modulus, H	338 MPa
Exponent coefficient, m	2.917

In addition to having a nonlinear power law to express the yield stress as a function of plastic strain, Figure 6.4a depicts the isotropic hardening law used in the plasticity model which is represented by the dashed lines as unloading occurs assuming a state of stress for a monotonic loading. Similarly, Figure 6.4b shows the isotropic hardening law for a 3D state of stress in which the yield surface expands as the stresses are greater than the

maximum yield stress, denoted as $\sqrt{2/3}Y_0$. This law states that the initial yield stress value, Y_0, is updated to Y_0' (by the nonlinear law in (6.5)) for a given value of plastic strain ε^p. As unloading occurs monotonically no further plastic strain will be accumulated unless the stress state is higher than the absolute value of Y_0', in the case of monotonic loading. Basically, the isotropic hardening law determines when the state of stress is in the plastic domain (i.e. is at the yield surface), which can be determined by the Von Mises stress. In summary, the model presented herein includes an isotropic yield surface and hardening law which are appropriate for ductile materials, such as the aluminum alloy used here.

After constructing the plasticity law from the experimental data, the second step consisted of determining the method to be used to generate the emissions at a region under plastic deformation. In this context, the computational models utilized three different loading conditions to not only study plastically deformed samples but also analyze a baseline using the undeformed state and applying similar pulses (i.e. a dynamic source to produce emissions). Figure 6.5 presents the different boundary conditions applied to all models including the supplemental tensile coupon.

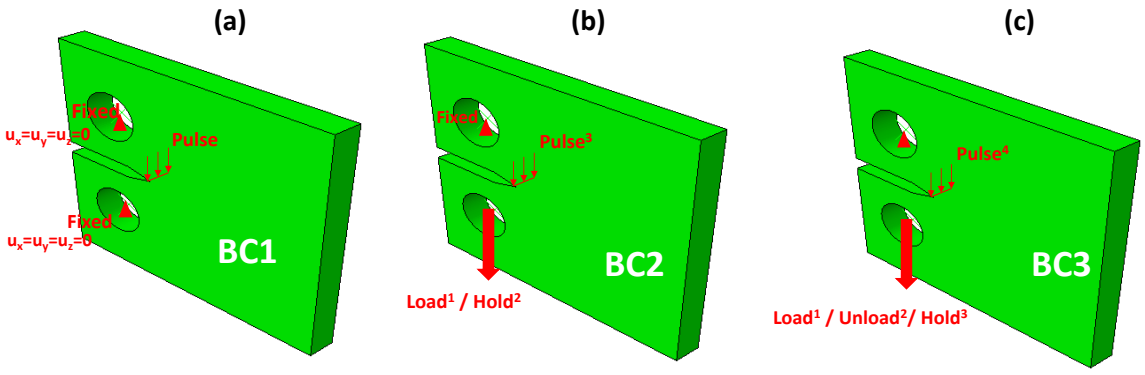

Figure 6.5: Boundary conditions imposed to study and characterize the effect of plasticity on wave propagation related to AE, denoted as (a) BC1, (b) BC2 and (c) BC3

For instance, BC1 consists of applying fixed displacements at the pins and imposing a pulse at the tip of the simulated machined notch, while the other two involved loading and holding (BC2) and in BC3 loading, unloading and then holding before imposing the pulse. The pulse is applied in all FEM nodes across the thickness to avoid any geometrical effects (i.e. reflections from the front and back surfaces, normal to the out-of-plane *z*-direction). The same type of boundary conditions were applied to a tensile coupon (with dimensions illustrated in Figure 6.6a). However, the boundary conditions at the gripping areas differed from those of the CT model since the rotations were additionally fixed (i.e. a clamp-type boundary condition), as shown in Figure 6.6b.

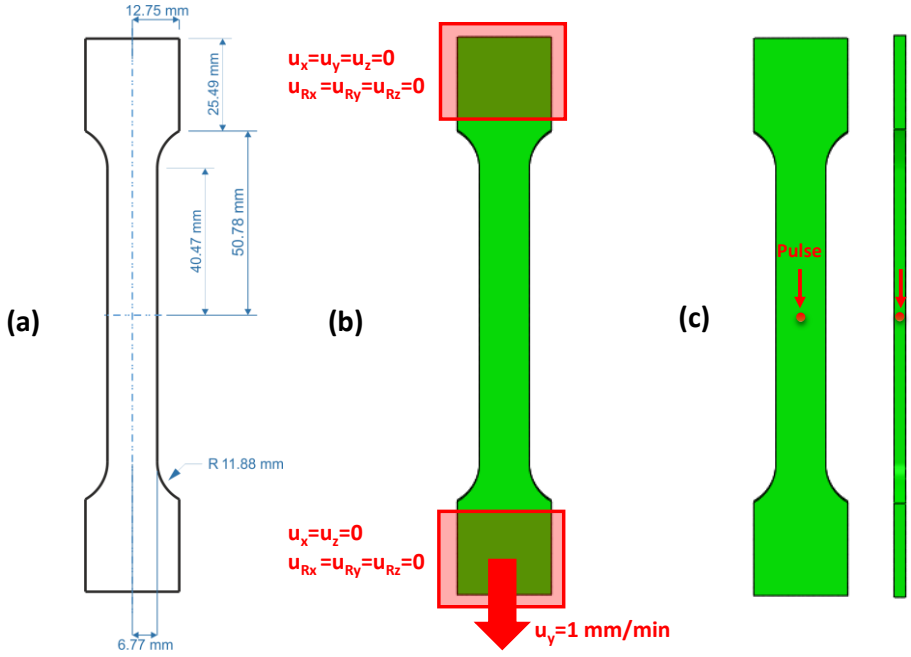

Figure 6.6: Tensile coupon (a) ASTM standard dimensions along with boundary conditions for (b) static and (c) dynamic analysis

Another difference in the boundary conditions is the single point pulse used in the tensile coupon compared to a series of nodes through the thickness. Figure 6.7 shows the applied pulses, which simulate an AE source with their corresponding spectral content obtained using both the Fast Fourier Transform (FFT) and Short Time Fast Transform

(STFT). Three different displacement or load pulses were imposed to investigate the frequency response of the two geometries investigated herein. The two tonebursts utilized included a sine and Hanning window pulse with 10 cycles with a duration of 20 μs, which were used to impose a dominant and narrow frequency content, as shown by the STFTs of Figure 6.7a and b. Two central frequencies of 300 kHz and 500 kHz, were applied with a maximum time step size of 100 ns. In addition, a Dirac pulse was applied in order to evaluate the response of a range of frequencies, from 200 kHz up to 2 MHz, and with a maximum time step of 50 ns to assure sufficient frequency resolution.

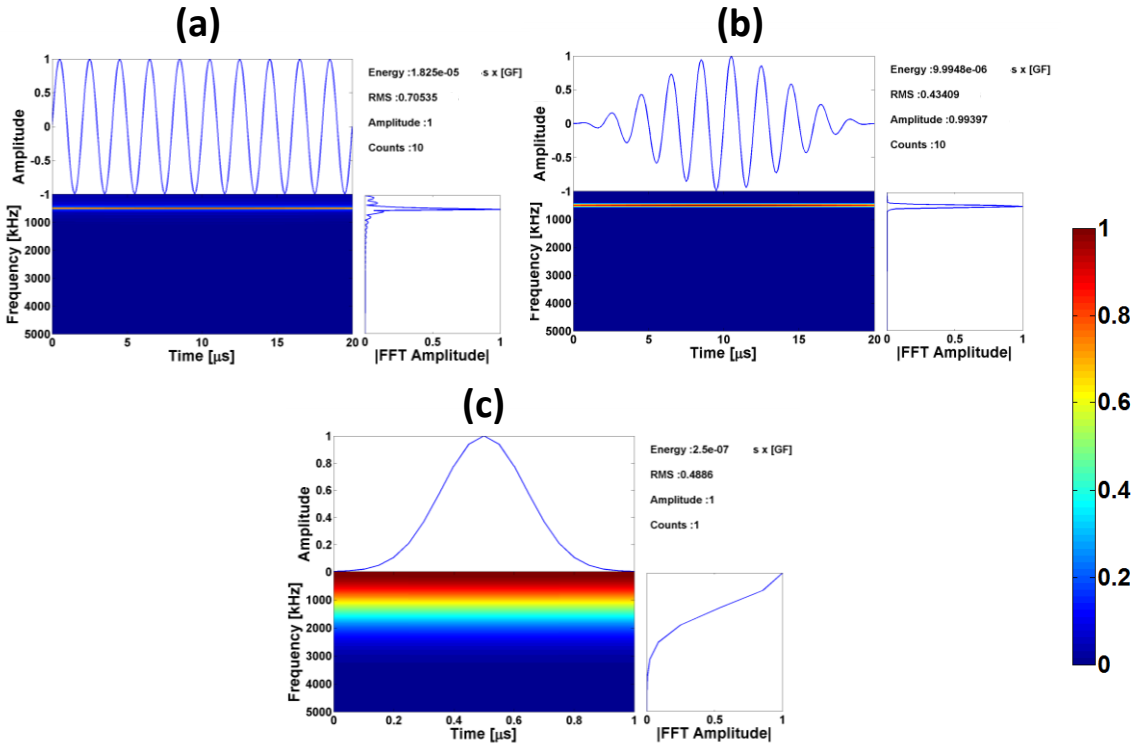

Figure 6.7: Load or displacement pulses imposed for wave propagation simulation including (a) sine and (b) Hanning window toneburst, as well as a (c) Dirac pulse

Several nodal locations for different loading conditions were examined as denoted in Figure 6.8, where the wave propagation is visualized by the deformed shape using the velocity vector results. The plasticity effects were investigated by using four different

points, depicted in Figure 6.8b. Such points were specifically selected ahead of the machined notch, so that the wavefront is not affected by geometrical features other than the edges (i.e. at point 4). The four nodal locations were at a distance of 0 μm, 400 μm, 8 mm, and 40.63 mm, respectively, ahead of the machined notch, and therefore points 1 and 2 were inside the plastic zone (illustrated in Figure 6.8b).

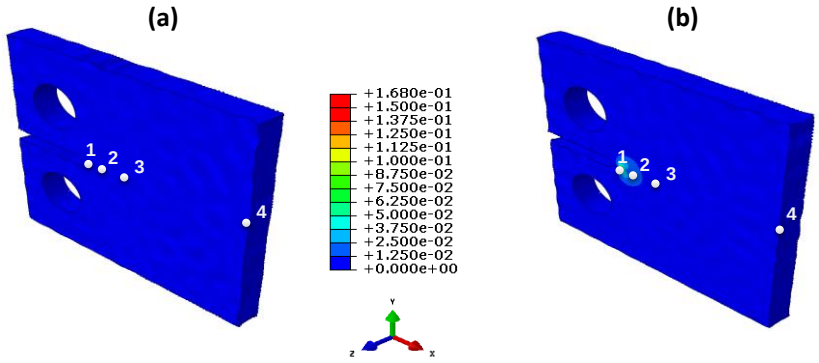

Figure 6.8: Nodal points utilized for data extraction for compact tension model both under (a) elastic and (b) plastic deformation

In the case of the tensile coupon model, two sets of data along the vertical and horizontal axes, for a total of 6 nodes were selected for waveform extraction, as shown in Figure 6.9.

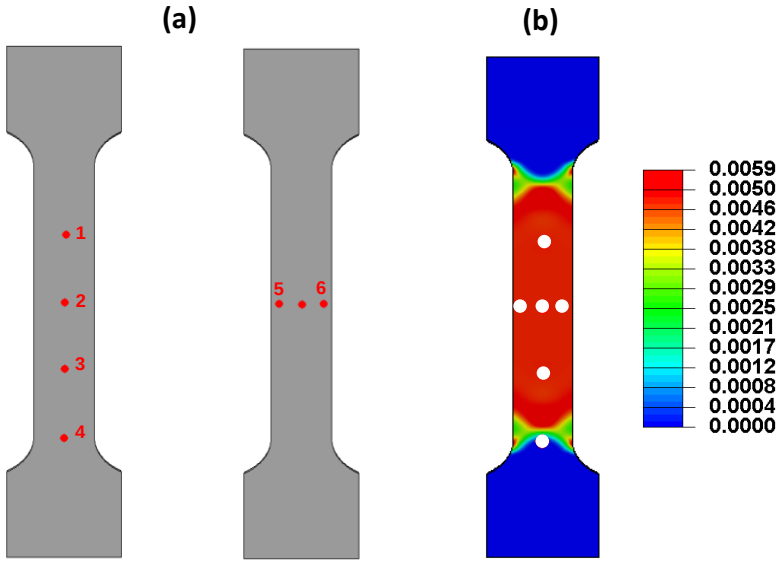

Figure 6.9: Nodal data points extracted for the tensile coupon (a) marked from 1-6 and also shown (b) on plastic accumulated contour plot

Figure 6.9b also shows these nodal points on the accumulated plastic strain plot, where for instance point 4 is out of this zone in contrast to all the others which are at high deformation levels. In order to verify the wave propagation problem, the CT model's bulk wave velocities were studied and compared to analytical calculations using their time of arrival and time difference. Figure 6.10 shows the FEM mesh with the two dimension utilized, i.e. on the surface and through the thickness, to calculate the bulk wave velocities from the FEM solution in order to verify the dynamic analysis.

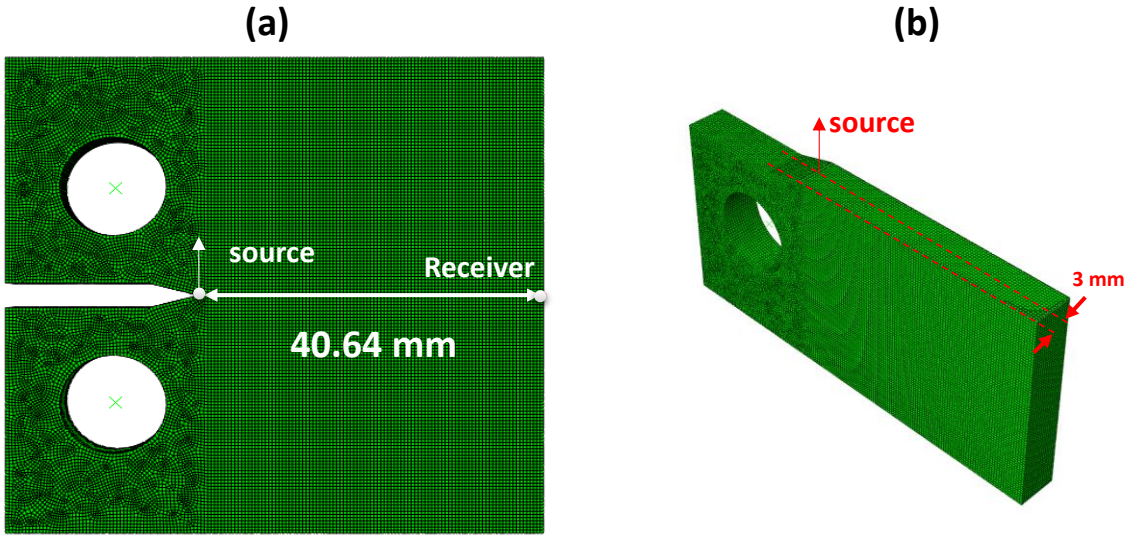

Figure 6.10: CT model for wave propagation model verification with distances from the source along the (a) surface to the receiver and (b) to the surface through thickness

The longitudinal velocity was calculated using the elastic properties to be 6333 m/s, this was then checked by using the out-plane-component waveform (*z*-direction) at the receiver shown in Figure 6.10a. The arrival time of the waveform at distance of 40.64 mm based on the longitudinal speed was calculated to be 6.42 μs, while the numerical waveform arrives within 2% difference of this analytically calculated value. Two points, one in the center and another one on the surface, with a distance of 3 mm (shown in

Figure 6.10b) were also used to verify the longitudinal velocity. The computed acceleration waveforms at the source and at the surface nodal locations along the *z* axis were utilized to calculate analytically the time difference between peaks. The two acceleration waveforms used for this verification are shown in Figure 6.11 with a zoomed time period of 1 μs. The two initial peaks are used as a reference of time travel from point to point instead of using a single waveform and calculating the time of arrival.

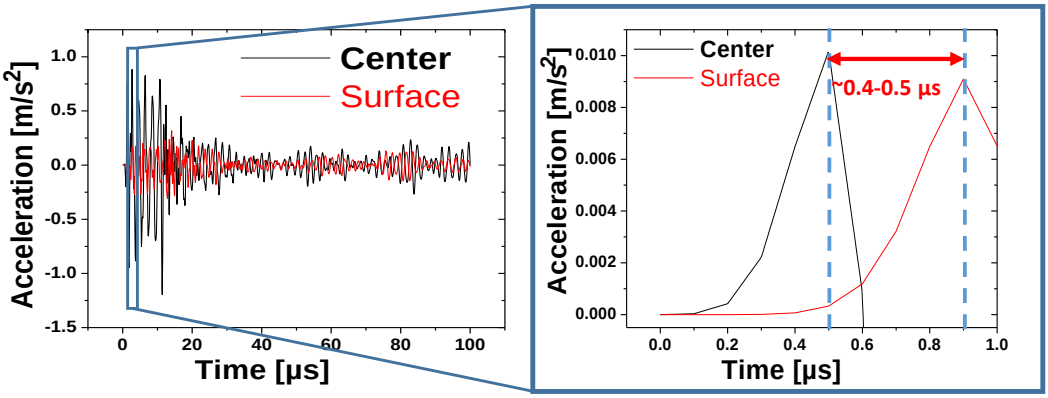

Figure 6.11: Acceleration waveforms calculated at the source (labeled as Center) and at the surface with zoomed in region for time arrival calculation for model verification

The calculated time value for a distance of 3 mm was 0.474 μs and it is shown in Figure 6.11 that the time difference is in the range of 0.4-0.5 μs. The same type of analysis was performed for the transversal/shear wave speed which resulted also within 2% difference. Such results provide a model verification and assure that the implicit solver scheme for the dynamic FEM formulation is providing reliable results.

The tensile coupon model was also evaluated to check for accuracy. The calculated numerical load-displacement curve was compared to that of experiments, depicted in Figure 6.12.

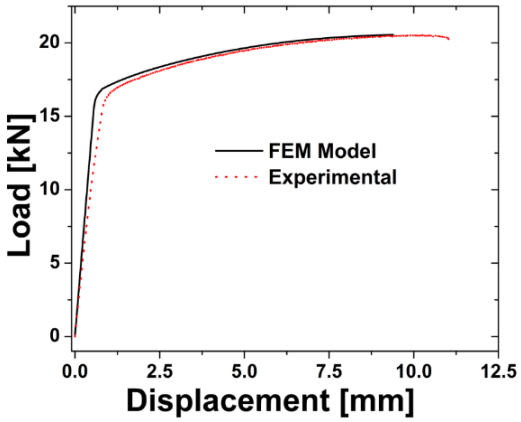

Figure 6.12: Load–displacement response obtained from the FEM model compared to experimental data from loading frame

It can be seen that the displacement results agreed with those obtained experimentally. Although some discrepancies were observed, the tensile model captured most of the linear and nonlinear behavior response. Furthermore, the verification and validation analyses quantify the numerical errors involved in the wave propagation simulation. However, the effects of plasticity on release of emissions, presented in this Chapter, were quantified and evaluated by using a comparative analysis of the results at different states of deformation, including mainly an undeformed and plastically deformed state in addition to a corresponding state after unloading. The deformation state after unloading serves as an additional stress state with possibly higher plastic strain accumulated to be studied as well as an application of the model to conditions similar to those encountered in fatigue.

6.4 RESULTS AND DISCUSSION

The numerical simulations were analyzed and quantitatively compared by characterizing mainly the frequency content of the computed velocity waveforms at various specific locations of the computational models and under different deformation conditions.

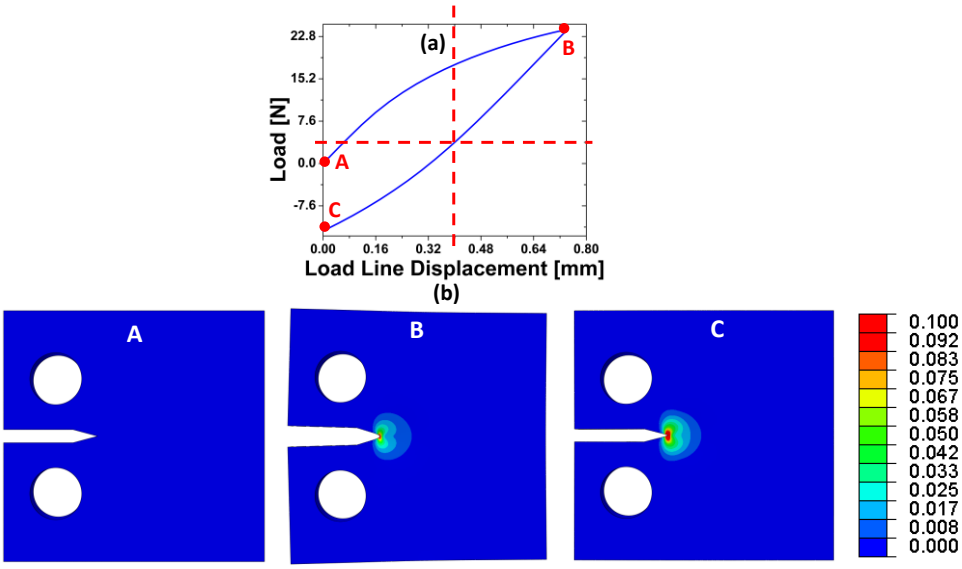

Figure 6.13: (a) Loading stages A-C marked on load-displacement curve with corresponding (b) plastic equivalent contour plots for compact tension sample

Furthermore, the velocity waveforms were generated by imposing a localized emission source (i.e. a load or displacement pulse), which were applied on the undeformed, as well as on the loaded and unloaded plastically deformed states by employing the BC1, BC2 and, BC3 conditions. These three stages are denoted as A, B and C in the load-displacement curve, as shown in Figure 6.13a. For instance, zero displacement is applied at stage C, yet the unloading response is not fully reversible due to accumulated plastic strain. Although the load response in the pins is negative at C, this result is not representative of the stresses at the machined notch which are not necessarily negative. To visualize the evolution of the plastic strain associated with these three stages, the corresponding plastic equivalent strain contours are shown in Figure 6.13. It can be seen that the plastic equivalent strain size around the crack tip increases from stage B to C. This is attributed to the isotropic hardening law which dictates that the stress state must be higher than the last updated maximum yield stress in order to accumulate additional plastic strain. According to the load-displacement response, such stress state at plastic

conditions could be at about 0.4 mm of applied load line displacement since the curve transitions from linear to a nonlinear behavior at this point, marked with dashed lines in Figure 6.13a.

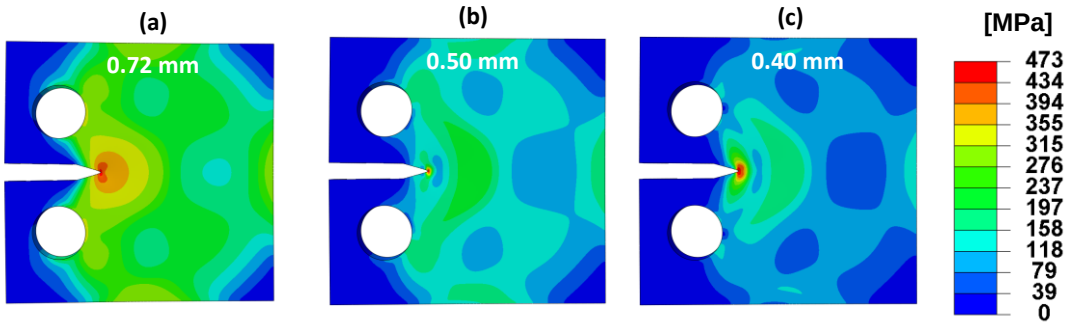

Figure 6.14: Von Mises stress contours for three displacements applied including (a) 0.72 mm, (b) 0.50 mm, and (c) 0.40 mm in decreasing order as the CT model is unloading

Moreover, this increase in plastic strain can also be explained by extracting the Von Mises contours at equilibrium states between stages B to C. Figure 6.14 illustrates the stress contours at three different displacements applied during unloading. It can be observed that at 0.50 mm the stress state is higher than the state at B (i.e. 0.72 mm of applied displacement) by checking the maximum Von Mises stress values at both states. In addition, this increase in stress state is clearly not sufficient to affect the load-displacement as it was the case for 0.4 mm of applied displacement.

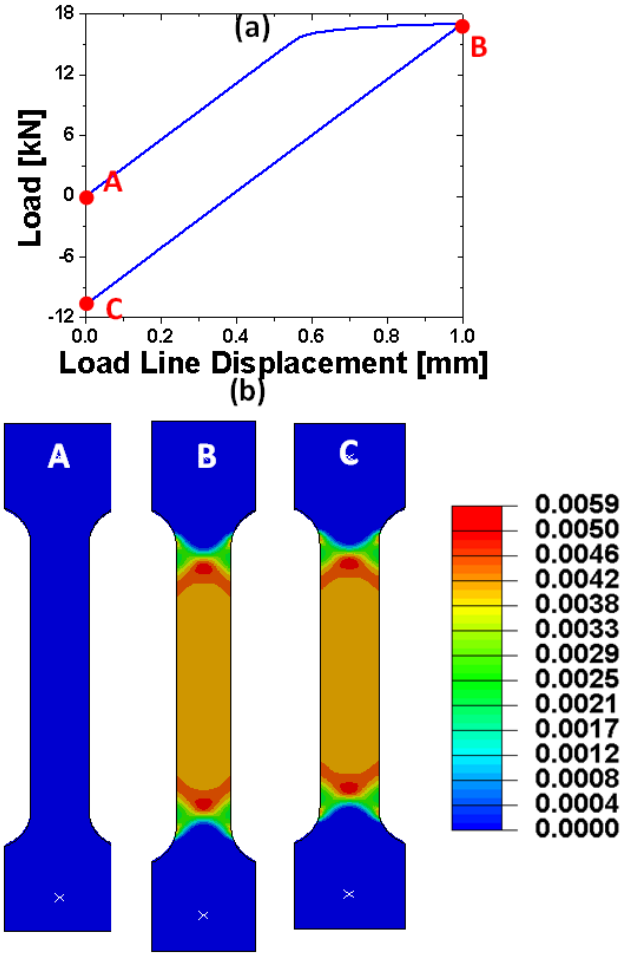

Figure 6.15: (a) Loading stages A-C marked on load-displacement curve with corresponding (b) plastic equivalent contour plots for tensile coupon geometry

In contrast to the loading response of the CT model, the tensile model unloads with a linear behavior to zero displacement, as shown in Figure 6.15a. It can also be observed that the tensile model did not accumulate any additional plastic strain as it unloaded from stages B to C, as illustrated by plastic equivalent strain in Figure 6.15b. This can be attributed to the fact that the loading conditions are monotonic, thus the stress state under unloading conditions could only be higher than the yield stress at B, if the stress state reaches a higher compressive stress value (i.e. at -17 kN).

6.4.1 WAVE PROPAGATION STUDY OF THE UNDEFORMED STATE

Prior to implementing the wave propagation problem on a plastically deformed model, the boundary conditions and effects of the type of pulse on the results were analyzed to better understand the undeformed state.

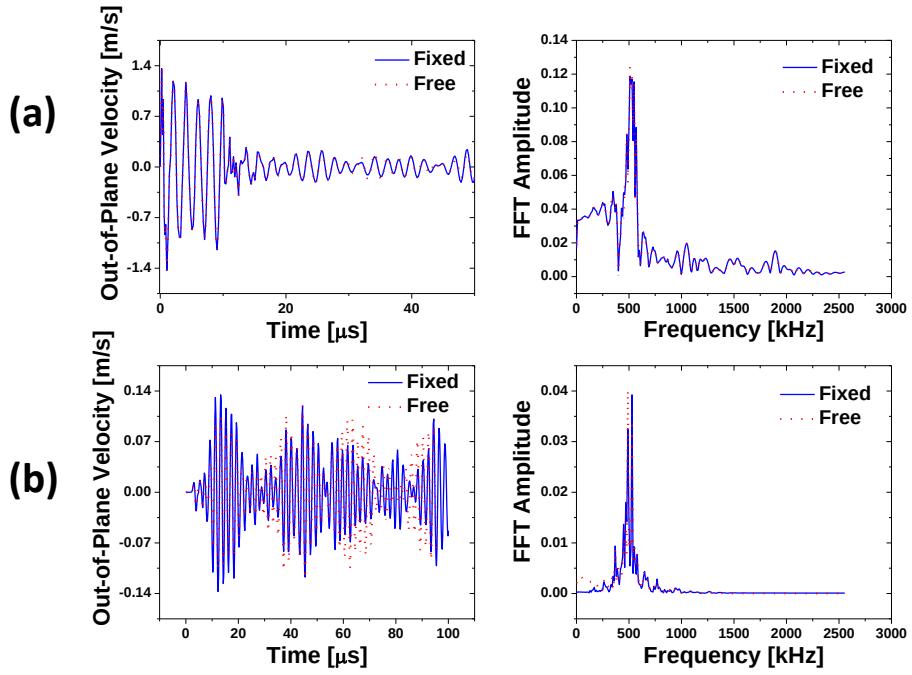

Figure 6.16: Velocity waveforms at a nodal location near (a) to the source and (b) to the pin holes with corresponding FFT analysis

The influence of the boundary conditions at the pins on propagating waves due to the used sources was analyzed using both a fixed and a set of free boundary conditions. In this context, fixed boundary conditions refer to fixing all the translation displacements (i.e. u_x, u_y, and u_z), while free refers to not imposing any constraints. The out-of-plane velocity waveforms for both cases were calculated for sinusoidal pulse, as shown in Figure 6.16. Figure 6.16 demonstrates that the boundary conditions affect more significantly the waveforms located closer to the pins due to reflections. Although the spectral content is similar for both cases, it was observed in Figure 6.16b that the

amplitudes were different as time progresses and at locations close to the pins. Hence, the computational models to study plasticity utilized fixed boundary conditions at the pin holes since the main parameter to analyze was the frequency content.

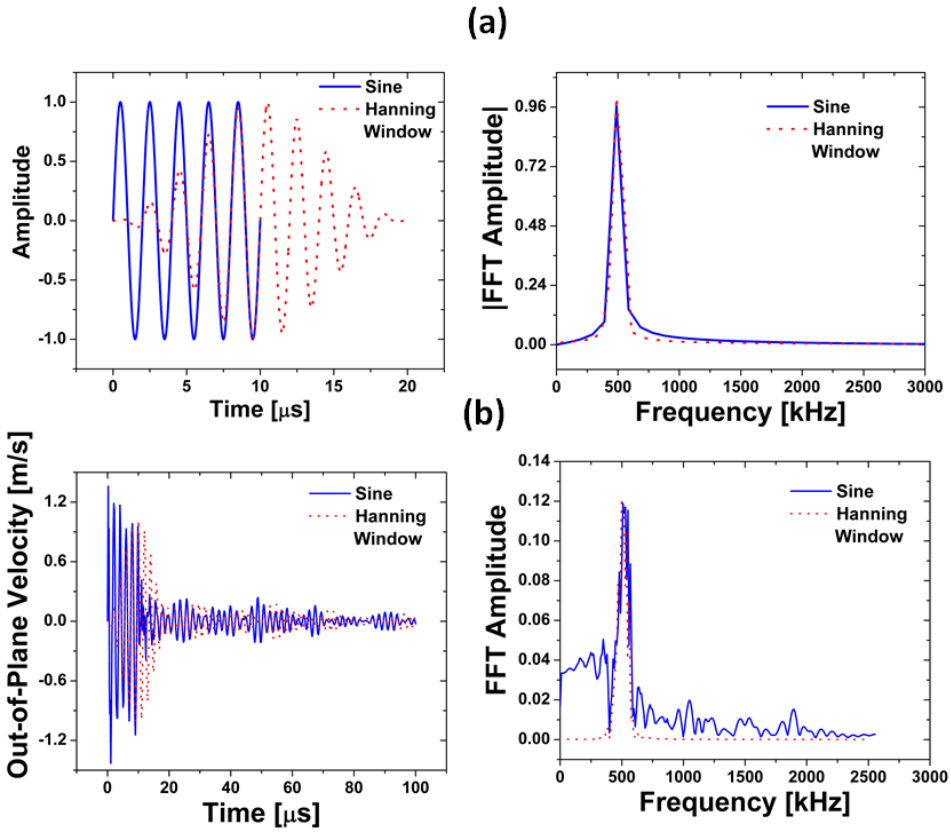

Figure 6.17: (a) Sine and Hanning window toneburst pulse input and FFT comparison. (b) Velocity waveform and FFT results at a point near the source for the two pulse inputs

Another evaluation of the boundary conditions entailed the pulse applied to generate emissions. Both the sine and Hanning window tonebursts produced a central frequency; however, in practical use in the field of ultrasonics, the sinusoidal waveform results in frequency leakage which could affect the results. Therefore, both pulses, portrayed in Figure 6.17a, were evaluated using BC1 at stage A. Although the corresponding FFT analysis of the input waveform is similar, the calculated velocity waveforms showed otherwise and confirmed that the sine pulse has additional spectral signatures that could

potentially affect more complicated analysis. Consequently, the Hanning window toneburst was applied to obtain a single dominant frequency response in all computational models.

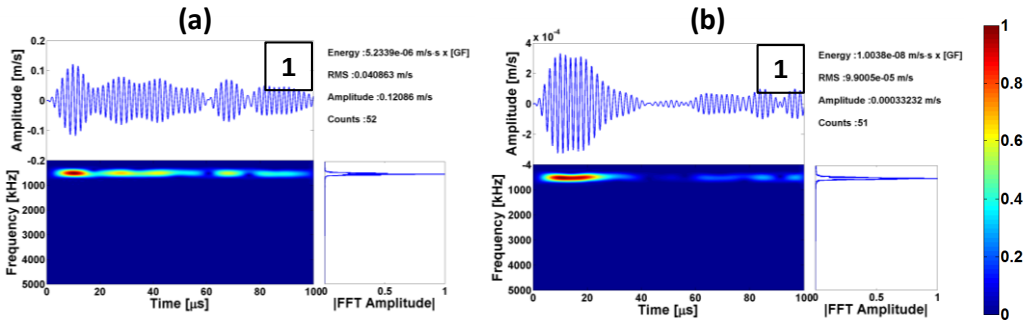

Figure 6.18: Compact tension model's BC1 velocity waveforms at point 1 for (a) displacement and (b) load pulse sources

The pulses could be applied using either a displacement or load boundary condition, thus it was necessary to take into consideration the differences between these two cases. In all the waveform analyses to be followed, the amplitude of the waveforms shown corresponds to the out-of-plane (*z*-direction) component of the velocity. In addition, each waveform is plotted along with its corresponding FFT and STFT results to characterize the frequency content and its evolution with time, respectively. Figure 6.18 shows the velocity waveforms at point 1 (i.e. located on the surface and near the source) calculated using BC1 with Hanning window pulse applying a maximum displacement and load amplitude of 1 μm and 10 mN, respectively. Although the calculated responses had different peak amplitudes and time evolution characteristics, their frequency content was similar.

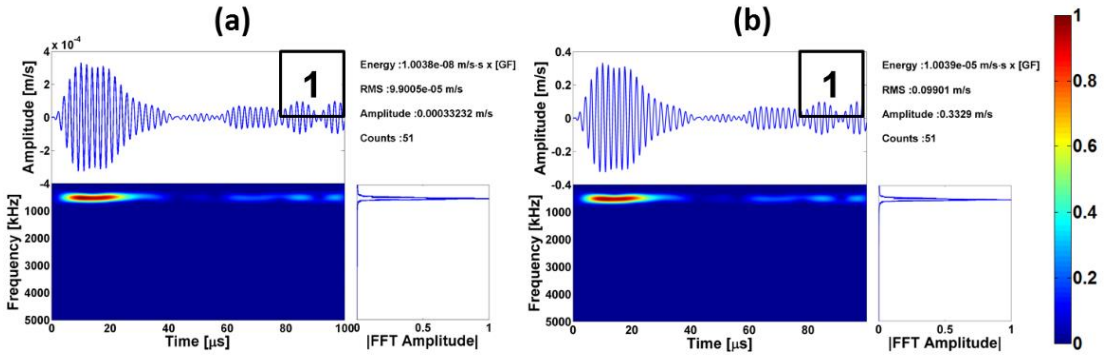

Figure 6.19: Velocity waveforms at point 1 from a load Hanning window toneburst with an amplitude of (a) 10 mN and (b) 10 N

It was also revealed that the 10 mN amplitude results in much lower amplitude responses, thus the effect of the amplitude was analyzed and it illustrated in Figure 6.19. The results at point 1 clearly showed that the amplitude did not alter the waveforms characteristics in both time and frequency domain; except that the waveform amplitude were proportional to one another with ratio of 1:1000 for 10 mN: 10 N.

In addition to studying and analyzing both time and frequency domain of the waveforms at a single point, the waveforms were extracted at the nodal locations (shown in Figure 6.8) for further analysis. Figure 6.20 and Figure 6.21 depict the velocity waveforms at the four points ahead of the machined notch in order to analyze and compare their spatial and temporal characteristics as the wave propagates within the model.

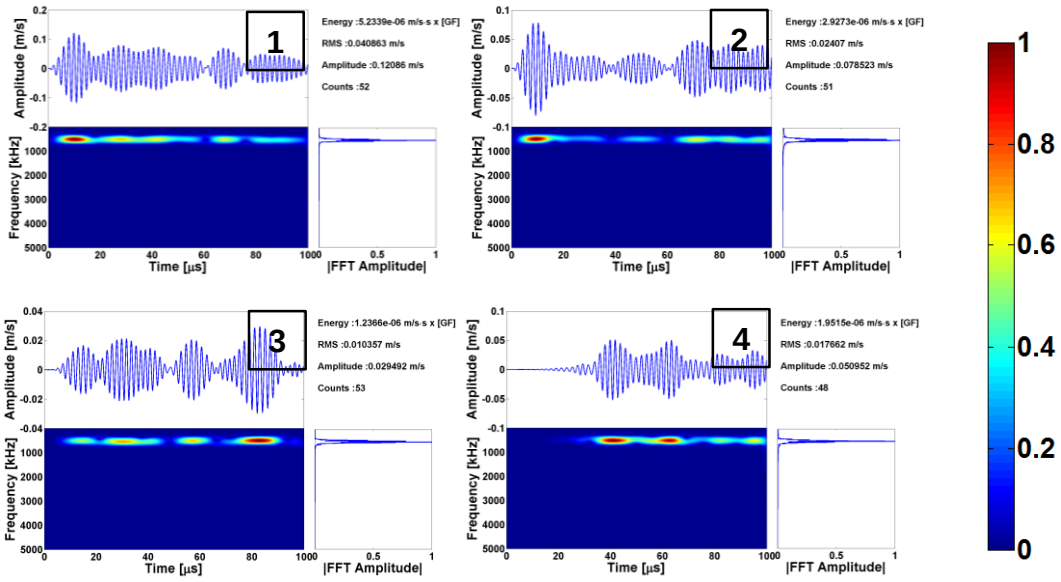

Figure 6.20: Velocity waveforms at locations 1-4 for CT BC1 with displacement pulse conditions

Together these results showed that regardless of the time and distance, type of pulse, and or maximum amplitude, the frequency content was preserved, which in this particular set of results was a dominant frequency of 500 kHz.

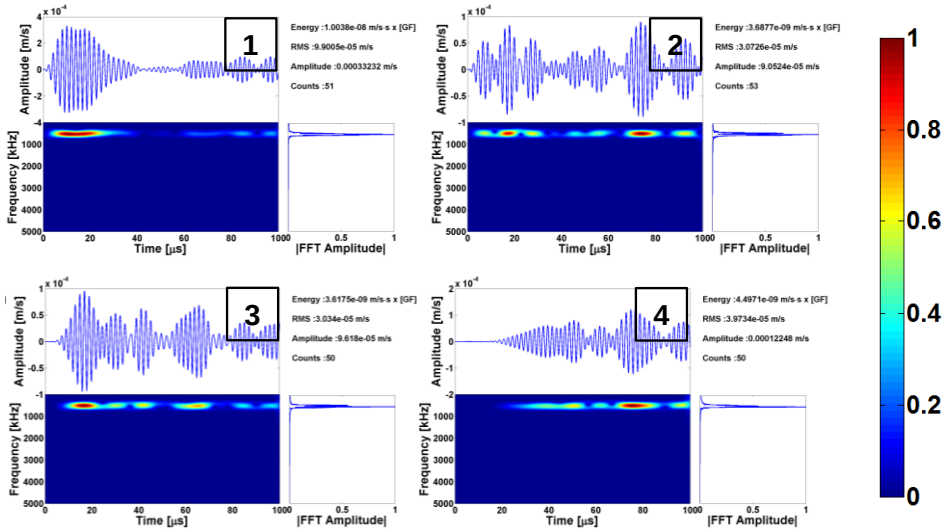

z

Figure 6.21: Velocity waveforms at locations 1-4 for CT BC1 with load pulse conditions

It is also revealed that the time waveforms of both pulse types are not only different at point 1, previously shown, but they showed discrepancies also as a function of time and distance. Regardless of these differences, both load and displacement pulses with a dominant frequency generate a single dominant frequency response.

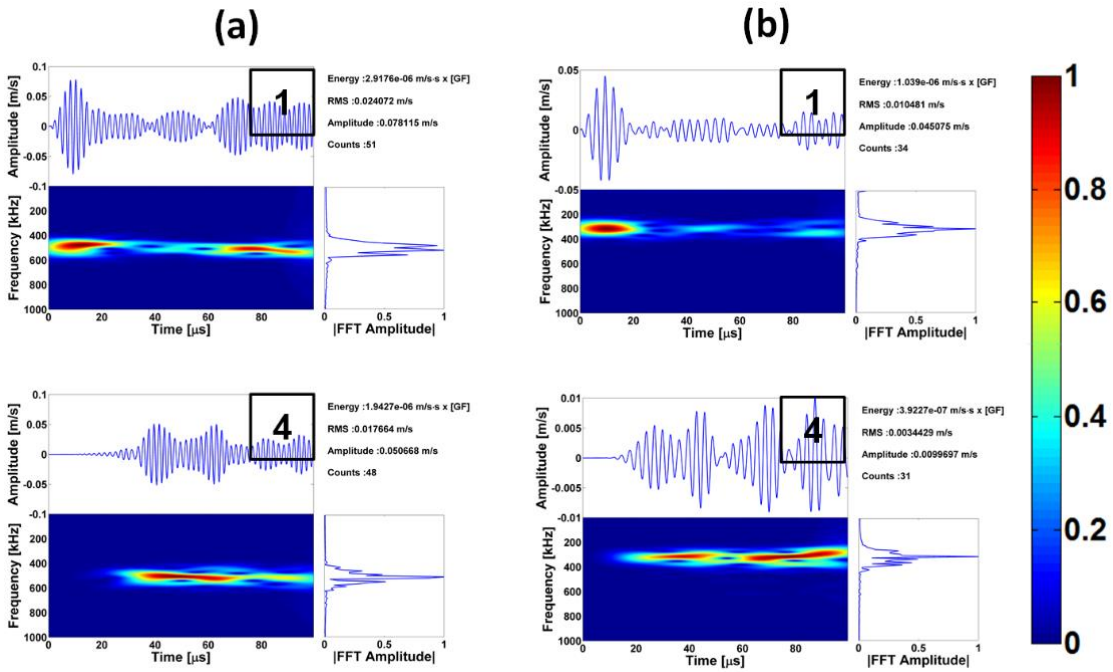

Figure 6.22: Comparison of the velocity waveforms at points 1 and 4 from an imposed Hanning window toneburst with a central frequency of (a) 500 kHz and (b) 300 kHz

These analyses yielded similar results for both types of pulses indicating that either source type would preserve the frequency content. Hence, the load type pulses were selected to characterize plasticity since they were simpler to impose in deformed regions such as in the plastic zone. To further validate the results obtained from the imposed 500 kHz central frequency, a lower central frequency was similarly applied using BC1 and a Hanning window toneburst with a maximum amplitude of 1 μm. The 300 kHz dominant pulse shows a shift in the spectral content compared to the 500 kHz as expected, portrayed in Figure 6.22b. Another apparent difference of imposing a lower frequency

pulse is the time waveform amplitude which is lower than the 500 kHz ones by approximately a factor 2 close to the source and a factor of 10 further away. This can be attributed to the nature of the velocities from the calculated waveforms, which are simply defined derivative/rate of the displacement. Hence, the 10 cycle toneburst with a 300 kHz central frequency evidently has a lower rate compared to the 500 kHz. The results also inferred that the waveforms from the 300 kHz attenuate at a higher rate as a function of time and distance due to the fact that the amplitudes from the source are lower, as shown in Figure 6.22b. This is a reasonable result since typically low amplitude sources tend to attenuate at higher rates in both time and distance.

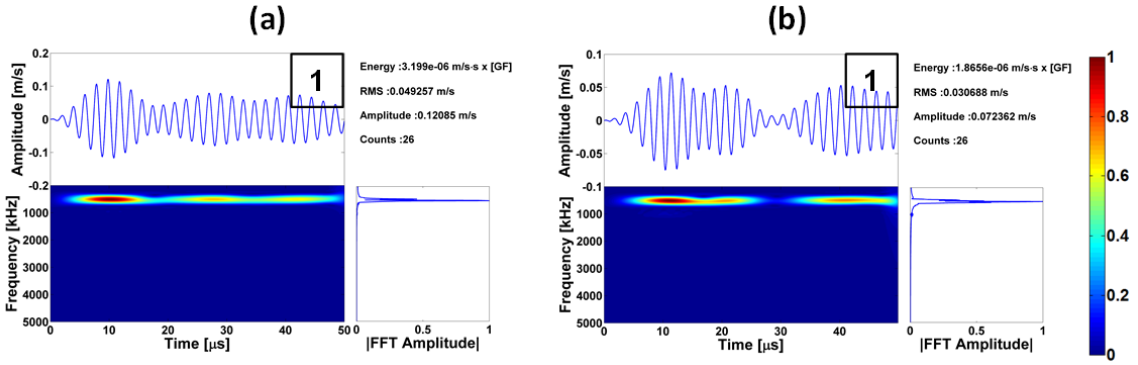

Figure 6.23: 500 kHz Hanning window toneburst results for compact tension coupon with (a) 6 mm and (b) 4 mm thickness (similar to CT-A with no precrack and CT-B, respectively)

The results obtained for the 500 kHz central frequency were further compared by implementing the model in a thinner CT model (i.e. similar to CT-B). These results indicated that the geometry of the model did not influence the frequency response and signatures for a dominant frequency, portrayed in Figure 6.23. Overall, both velocity waveforms had similar trends, although they had different amplitudes and STFT distributions. Ultimately, the geometry effects were further evaluated using the even thinner tensile model. The six nodal locations showed that the velocity waveforms, depicted in Figure 6.24, had a consistent frequency content, which again confirms that a

pulse with a dominant frequency for the three geometries tested on their undeformed state had a frequency response that agreed with the imposed source.

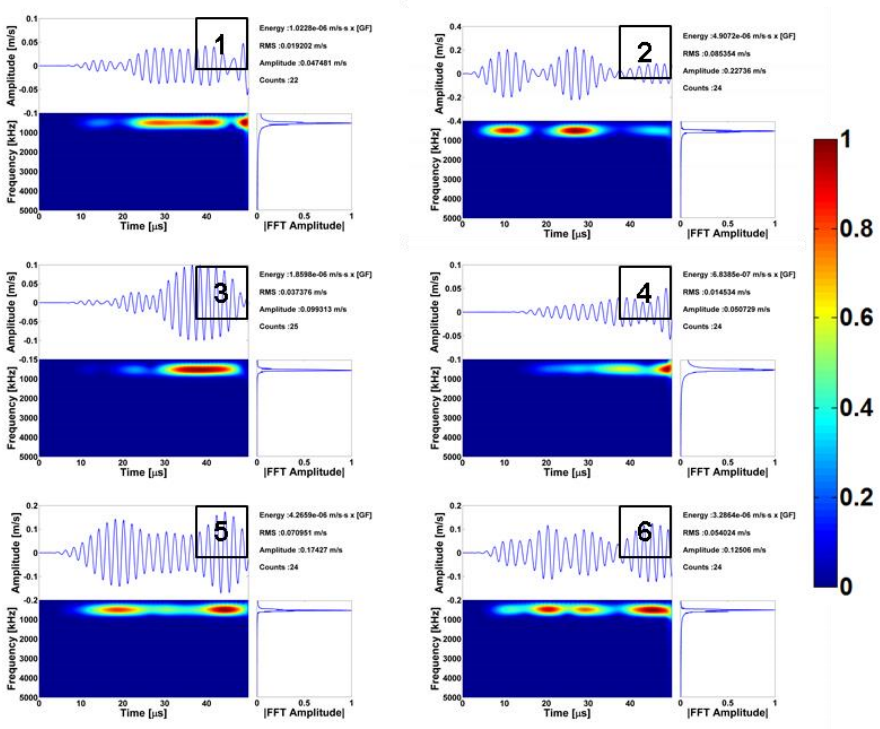

Figure 6.24: Calculated velocity waveforms at 6 locations marked in Figure 6.9 from tensile coupon subjected to 500 kHz toneburst point source

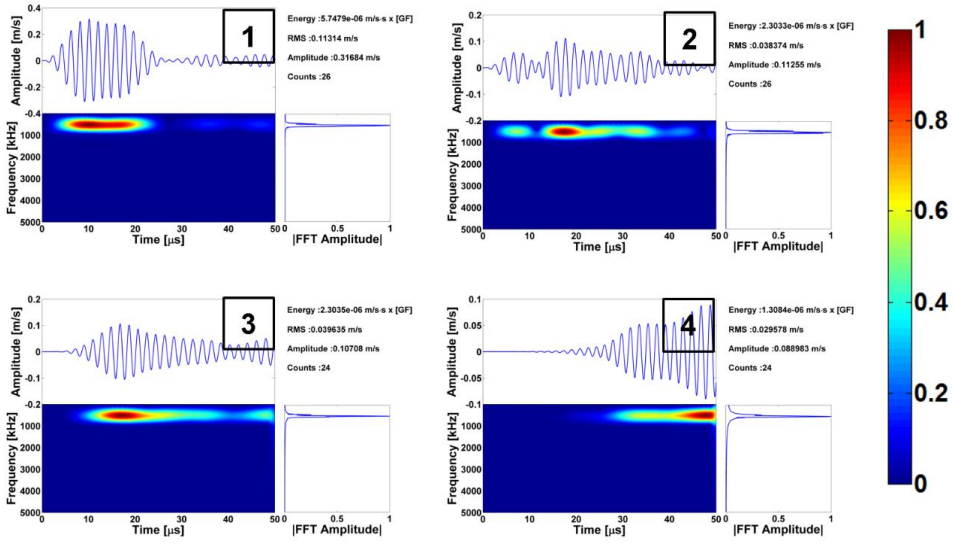

Figure 6.25: Velocity waveforms for 4 points in CT BC1 model subjected to a small deformation due to loading and a 500 kHz Hanning window pulse

The 500 kHz pulse was also imposed at a stage between load points A and B in Figure 6.13a (i.e. 42 μm of load line displacement and 2800 N in the load-displacement curve), which was found by checking the plastic strain accumulated. The results from this model are also utilized to confirm that the waveforms are not affected by a deformed state using low loading conditions. Such deformation conditions infer that the material points in computational CT model mathematically belong to the elastic region. In addition, the results showed that the loading conditions do not modify or distort the frequency content of the velocity waveforms, as it is shown in Figure 6.25. Therefore, it can be concluded that the imposed pulse travels through a medium under elastic conditions without accumulating any plasticity. All of these results, besides verifying the material response due to a pulse with a central frequency, provide a set of baseline results for the three different geometries at nodal locations in order to be used as a comparison of the stage A with the other stages B and C.

One of the main goals of the computational models was also to see the effect of plasticity in AE related emissions. To simulate an AE-like source, a Dirac pulse was applied which instead of having a single dominant frequency, it has a range of frequencies, as shown in Figure 6.26. This input source was applied to the three geometries, including the 6 mm thick and 4 mm thick CT model as well as the tensile coupon model. The results for the 6 mm thick CT showed that the range of activate frequency values was between 500 kHz to 2.5 MHz according to point 1, which is close to the source, as portrayed in Figure 6.26. It can also be seen that the high frequencies and the waveforms' amplitude attenuate as a function both of distance and time. A common characteristic in all waveforms is that the peak frequency is around 1.2 MHz which is suggested by the FFT and STFT analysis.

Furthermore, the directionality of the pulse was also captured by the waveform at point 1 close to the source, where the negative amplitude is close to -6 x 10^{-4} m/s and the positive one is 4 x10^{-4}; however, this asymmetry vanished as wave propagated as it is shown in the waveforms from 2 to 4.

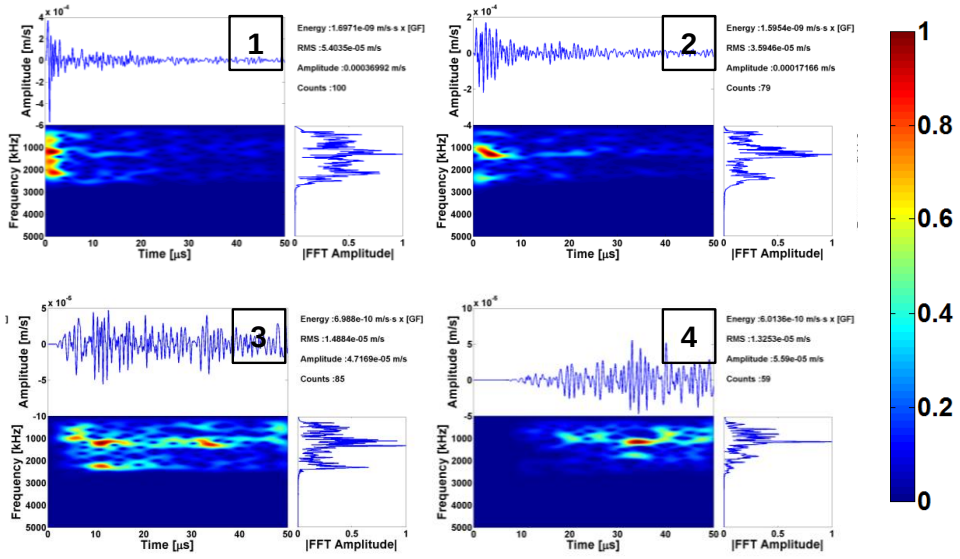

Figure 6.26: 10 mN Dirac pulse using BC1 boundary conditions results for points 1-4 for the 6 mm thick compact tension model

Compared to the 6 mm thickness, the 4 mm thick model showed that the waveforms have different characteristics. For instance, the asymmetry due the pulse was not as pronounced in the velocity waveform at 1. In addition, although the high frequencies and amplitude attenuated in a similar manner as the 6 mm thick specimen, the frequency content had different peak values. Such dominant frequencies were not carried over as a function of distance; for example, at points 1 and 2 the peak values of the FFT showed a 200-300 kHz which was not the case for the other two nodal locations that had 1-1.2 MHz peak value. Therefore, the geometry affected the velocity waveforms both in the time and frequency domain. Regardless of the differences between the two geometries,

each of these results from each datasets can be compared with a case in which plasticity is accumulated.

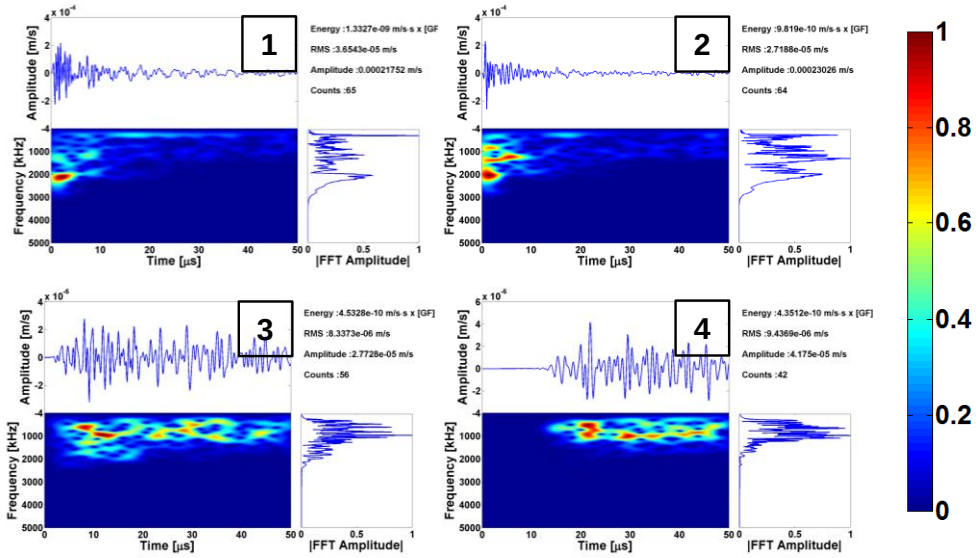

Figure 6.27: 4 mm thick compact tension model velocity waveforms for points 1-4 using a 10 mN Dirac pulse source

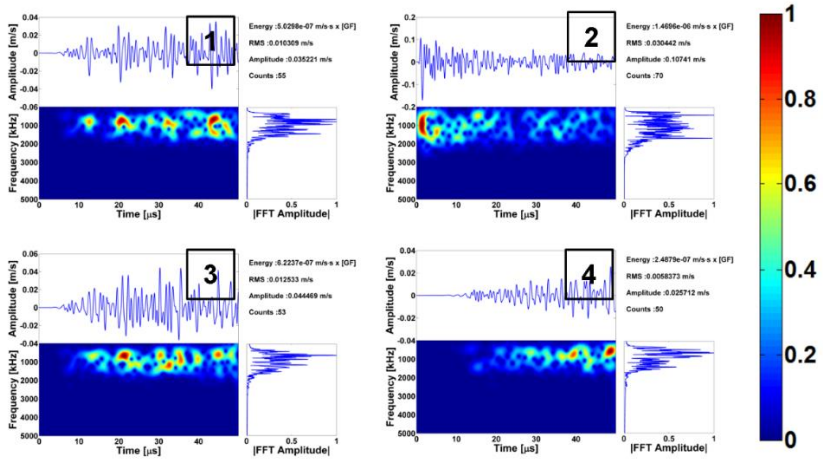

Figure 6.28: Velocity waveforms for the 4 nodal locations along the tensile coupon's surface resulting from a 10 N Dirac pulse

Furthermore, the tensile coupon was also studied as another set of results in order to characterize the effect of geometry. Similar to the results of the 4 mm thick CT model, the peak frequency closer to source (i.e. in this case point 2) were different than all other points. For instance, point 2 had a peak frequency of 200-300 kHz and 1.8-2 MHz while

other points had a common peak frequency of 800 kHz-1 MHz. Besides these differences, the spectral characteristics were similar to the other cases of imposing a Dirac pulse.

6.4.2 GENERATION OF HIGHER HARMONICS DUE TO PLASTICITY

The second part of the comparative analysis consisted in using stage B, i.e. a plastically deformed medium, in order to examine the influence of plasticity on wave propagation. Compared to the results obtained in stage A, the velocity waveforms at stage B for the 6 mm thick compact tension from a 500 kHz central frequency clearly showed at all nodal locations that a second harmonic as well as higher harmonics were generated due to the presence of plasticity.

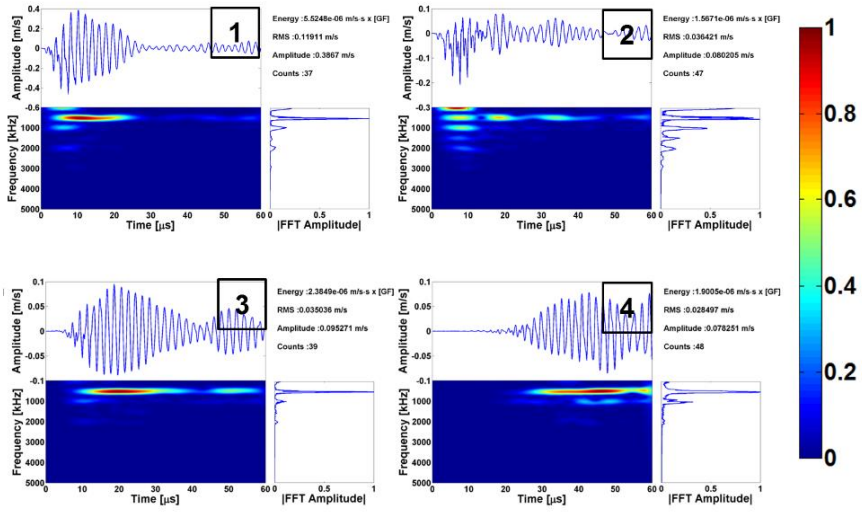

Figure 6.29: Velocity waveforms for 4 points in CT BC1 model under plastic deformation around the machined notch and subjected to a 500 kHz Hanning window pulse

Taking a closer look at each of the waveforms and considering their locations with respect to the plasticity zone, it can be concluded that those near the plastic zone (i.e. 1 and 2) generate higher harmonics with higher amplitudes compared to those nodal

locations outside (i.e. 3 and 4), as shown in Figure 6.29. Furthermore, such alterations in the waveforms can be seen both in the time and frequency, where the waveform is highly distorted at an initial period of time at points 1 and 2. The distortion of the waveforms and the amplitude of these higher harmonics however depend on the Von Mises stress state (based on the isotropic hardening law) that the input source and concomitant traveling wave produces around the plastic zone since this determines if the medium remains in the elastic or plastic domain. This high frequency content is then carried over from the plastic to the elastic domain which causes the amplitude of these higher frequencies to decrease, as shown point 3 and 4. In addition, point 4 distinctively showed to have a higher amplitude for the higher harmonic compared to point 3; however, this effect is mainly attributed to the reflections caused at this boundary and it is relative to the amplitude of the waveforms since the FFT analysis provides normalized values. To better illustrate the effect of plasticity on the waveforms, a comparison of stage A with stage B, along with a loading state in between with plasticity, is presented in Figure 6.30 .

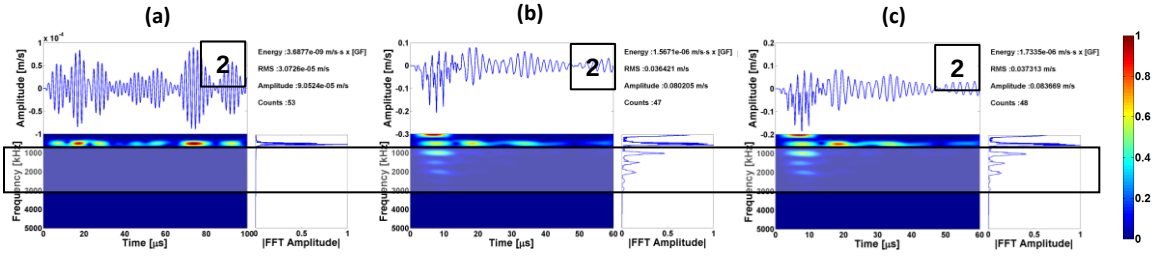

Figure 6.30: Velocity waveforms at point 2 for the case of (a) no plasticity, (b) plasticity and (c) a lower plasticity level than (b) present for the 6 mm thick compact tension

It is clearly shown that the waveforms at point 2 (which had the most effect according to Figure 6.29) were similarly distorted due to the presence of plasticity regardless of the level of plasticity acquired. Another effect that could be associated with the amplitude of the higher harmonics can be attributed to the intensity, i.e. strength, of the applied pulse.

Therefore, Figure 6.31 portrays a comparative analysis of the waveforms at nodal locations applying two different maximum amplitudes of the Hanning window toneburst. The results demonstrating that the strength of the pulse affects the amplitude of these higher harmonics; for instance the waveforms from a 10 N-pulse (shown previously in Figure 6.29) evidently discriminate the proportional higher harmonics. In addition, a lower amplitude source excitation to some extent colors the frequency content which is in the case at point 4 in Figure 6.31b. An important factor to generating these higher harmonic is the plasticity law implemented.

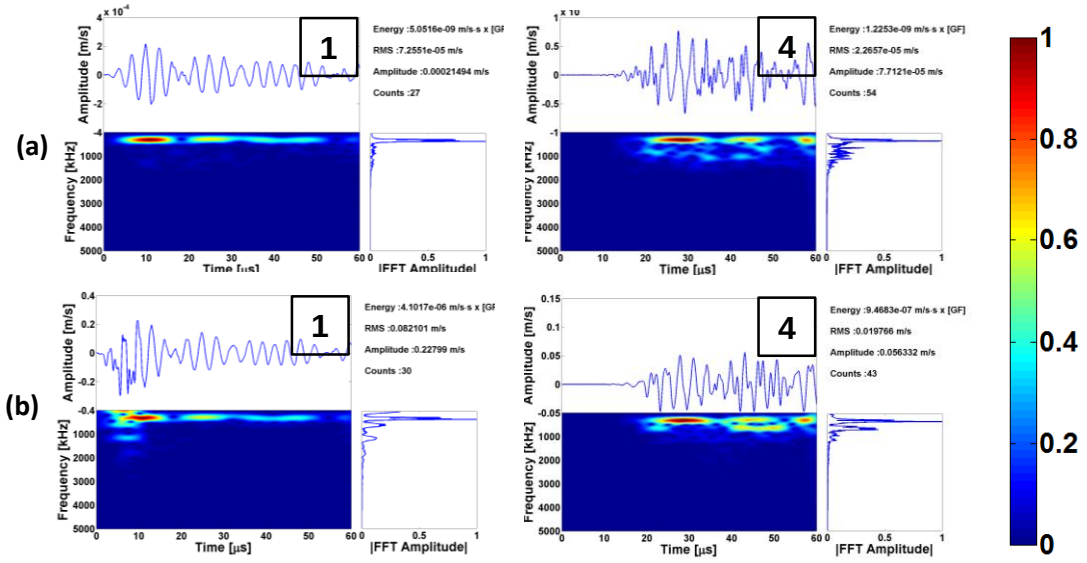

Figure 6.31: Comparison of velocity waveforms at points 1 and 4 for a compact tension model with plastic accumulation (stage B) and with an imposed Hanning window toneburst of (a) 10 mN and (b) 10 N maximum amplitude

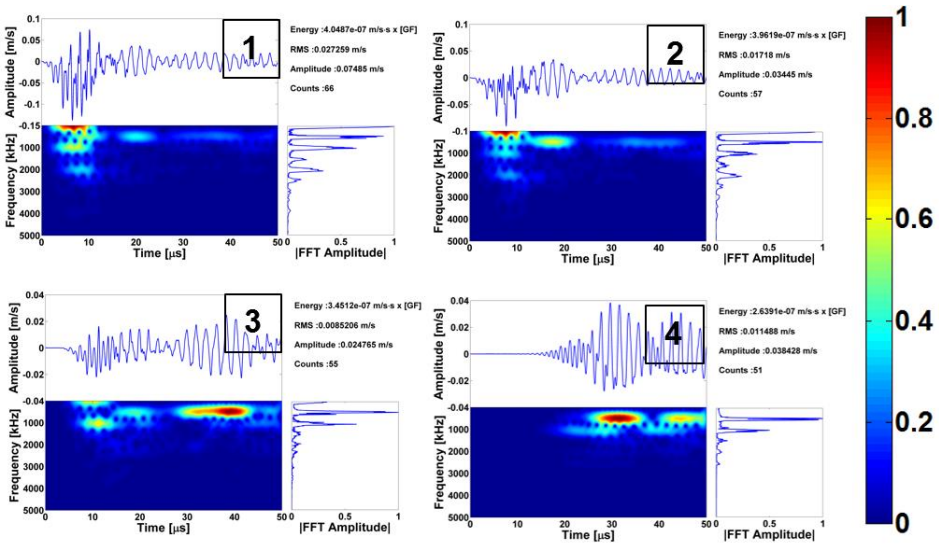

Figure 6.32: Velocity waveforms at 4 points in a 4 mm thick compact tension test with a Chaboche plasticity law for a Nickel alloy

Therefore in order to validate these effects, a 4 mm thick compact tension model with Chaboche plasticity law [11] was implemented using BC2 at stage B. The calculated velocity waveforms yielded similar results with the same trend of the higher harmonics created at the plastic region, as illustrated by Figure 6.32. Furthermore, the geometrical effects caused by the boundaries were also studied by applying the same type of conditions to the tensile coupon model. A comparative analysis for point 2 and 4 (inside and outside the plastic zone) are presented in Figure 6.33. The results showed that the effect of plasticity on the waveform was more significant at point 2 which was at the same in-plane coordinates as the source but on the surface. In addition, the stress state at nodal location 2 is clearly in the plastic regime while at 4 is in the elastic, as depicted previously in Figure 6.9b.

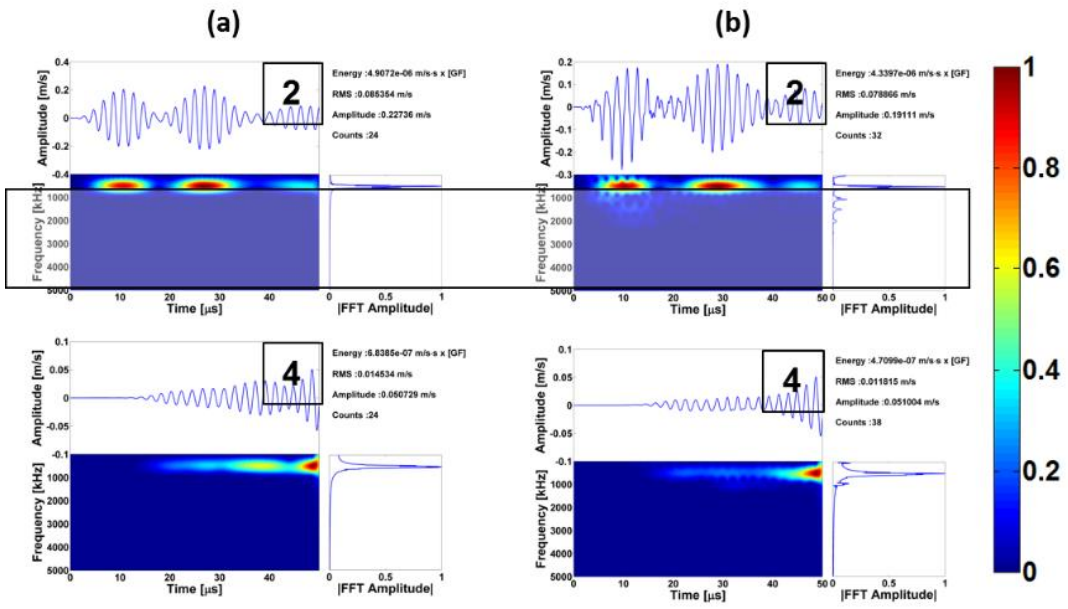

Figure 6.33: Comparison of velocity waveform analyses at points 2 and 4 at stage (a) A and (b) B of loading curve resulting from a 500 kHz Hanning window toneburst in the tensile coupon model

The amplitude of the higher harmonics were distinctively much lower than compared to the results obtained in compact tension, which can be attributed to the source. In the tensile coupon, the source is buried within the volume of the model while in the compact tension model where the source was imposed at all nodes through the thickness. Consequently, this type of boundary conditions reduced the strength of the source, thus the effect of plasticity was less substantial, as it was previously shown.

The last set of analyses consisted of studying the last loading state, i.e. stage C, which involved applying unloading conditions to achieve zero displacement. This type of analysis was an extension to the study of the effect of plasticity, which was used to analyze an additional stress state as well as to simulate conditions similar to those obtained under fatigue. Both of the computational models unloaded to a negative load range due to plastic strain accumulation, as it was depicted in Figure 6.13 and Figure 6.15. Regardless of the load reached after returning to zero displacement, the two models

had discrepancies on the plastic strain accumulated after unloading, going from stage B to C. The CT model accumulated plastic strain when unloading to 0.4 mm of displacement applied while the tensile coupon model did not acquire any additional plastic strain. These results suggested that stress state for CT model at the machined notch is possibly in the plastic domain while the tensile coupon is at the elastic regime. Such preliminary conclusions can be further confirmed by using BC3 and studying the effects of wave propagation on deformed state.

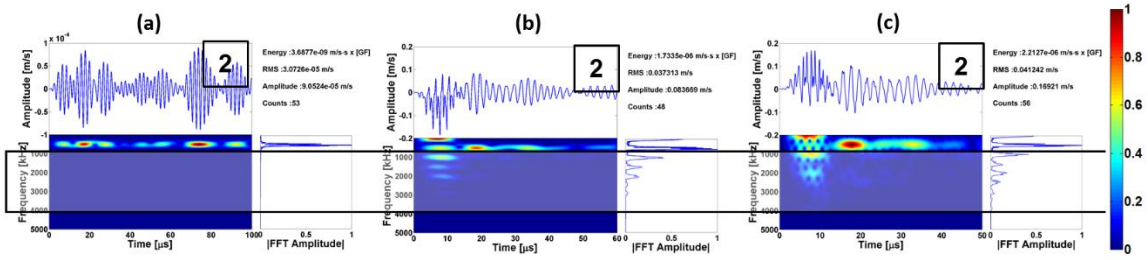

Figure 6.34: Comparison of velocity waveform at points 2 subjected to 500 kHz Hanning window toneburst when loaded to stage (a) A and (b) B and (c) of loading curve in the 6 mm thick compact tension model

The velocity waveforms at point 2 for the three loading stages is presented in Figure 6.34. The results portrayed the same effect in stage C as in stage B, which was characteristic of the generation of higher harmonics. Nevertheless, one difference between these two stages was that the time waveform in C was distorted initially in the positive direction compared to the negative direction obtained in B, illustrated in Figure 6.34b and c.

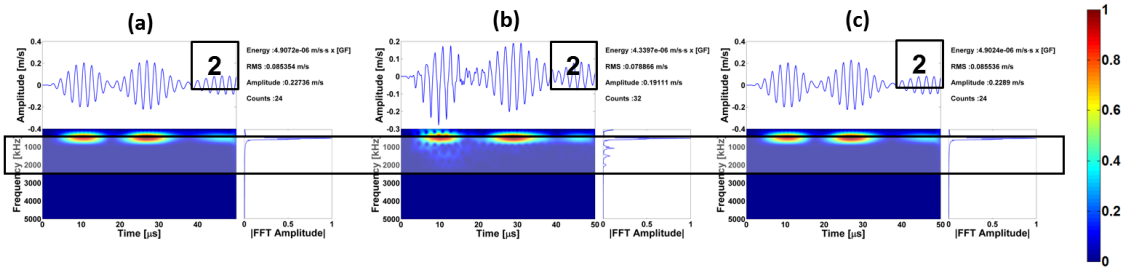

Figure 6.35: Comparison of velocity waveform at points 2 subjected to 500 kHz Hanning window toneburst when loaded to stage (a) A and (b) B and (c) of loading curve in the tensile coupon model

Ultimately, the same type of comparative analysis was performed to evaluate the tensile coupon model which was suggested to be in the elastic domain when unloaded. The velocity waveforms, shown in Figure 6.35, from the model confirmed those preliminary conclusions about the state of plasticity in the unloaded stage C. The results were similar to those obtained at stage A, which indicated that there is no plasticity effect on the frequency content of the time waveforms. This can be attributed to the fact that the model is under elastic conditions (i.e. all elements belong to the elastic regime).

The results by the Hanning window toneburst evidently showed the generation of proportional higher harmonics due to plastic deformation since a single dominant frequency was imposed. However, this is not the case for AE sources which typically involved a more complex frequency content comprised of a range of values. To link the AE concept to the study of the effect of plasticity, a Dirac pulse with a frequency content of 500 kHz to 2.5 MHz was imposed at the plastic zone (using BC2 with the corresponding values of stage B).

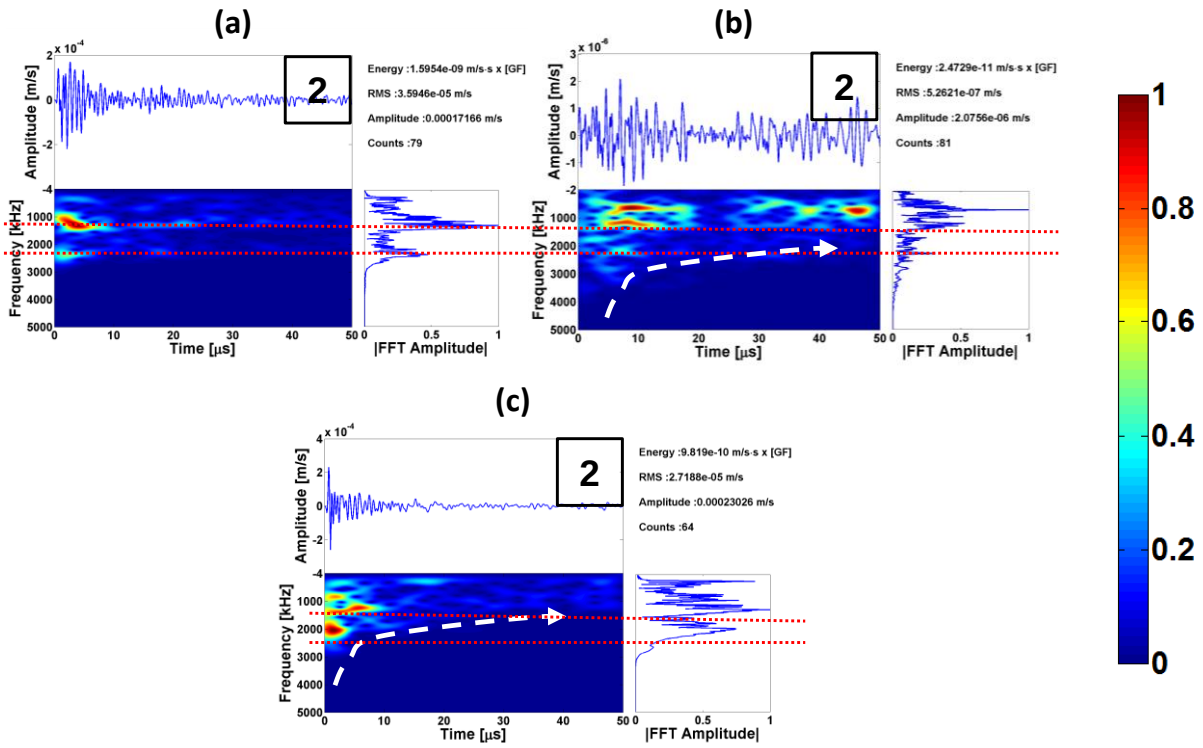

Figure 6.36: Comparison between velocity waveform analyses at point 2 resulting for (a) no plasticity, and stage B plasticity subjected to a Dirac pulse amplitude of (b) 10 mN (also used in a) and (c) 10 N in the 6 mm thick compact tension model

Using the results from the Dirac pulse at stage A, the effect of plasticity can be analyzed by comparing the frequency described by the FFT and STFT analyses. The results in Figure 6.36 showed that the velocity waveforms were altered both in time and frequency domain. The peak and dominant frequencies as well as the amplitude of the waveform were different for the underformed and plastically deformed state only for the case of a 10 N pulse, as shown in Figure 6.36c by the red marked dashed lines. Therefore, it can also be shown that the higher the amplitude of the source the more distorted and colored the frequency content is for the plastic solid medium. In addition, it can be clearly observed that the high frequency content disperses to lower frequencies as a function of time (marked by the curved dashed lines in Figure 6.36b and c)

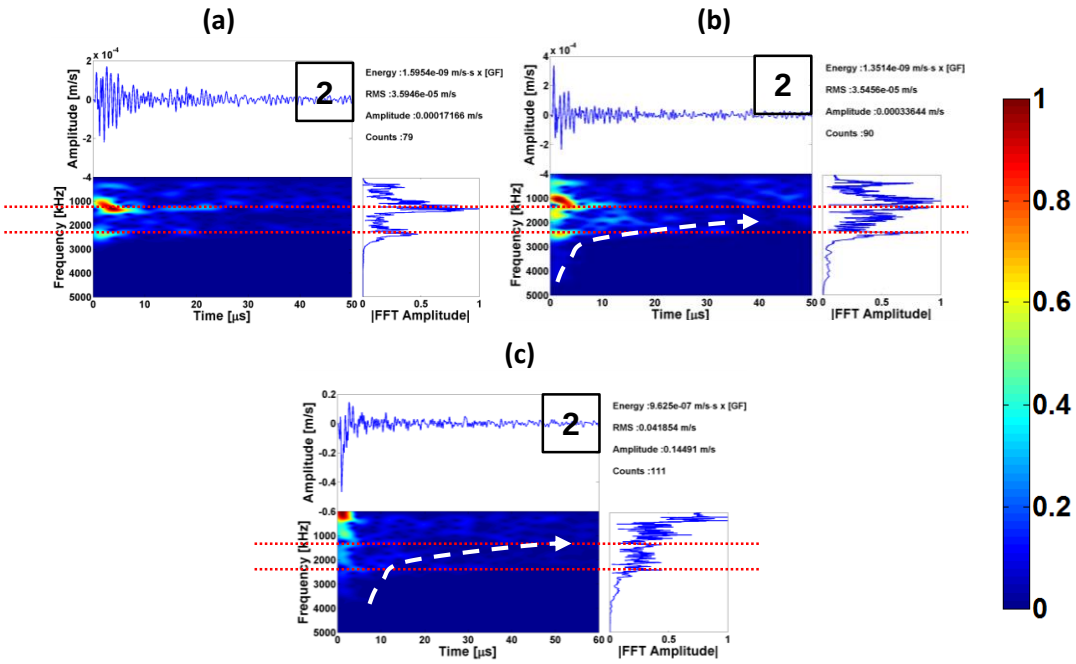

Figure 6.37: Comparison between velocity waveform analyses at point 2 resulting for (a) no plasticity, and stage B plasticity subjected to a Dirac pulse amplitude of (b) 10 mN (also used in a) and (c) 10 N in the 4 mm thick compact tension model

A similar type of analysis was performed using the 4 mm thick compact tension model in order to see the effect of the geometry on these results. The obtained velocity waveforms in Figure 6.37, in contrast to the 6 mm thick model, are different for the three studied cases. It can be observed that the frequency content was either shifted to lower or higher dominant frequencies, generating new peak frequencies mostly during the initiation time. Furthermore, the frequency content at the plastically deformed medium definitely attenuated at a higher rate as a function of time, as shown in both Figure 6.36 and Figure 6.37 marked with a dashed-line arrow. Additionally the results from the buried Dirac pulse in the tensile coupon model were also analyzed to see the effect of the geometry and the elastic and plastic solid medium. The velocity waveforms at 2, illustrated in Figure 6.38, for both deformed states showed clearly that the frequency was distorted due to plasticity and additional higher frequency values were produced while point 4 showed

a less pronounced effect. Similarly, the results at point 2 also demonstrated the same trend, as compared to the results of the compact tension model, in which the high frequencies attenuated faster on the plastic medium.

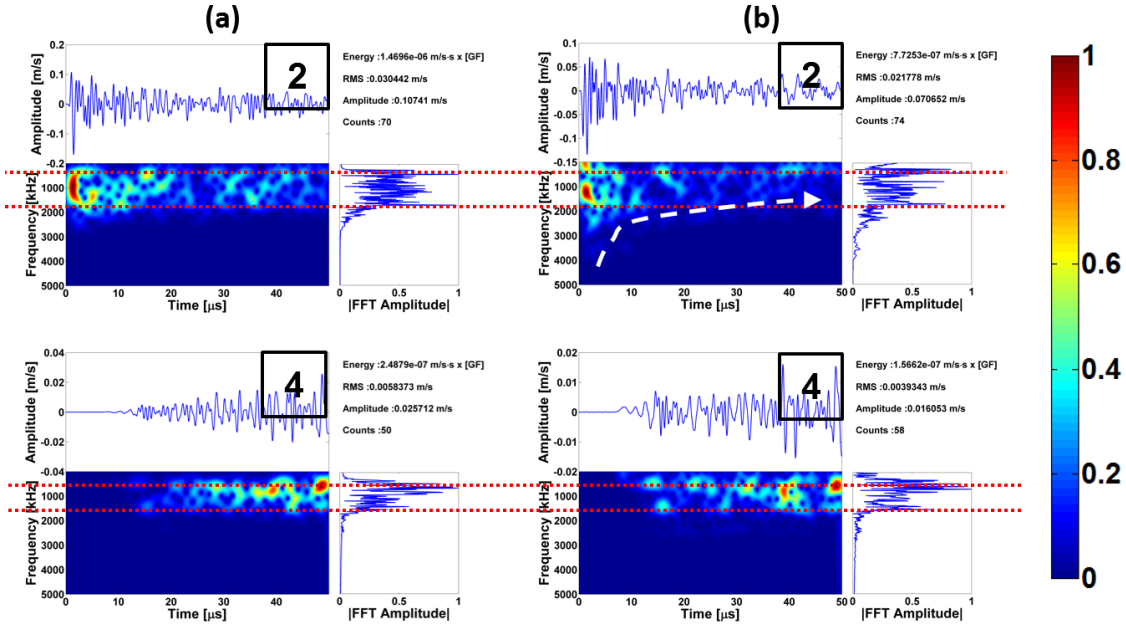

Figure 6.38: Comparison of velocity waveform analyses at points 2 and 4 at stage (a) A and (b) B of the loading curve presented in Figure 6.15 resulting from applying a Dirac pulse in the tensile coupon model

6.5 CONCLUSION

A great portion on understanding the process of AE involves characterizing the series of wave effects that occur to an emission as the associated wave travels through a bounded solid. A plastically deformed medium is one of these effects which colors and alters the signatures of an original source. The computational model presented in this Chapter successfully captured the influence of plasticity on the traveling waves generated by simulated AE sources, which were evaluated using a comparative analysis at different levels of plasticity. Regardless of the implemented incremental plasticity law and the geometry of the models, the results of a single dominant frequency pulse agreed with

previous investigations which suggested that proportional higher harmonics are generated due to traveling emissions through a medium with plastic accumulation. The analysis was then extended to study a comparable AE source (i.e. a Dirac pulse) which could be evaluated to characterize the behavior and the effects at the plastic region. In addition to distorting the original source, the results of the Dirac pulse with plastic accumulation showed that the strength of the source was a significant factor to alter for example the peak amplitudes and frequency content. Furthermore, the generation of higher harmonics was characteristic of relatively lower strength compared to that of single dominant frequency source. This can be attributed to the fact that the higher harmonics were created at high frequency vales, which were greater than the maximum frequency value of the imposed original source. Ultimately, the same type of analysis was performed to an unloaded stage, which consisted of unloading to a zero displacement applied. The results showed that when unloaded the CT model accumulated plastic strain, thus similar higher harmonics were produced. On the other hand, the results obtained from the tensile coupon model showed that no additional plastic strain was accumulated, in which the calculated waveforms did not show any distortions of the frequency content.

In summary, the computational model presented in this Chapter successfully captured the effects of plasticity in an AE-related wave propagation by reveling the generation of higher harmonics and distortions in the frequency content of the traveling waves. Furthermore, the model was analyzed under different deformation states and boundary conditions providing insightful results about the characteristics and significance of such effects due to plasticity. The generation of higher harmonics and changes in the frequency content can be explained by the fact that the numerical waveforms in sites

under plastic conditions are reliant on of the amount of plastic strain accumulated. Accordingly, depending on the strength of the source, these distorted waves continue to accrue plasticity as they travel and carry over the higher frequency content, thus resulting in similar effects in regions that are not necessarily under plastic deformation.

CHAPTER 7: APPLICATION OF ACOUSTIC SOURCE MODELING ON STRUCTURAL COMPONENTS

7.1 INTRODUCTION

The application of AE, to detect and identify nucleation and progression of critical damage, on structural components in civil, aerospace, and other types of infrastructures is still limited by the challenges associated with both understanding the damage source and its concomitant emission [8, 11, 95]. Although AE has been implemented extensively [8, 13, 77, 217-220] as a structural health monitoring for diagnostics and prognostics, the approach taken by many has considered mostly and typically the use of statistical and probabilistic tools that identify empirical trends in the recorded data disregarding the fundamental science and mechanics involved in AE [8, 95]. Furthermore, the suitability and success of these approaches relies on the repetitive nature of the experimental AE events which potentially makes them less appropriate for monitoring limited numbers of complex, high value, and safety-critical structures [95, 96], for instance as it is the case in structural health monitoring. Therefore, the need for a deterministic and targeted computational model that characterizes the signatures of particular AE sources in structural components is required for enhancing the data analysis and interpretation obtained in the field while also contributing to improve the clustering and classification methodologies. To address some of these challenges as well as possibly providing an additional tool for the AE experimental methodology in a broader aspect, this Chapter extends the concept and methodology of AE damage source modeling to a debonding failure mechanism for a structural component application. The methodology follows the

scheme of forward AE source modeling in order to evaluate and study the transient emissions due to debonding. The results are then compared to available experimental acoustic emission data in order to validate both the quasi-static loading conditions as well as the effectiveness of the model to capture the emissions due to a debonding damage mechanism.

7.2 COMPUTATIONAL MODEL DESCRIPTION

The overall objective of the computational model was to create a debonding related AE source by implementing the forward AE approach, previously described in Chapter 3 which was then applied for a fracture-induced model in Chapter 4. In order to simulate such damage mechanism, a stiffener component (experimentally analyzed and evaluated using acoustic emission in an earlier investigation [220]) was modeled using a FEM approach with cohesive interactions. The stiffener specimen consisted of an aluminum alloy plate and I-beam configuration, which were bonded into one component by an aerospace-grade epoxy paste adhesive (Hysol EA9394). Figure 7.1 shows the stiffener sample and experimental setup for detecting debonding using AE.

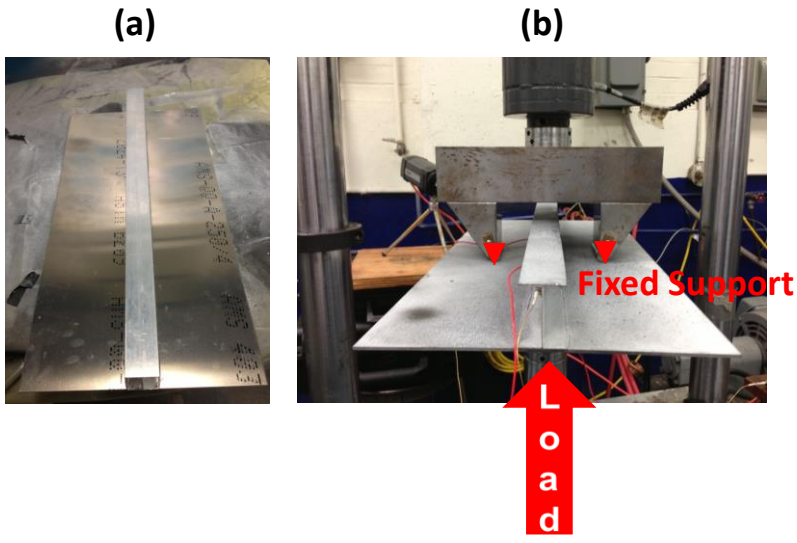

Figure 7.1: (a) Stiffener component composed of an aluminum alloy I-beam and plate. (b) Experimental setup for debonding of the stiffener with a 3 point bending loading fixture

The debonding failure mechanism between the two parts was activated by applying 3-point bending loading conditions, as depicted in Figure 7.1b. In both load- and displacement-control experiments, the AE was capable to record signals at critical stages of deformation. Based on these results and in order to avoid boundary condition-related instabilities, the computational model utilized displacement-based boundary conditions having an applied displacement rate of 2 mm/min, as portrayed in Figure 7.2a. These boundary conditions allowed for a stable convergence of both the static and dynamic analyses. The specimen dimensions along with the deformed configurations are shown in Figure 7.2c.

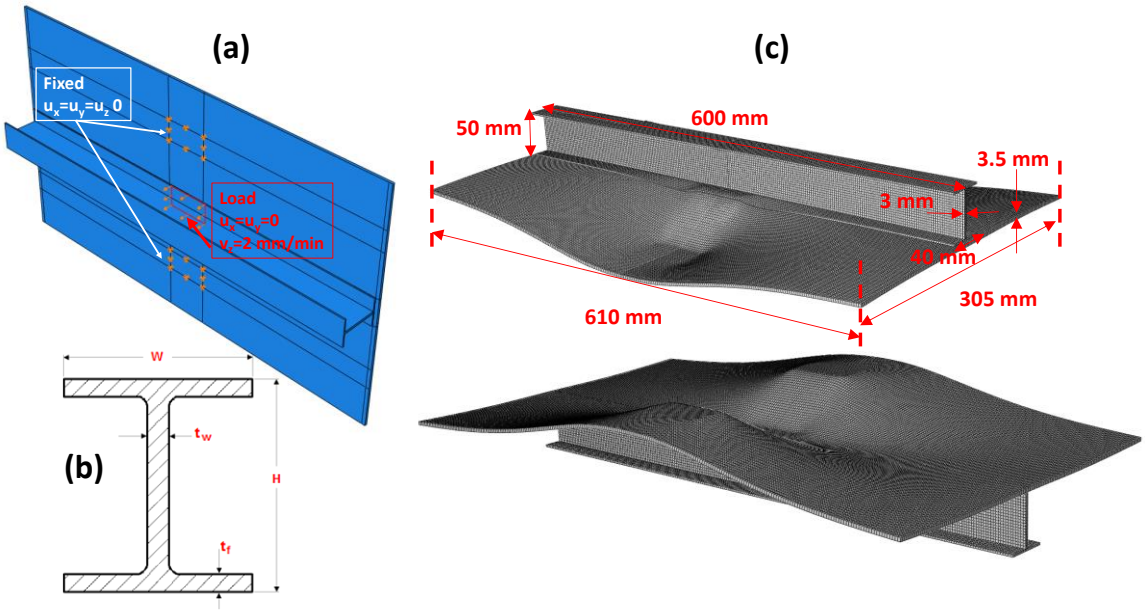

Figure 7.2: (a) Stiffener model denoting displacement boundary conditions (3 point bending representation of the rollers as rectangular contact surfaces). Stiffener model's (b) I-beam detailed and (c) overall dimensions along with deformed shaped after implementing boundary conditions from (a)

The detailed dimensions, shown Figure 7.2b, of the I-beam are summarized in Table 7.1. It is important to mention that the boundary conditions illustrated in Figure 7.2a were

investigated extensively since these were crucial to obtain a realistic and accurate solution for both the static and dynamic analyses, regardless of convergence.

TABLE 7.1: I-BEAM DETAILED DIMENSIONS

Dimension Parameter	Values
Depth, H	50 mm
Web thickness, t_w	3 mm
Flange width, W	40 mm
Flange thickness, t_f	2 mm

In addition, the boundary conditions also affected the solution depending on the type of method used for modeling the debonding failure. For instance, in a practical aspect using cohesive elements as opposed to cohesive interactions could cause rigid body motion (i.e. numerically causing a singular stiffness matrix) of the I-beam since it did not have any constraints in this case. As a result of these studies and taking under consideration the symmetry of the model geometry, the bonding adhesive was modeled as a cohesive interaction, which consist in enforcing a constraint at nodal locations on the interface that follows a traction separation law as compared with cohesive elements that enforce this law at material points (as previously explained in Section 3.4.2 and Section 3.5). The 600 mm x 40 mm interface section between the I-beam and plate was selected as the cohesive zone with properties based on a bilinear traction separation law. This interface and the traction separation law along with linear 8-noded elements are shown in Figure 7.3.

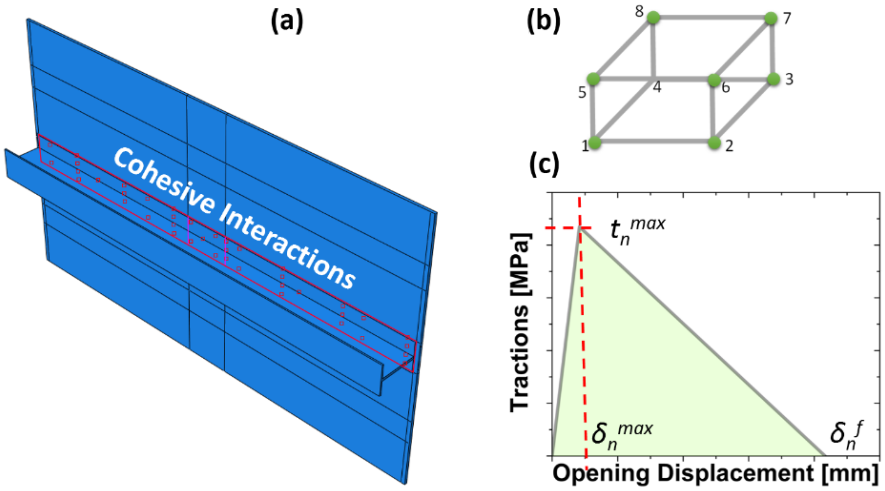

Figure 7.3: (a) Cohesive layer between I-beam spar and plate with (c) bilinear interaction properties (i.e. traction separation law). (b) Linear 8-noded elements used in stiffener model

The bilinear traction separation law is typically characterized by three parameters including the maximum normal traction, $t_n^{\max}$, and opening displacement, $\delta_n^{\max}$ as well as the final critical opening displacement, δ_n^f.

TABLE 7.2: COHESIVE PARAMETERS

Parameter	Input
Cohesive Stiffness	4.2 GPa
Damage Initiation Displacement ($\delta_n^{\max}$)	35 μm
Damage Evolution Displacement (δ_n^f)	1 nm

The linear stiffness from the traction separation law can be seen as the initial elastic properties that when reaching a maximum traction and opening (i.e. damage initiates) causes the material to soften (i.e. damage evolves as a decreasing linear function) and ultimately reaches a final failure or separation. All the cohesive properties used in the

model are listed in Table 7.2. It is important to note that the cohesive stiffness along with all the other parameters in Table 7.2 were obtained from the manufacturer of the Hysol adhesive.

A second set of boundary conditions were imposed in order to visualize, analyze and quantify wave propagation in the stiffener component before analyzing the transient dynamic effects due to debonding. The boundary conditions in the stiffener's quarter model (which will later be described and proved to be a valid simplification) were similar to those impose in the static test except that the contact areas of the 3-point loading fixture were all fixed and a nodal point was selected to apply a pulse, as shown in Figure 7.4a. The nodal point was selected utilizing the quasi-static simulations which showed that debonding initiated near this location.

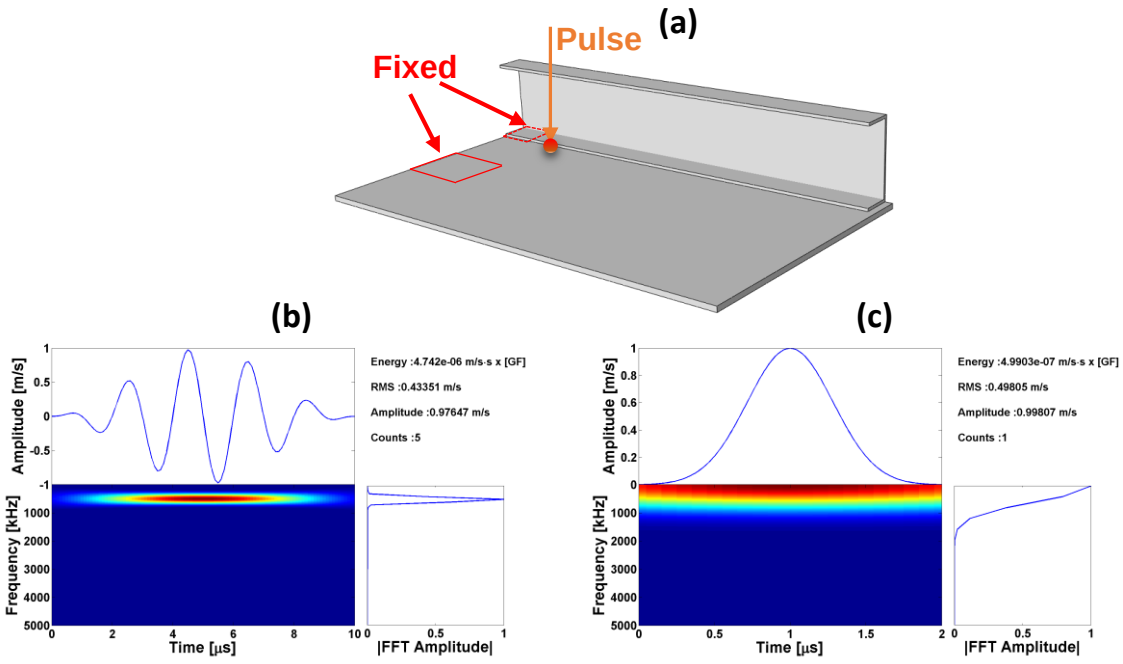

Figure 7.4: (a) Boundary conditions for dynamic FEM analysis to study wave propagation with imposed displacement profile (b) Hanning window toneburst and (c) Dirac pulse

The objective of using pulse functions as inputs for the wave propagation analysis was to target certain frequencies and observe the effects that the geometry or other factors cause by analyzing the waveforms (mainly the velocity waveforms normal to the surface). Two short duration pulses were utilized which included a Hanning window with a central frequency and a Dirac pulse for a range of frequency values (0-1.5 MHz), both shown in Figure 7.4b and c. The quasi-static and dynamic simulations included complex formulations which require high performance computing depending on the number of elements. Consequently, besides using symmetry property to reduce the computational time, the mesh global size was increased to 2500 μm from the 500 μm, which could possibly be required to capture all modes more specifically in the dynamic analysis. A comparison between the specifications of the two mesh sizes are presented in Table 7.3.

TABLE 7.3: MODEL SPECIFICATIONS

Mesh Uniform Size	2500 μm	500 μm
Element Type	Linear/ 8-noded	Linear/ 8-noded
Degrees of Freedom	82527	6787794

7.3 STATIC SIMULATION ANALYSIS

The first part of the simulation, before obtaining the emissions related to debonding, consisted in defining the critical stage, i.e. the quasi-static equilibrium state where damage initiates or it causes an instability due to a large debonding separation. Similar to the fracture-induced model, this was found by performing quasi-static simulation which was then validated with experiments in order to assure that the results are reliable.

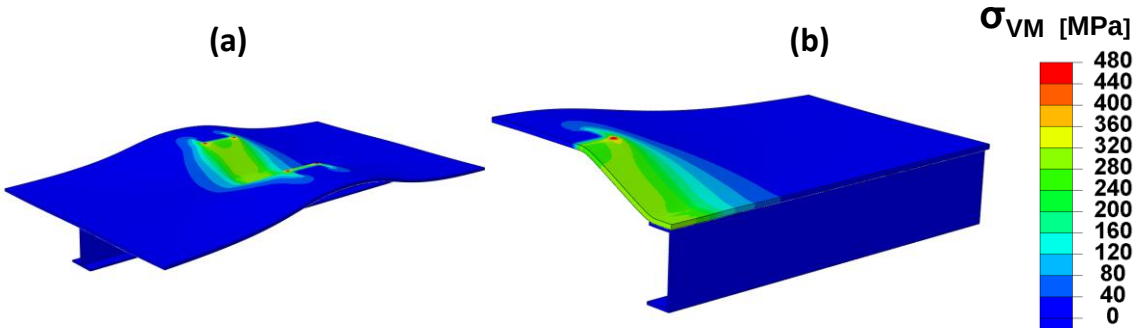

Figure 7.5: Von Mises stress contour plot for (a) full and (b) quarter stiffener model

In the previous section, it was mentioned that two simplifications were implemented in order to decrease the computational time. For instance, Figure 7.5 shows the similarities of the Von Mises stress contour plotted on the full and quarter model, thus confirming the validity of the simplification achieved by using the model symmetry. Furthermore, the specifications listed in Table 7.3 can be visualized in Figure 7.6 which shows the FEM mesh of the quarter model for the global size of 2500 μm and 500 μm.

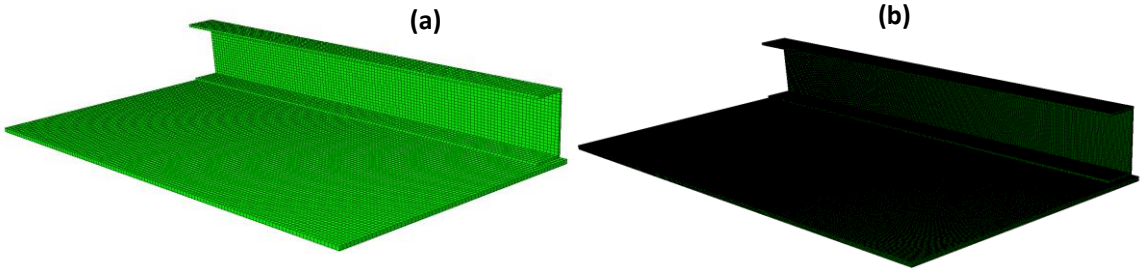

Figure 7.6: FEM mesh for using a global seed size of (a) 2500 μm and (b) 500μm

It can be clearly seen the difference and to some extent the effects that this can have in the solution of the FEM, in particular through the thicknesses of the thin plate and I-beam. In order to study these effects, a mesh dependence analysis was performed for different global sizes. Figure 7.7 illustrates two of these studies which are related to debonding initiation. The results showed that the static time increment for both initiation and final separation when the global size reaches 500 μm starts to converge.

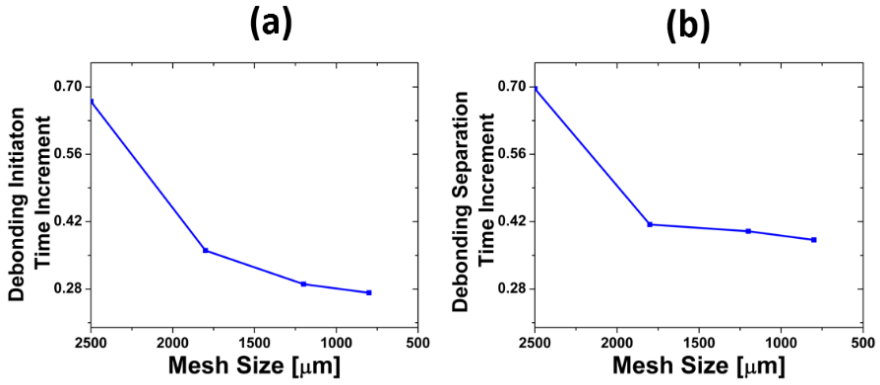

Figure 7.7: Mesh dependence analysis on debonding (a) initiation and (b) separation time

These results showed the influence of the mesh when solving the static analysis by defining the critical stage when debonding initiates. Since the main objective of the computational model was to validate and confirm that the forward AE approach can be implemented for a debonding related damage and regardless of mesh results, the 2500 μm quarter model was utilized in order to reduce the computational time and complexity.

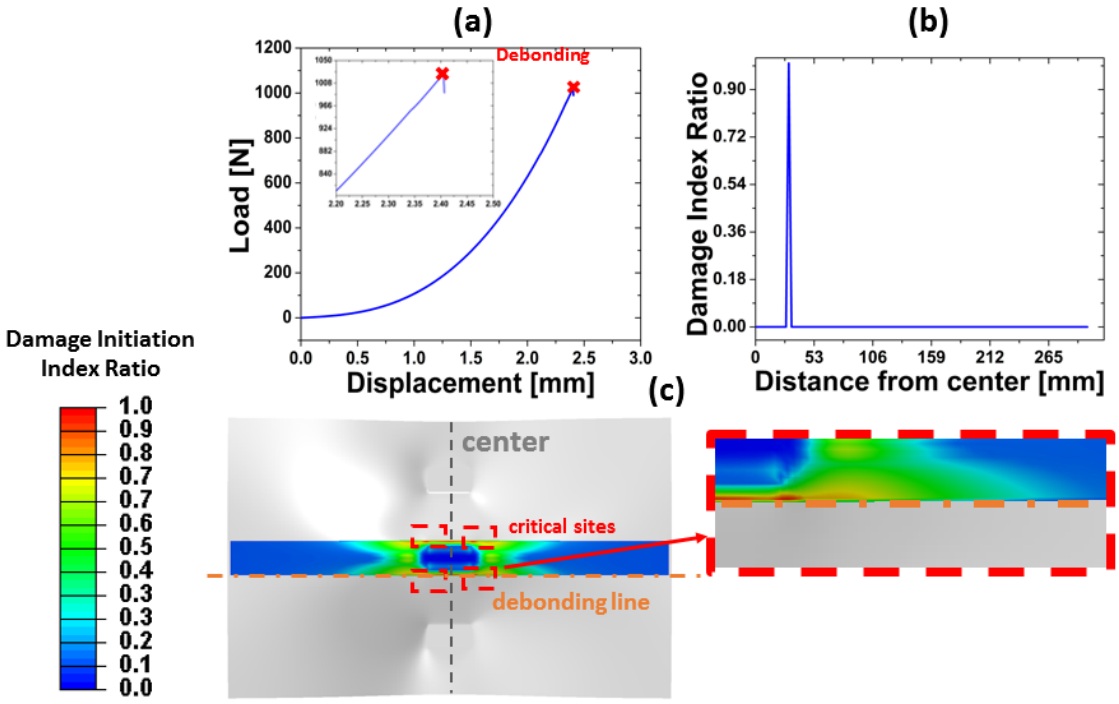

Figure 7.8: (a) Load versus displacement applied curve marked at debonding. (b) Damage initiation index as a function of the distance from the center along debonding line marked by dash-point lines overlaid on damage index contour on the cohesive interface

The results in the static simulation included mainly the carrying load evolution which could potentially be used for experimental validation and the damage initiation field at the cohesive interface which determines the debonded sections, as shown in Figure 7.8. The load-displacement curve illustrated a nonlinear behavior under the displacement control boundary conditions in addition to a sudden drop due to a critical debonding separation. In addition, the damage index was plotted in Figure 7.8b along the debonding line, where "1" denotes damage that has initiated and can be used to identify the critical sites as a function of distance from the center. Such critical sites can also be illustrated by the contour plot of the damage index, as depicted in Figure 7.8c, which is similar to those results obtained for the Von Mises stress in Figure 7.5.

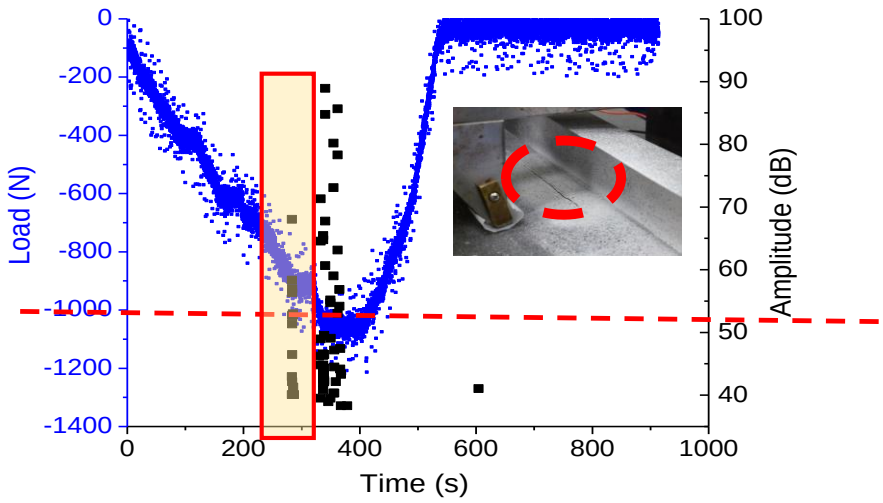

Figure 7.9: Experimental load history plotted with AE events and the debonding site denoted by a dashed circle on the stiffener specimen

The results obtained from the static simulations were then compared to those recorded in the experiment. Figure 7.9 shows the load-time data and AE events as the specimen is loaded statically under displacement-control conditions. Although the experimental recorded load history did not show the nonlinearity in load as it was shown in the

numerical solution, the first AE event occurs at an imposed load of 1000 N. These results were later postprocessed and identified to be related to debonding based on experimental location methods. Moreover, these results were comparable to the load response obtained from the stiffener model, presented in Figure 7.8a since a critical debonded stage was computed to be at 1000 N . Regardless of all the other factor that can affect the solution of the simulation (such as the type of mesh or cohesive properties), the model successfully agreed with the experimental results, thus it was then used for a dynamic analysis.

7.4 DYNAMIC SIMULATION ANALYSIS

The identification of the critical stage using the static simulation was crucial to perform the dynamic analysis. Then by applying dynamic conditions, the associated emissions can be studied and evaluated using the calculated displacement, velocity, or acceleration time waveforms. Figure 7.10 provides a visualization of an emission propagating from an AE source due to debonding using the acceleration contour plot in the z-direction.

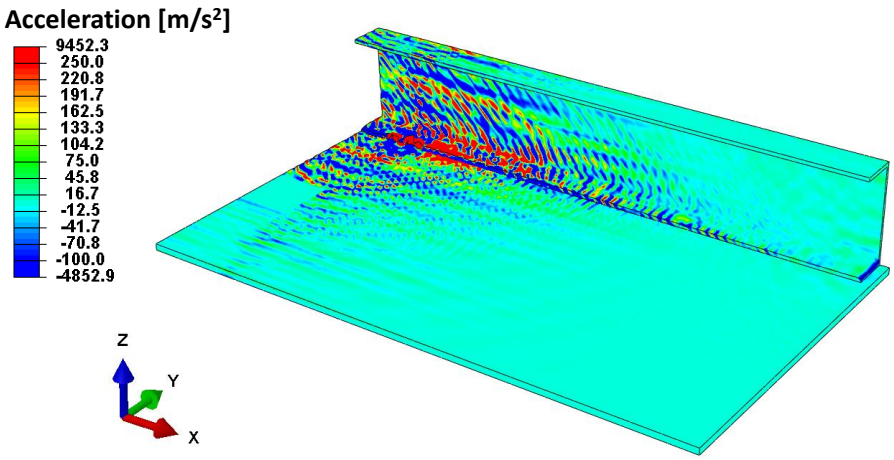

Figure 7.10: Wave propagation due to debonding separation illustrated by illustrated by the acceleration contour plot in the z-direction

However, before implementing the dynamic debonding simulation, it was necessary to first understand wave propagation in the stiffener geometry (i.e. apply an ultrasonic-type simulation, in which the source is controlled/imposed). These analyses were implemented using the boundary conditions described in the previous section and illustrated in Figure 7.4a. The applied pulses included a Hanning window toneburst with a central frequency of 500 kHz and a Dirac pulse ranging from 0-1.5 MHz frequency values. Three nodal points were selected including a point near the source, one on the plate at a diagonal distance approximately 30 mm from the source, and a point on the I-beam where the AE sensors were placed during the experiment.

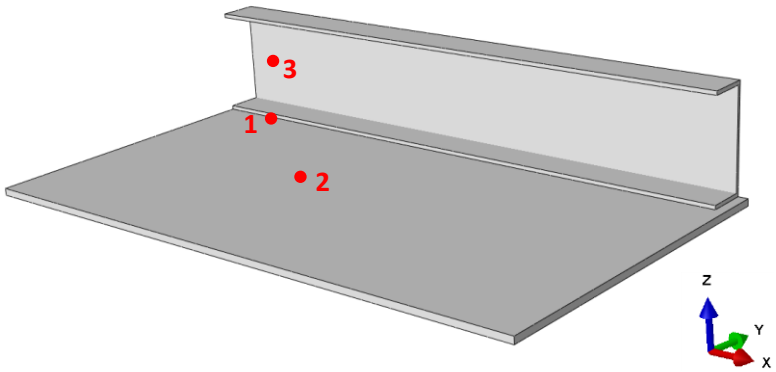

Figure 7.11: Stiffener model's nodal points utilized for velocity data extraction in order to perform time and frequency analysis

The wave propagation analyses presented in this section used the Fast Fourier Transform (FFT) and Short Time Fourier Transform (STFT) methods to analyze the waveform characteristics in the time and frequency domain. In addition, the extracted time waveforms corresponded to only the component of velocity normal to the surface since these are found to have the highest amplitudes. Hence, the *z*-component for the plate at points 1 and 2 and the *y*-component for the I-beam at point 3 were investigated. The first analysis consisted in determining the effect of the mesh size on the solution of the

imposed sources. Two sets of data, one from the 2500 μm (shown in Figure 7.12a) and the other from the 500 μm (shown in Figure 7.12b) were extracted for points 1 and 3 to be compared and analyzed individually. The simulation applied a Dirac pulse as a source with a duration 2 μs and a maximum amplitude of 1 μm. The results were calculated for a 30 μs time span and showed that there are some difference in the peak frequencies as shown in the FFT analysis. In addition, STFT showed discrepancies in the distributions over time, in which the dominant frequencies were found to be different. Although the dominant frequencies altered for both mesh sizes, the range of active frequency values was found to be similar, in the rage of 200 kHz to 700 kHz, thus suggesting that a 2500 μm is to some extent valid. Furthermore, it can be concluded that these discrepancies are attributed mainly to the number of elements through thickness which typically modifies both the time-bsed amplitude and frequency content of the numerical time waveforms.

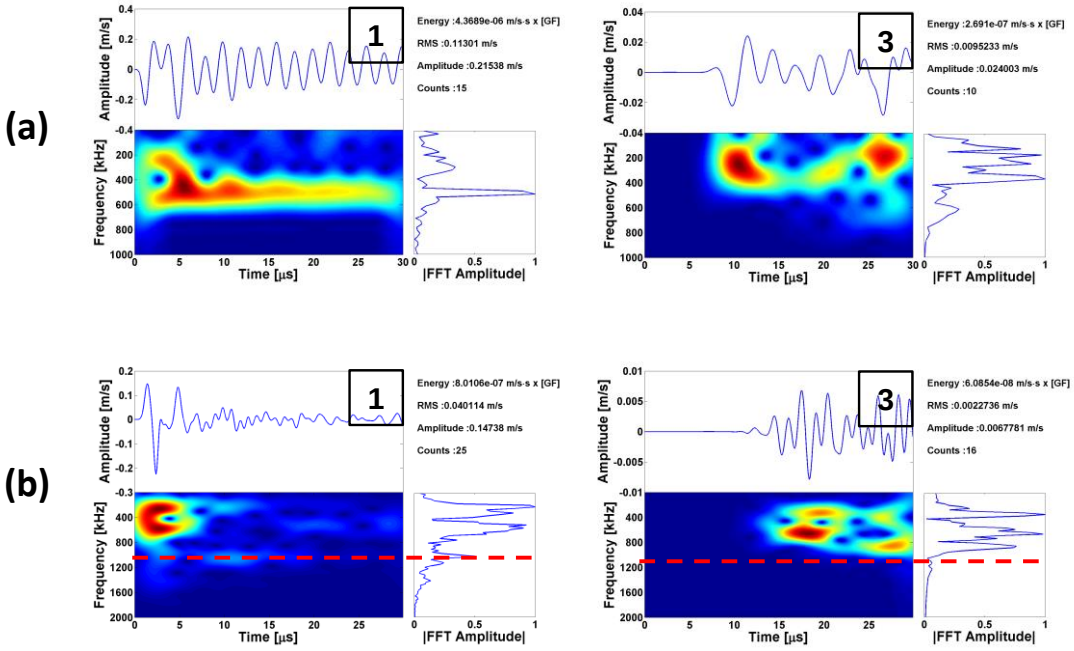

Figure 7.12: Influence of the mesh size on wave propagation due to a Dirac pulse. Velocity waveforms at points 1 and 3 for a stiffener model with a global mesh size of (a) 2500 μm and (b) 500 μm where the dashed line represents the maximum 1 MHz plotted in (a)

The second analysis involved studying the effects of simplifying the model to a quarter model. It is important to note that if the boundary conditions in Figure 7.4 are applied in a quarter model, it is implicitly assumed that four interacting sources are propagating in the stiffener, which might not be realistic in practice. The velocity waveforms were extracted similarly at point 1 and 3 to be compared, as illustrated in Figure 7.13. It can be clearly observed that the quarter model waveform at both points maintains the same amplitude while the full model's velocity waveform amplitude decays; however, the peak frequencies and STFT distributions showed agreement. As mentioned earlier, this can be attributed mainly to the fact that the quarter models four sources which can interact with one another causing the amplitudes to have higher strength.

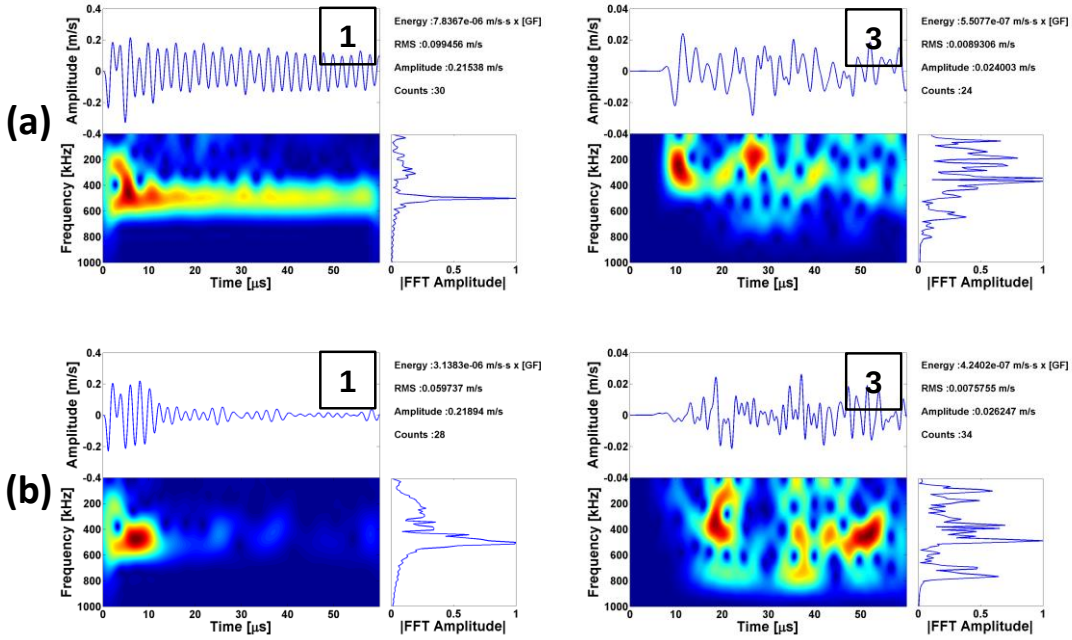

Figure 7.13: Velocity waveform comparison at points 1 and 3 obtained imposing a Dirac pulse for a (a) quarter and (b) full stiffener model

Furthermore, point 3 at the I-beam also showed similar frequency content in addition to a comparable amplitude. It had been shown in earlier investigations [220, 221] that

depending on the location of the source the waves could potentially be trapped in the thin spar attached to the plate, which is related to the thickness and wave modes active on the component and could be actual the reason associated to the similar amplitude values in the two simulation cases. Consequently, in order to analyze the effects of the thickness, it was necessary to study the guided waves characteristics associated with this geometry. Hence, the plate with a thickness of 3.5 mm, as shown in Figure 7.14a, was used to obtain the dispersive curves related to the guided waves (i.e. known as Lamb waves in plates). Using the given thickness value and the elastic properties of the aluminum alloy, the dispersive curves portrayed in Figure 7.14b were computed. This plot shows 3 symmetric modes and 3 anti-symmetric modes denoted as S_n and A_n, respectively.

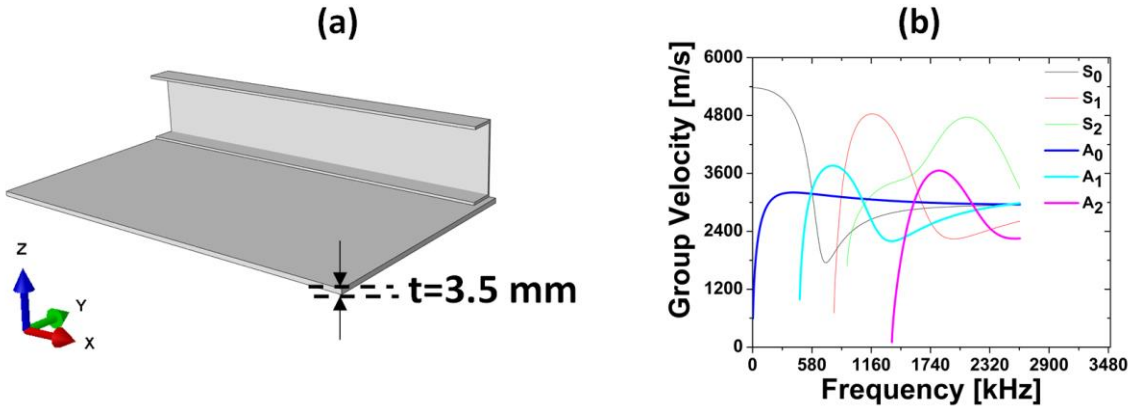

Figure 7.14: (a) Quarter model with plate thickness dimension of 3.5 mm thickness used in addition to the aluminum alloy elastic properties to calculate the (b) dispersion curves

Besides providing the evolution of the group velocity in each mode with respect to the frequency, the dispersive curves can be used to compare the dominant frequency values to the STFT distributions obtain from the simulation. The results for such analysis are shown in Figure 7.15. Specifically, Figure 7.15a shows the dispersion curves transformed from group velocity to the time domain using the distance of the nodal location, which was 2.5 mm.

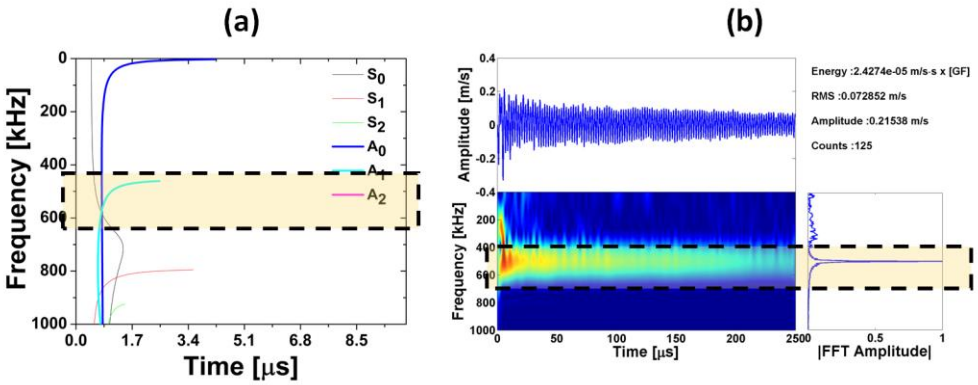

Figure 7.15: (a) Dispersion curves transformed from group velocity to time domain using a distance of 2.5 mm and (b) velocity waveform analysis from a Dirac pulse boundary condition at a distance of approximately 2.5 mm

It can be observed that although the peak frequency is at 500 kHz, the STFT showed that initially there are lower frequencies as dominant. By comparing these results to the dispersion curves, it is clearly demonstrated that the S_0 and A_1 modes are dominant in the plate near this location. In addition, these findings provide are evidence that the 3.5 mm thickness, generates Lamb waves that could cause dispersion of the original frequency content of the source. Therefore, it is important to understand such wave effects since these could potentially affect an emission from an AE source. However, it should be noted that these results are specific to a mesh size and could alter by modifications in the number and type of elements, as it was shown earlier by the results in Figure 7.12.

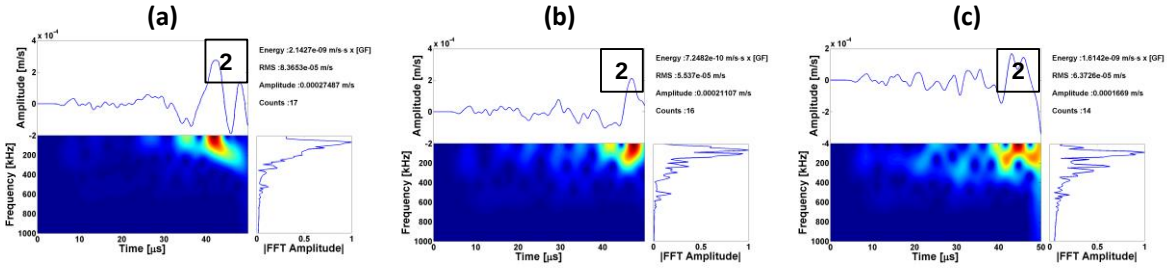

Figure 7.16: Analysis of the effect loading rate and used boundary conditions on wave propagation due to debonding comparing velocity waveforms at point 2. Displacement-control loading rates include (a) 2 mm/min with unconstrained and (b) constrained in-plane displacement components, as well as (c) 135 mm/min with unconstrained conditions

After studying the effects that the geometry, including the interface and the two components, the deformed state computed by static analysis solved at the critical stage was used as initial condition for the dynamic analysis in order to capture the emissions related to debonding. The first analysis performed for debonding was to evaluate if the loading rate of the applied displacement in addition to the other degrees had an effect on the numerical debonding emissions. Three different sets of boundary conditions were evaluated to characterize the effect of the loading rate (i.e. 2 mm/min and 135 mm/min) and constraining the in-plane degrees of freedom at the loading surface, shown in Figure 7.4 as fully constraint. These were applied to calculate the numerical velocity waveforms at point 2 in order to be compared, shown in Figure 7.16. The results showed that the rate of the displacement applied with unconstrained conditions (i.e. in-plane translations are not fixed where the loading displacement is applied) did have an effect on the calculated velocity waveforms, which showed that the emissions start to be significant around 20-30 μs compared to the lower rate waveforms in which activity is seen around 40 μs. Moreover, it can be observed that the unconstraint and constraint had some differences in time waveform, in which the constraint boundary condition results showed a more stable waveform. Therefore, the constraint with 2 mm/min displacement rate applied were selected for further analysis

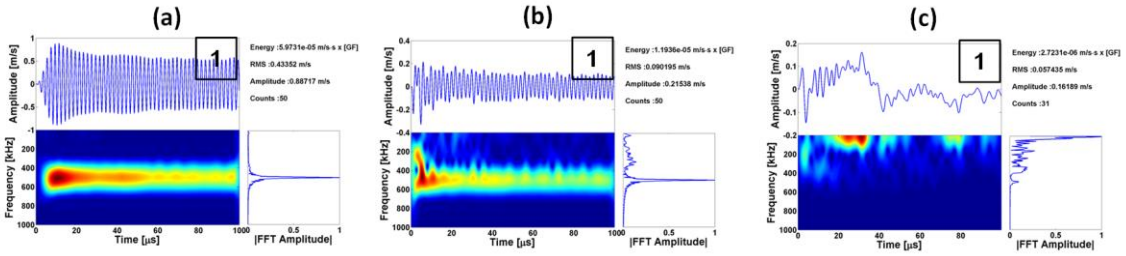

Figure 7.17: Comparison of velocity waveforms at point 1 subjected to (a) 500 kHz toneburst, (b) Dirac pulse, and (c) due debonding separation

The waveforms from the debonding were additionally compared to those obtained applying an imposed source including a 500 kHz Hanning window toneburst and a Dirac pulse.

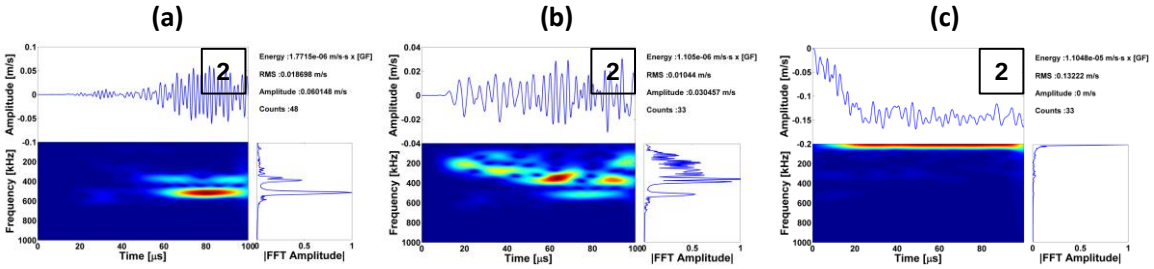

Figure 7.18: Comparison of velocity waveforms at point 2 subjected to (a) 500 kHz toneburst, (b) Dirac pulse, and (c) due debonding separation z

The results at point 1, depicted in Figure 7.17, demonstrated evidently that the debonding source had lower dominant frequencies compared to the results from the imposed Hanning or Dirac sources. In addition, at a location close to the source the imposed pulses had different peak frequencies. However, the frequency content of the Dirac source was more comparable to the debonding source. This suggested that the debonding has a similar to the Dirac with different peak frequency values. A second nodal location was studied and compared to other two imposed sources, the corresponding velocity waveforms are portrayed in Figure 7.18a-c. The numerical waveforms showed that the two imposed sources have the similar peak frequency values. Although the peak frequency between these two imposed sources was not identical, the debonding waveforms showed a much lower dominant frequency content and it can be observed that the higher frequencies than 150 kHz are active. In order to extract these results, an additional postprocess tool was utilized. The tool consisted of a high pass filter with a cutoff frequency of 150 kHz. This low frequency content can be attributed to the continuous loading while the emission propagates. The postprocessed numerical

waveforms are shown in Figure 7.19b. The high pass filter revealed higher frequencies including 300 kHz and 500 kHz, which were also found to be dominant in the imposed sources.

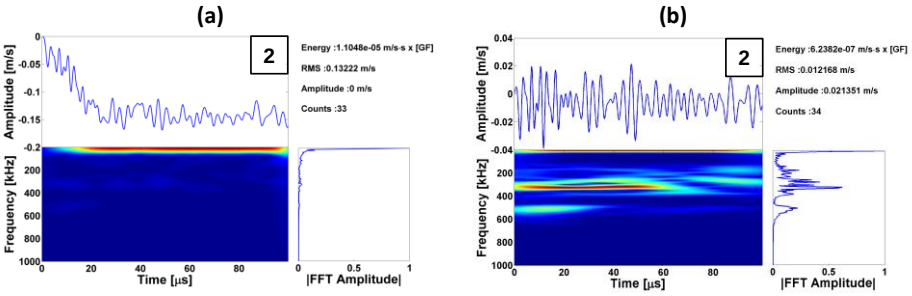

Figure 7.19: (a) Original velocity waveform obtained at point from a debonding AE source and (b) postprocessed waveform using a high pass filter

Finally, another important nodal location close to the source was point 3, which is the location where the AE sensors were placed in the experiment. The velocity waveforms without any postprocessing for the imposed sources portrayed several similarities including the waveform shape and the frequency content shown in Figure 7.20a and b.

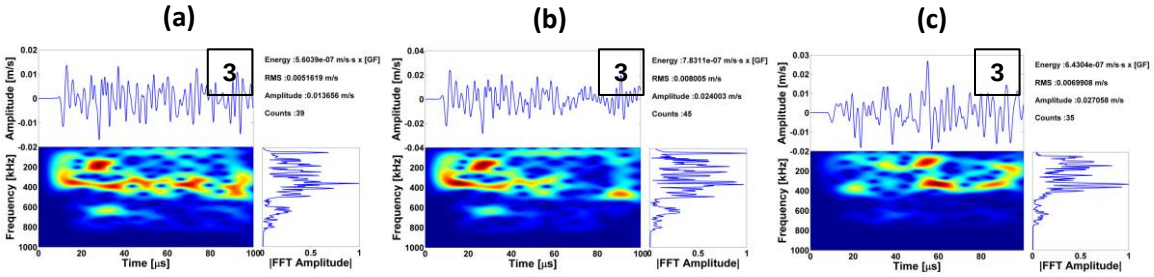

Figure 7.20: Comparison of velocity waveforms at point 3 subjected to (a) 500 kHz toneburst, (b) Dirac pulse, and (c) due debonding separation

In addition, as shown in Figure 7.20c, the debonding emission also has some similarities for instance the peak frequencies 300 kHz and 500 kHz. Similarly, this waveform at point 3 was compared to one AE signal which was representative of debonding. The comparison with experimentally obtained data revealed that the peak frequencies and STFT distributions had similar dominant values. For instance, the numerical waveforms

had a peak frequency close 400 kHz and 200 kHz. Evidently, the results for the simplified quarter stiffener model were encouraging regardless of the limitations.

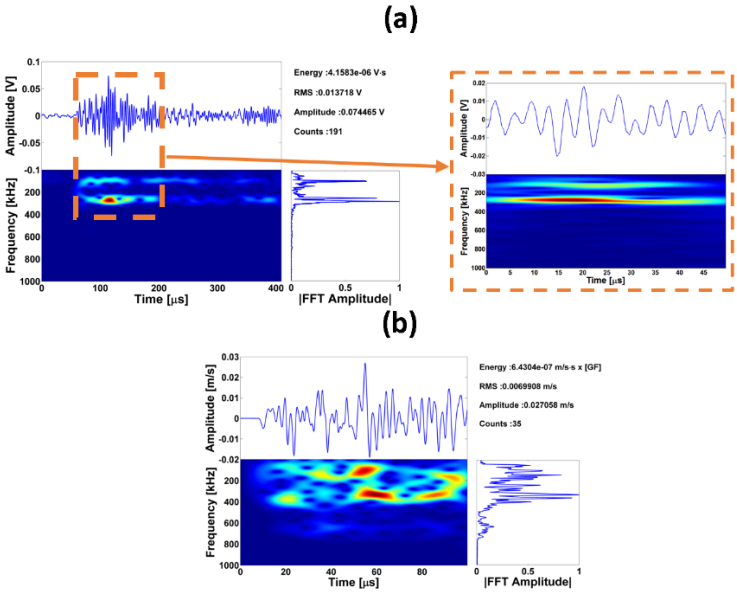

Figure 7.21: (a) AE experimental signal near a comparable location to point 3 associated to debonding with zoomed in frequency content in STFT, and corresponding (b) numerical velocity waveform

7.5 CONCLUSION

The forward AE approach was successfully implemented for a debonding related AE source. Both a static and dynamic analysis were performed and validated in order to obtain reliable results. Aside from the fact that the source is complex, the geometry of the stiffener model caused wave effects which included mainly dispersion on the emissions. The comparison with experiments showed good agreement providing reliability and validation of the methods used to obtain the results. In addition to the experimental data, the dynamic simulation was verified and analyzed by imposing sources. Despite the simplifications of the model, the calculated waveforms captured efficiently the low frequencies related to debonding; in addition, it provided a methodology for implementing the forward AE approach.

CHAPTER 8: CONCLUDING REMARKS AND FUTURE WORK

8.1 CONCLUDING REMARKS

A new computational approach for modeling acoustic emission (AE), based on the concept of forward modeling, is presented in this dissertation. Most existing methods for modeling AE either consist of imposing an artificial or experimentally obtained source excitation which is then used as an input to another computational model or are limited by their length scale. Such methods, specifically those that impose the source, do not explicitly account for the effects that the source characteristics impose on the solution of the AE-related wave propagation. For instance, it has been demonstrated that these models cannot account for the dynamic processes around the source in the case that the imposed region of the source reaches the size of its wavelength [4, 97]. Furthermore, although the micro- and atomistic scale models capture the wave effects due to a localized AE source, their results to some extent are limited to that scale and typically cannot be validated in order to be applied to larger scales, e.g. in components or structures. In this context, the approach presented in this dissertation consisted of using state-of-the-art fracture mechanics models at the continuum scale, namely cohesive zone modeling and XFEM, to generate numerically a realistic AE source related crack initiation, which is of primary interest for several engineering applications, while theoretically is also related with the emerging need to describe pre-failure conditions and related them with appropriate means for early diagnostics. Compared to previous proposed models, this modeling approach captures two main components of the AE

process, i.e. source characteristics and associated wave propagation, in the particular cases of aluminum alloys at both coupon and component scales.

The proposed method is essentially also data-driven since related experimentally-defined information was used to appropriately define key parameters of the model, while such information was further used to validate the produced results, as described in Chapter 3. These results were then linked to a dynamic analysis procedure which accounted for the transient effects associated to the release of stress waves due to a localized damage source. In Chapter 4, this dynamic analysis was implemented for a compact tension (CT) specimen which targeted to model fracture-induced acoustic emission. The computational model was developed numerically using first a phenomenological model that of the cohesive zone approach, which was calibrated by using experimental data and proved successful in representing the fracture-related source by calculating the displacement jump associated with crack initiation in a ductile fracture process. Similarly, a fracture model was developed using a cohesive-based Extended Finite Element Method (XFEM) formulation which was calibrated with experimental parameters. The XFEM model for the fracture-induced AE provided the capabilities to link the critical states before crack formation to its concomitant transient effects related to AE. The results from these models provided a comprehensive description of the fracture-induced AE source which was found to consist of a displacement jump in all three Cartesian coordinates which resulted in a mixture of low and high frequency values around the crack formation sites which quickly evolved in both time and space. Regardless of the complexity of the source, the propagation of stress waves investigated further yielded substantial information about the waveform characteristics which are shaped as the primitive wave

travels further away from the crack tip location. Such characteristics included the amplitude attenuation and the frequency content evolution which can be utilized for optimal sensor location and selection, respectively. The relevant analyses described in the dissertation consisted of identifying the interaction of AE-related waves with geometrical features that cause attenuation, dispersion, etc. The results showed that the high frequency values attenuate at higher rate with respect to distance and time, compared to low frequency values which agrees with what has been known by experimental methods. In addition, although only the source and propagation in the AE process were modeled disregarding the detection (i.e. excluding all sensor recording related effects), the frequency content was comparable and agreed to experimental measurements performed in the same specimen. In summary, the fracture-induced model based on a forward AE model approach provided encouraging and substantial results about the AE source due to crack initiation and the concomitant propagation effects.

In Chapter 5, the fracture-induced AE model was further analyzed to investigate the energy balance associated with crack formation and subsequent initiation. This chapter implemented two approaches based on an energy balance approach, in addition to a radiated power and energy flux approach which quantified the energy corresponding to the extension of the crack front by an increment. The overall objective was to quantify the energy states at critical stages (i.e. before and after crack initiation or transiently towards steady state after the release of energy) in which the redistribution of energy, specific to AE sources, could potentially be captured. Basically, the concept consisted of identifying the stages at crack formation, defining the calculation volume and implementing the appropriate formulation of the approach. The results revealed that the

energy states at the source were much higher compared to the energy that radiates within the volume, which directly implied various sources of dissipation. The computed energy values at the source although they varied based on the different approaches used they were found to be in the same order of magnitude which verifies the success of the combined analytical/computational methods used to quantify them. Overall, quantitative energy information is another important provided by the research in this dissertation which assists in better understanding the AE process, while if further investigated this information could be applied directly to tailor the design of novel sensors and other AE signal detection equipment.

The signal shaping effects, which the AE process is subjected to, consists of all the factors that affect the AE source before related signals are recorded, and include material and geometry, as well as sensor type, amplifier and other data acquisition parameters. Chapter 6 examined part of these wave effects involved as the emission from the source travels through a medium under plastic deformation conditions. By imposing a source with a dominant peak frequency value at the plastic region, the model showed that the plastic zone contributed to the generation of higher harmonics proportional to the fundamental frequency value (i.e. the input peak frequency value), which were postulated previously and have been extensively used to detect flaws associated with plastic deformation. Regardless of the incremental plasticity and hardening laws implemented in the computational model, the results demonstrated that the computational model captured successfully the effects due to plasticity on the frequency content of travelling waves. In this context, a second model was developed to further study an AE source. In this second model, the simulated source contained a wide range of active frequency values and was

similarly evaluated to account for the influence of plasticity. The results showed that the amplitude of the source determined the significance of the alterations in the frequency content, which included a shift in the peak frequencies and the generation of higher harmonics. In conclusion, by examining the plastic region around the crack and the elastic region away from the crack, it was determined numerically that the plastic effects were attributed to and depended on the accumulated plastic strain, while this investigation is related to the overall need to quantitatively explain the AE process.

The application of the developed computational AE modeling approach to structural components was addressed in Chapter 7. Specifically, the novel forward AE approach was applied to an aerospace stiffener component to validate its practicality and capabilities for larger geometries and for modeling a debonding failure mechanism. A series of both static and dynamic analyses were performed to decrease the computational time by simplifying the geometry of the model (i.e. using symmetric boundary conditions) and decreasing the associated degrees of freedom (by using a quarter-sized model). The results obtained from both the static and dynamic analyses showed good agreement with relevant experimental results, previously obtained. For instance, in the case of the static analysis, the load-displacement response showed that the same load level for the first indication of debonding was successfully computed. Similarly, the waveforms calculated from the dynamic analysis had a comparable frequency content to that of the recorded AE experimental signals, which were dominated by low frequency peak values.

In summary, this dissertation provided a novel approach to model AE mainly for ductile fracture and extended to interfacial debonding, using state-of-the art experimental

procedures in conjunction with computational fracture techniques. In essence, the computational model developed provided a platform for visualization and analysis tools for better quantifying and understanding the AE source and concomitant wave propagation. In addition, the model allows the deeper investigation of the AE process from generation to propagation serving as a tool to identify AE features that are most sensitive to the damage process. Furthermore, this dissertation also developed a methodology to estimate the energy release associated with crack formation in a quasi-static and transient environment. Regarding the AE source propagation, the linkage of AE to fundamental geometrical factors and material processes, in specific plasticity, was also evaluated as a method of deconvolving the AE process for accurately characterizing such wave effects and identifying the signature of the propagating source.

8.2 EXTENSIONS AND FUTURE WORK

The broader impacts of modeling AE include mainly enhancing the interpretation of AE sources by tackling the current challenges faced by the AE experimental methodology for advanced applications including Structural Health Monitoring (SHM) [7-9], Intelligent Processing of Materials (IPM) [6, 10] and other similar applications [5, 11-13] in which AE serves as a technique that detects, identifies, and characterizes critical mechanisms. For instance, in SHM applications, the AE model becomes a tool for: (i) optimizing sensor selection and location, (ii) assisting in the identification of damage precursors and diagnosis as a complementary tool for signal processing and qualitative source analysis, (iii) the development of life prognosis form AE damage parameters which could potentially assist to reliably retrofit, optimize maintenance plan, and predict the retired life of structures. In addition, in the case of manufacturing processes, the AE

experimental methodology and complementary computational tools have promising real-time monitoring capabilities which could potentially characterize the manufacturing processes, while also detecting discontinuities or process abnormalities.

The numerous applications of AE and the challenges for reliable damage detection demonstrate the need for reliable and predictive AE modeling to assist by mitigating and improving the limitations of current AE experimental methodologies. The following sections provide specific comments on the future development and use of this approach.

8.2.1 MULTISCALE MODELING OF AE

The practical use of the AE methodology is generally more applicable to larger scales involving structural components with several types of damage. To some extent, this fact limits the usefulness of the micro- and atomistic models that can capture the AE source and propagation in small time and length scales, except when the experimental results are available at these scales [97]. To mitigate and tackle such challenges, a multiscale modeling approach may be implemented [93, 94, 222, 223]. In such models, the multi-physics hierarchy comprised of Quantum Mechanics, Molecular Dynamics, Kinetic Theory, and Continuum Mechanics, all listed in ascending order with respect to time and length scale, could be involved. For instance, in the case of Molecular Dynamics (~ ps and ~ nm scale), some efforts have been attempted to model AE [92-94]; however, these were limited by the solution at the nanoscale and produce inaccurate results at the continuum scale. In general, multiscale models intend to capture the effects by transferring crucial information from scale to scale. Nevertheless, this approach is still under investigation for various applications other than AE, and has demonstrated

limitations as well as discrepancies with experimental results in some cases [222]. Therefore, a future goal of this research framework is to implement multiscale models that can capture microstructural damage mechanism such as twinning, dislocation motion, grain boundary sliding and intra- as well as transgranular fracture, to name a few. The computational model could then incorporate theories from Molecular Dynamics, Crystal Plasticity, and Dislocation Theory, among others. A recent work by Yamakov et al. [223] related to AE type sensor materials, in specific shape memory alloys, involved the development of a multiscale model that can capture the effects of the crystallographic orientation on the material response. Figure 5.1 illustrates the schematic of the proposed computational model which is composed of the two modeling techniques i.e. Molecular Dynamics and FEM.

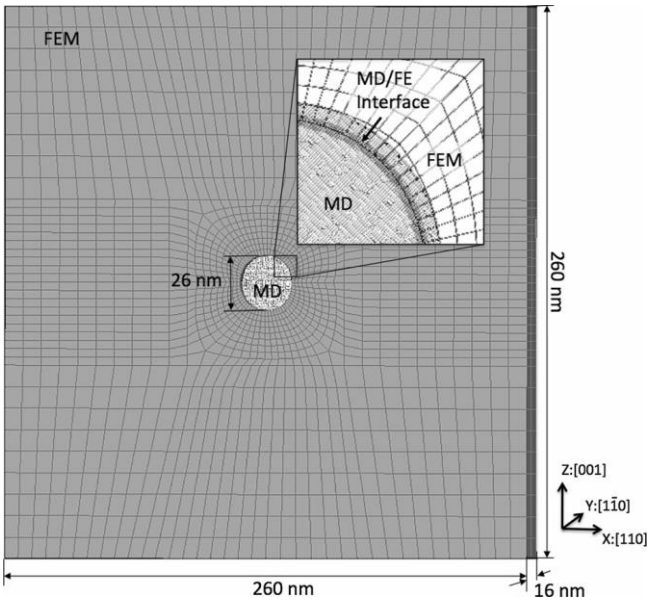

Figure 8.1: Multiscale model constituents including a shape memory alloy modeled using Molecular dynamics and a metallic alloy matrix modeled using FEM

The multiscale model in this research employed an embedded statistical coupling method (previously developed in [224]) that linked both computational techniques. Although the

model was able to quantify microstructural effects and transfer them to the continuum scale in the FEM, the model was limited to small length scales and time scales, thus it was unable to obtain comparable dynamic effects to those in AE. Regardless of these limitations, the reported multiscale model was capable of depicting solid-state transformation, which showed the potential and the capability of combining the two computational techniques.

8.2.2 MODELING OF THE AE DETECTION PROCESS

The AE detection component in the AE process is a possible extension of the computational model AE model presented in this dissertation. This additional component of the model could potentially provide a one-to-one comparison between simulations and experiments. The AE detection is related directly to the AE experimental methodology's instrumentation, which is comprised of three parts: (i) sensors, (ii) preamplifiers, and (iii) signal analysis and recording unit. All of which are part of the AE detection component in the AE process which modifies the signal content as it is acquired by the AE system. Typical AE sensors use piezoelectric crystals that are acoustically coupled to the surface in order to capture the dynamic surface motion as it propagates in the piezoelectric element. These sensors can be classified as resonant or wide band sensors depending on their frequency response which can be accomplished upon using appropriate dimensions of the piezoelectric elements [32].

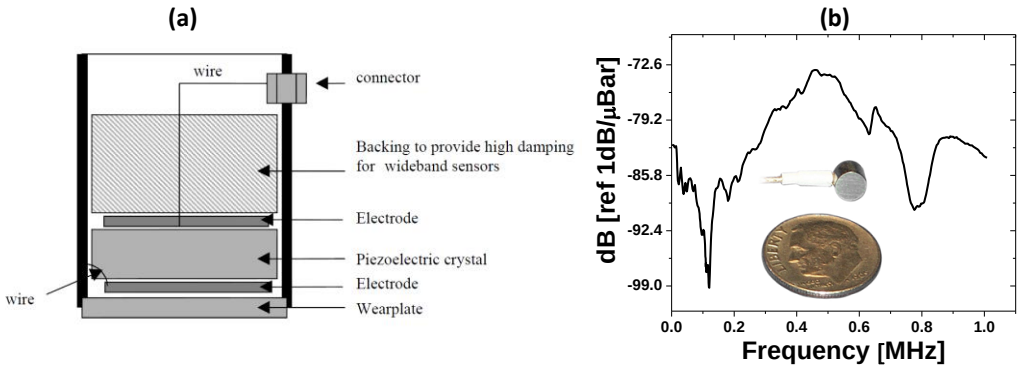

Figure 8.2: (a) Schematic diagram and (b) sensor calibration chart (i.e. frequency response) of a typical AE piezoelectric sensor [32]

Figure 8.2 portrays the components of a piezoelectric model and a typical frequency response for a PICO wide band-type AE sensor. Two different methods in previous investigations have been mainly used to model AE sensors which mainly included: explicit FEM modeling [70, 225-227] and extraction of transfer functions via experiments or simulations [91, 228-230]. For instance, the explicit FEM model of AE sensor has been constructed and studied by Sause et al. in which all possible effects due to the detection process were considered for a WD sensor, shown in Figure 8.3, including all sensor components, and a P-SPICE circuit simulation that accounted for the influence of the attached cable and the preamplifier.

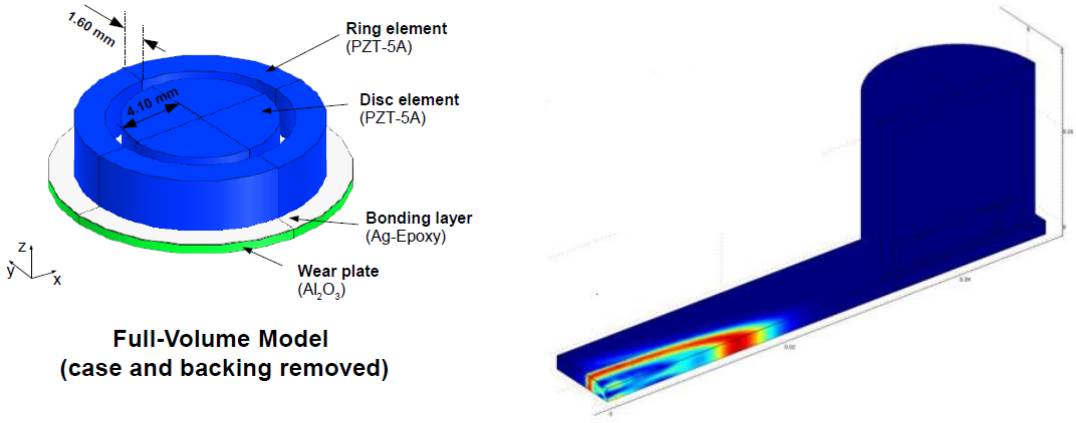

Figure 8.3: Schematic of the computational FEM model for a WD sensor [225]

The results of the model suggested that the model was computational expensive and that a simplified version which consisted of a transfer functions constructed from a reciprocity calibration using FEM was sufficient to capture the influence of the detection process. Therefore, a similar approach can be taken to construct a transfer function from the simulation and apply it to the calculated numerical waveforms from the fracture-induced computational model from this dissertation.

In addition to extending the computational model to include a sensor model, the results from this dissertation may be applicable to improve the design of novel AE sensors.

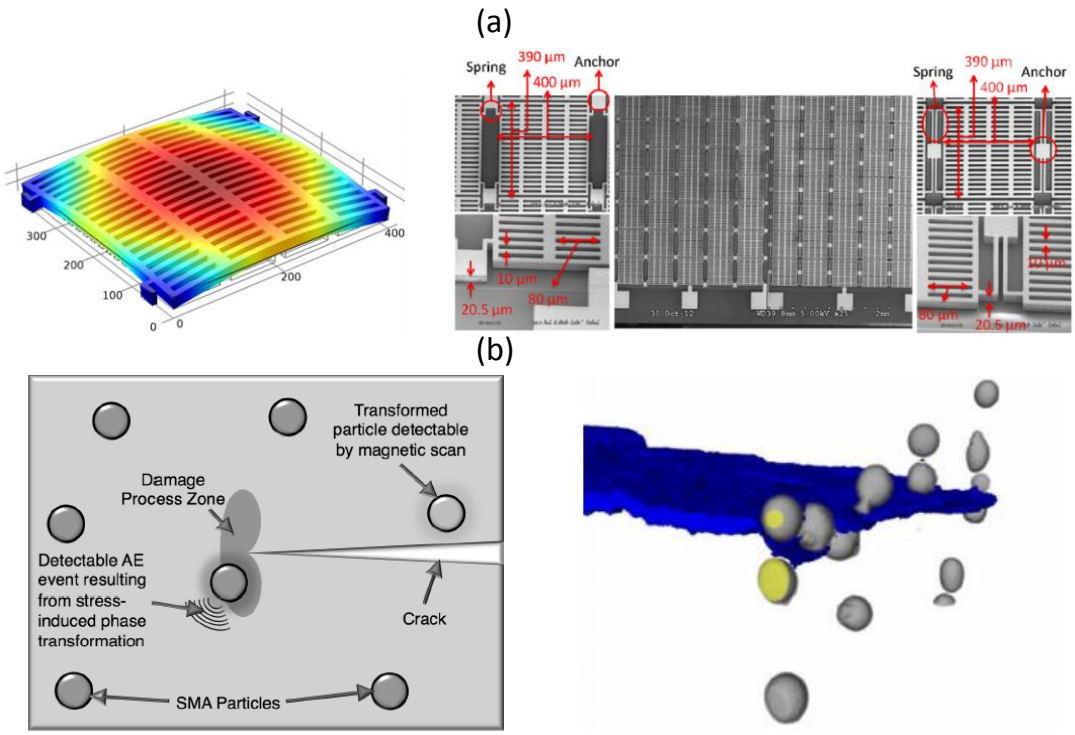

Figure 8.4: (a) In-Plane MEMS AE sensor with corresponding scanning electron image and (b) schematic of concept of using self-sensing materials for AE detection with corresponding 3D model obtained from computed tomography [231]

For instance, a recent work by Saboonchi et al. [232] to develop MEMS AE sensors sensitive to in-plane motion, depicted in Figure 8.4a, has shown some discrepancies

compared to results obtained using a laser. Along the same lines, Hochhalter et al. [231] and Yamakov et al. [223] have investigated the use of shape memory alloys as self-sensing materials for damage detections by building a multiscale model, as shown in Figure 8.4b. Both of these sensor developments still have some challenges which could be tackled by coupling or implementing the forward AE computational approach presented in this dissertation. By applying the novel forward AE model for an isolated damage source, the sensors could be targeted to specific AE sources as well as determining the deficiencies and possible improvements of the design.

8.2.3 APPLICATION TO COMPOSITE MATERIALS

Composites materials are used in a wide variety of applications which is justified by their exceptional tailored properties, namely high specific strength and stiffness. Despite its attractive mechanical properties, the reliable detection of the dominant failure mechanism, including matrix cracking, delamination to name a few, is still ongoing research.

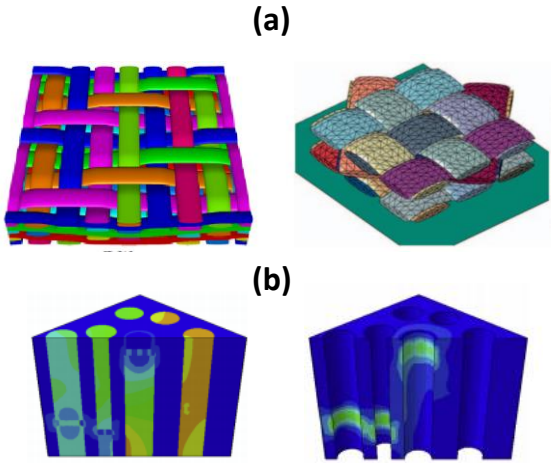

Figure 8.5: (a) 3D CAD model for a woven composite unit cell along with meshed microstructure [233, 234], (b) calculated stress contours in a microstructural unit cell of a fiber reinforce composite[235]

Current proposed models have attempted to account for the microstructure in addition to criteria associated with each damage mechanisms in order to predict and characterize the accumulation of failure mechanisms associated with final fracture [236-238]. In this context, a future goal related to this research is to adapt the current modeling approaches to the forward AE methodology in order to capture the transient effects due to damage mechanisms in composite materials.

APPENDIX A: COHESIVE ZONE MODEL

A.1 USER ELEMENT (UEL) SUBROUTINE

The ABAQUS user element subroutine (UEL) is comprised of two subroutines besides other additional which are mainly utilized to do matrix operations or to define stored variables. The two subroutines are called UEL and ktracn while the additional ones are KASET1 and KASET2. It is important to mention that this code is a modification for 3D elements as opposed to the 2D element implementation presented in [174].

The main subroutine constructs the shape functions and the quadrature related to the 16-noded zero-thickness elements, which belong to the cohesive zone. The second subroutine defines the traction separation law and the different regions corresponding the state of deformation. For instance, at a critical value of 150 μm, the stresses will be set to zero since it reached the maximum criteria. The main subroutine which runs all the other subroutines, denoted as UEL, is defined below:

```
      SUBROUTINE UEL(RHS,AMATRX,SVARS,ENERGY,NDOFEL,NRHS,NSVARS,
     1 PROPS,NPROPS,COORDS,MCRD,NNODE,U,DU,V,A,JTYPE,TIME,DTIME,
     2 KSTEP,KINC,JELEM,PARAMS,NDLOAD,JDLTYP,ADLMAG,PREDEF,NPREDF,
     3 LFLAGS,MLVARX,DDLMAG,MDLOAD,PNEWDT,JPROPS,NJPROP,PERIOD)
C
      INCLUDE 'ABA_PARAM.INC'
      PARAMETER (ZERO = 0.0D0, HALF=0.5D0, ONE= 1.0D0, TWO=2.0d0,
     1 THREE= 3.0d0, TOL=-1E-5)
      PARAMETER (FOUR= 4.0d0, EIGHT= 8.0d0)
      DIMENSION RHS(MLVARX,*),AMATRX(NDOFEL,NDOFEL),PROPS(*),
     1 SVARS(NSVARS),ENERGY(8),COORDS(MCRD,NNODE),U(NDOFEL),
     2 DU(MLVARX,*),V(NDOFEL),A(NDOFEL),TIME(2),PARAMS(3),
     3 JDLTYP(MDLOAD,*),ADLMAG(MDLOAD,*),DDLMAG(MDLOAD,*),
     4 PREDEF(2,NPREDF,NNODE),LFLAGS(*),JPROPS(*)
C     GAUSS INTEGRATION VARIABLES (3 INTEG POINT)
      DIMENSION GAUSS3(3), WEIGHT3(3), GAUSS9(9,2), WEIGHT9(9)
C     ARRAYS FOR QUADRATIC LINE ELEMENT
C     ARRAYS FOR QUADRATIC PLANAR ELEMENT
      DIMENSION DNDXI(8,2), DELTA_U(16), DU_CONT(MCRD), DU_LOC(MCRD)
      DIMENSION C_COOR(MCRD,NNODE), PSI(24,NDOFEL)
      DIMENSION B(MCRD, NDOFEL), BT(NDOFEL, MCRD)
      DIMENSION A1(NDOFEL, MCRD), A2(NDOFEL, NDOFEL)
      DIMENSION AV_COOR(MCRD, 8), V_XI(MCRD), V_ZI(MCRD), V_N(MCRD)
      DIMENSION THETA(MCRD, MCRD), STR_GLOB(MCRD)
      DIMENSION D_GLOB(MCRD, MCRD), DD1(MCRD, MCRD), ETA(16,NDOFEL)
      DIMENSION H(MCRD,12), HH(MCRD,12)
C     GENERAL ELEMENT VALUES
```

```
      DIMENSION DDSDDR(MCRD,MCRD)
      DIMENSION STRESS(MCRD)
C     H-Variables
      DOUBLE PRECISION H1, H2, H3, H4,
     H5, H6, H7, H8
      data iuel/0/
      save iuel
C     ------------------------------------------------------------------
C     QUADRATIC PLANE ELEMENT
C     SVARS - In 1, contains the lOpenClose identifier
C     - In 3-4, contains the traction stiffness
C     - In 5-6, contains the traction opening
C     SINGLES VALUES
C     NNODE=16, MCRD=3, NDOFEL=48, MLVARX=64, MDLOAD=1, NSVARS=63, NRHS=1
C     INITIALIZATION: IMPORTANT!! FORTRAN DOES NOT PUT ZEROS IN THERE AUTOMATICALLY
C     ------------------------------------------------------------------
C     CREATE MATRICES AND VECTORS FOR CALCULATIONS
C     ------------------------------------------------------------------
      CALL KASET2(AMATRX, NDOFEL, NDOFEL)
C     AMATRIX Initialized
      IF (NRHS.EQ.1) THEN
        CALL KASET1(RHS, MLVARX)
C        RHS Initialized, NHRS
      ELSE
        CALL KASET2(RHS, MLVARX, NRHS)
C       RHS Initialized, NHRS /= 1
      END IF
      CALL KASET2(PSI, 24, NDOFEL)
C     PSI Initialized
      CALL KASET2(H, MCRD, 12)
      CALL KASET2(HH, MCRD, 12)
      write(7,*) 'H-Matrix', H(1,1)
      write(7,*) 'HH-Matrix', HH(1,1)
C     H Initialized
      CALL KASET2(AV_COOR, MCRD, 8)
C     AV_COOR Initialized
      CALL KASET1(V_XI, MCRD)
C     V_XI Initialized
      CALL KASET1(V_YI, MCRD)
C     V_YI Initialized
      CALL KASET1(V_N, MCRD)
C     V_N Initialized
      CALL KASET2(THETA, MCRD, MCRD)
C     THETA Initialized
      CALL KASET2(DDSDDR, MCRD, MCRD)
C     DDSDDR Initialized
      CALL KASET2(D_GLOB, MCRD, MCRD)
C     D_GLOB Initialized
      CALL KASET1(STRESS, MCRD)
C     STRESS Initialized
      CALL KASET1(STR_GLOB, MCRD)
C     STR_GLOB Initialized
C     Parameters Initialized
C     REAL INPUT PROPERTIES
C     Width of elements (same as solid section width for solid elements)
      WIDTH = PROPS(7)
C     INTEGER INPUT PROPERTIES
      NINTP = JPROPS(1) ! Number of integration points
C     Integration point scheme (1: gauss, 2: newton cotes)
      INTS = JPROPS(2)
C     INFORMATION OUTPUT AND CHECK
      IF (iuel.EQ.0) THEN
      write(7,*) 'First call to UEL-----------------'
      WRITE(7,*) 'DEGREES OF FREEDOM:',NDOFEL
      write(7,*) 'number of nodes:', NNODE
      write(7,*) 'number of integration points:', NINTP
      write(7,*) 'Integration scheme:', INTS
      write(7,*) 'maximum coords:', MCRD
      write(7,*) 'number of variables:', NSVARS
      write(7,*) 'number of real properties', NPROPS
      write(7,*) 'number of integer properties', NJPROP
```

```
      write(7,*) 'dimensioning parameter:', MLVARX
      write(7,*) 'KINC:', KINC
      write(7,*) 'LFLAGS(1)=', LFLAGS(1)
      write(7,*) 'LFLAGS(2)=', LFLAGS(2)
      write(7,*) 'LFLAGS(3)=', LFLAGS(3)
      write(7,*) 'LFLAGS(4)=', LFLAGS(4)
      write(7,*) 'LFLAGS(5)=', LFLAGS(5)
C     CHECKING FOR THE RIGHT NUMBER OF NODES
        IF (NNODE.NE.16) THEN
            CALL STDB_ABQERR(-3, '16 nodes required for interface element:
            specified number of nodes is incorrect',0,0.0,' ')
        END IF
C     CHECKING FOR NUMBER OF STATE VARIABLES (SVARS)
      minnum = NINTP*7
        IF (NSVARS.LT.minnum) THEN
           CALL STDB_ABQERR(-3, 'Number of state variables too small for
           chosen number of integration points!',MINNUM,0.0,' ')
        END IF
        IUEL = 1
      END IF
      WRITE(7,*) 'New call to UEL'
      write(7,*) 'Element', JELEM
C     CREATE PSI
      DO 10 K = 1, NDOFEL/2
        PSI(K, K) = -ONE
        PSI(K, K+NDOFEL/2) = ONE
   10 END DO
C     COMPUTE NODAL COORDINATES IN DEFORMED STATE
C     ADD PROPER COORDINATE TRANSFORMATION LATER
      DO 20 I=1,MCRD
        DO 30 J=1, NNODE
        NN=I+(J-1)*MCRD
        C_COOR(I,J)=COORDS(I,J) + U(NN)
   30   END DO
   20 END DO
C     REFERENCE COORDINATE SYSTEM (MIDPOINT AVERAGES)
      DO 31 I=1, MCRD
        DO 32 J=1, NNODE/2
            AV_COOR(I,J)=ONE/TWO*(C_COOR(I,J)+C_COOR(I,J+(NNODE/2)))
   32   END DO
   31 END DO
C     GAUSSIAN INTEGRATION (3 GAUSS POINTS)
      GAUSS3(1) = -SQRT(0.6)
      GAUSS3(2) = ZERO
      GAUSS3(3) = SQRT(0.6)
      WEIGHT3(1) = 0.55555555555555
      WEIGHT3(2) = 0.88888888888888
      WEIGHT3(3) = 0.55555555555555
C     GAUSSIAN INTEGRATION (9 GAUSS POINTS; 3X3 2D CASE)
      GAUSS9(1,1) = GAUSS3(1)
      GAUSS9(2,1) = GAUSS3(2)
      GAUSS9(3,1) = GAUSS3(3)
      GAUSS9(4,1) = GAUSS3(1)
      GAUSS9(5,1) = GAUSS3(2)
      GAUSS9(6,1) = GAUSS3(3)
      GAUSS9(7,1) = GAUSS3(1)
      GAUSS9(8,1) = GAUSS3(2)
      GAUSS9(9,1) = GAUSS3(3)
      GAUSS9(1,2) = GAUSS3(1)
      GAUSS9(2,2) = GAUSS3(1)
      GAUSS9(3,2) = GAUSS3(1)
      GAUSS9(4,2) = GAUSS3(2)
      GAUSS9(5,2) = GAUSS3(2)
      GAUSS9(6,2) = GAUSS3(2)
      GAUSS9(7,2) = GAUSS3(3)
      GAUSS9(8,2) = GAUSS3(3)
      GAUSS9(9,2) = GAUSS3(3)
      WEIGHT9(1) = WEIGHT3(1)*WEIGHT3(1)
      WEIGHT9(2) = WEIGHT3(2)*WEIGHT3(1)
      WEIGHT9(3) = WEIGHT3(3)*WEIGHT3(1)
      WEIGHT9(4) = WEIGHT3(1)*WEIGHT3(2)
```

```
      WEIGHT9(5) = WEIGHT3(2)*WEIGHT3(2)
      WEIGHT9(6) = WEIGHT3(3)*WEIGHT3(2)
      WEIGHT9(7) = WEIGHT3(1)*WEIGHT3(3)
      WEIGHT9(8) = WEIGHT3(2)*WEIGHT3(3)
      WEIGHT9(9) = WEIGHT3(3)*WEIGHT3(3)
C
      IF (LFLAGS(3).EQ.1) THEN
C     Normal incrementation (RHS and AMATRX required)
         IF (LFLAGS(1).EQ.1.OR.LFLAGS(1).EQ.2) THEN
C     *STATIC AND *STATIC, DIRECT
C     ----------------------------------------------------------------
C     LOOP OVER INTEGRATION POINTS
C     ----------------------------------------------------------------
      DO 100 IINTP = 1,NINTP
        POINT1 = GAUSS9(IINTP,1)
        POINT2 = GAUSS9(IINTP,2)
        WEIGHT = WEIGHT9(IINTP)
C     Shape function value
      H5 = ONE/TWO*(ONE - POINT1**TWO)*(ONE - POINT2)
      H6 = ONE/TWO*(ONE + POINT1)*(ONE - POINT2**TWO)
      H7 = ONE/TWO*(ONE - POINT1**TWO)*(ONE + POINT2)
      H8 = ONE/TWO*(ONE - POINT1)*(ONE - POINT2**TWO)
      H1 = ONE/FOUR*(ONE - POINT1)*(ONE - POINT2) - ONE/TWO*(H5 + H8)
      H2 = ONE/FOUR*(ONE + POINT1)*(ONE - POINT2) - ONE/TWO*(H5 + H6)
      H3 = ONE/FOUR*(ONE + POINT1)*(ONE + POINT2) - ONE/TWO*(H6 + H7)
      H4 = ONE/FOUR*(ONE - POINT1)*(ONE + POINT2) - ONE/TWO*(H7 + H8)
C     DERIVATIVE OF SHAPE FUNCTION VALUE (8X2 MATRIX)
      DNDXI(5,1) = -POINT1*(ONE - POINT2)
      DNDXI(6,1) = ONE/TWO*(ONE - POINT2**TWO)
      DNDXI(7,1) = -POINT1*(ONE + POINT2)
      DNDXI(8,1) = -ONE/TWO*(ONE - POINT2**TWO)
      DNDXI(1,1) = -ONE/FOUR*(ONE - POINT2) - ONE/TWO*(DNDXI(5,1)
       + DNDXI(8,1))
      DNDXI(2,1) = ONE/FOUR*(ONE - POINT2) - ONE/TWO*(DNDXI(5,1)
       + DNDXI(6,1))
      DNDXI(3,1) = ONE/FOUR*(ONE + POINT2) - ONE/TWO*(DNDXI(6,1)
       + DNDXI(7,1))
      DNDXI(4,1) = -ONE/FOUR*(ONE + POINT2) - ONE/TWO*(DNDXI(7,1)
       + DNDXI(8,1))
      DNDXI(5,2) = -ONE/TWO*(1 - POINT1**TWO)
      DNDXI(6,2) = -POINT2*(1 + POINT1)
      DNDXI(7,2) = ONE/TWO*(1 - POINT1**TWO)
      DNDXI(8,2) = -POINT2*(1 - POINT1)
      DNDXI(1,2) = -ONE/FOUR*(ONE - POINT1) - ONE/TWO*(DNDXI(5,2)
       + DNDXI(8,2))
      DNDXI(2,2) = -ONE/FOUR*(ONE + POINT1) - ONE/TWO*(DNDXI(5,2)
       + DNDXI(6,2))
      DNDXI(3,2) = ONE/FOUR*(ONE + POINT1) - ONE/TWO*(DNDXI(6,2)
       + DNDXI(7,2))
      DNDXI(4,2) = ONE/FOUR*(ONE - POINT1) - ONE/TWO*(DNDXI(7,2)
       + DNDXI(8,2))
C     H matrix (3X24 MATRIX)
      H(1,1) = H1
      H(2,2) = H1
      H(3,3) = H1
C     H1 Complete
      H(1,4) = H2
      H(2,5) = H2
      H(3,6) = H2
C     H2 Complete
      H(1,7) = H3
      H(2,8) = H3
      H(3,9) = H3
C     H3 Complete
      H(1,10) = H4
      H(2,11) = H4
      H(3,12) = H4
C     H4 Complete
      HH(1,1) = H5
      HH(2,2) = H5
      HH(3,3) = H5
```

```
C     H5 Complete
      HH(1,4) = H6
      HH(2,5) = H6
      HH(3,6) = H6
C     H6 Complete
      HH(1,7) = H7
      HH(2,8) = H7
      HH(3,9) = H7
C     H7 Complete
      HH(1,10) = H8
      HH(2,11) = H8
      HH(3,12) = H8
C     INTP POINT and WEIGHT, IINTP, POINT, WEIGHT
      CALL KASET2(B, MCRD, NDOFEL)
      DO 110 I=1, MCRD
        DO 120 J=1, NDOFEL
            DO 130 K=1, NDOFEL/2
                IF (K.LT.13) THEN
                B(I,J) = B(I,J) + H(I,K)*PSI(K,J)
                ELSE
                B(I,J) = B(I,J) + HH(I,K-12)*PSI(K,J)
                END IF
  130       END DO
  120   END DO
  110 END DO
C     TRANSPOSED B MATRIX
      DO 140 I=1, MCRD
        DO 150 J=1, NDOFEL
            BT(J,I) = B(I,J)
  150   END DO
  140 END DO
C     CALCULATE GLOBAL DISPLACEMENT AT INTEGRATION POINT
C     FROM CONTINUOUS DISPLACEMENT
      CALL KASET1(DU_CONT, MCRD)
      DO 160 I=1, MCRD
        DO 170 J=1, NDOFEL
            DU_CONT(I) = DU_CONT(I) + B(I,J)*U(J)
  170   END DO
  160 END DO
      DU_CONT(2)=DU_CONT(2)
C     LOCAL COORDINATE SYSTEM
C     (USE AVERAGE OF DEFORMED X-POSITIONS OF TOP AND BOTTOM)
      X_xi = ZERO
      Y_xi = ZERO
      Z_xi = ZERO
      X_zi = ZERO
      Y_zi = ZERO
      Z_zi = ZERO
      DO 180 I=1,8
          X_xi = X_xi + DNDXI(I,1)*AV_COOR(1,I)
          Y_xi = Y_xi + DNDXI(I,1)*AV_COOR(2,I)
          Z_xi = Z_xi + DNDXI(I,1)*AV_COOR(3,I)
          X_zi = X_zi + DNDXI(I,2)*AV_COOR(1,I)
          Y_zi = Y_zi + DNDXI(I,2)*AV_COOR(2,I)
          Z_zi = Z_zi + DNDXI(I,2)*AV_COOR(3,I)
  180 END DO
C     Jacobian (vector length in x -direction)
      DETJ1 = Y_xi*Z_zi - Z_xi*Y_zi
      DETJ2 = Z_xi*X_zi - X_xi*Z_zi
      DETJ3 = X_xi*Y_zi - Y_xi*X_zi
      DETJ = sqrt(DETJ1**TWO + DETJ2**TWO + DETJ3**TWO)
C
      IF (DETJ.LT.ZERO) THEN
        write(7,*) 'Negative Jacobian encountered!
       Check element and nodal definition for elem', JELEM
        CALL XIT
      END IF
C     NORMAL VECTOR
      V_N(1) = DETJ1/DETJ
      V_N(2) = DETJ2/DETJ
      V_N(3) = DETJ3/DETJ
```

```
C     LOCAL COORDINATE VECTOR.  FOR X AND Z
      V_xi(1) = X_xi/SQRT(X_xi**TWO + Y_xi**TWO + Z_xi**TWO)
      V_xi(2) = Y_xi/SQRT(X_xi**TWO + Y_xi**TWO + Z_xi**TWO)
      V_xi(3) = Z_xi/SQRT(X_xi**TWO + Y_xi**TWO + Z_xi**TWO)
      V_zi(1) = V_N(2)*V_xi(3) - V_N(3)*V_xi(2)
      V_zi(2) = V_N(3)*V_xi(1) - V_N(1)*V_xi(3)
      V_zi(3) = V_N(1)*V_xi(2) - V_N(2)*V_xi(1)
C     ROTATIONAL MATRIX
      THETA(1,1) = V_xi(1)
      THETA(2,1) = V_xi(2)
      THETA(3,1) = V_xi(3)
      THETA(1,2) = V_N(1)
      THETA(2,2) = V_N(2)
      THETA(3,2) = V_N(3)
      THETA(1,3) = V_zi(1)
      THETA(2,3) = V_zi(2)
      THETA(3,3) = V_zi(3)
C     RELATIVE DISPLACEMENT IN LOCAL COORDINATE SYSTEM
      CALL KASET1(DU_LOC, MCRD)
      DO 181 I=1, MCRD
        DO 182 J=1, MCRD
            DU_LOC(I) = DU_LOC(I) + THETA(J,I)*DU_CONT(J)
  182   END DO
  181 END DO
C     over-closure check (can be used as re-start criterion - see uinter)
      IF (DU_LOC(2).LT.TOL) THEN
        write(7,*) 'Over-closure at element', JELEM
      END IF
C     ----------------------------------------------------------------
C     CALL TRACTION SEPARATION LAW PARAMETERS
C     ----------------------------------------------------------------
      CALL KTRACN(DU_LOC, PROPS, STRESS, DDSDDR,
       MCRD, SVARS, NSVARS, IINTP, NINTP, KINC, JELEM, TIME)
C     OUTPUTS:  DDSDDR, STRESS
C     USED AFTER:  DU_LOC (OPENNING) AS STATE VARIABLE [SVARS]
C     ----------------------------------------------------------------
C     NOTE:
C     Dummy stiffness for friction (no influence under mode
C     I opening when coupled with equation) for accuracy there should be coupling terms,
C     but again: no influence under mode I opening
C     ----------------------------------------------------------------
      DDSDDR(1,1) = 10000
C     RHS ASSEMBLY
C     CHECK FOR APPLIED LOADS ON STRUCTURE
      IF (NDLOAD.NE.0) THEN
        WRITE(7,*) 'Element loads not implemented'
        CALL XIT
      END IF
C     STIFFNESS MATRIX
      CALL KASET2(DD1, MCRD, MCRD)
      DO 183 I=1, MCRD
        DO 184 J=1, MCRD
            DO 185 K=1, MCRD
                DD1(I,J) = DD1(I,J) + DDSDDR(I,K)*THETA(J,K)
  185       END DO
  184   END DO
  183 END DO
      CALL KASET2(D_GLOB, MCRD, MCRD)
      DO 186 I=1, MCRD
        DO 187 J=1, MCRD
            DO 188 K=1, MCRD
                D_GLOB(I,J) = D_GLOB(I,J) + THETA(I,K)*DD1(K,J)
  188       END DO
  187   END DO
  186 END DO
      CALL KASET2 (A1, NDOFEL, MCRD)
      DO 190 I=1, NDOFEL
        DO 191 J=1, MCRD
            DO 192 K=1, MCRD
                A1(I,J) = A1(I,J) + BT(I,K)*D_GLOB(K,J)
  192       END DO
```

```
  191   END DO
  190 END DO
      CALL KASET2 (A2, NDOFEL, NDOFEL)
      DO 195 I=1, NDOFEL
        DO 196 J=1, NDOFEL
            DO 197 K=1, MCRD
                A2(I,J) = A2(I,J) + A1(I,K)*B(K,J)
  197       END DO
  196   END DO
  195 END DO
      DO 200 I=1, NDOFEL
        DO 201 J=1, NDOFEL
            AMATRX(I,J) = AMATRX(I,J) + WIDTH*WEIGHT*DETJ*A2(I,J)
  201   END DO
  200 END DO
C     RIGHT HAND SIDE
C     TRANSFORMATION
C     STRESS IS tloc
      CALL KASET1(STR_GLOB, MCRD)
      DO 202 I=1, MCRD
        DO 203 J=1, MCRD
            STR_GLOB(I) = STR_GLOB(I) + THETA(I,J)*STRESS(J)
  203   END DO
  202 END DO
      write(7,*) 'Global Stress', STR_GLOB
      DO 230 I=1, NDOFEL
        DO 240 K=1,MCRD
            RHS(I,1) = RHS(I,1) + DETJ*WIDTH*WEIGHT*BT(I,K)*STR_GLOB(K)
  240   END DO
  230 END DO
      IF (NRHS.EQ.2) THEN
        WRITE(7,*) 'Riks solution not supported by element'
        CALL XIT
      END IF
      IF (LFLAGS(4).EQ.1) THEN
C     PERTURBATION STEP
        WRITE(7,*) 'Perturbation step not supported by element'
        CALL XIT
      END IF
C     SAVE OPENING AND STRESSES AT INTEGRATION POINT AS STATE VARIABLES
      SVARS(IINTP+NINTP) = DU_LOC(1)
      SVARS(IINTP+2*NINTP) = DU_LOC(2)
      SVARS(IINTP+3*NINTP) = DU_LOC(3)
      SVARS(IINTP+4*NINTP) = STRESS(1)
      SVARS(IINTP+5*NINTP) = STRESS(2)
      SVARS(IINTP+6*NINTP) = STRESS(3)
C     ------------------------------------------------------------------
  100 END DO
C     END OF INTEGRATION POINT CALCULATION
C     ------------------------------------------------------------------
C     IF STATEMENT:  (LFLAGS(3).EQ.1) THEN
C     Normal incrementation (RHS and AMATRX required)
      ELSE
        WRITE(7,*) 'Only static procedure supported by element'
        CALL XIT
      END IF
C     ENDED NESTED IF LOOP
C     ------------------------------------------------------------------
C     (LFLAGS(1).EQ.1.OR.LFLAGS(1).EQ.2) THEN
      ELSE IF (LFLAGS(3).EQ.4) THEN
        DO I=1, NDOFEL
            AMATRX(I,I)= 1.0d0
        END DO
      ELSE
        WRITE(7,*) 'Only normal incrementation supported by element'
        CALL XIT
      END IF
C     ENDED NESTED IF LOOP (OUTTER)
C     ------------------------------------------------------------------
      RETURN
      END
```

In this section, the subroutine for the nonlinear traction separation law is defined. This subroutine takes the displacement or separation of the cohesive element and defines a corresponding traction based on the traction separation law.

```
      subroutine ktracn(RDISP, PROPS, STRESS, DDSDDR, MCRD, SVARS,
     1 NSVARS, IINTP, NINTP, KINC, JELEM, TIME)
      INCLUDE 'ABA_PARAM.INC'
      PARAMETER (ZERO = 0.D0, TWO=2.0D0, ONE= 1.0D0, THREE= 3.0d0)
      DIMENSION PROPS(*), RDISP(MCRD), STRESS(MCRD), DDSDDR(MCRD, MCRD)
      DIMENSION SVARS(NSVARS), TIME(2)
      data ifirst/0/
      data iopen/0/
      data iclose/0/
      save ifirst, nodefirst, iopen, iclose
C     REAL INPUT PROPERTIES
C     INCREASE IN FRACTURE TOUGHNESS
      dJss = props(1)
C     MAX CRACK BRIDGING OPENING
      deltac = props(2)
C     INITIAL LINEAR DECREASE/INCREASE, SOFTENING AFTERWARDS
      delta1 = props(3)
C     VALUE OF J0 (FROM MEASUREMENTS)
      dJ0 = props(4)
C     STRESS INCREASE FACTOR FOR POWER LAW
      fac1 = props(5)
C     PENALTY FACTOR ON CONTACT
      penalty = props(6)
C     SIGMA0
      sigma0 = 1.5d0*dJss/delta1*sqrt(delta1/deltac)
C     SLOPE 1
      slope1 = -dJss/(delta1*deltac*sqrt(delta1/deltac))
C     FAC
      fac = dJss/(two*sqrt(deltac))
C     SIGMA 1
      sigma1 = fac/sqrt(delta1)
C     SLOPE
      slope = sigma1/delta1
C     PRINTING PARAMETER FIRST COHESIVE ELEMENT
      firstel = PROPS(9)
C     J0 IS INCLUDED SEPARATELY NOW WITH ZERO START POWER LAW
      alpha = PROPS(8)
      delta2 = dJ0/(sigma0*fac1)*(alpha+1)/alpha
C     Code checks for change in opening status. If too many contact points change status,
C     increment can be restarted
C     Checks for opening/closing behaviour
C     ------------------------------------------------------------------
C     get values from state variables
      iold = SVARS(IINTP)
      stressold = SVARS(IINTP + 5*NINTP)
      rdispold = SVARS(IINTP + 2*NINTP)
C     ------------------------------------------------------------------
C     Code checks for change in contact status. If too many contact points change status,
C     increment can be restarted
C     Checks for opening/closing behaviour
      IF (ifirst.eq.0) THEN
        ifirst = 1
        NODEFIRST = NODE
      END IF
C     new increment detection (includes restart) to count contact changes
      IF (NODE.EQ.NODEFIRST.AND.KIT.EQ.1) THEN
```

```
        iopen = 0
        iclose = 0
      END IF
-----------------------------------------------------------------
C     ------------------------TSL PIECEWISE FUNCTION-------------------------

C     Check for increasing opening displacement (start in increment 2,
C     once all contact points are closed)
C     Only applies in opening stage (rdisp < 0)
C     Not included right now (KINC.GE.1000)
      IF (rdisp(2).LT.rdispold.AND.rdisp(2).GT.delta1.AND.
       KINC.GE.1000) THEN
C     ELASTIC UNLOADING AND RELOADING
        stress(2) = stressold/rdispold*rdisp(2)!rdips is DU_LOC
        ddsddr(2,2) = stressold/rdispold
        write(7,*) 'Elastic unloading encountered'
      ELSE
C     Check for penetration of surfaces and indicate status
C     Compute Strain and apply Linear Elastic curve to compute overclosure stress
       IF (rdisp(2).LT.zero) THEN
              write(7,*) 'Pen Stress', penalty*slope*rdisp(2)
              stress(2) = penalty*slope*rdisp(2)
              ddsddr(2,2) = penalty*slope
              lOpenClose = 0

C              write(7,*) 'Pen Stress', -sigma0
C              stress(2) = -sigma0
C              ddsddr(2,2) = 0
C              lOpenClose = 0
          IF (JELEM.eq.firstel) THEN
           write(*,*) 'Area I'
           write(*,*) 'Int Pt', IINTP
           write(*,*) 'rdisp', rdisp(2)
           write(*,*) 'Stress', stress(2)
           write(*,*) 'Time' , TIME(1)
           END IF
C     Check for opening of crack
C     Stresses will be negative (tension)
C     First slope bit (different from square root law)
        ELSE IF (rdisp(2).GE.zero.and.rdisp(2).LT.delta2) then
C     Initial increase
C     AREA II
          stress(2) = fac1*sigma0*
          (1.0-((delta2-rdisp(2))/delta2)**alpha)
          ddsddr(2,2) = fac1*alpha*sigma0/delta2*
          (((delta2-rdisp(2))/delta2)**(alpha-1))
          lOpenClose = 1
          IF (JELEM.eq.firstel) then
             write(*,*) 'Area II'
             write(*,*) 'Int Pt', IINTP
             write(*,*) 'rdisp', rdisp(2)
             write(*,*) 'Stress', stress(2)
             write(*,*) 'Time' , TIME(1)
           END IF
C     -----------------------------------------------------------------
C     SOFTENING BEHAVIOR
        ELSE IF (rdisp(2).GE.delta2.and.rdisp(2).LT.(delta1+delta2)) THEN
C     AREA III
          stress(2) = sigma0 + slope1*(rdisp(2)-delta2)
          ddsddr(2,2) = slope1
          lOpenClose = 2
          IF (JELEM.eq.firstel) THEN
             write(*,*) 'Area III'
             write(*,*) 'Int Pt', IINTP
             write(*,*) 'rdisp', rdisp(2)
             write(*,*) 'Stress', stress(2)
             write(*,*) 'Time' , TIME(1)
           END IF
        ELSE IF (rdisp(2).GT.(delta1+delta2).and.rdisp(2).LT.(deltac+delta2)) THEN
C     AREA IV
          stress(2) = fac*sqrt((rdisp(2) - delta2))
```

```
            ddsddr(2,2) = -fac/2*((rdisp(2)-delta2))**(-3.d0/2.d0)
            lOpenClose = 3
           IF (JELEM.eq.firstel) THEN
              write(*,*) 'Area IV'
              write(*,*) 'Int Pt', IINTP
              write(*,*) 'rdisp', rdisp(2)
              write(*,*) 'Stress', stress(2)
              write(*,*) 'Time' , TIME(1)
            END IF
         ELSE IF (rdisp(2).GT.(deltac+delta2)) THEN
C     AREA V
            stress(2) = 0
            ddsddr(2,2) = 0
            lOpenClose = 4
           IF (JELEM.eq.firstel) THEN
             write(*,*) 'Area V'
            write(*,*) 'Int Pt', IINTP
            write(*,*) 'rdisp', rdisp(2)
            write(*,*) 'Stress', stress(2)
            write(*,*) 'Time' , TIME(1)
           END IF
         END IF
       END IF


       IF (lOpenClose.NE.iold.AND.iold.EQ.0.AND.KINC.GT.3) THEN
C     Restart if more than one contact pair opens (iold=0) in 2nd call
         IF (KIT.EQ.2) THEN
            iopen = iopen + 1
         END IF
         write(7,*) 'Status: iopen=', iopen, 'at int point', IINTP,
        'in element', JELEM, 'and increment', KINC
         write(7,*) 'lOpenClose =',lOpenclose,'iold=',iold,'KIT=', KIT
C     Possible restart procedure
         IF (iopen.gt.1) THEN
          write(7,*) 'Too many contact openings: reduce increment'
         END IF
       END IF
C     Restart if one contact pair closes (iold=1/lOpenClose=0)
       IF (lOpenClose.EQ.0.AND.iold.EQ.1.AND.KINC.GE.2) THEN
         iclose = iclose + 1
         write(7,*) 'Status: iclose=', iclose, 'at int point', IINTP,
        'in element', JELEM, 'and increment', KINC
         write(7,*) 'lOpenClose =',lOpenclose,'iold=',iold,'KIT=', KIT
         IF (iclose.gt.0) THEN
             write(7,*) 'Elastic unloading possible: reduce increment'
         END IF
       END IF
C     Restart with PNEWDT (if PNEWDT less than 1)
       IF (iclose.gt.0) THEN
         PNEWDT = 1.0
       ELSE IF (iopen.gt.4) THEN
         PNEWDT = 1.0
       END IF
C     Sign definition (bridging stress acts as closure stress on structure
C     as in contact analysis)
C     Stiffness matrix according to ABAQUS definition: -dF/du!!
C     ----------------------------------------------------------------
C     NEW STRESS
C     ----------------------------------------------------------------
       stress(2) = -stress(2)/2
       write(7,*) 'stress', stress(2)
       write(7,*) 'rdisp', rdisp(2)
C     ----------------------------------------------------------------
C     STATE VARIABLE UPDATE
       SVARS(IINTP) = lOpenClose
       RETURN
       END
C     ----------------------------------------------------------------
       subroutine KASET1(DMATRIX, IDIMX)
       INCLUDE 'ABA_PARAM.INC'
```

```
      PARAMETER (ZERO = 0.0D0)
      DIMENSION DMATRIX(IDIMX)
C      write(7,*) 'Begin Setting to Zeros'
      DO i=1, IDIMX
C        write(7,*) 'Component Number', i
        DMATRIX(i) = ZERO
C        write(7,*) 'Component Number', i
      END DO
C      write(7,*) 'End Setting to Zeros'
      RETURN
      END
```

The two additional subroutines, KASET1 and KASET2, define empty vectors and 2-D matrices for variable storage.

```
      subroutine KASET1(DMATRIX, IDIMX)
      INCLUDE 'ABA_PARAM.INC'
      PARAMETER (ZERO = 0.0D0)
      DIMENSION DMATRIX(IDIMX)
C      write(7,*) 'Begin Setting to Zeros'
      DO i=1, IDIMX
C        write(7,*) 'Component Number', i
        DMATRIX(i) = ZERO
C        write(7,*) 'Component Number', i
      END DO
C      write(7,*) 'End Setting to Zeros'
      RETURN
      END
C-----------------------------------------------------------------------------------------
-
      subroutine KASET2(DMATRIX, IDIMX, IDIMY)
        INCLUDE 'ABA_PARAM.INC'
        PARAMETER (ZERO = 0.0D0)
        DIMENSION DMATRIX(IDIMX, IDIMY)
        DO I = 1, IDIMX
            DO J = 1, IDIMY
            DMATRIX(I,J) = ZERO
            END DO
        END DO
      RETURN
      END
            D = I-1
            hh=hh+1
         ENDIF
      END DO
      RETURN
      END
```

APPENDIX B: WAVE ANALYSIS TOOL

B.1 MATLAB CODE

The numerical waveforms calculated from the computational model were all analyzed using FFT and STFT analysis. In order to have consistent results and conclusions, all waveforms were postprocessed using a customized MATLAB code. This code was comprised of 5 subroutines, in which 4 of them were functions.

```
%%
% Author:  Jefferson A. Cuadra
% March 23, 2015
%%
% SIGNAL ANALYSIS FOR ABAQUS TXT OUTPUTS
clear,clc
%% OUTPUT FILE  NAME
%----------------------
foutn='CTPW500_10N';
%VsctpHW300%----------------------
%%
askt=input('Step time needs to be uploaded? [1]Yes [2]No:  ');
askI=input('Data needs to be interpolated? [1]Yes [2]No:  ');
askS=input('Save Data [1]Yes [2]No:  ');
askTi=input('Enter [1] cutting time window or [2] for using default time span:
');
ndatasets=input('Enter number of datasets per parameter: '); % This only
affects Plots
typsets=input('Enter 1 for [A, U, V], 2 for [U, V]  3 for [V]:  ');% This only
affects Plots
%% WINDOW CUT TIME
if askTi==1
    tfspan=50e-06;
end
%% Interpolation Step for FFT
step= .1e-7;
%% FOR PLOTTING MAX FREQUENCY
tpfreq=5000;%(kHz)
%% ------------------------------------------------------------------------
% Check Header (Number of rows) importdata(filename,' Delimeter Type',
% Header Size)
hsize=4;
%%
if askt==1
    display('Download .sta file and correct for time vector in mat-file')
    display('Press enter to continue')
    dummy=waitforbuttonpress;close all;
    [filenamet,patht]=uigetfile('*mat');%Choose largest name file
    addpath(patht)
    t=importdata(filenamet);
end
%Obtain data
[filenamed,pathd]=uigetfile('*txt');%Choose largest name file
addpath(pathd)
```

```
S=importdata(filenamed,' ',hsize);
if hsize==0
    SS=S;
else
    SS=S.data;
end
% SS(:,2:end)=SS(:,2:end)/1000;
%% Offset data to zero if necessary
[m,n]=size(SS);
SStemp=SS-((SS(1,:)')*ones(1,m))';
%check
clear SS
SS=SStemp;
clear SStemp
%%
if askTi~=1
    clear tfspan
    if askt==1
        tfspan=t(end);
    else
        tfspan=SS(end,1);
    end
end
clear m n
[m,n]=size(SS);
if askI==2
    clear step
    step=abs(SS(2,1)-SS(1,1));
end
if askt==1
    %adding time if uploaded
    D=SS(:,2:end);
    clear SS;
    SS=zeros(m,n);
    SS=[t D];
    clear D
end
%%
%Modify end time if needed
td=0:step:tfspan;
mt=length(td);
% Calculate Frequency
%% FFT Calculation of interpolated data
N=length(td);
delta=step;
fs=1/delta;
% FFT Calculation
NFFT=2^nextpow2(N);
f=fs/2*linspace(0,1,NFFT/2+1);
mf=length(f);
DATAw=zeros(mt,n);
DATAfft=zeros(mf,n);
DATAw(:,1)=td;
DATAfft(:,1)=f';
%% Noesis Parameters
Nm=20+N;
Nn=2;
Noe=zeros(Nm,Nn);
Noe(:,1)=1:Nm;
%Fictitious Channel
Noe(1,2)=1;
%Start Time
Noe(2,2)=0;
```

```
%Sampling Rate
Noe(3,2)=fs/1000;
%Number of Samples
Noe(20,2)=N;
%n-1 columns to calculate
for i=2:n
    status=strcat('Data Number: ',num2str(i-1));
    display(status),
    xf=[SS(:,1),SS(:,i)];
    %% Interpolation
    if askI==1
        [NDTi]=NDTinterp(td',xf);
    else
        [NDTi]=xf;
    end
    %%
    n=ceil(log(mt)/log(2));
    bits=2^n;
    WV=zeros(bits,1);
    WV(1:mt)=NDTi(:,2);
%-------------------------------------------------
    %% Choose Units for Plot (Amplitude)
% Units (Change both if needed)
    nd=ndatasets;
    typ=typsets;
    nplot=i-1;
if typ==1
    if nplot<=nd*3
        ylbl=' [m/s^2]';
    elseif nplot>nd*3 && nplot<=(2*nd*3)
        ylbl=' [m]';% For Amplitude plot
    else
        ylbl=' [m/s]';
    end
elseif typ==2
    if nplot<=(nd*3)%3 components
        ylbl=' [m]';% For Amplitude plot
    else
        ylbl=' [m/s]';
    end
%     elseif typ==2
%     if nplot<=(nd*3)%3 components
%         ylbl=' [m/s^2]';% For Amplitude plot
%     else
%         ylbl=' [m/s]';
%     end
else
    ylbl=' [m/s]';% For Amplitude plot
end
    %% ---- PLOT INTERPOLATION
    close all,
    figureI=figure('units','normalized','outerposition',[0 0 1 1],'Color',[1 1
1]);
    axesI = axes('Parent',figureI,...
        'FontWeight','bold',...
        'FontSize',20,...
        'FontName','Arial');
    box(axesI,'on');
    hold(axesI,'all');
    ylblf=strcat('Amplitude ',ylbl);
    plot(NDTi(:,1),NDTi(:,2),'-x','Parent',axesI,'LineWidth',1.5),hold
all,plot(xf(:,1),xf(:,2),'Parent',axesI,'LineWidth',1.5)
```

```
    title('Waveform
Interpolation','FontWeight','bold','FontSize',30,'FontName','Arial')
    xlabel('Time [\mus]','FontWeight','bold','FontSize',26,'FontName','Arial')
    ylabel(ylblf,'FontWeight','bold','FontSize',26,'FontName','Arial')
    xlim([NDTi(1,1) NDTi(end,1)])
    legend('Interpolated','Original')
%% ----------------------FFT Calculation--------------------------------
    s=NDTi(:,2);
    FFTA=abs(fft(s,NFFT));%/N This use to normalize without it is what NOEISIS
does
    % Cut Size to Half
    FFTA=abs(FFTA(1:NFFT/2+1))/N;
    FFTA=FFTA/(max(FFTA));

    %% -------------SHORT TIME FOURIER TRANSFORM CALCULATION------------

    LENX = N;
    sampling_rate = delta;
    step_dist = 10;
    padding = 51200;
    IMGY = 25600;
    t=linspace(0,(sampling_rate*(LENX-1)),LENX);
    tp=[0:(step_dist*sampling_rate):(sampling_rate*(LENX-1))];

    window_length = 800;
    window = 3;
    ystft = STFT(NDTi(:,2), sampling_rate, window, window_length, step_dist,
padding);
    EEsf = ystft';

    freqsf = (1/sampling_rate)/2;
    freqp=(0:(freqsf/(IMGY-1)):freqsf);
    EEsf=EEsf/max(max(EEsf));

    %% --------- PLOT ALL ------------------
    %Convert NDTi(:,1) to ?s
    %Convert tp to to ?s
    %Convert f to kHz
    WVAplot(NDTi(:,1)*1e6,NDTi(:,2), tp*1e6, freqp/1000, EEsf, tpfreq, FFTA,
f/1000,foutn, askS,i-1,nd,typsets)
    %% ------------
%     clear dummy
%     dummy=waitforbuttonpress;close all;
    DATAw(:,i)=NDTi(:,2);
    DATAfft(:,i)=FFTA;
end
%DATA EXPORT
if askS==1
    fout1=strcat(foutn,'_waves.txt');
    fout2=strcat(foutn,'_fft.txt');
    save(fout1,'-ascii','DATAw')
    save(fout2,'-ascii','DATAfft')
end
```

```
function [NDTi]=NDTinterp(Tdomain,NDT)
```

```
%Author:  Jefferson A Cuadra
%NDT Interpolation Parameters
[m]=length(Tdomain);
NDTi=zeros(m,2);
%Column 1: NDT time
%Column 2: NDT parameter
%Code starts to interpolates
for k=1:m
    if NDT(end,1)<=Tdomain(k)
        NDTi(k,1)=NDT(end,1);
        NDTi(k,2)=NDT(end,2);
    else
        [r,~]=find(NDT(:,1)>Tdomain(k),1,'first');
        NDTi(k,1)=Tdomain(k,1);
        NDTi(k,2)=(((NDT(r,2)-NDT(r-1,2))/(NDT(r,1)-NDT(r-1,1)))*(Tdomain(k)-
NDT(r-1,1)))+NDT(r-1,2);
    end
end
end
```

```
function y = STFT(x, sampling_rate, window, window_length, step_dist, padding)
%
%  y = STFT(x, sampling_rate, window, window_length, step_dist, padding)
%
%  STFT produces a TF image of "x".
%  The output is also stored in "y".
%
%  For "window", use one of the following inputs:
%  rectangular    = 1
%  Hamming        = 2
%  Hanning        = 3
%  Blackman-Tukey = 4
%
%  The time scale is associated with the center of the window,
%  if the window is of odd length.  Otherwise, the window_length/2
%  is used.  "Step_dist" determines the stepping distance between the number
%  of samples, and is arranged to maintain the proper time index
%  provided by "sampling_rate" in seconds.  "Padding" is the
%  total length of the windowed signal before the fft, which is
%  accomplished by zero padding.
%
%  Developed by Timothy D. Dorney
%               Rice University
%               April, 1999
%               tdorney@ieee.org
%
%  Coded using MATLAB 5.X.X.
%
%   REVISION HISTORY
%
%   VERSION 1.0.0       APR. 21, 1999   TIM DORNEY
%

if (nargin ~= 6)
        disp('STFT requires 6 input arguments!')
    return
```

```
end
if ((window < 1) | (window > 4))
    window = 1;
    disp('The argument "window" must be between 1-4, inclusively.  Window set
to 1!');
end
if ((step_dist < 1) | (round(step_dist) ~= step_dist))
    step_dist = 1;
    disp('The argument "step_dist" must be an integer greater than 0.
Step_dist set to 1!');
end
if (sampling_rate <= 0)
    disp('The argument "sampling_rate" must be greater than 0.');
    return
end
if (padding < window_length)
    padding = window_length;
    disp('The argument "padding" must be non-negative.  Padding set to
"window_length"!');
end

if (window == 1)
    WIN = ones(1,window_length);
elseif (window == 2)
    WIN = hamming(window_length)';
elseif (window == 3)
    WIN = hanning(window_length)';
elseif (window == 4)
    WIN = blackman(window_length)';
end

[m,n] = size(x);
if (m ~= 1)
    X = x';
else
    X = x;
end
[m,n] = size(X);
if (m ~= 1)
    disp('X must be a vector, not a matrix!');
    return
end

LENX = length(X);
IMGX = ceil(LENX/step_dist);
if (padding/2 == round(padding/2))
    IMGY = (padding/2) + 1;
else
    IMGY = ceil(padding/2);
end

y = zeros(IMGX,IMGY);

if (window_length/2 == round(window_length/2))
    CENTER = window_length/2;
    x_pad_st = window_length - CENTER - 1;
    x_pad_fi = window_length - CENTER;
else
    CENTER = (window_length+1)/2;
    x_pad_st = window_length - CENTER;
    x_pad_fi = window_length - CENTER;
end
```

```
X = [zeros(1,x_pad_st) X zeros(1,x_pad_fi)];

iter = 0;
for kk = 1:step_dist:LENX
    iter = iter + 1;
    XX = X(kk:(kk + window_length - 1));
    YY = XX .* WIN;
    ZZ = abs(fft(YY, padding));
    y(iter,:) = ZZ(1:IMGY);
end

% freq = (1/sampling_rate)/2;
% imagesc([0:(step_dist*sampling_rate):(sampling_rate*(LENX-1))], ...
%   [0:(freq/(IMGY-1)):freq],y');
% xlabel('Time (seconds)');
% ylabel('Frequency (Hz)');
% axis('xy')
```

```
function WVAplot(X, Y, tsf, freqsf, cdata1, fp, FFTA, FFTF, PName, askP,
nplot,nd,typ)
%%
%Author:  Jefferson A. Cuadra
% March 23, 2015
%CREATEFIGURE(X1, Y1, CDATA1, X2, Y2)
%  X:  Time History in ?s
%  Y:  Signal Amplitude (usually m/s)
%  cdata1:  Power Density Data
%  tsf:   Short Time Fourier Transform (SFFT) Time
%  freqsf: STFT Frequency
%  fp:    Max frequency for plotting
%  FFTA:  Normalized FFT Amplitude
%  FFTF:  Frequency Range
%  askP:  Yes or No Plot
%  nplot: Number of plot (from Data number)
%% Units (Change both if needed)
if typ==1
    if nplot<=nd*3
        Unit=' m/s^2';
        Unitp=' [m/s^2]';
    elseif nplot>nd*3 && nplot<=(2*nd*3)
        Unit=' m';% For Textbox
        Unitp=' [m]';% For Amplitude plot
    else
        Unit=' m/s';
        Unitp=' [m/s]';
    end
elseif typ==2
    if nplot<=(nd*3)
        Unit=' m';% For Textbox
        Unitp=' [m]';% For Amplitude plot
    else
        Unit=' m/s';
        Unitp=' [m/s]';
    end
%     elseif typ==2
%     if nplot<=(nd*3)
```

```
%         Unit=' m/s^2';% For Textbox
%         Unitp=' [m/s^2]';% For Amplitude plot
%     else
%         Unit=' m/s';
%         Unitp=' [m/s]';
%     end
else
    Unit=' m/s';% For Textbox
    Unitp=' [m/s]';% For Amplitude plot
end
%% JPEG LETTER SIZE AND RESOLUTION
% The lower the number the bigger the axes letters and clearer
xrs=8.12; % this horizontal size is in inches
yrs=5; % this vertical size is in inches
rsz=1.75;
dpi=500;
%%
% Create figure

figure1=figure('units','normalized','outerposition',[0 0 1 1],'Color',[1 1 1]);
%
%
% Create axes
axes1 = axes('Parent',figure1,'XTick',zeros(1,0),...
    'Position',[0.13 0.562962962962963 0.494202898550725 0.362037037037037],...
    'FontWeight','bold',...
    'FontSize',20,...
    'FontName','Arial');
box(axes1,'on');
hold(axes1,'all');
%% Uncomment the following line to preserve the X-limits of the axes
% xlim(axes1,[0 12]);

% Create plot
plot(X,Y,'Parent',axes1,'Parent',axes1,'LineWidth',1.5);

% Create xlabel
xlabel('Time [\mus]','FontWeight','bold','FontSize',26,'FontName','Arial');

% Create ylabel
ylb=strcat('Amplitude ',Unitp);
ylabel(ylb,'FontWeight','bold','FontSize',26,...
    'FontName','Arial');

% Create axes
% Create axes
% Create axes
tscl=5;
stps=fp/5;
scl=0+(stps):stps:fp;
axes2 = axes('Parent',figure1,'YTick',scl,...
    'YDir','reverse',...
    'Position',[0.13 0.19 0.494202898550725 0.372962962962963],...
    'Layer','top',...
    'FontWeight','bold',...
    'FontSize',20,...
    'FontName','Arial');
box(axes2,'on');
hold(axes2,'all');
%% Uncomment the following line to preserve the X-limits of the axes
% xlim(axes2,[0.240909090909091 12.0590909090909]);
%% Uncomment the following line to preserve the Y-limits of the axes
```

```
% ylim(axes2,[0.0386839512395976 0.461844930418374]);

% Create image
imagesc(tsf, ...
    freqsf,...
    cdata1,'Parent',axes2,'CDataMapping','scaled');

% Create xlabel
xlabel('Time [\mus]','FontWeight','bold','FontSize',26,'FontName','Arial');

% Create ylabel
ylabel('Frequency [kHz]','FontWeight','bold','FontSize',26,...
    'FontName','Arial');
xlim(axes2,[0 tsf(end)]);
ylim(axes2,[0 fp]);

% colorbar('peer',axes1,...
%     [0.924574209245742 0.142962962962963 0.0216274668829413
0.777777777777778],...
%     'FontWeight','bold',...
%     'FontSize',22,...
%     'FontName','Arial');

% Create axes
% Create axes
axes3 = axes('Parent',figure1,'YDir','reverse','YTick',zeros(1,0),...
    'Position',[0.644554462428156 0.191481481481481 0.223247646249866
0.368518518518519],...
    'FontWeight','bold',...
    'FontSize',20,...
    'FontName','Arial');
box(axes3,'on');
hold(axes3,'all');
%% Uncomment the following line to preserve the X-limits of the axes
ylim(axes3,[0 fp]);

% Create plot
plot(FFTA,FFTF,'Parent',axes3,'Parent',axes3,'LineWidth',1.5);

% Create xlabel
xlabel('|FFT Amplitude|','FontWeight','bold','FontSize',26,...
    'FontName','Arial');

%% Calculate data in the created textbox
RMSv=rms(Y);
amp=max(Y);
[En,np]=EDYNFEM(X,Y);
% Dur=max(abs(X(end)-X(1)));

Enlb=strcat('Energy : ',num2str(En),Unit,'\cdot', 's x [GF]');
RMSlb=strcat('RMS : ',num2str(RMSv),Unit);
Amplb=strcat('Amplitude : ',num2str(amp),Unit);
Colb=strcat('Counts : ',num2str(np));

annotation(figure1,'textbox',...
    [0.645531911119777 0.57189773844641 0.353633364339321
0.339259259259254],...
    'String',{Enlb,'',RMSlb,'',Amplb,'',Colb},...
    'FontWeight','bold',...
    'FontSize',18,...
    'FontName','Arial',...
```

```
    'FitBoxToText','off',...
    'LineStyle','none');
if askP==1
    nplotb=num2str(nplot);
    plotname=strcat(PName,nplotb,'.png');
    dpin=strcat('-r',num2str(dpi));
    set(figure1,'PaperUnits','inches','PaperPosition',[0 0 xrs*rsz yrs*rsz])
    % set(figure1,'units','normalized','OuterPosition',[0 0 1 1])
    print(figure1,'-dpng', plotname, dpin)
    %     saveas(figure1,plotname,'emf')
end

end
```

```
function [En,np]=EDYNFEM(xs,ys)
% Author:  Jefferson Cuadra
% 03/10/2015
% Function calculates Energy and number of peaks (Counts)
% Energy: Area under the curve, Units [amplitude sec {GF} ] - GF is the
% gain factor of units [amp/V]
[sp,lp]=findpeaks(ys);
np=length(sp);
tp=xs(lp);
yp=ys(lp);
Earx=[xs(1) tp' tp(end) xs(1)];
Eary=[ys(1) yp' 0 ys(1)];
En=polyarea(Earx/1e6,Eary);
end
```

LIST OF REFERENCES

1. *ASTM E976-10, Standard Guide for Determining the Reproducibility of Acoustic Emission Sensor Response, ASTM International, West Conshohocken, PA, 2010,* www.astm.org.

2. *Acoustic Emission Testing*. Third ed. Nondestructive Testing Handbook, ed. P. Moore. Vol. 6. 2005.

3. *Acoustic Emission Testing*. Basics for Research-Applications in Civil Engineering, ed. C. Grosse and M. Ohtsu. 2008: Springer Berlin Heidelberg.

4. Ono, K., *Acoustic emission*, in *Springer Handbook of Acoustics*. 2014, Springer. p. 1209-1229.

5. Bently, P.G., *A review of acoustic emission for pressurised water reactor applications.* NDT International, 1981. **14**(6): p. 329-335.

6. Jayakumar, T., et al., *A review of the application of acoustic emission techniques for monitoring forming and grinding processes.* Journal of Materials Processing Technology, 2005. **159**(1): p. 48-61.

7. Kaphle, M.R., et al. *Study of acoustic emission data analysis tools for structural health monitoring applications*. in *Progress in Acoustic Emission XV: Proceedings of the 20th International Acoustic Emission Symposium*. 2010. Japanese Society for Non-Destructive Inspection.

8. Ono, K., *Application of acoustic emission for structure diagnosis.* Diagnostyka, 2011: p. 3-18.

9. Lopez, I. and N. Sarigul-Klijn, *A review of uncertainty in flight vehicle structural damage monitoring, diagnosis and control: Challenges and opportunities.* Progress in Aerospace Sciences, 2010. **46**(7): p. 247-273.

10. Wadley, H. and R. Mehrabian, *Acoustic emission for materials processing: a review.* Materials Science and Engineering, 1984. **65**(2): p. 245-263.

11. Kaphle, M.R., et al., *Review: acoustic emission technique-opportunities, challenges and current work at QUT.* 2011.

12. Lindgren, E., Buynak Charles *Materials state awareness for structures needs and challenges*. in *12th International Symposium on Nondestructive Characterization of Materials*. 2011. Blacksburg, VA.

13. Nair, A. and C. Cai, *Acoustic emission monitoring of bridges: Review and case studies.* Engineering structures, 2010. **32**(6): p. 1704-1714.

14. Boller, C., *Next generation structural health monitoring and its integration into aircraft design.* International Journal of Systems Science, 2000. **31**(11): p. 1333-1349.

15. Dixon, M.C., *The maintenance costs of aging aircraft: insights from commercial aviation*. Vol. 486. 2006: Rand Corporation.

16. System, I.S.H.M. *Fiber optic structural health monitoring system installed on the Indian River Inlet Bridge in Delaware*. 2009 [cited 2015; Available from: https://www.facebook.com/IRIBSHMS.

17. Laboratory, S.D.a.A.S. *Dynamic stress/strain prediction for structural health monitoring and system load prediction*. 2007 [cited 2015; Available from: http://sdasl.uml.edu/Research/Areas/Dynamic_StressStrain_Load_Prediction_StructHealth.htm.

18. Aeronautics, A.H.R.D.i. *Structural Health Monitoring of Composites*. 2015 [cited 2015; Available from: http://aeronautics.sd.tmu.ac.jp/en/research_facilities/structures.html.

19. Wilcox, P.D., et al., *Progress towards a forward model of the complete acoustic emission process.* Advanced Materials Research, 2006. **13**: p. 69-76.

20. Sause, M.G.R. and S. Horn, *Simulation of Lamb Wave Excitation For Different Elastic Properties and Acoustic Emission Source Geomtries.* Journal of Acoustic Emission, 2010. **28**: p. 142-154.

21. Kostopoulos, V., et al., *On the identification of the failure mechanisms in oxide/oxide composites using acoustic emission.* NDT&E International, 2003. **36**: p. 571–580.

22. Loutas, T., et al., *Fatigue damage monitoring in carbon fiber reinforced polymers using the acousto-ultrasonics technique.* Polymer Composites, 2010. **31**(8): p. 1409-1417.

23. Koslowski, M., R. LeSar, and R. Thomson, *Avalanches and Scaling in Plastic Deformation.* Physical Review Letters, 2004. **93**: p. 125502-1 to 4.

24. Sause, M.G.R., et al., *Pattern recognition approach to identify natural clusters of acoustic emission signals.* Pattern Recognit Lett, 2012. **33**(1): p. 7-7.

25. Cuadra, J.A., *Damage Quantification in Fiber Reinforced Polymer Composites using a Hybrid Non-Destructive Testing Approach*, in *Mechanical Engineering & Mechanics*. 2012, Drexel University.

26. Vanniamparambil, P.A., et al., *An integrated structural health monitoring approach for crack growth monitoring.* Journal of Intelligent Material Systems and Structures, 2012.

27. Chung, J.-B. and E. Kannatey - Asibo, *Accoustic Emission from Plastic Deformation of a Pure single Crystal.* Journal of Applied Physics, 1992. **72**.

28. Prosser, W.H., et al., *Finite element and plate theory modeling of acoustic emission waveforms.* Journal of Nondestructive Evaluation, 1999. **18**(3): p. 83-90.

29. Ohtsu, M. and K. Ono, *AE source location and orientation determination of tensile cracks from surface observation.* NDT International, 1988. **21**(3): p. 143-150.

30. Prosser, W.H., et al., *Finite Element and Plate Theory Modeling of Acoustic Emission Waveforms.* Journal of Nondestructive Evaluation, 1999. **18**(3): p. 83-90.

31. Ouyang, C., E. Landis, and S.P. Shah, *Damage Assessment in Concrete Using Quantitative Acoustic Emission.* Journal of Engineering Mechanics, 1991. **117**(11): p. 2681-2698.

32. Shull, P.J., *Nondestructive evaluation: theory, techniques, and applications*. Vol. 142. 2002: CRC.

33. Prakash, R., *Non-Destructive Testing Techniques*. 2009: New Age Science.

34. Miller, R.K. and P. McIntire, *Nondestructive Testing Handbook. Vol. 5: Acoustic Emission Testing.* American Society for Nondestructive Testing, 4153 Arlingate Plaza, Caller# 28518, Columbus, Ohio 43228, USA, 1987. 603, 1987.

35. Center, N.R. *NDT Course Material*. [cited 2014 November 14].

36. Gautschi, G., *Piezoelectric sensorics: force, strain, pressure, acceleration and acoustic emission sensors, materials and amplifiers*. 2002: Springer.

37. Hellier, C., *Handbook of Nondestructive Evaluation*. 2003, McGraw-Hill.

38. Ohtsu, M., *Acoustic emission theory for moment tensor analysis.* Research in Nondestructive Evaluation, 1995. **6**(3): p. 169-184.

39. *Theory-AE Sources*. NDT Resource Center, 2014.

40. Fowler, T.J. *Acoustic Emission Testing of Fiber Reinforced Plastics*. in *ASCE Fall Convention and Exhibit*. 1977. San Francisco, CA.

41. Dunegan, H., Harris, D., Tetelman, A., *Detection of Fatigue Crack Growth by Acoustic Emission Techniques.* Materials Evaluation, 1970. **28**(10).

42. Roberts, T.M. and M. Talebzadeh, *Acoustic emission monitoring of fatigue crack propagation.* Journal of Constructional Steel Research, 2003. **59**(6): p. 695-712.

43. Scala, C.M. and R.A. Coyle, *Acoustic emission waveform analysis to identify fatigue crack propagation in a mirage aircraft: Journal of Acoustic Emission, Vol. 6, No. 4, pp. 249–256 (Oct.–Dec. 1987).* NDT & E International, 1992. **25**(6): p. 304.

44. Muránsky, O., et al., *Investigation of deformation twinning in a fine-grained and coarse-grained ZM20 Mg alloy: Combined in situ neutron diffraction and acoustic emission.* Acta Materialia, 2010. **58**(5): p. 1503-1517.

45. Hazeli, K., et al., *In situ identification of twin-related bands near yielding in a magnesium alloy.* Scripta Materialia, 2013. **68**(1): p. 83-86.

46. Li, H., et al., *Non-destructive examination of interfacial debonding using acoustic emission.* Dental Materials, 2011. **27**(10): p. 964-971.

47. Yuyama, S., et al., *Detection and evaluation of failures in high-strength tendon of prestressed concrete bridges by acoustic emission.* Construction and Building Materials, 2007. **21**(3): p. 491-500.

48. Jihan, S., A.M. Siddiqui, and M.A.S. Sweet, *Fracture strength of E-glass fibre strands using acoustic emission.* NDT & E International, 1997. **30**(6): p. 383-388.

49. Qi, G., et al., *Discrete wavelet decomposition of acoustic emission signals from carbon-fiber-reinforced composites.* Composites Science and Technology, 1997. **57**(4): p. 389-403.

50. Gutkin, R., et al., *On acoustic emission for failure investigation in CFRP: Pattern recognition and peak frequency analyses.* Mechanical Systems and Signal Processing, 2011. **25**(4): p. 1393-1407.

51. Bassim, M.N., S.S. Lawrence, and C.D. Liu, *Detection of the onset of fatigue crack growth in rail steels using acoustic emission.* Engineering Fracture Mechanics, 1994. **47**(2): p. 207-214.

52. Berkovits, A. and D. Fang, *Study of fatigue crack characteristics by acoustic emission.* Engineering Fracture Mechanics, 1995. **51**(3): p. 401-416.

53. Prasad, M.S.S., C.S. Venkatesha, and T. Jayaraju, *Experimental Methods of Determining Fracture Toughness of Fiber Reinforced Polymer Composites under Various Loading Conditions.* 2011. **10**(13): p. 1263-1275.

54. Roberts, T. and M. Talebzadeh, *Acoustic emission monitoring of fatigue crack propagation.* Journal of Constructional Steel Research, 2003. **59**(6): p. 695-712.

55. Miguel, M.-C., et al., *Intermittent dislocation flow in viscoplastic deformation.* Nature, 2001. **410**: p. 667-671.

56. Richeton, T., et al., *On the critical character of plasticity in metallic single crystals.* Materials Science and Engineering A, 2006. **424**: p. 190–195.

57. Vinogradov, A., S. Hashimoto, and S. Miura, *Effect of Grain Boundry on Accostic Emmision During Plastic Deformation of Copper-Aluminium Bicrystals.* Acta Materialia, 1996. **44**: p. 2883-2890.

58. Cuadra, J., et al., *Damage quantification in polymer composites using a hybrid NDT approach.* Composites Science and Technology, 2013. **83**(0): p. 11-21.

59. Mal, a., *A Conceptual Structural Health Monitoring System based on Vibration and Wave Propagation.* Structural Health Monitoring, 2005. **4**(3): p. 283-293.

60. Banerjee, S., A.K. Mal, and W.H. Prosser, *Analysis of transient Lamb waves generated by dynamic surface sources in thin composite plates.* The Journal of the Acoustical Society of America, 2004. **115**(5): p. 1905-1905.

61. Kundu, T., S. Das, and K.V. Jata, *Point of impact prediction in isotropic and anisotropic plates from the acoustic emission data.* The Journal of the Acoustical Society of America, 2007. **122**(4): p. 2057-66.

62. Vanniamparambil, P.A., et al., *A data fusion approach for progressive damage quantification in reinforced concrete masonry walls.* Smart Materials and Structures, 2014. **23**(1): p. 015007.

63. Yu, J., et al., *Prediction of fatigue crack growth in steel bridge components using acoustic emission.* Journal of Constructional Steel Research, 2011. **67**(8): p. 1254-1260.

64. Zárate, B.A., et al., *Probabilistic Prognosis of Fatigue Crack Growth Using Acoustic Emission Data.* 2012(September): p. 1101-1111.

65. Farrar, C., R and K. Worden, *An introduction to structural health monitoring.* Philosophical Transactions of the Royal Society, 2007. **365**: p. 303-315.

66. Alan, V.O., W.S. Ronald, and R. John, *Discrete-time signal processing.* New Jersey, Printice Hall Inc, 1989.

67. Vanniamparambil, P.A., *A novel cross-validated nondestructive evaluation framework for damage detection using acoustic emission*, in *Mechancal Engineering and Mechanics*. 2014, Drexel University: Philadelphia.

68. Hamstad, M., *Comparison of wavelet transform and Choi-Williams distribution to determine group velocities for different acoustic emission sensors.* Journal of Acoustic Emission, 2008. **26**: p. 40-59.

69. Hamstad, M., *On lamb modes as a function of acoustic emission source rise time.* Journal of Acoustic Emission, 2010. **28**: p. 41-58.

70. Sause, M.G., M.A. Hamstad, and S. Horn, *Finite element modeling of conical acoustic emission sensors and corresponding experiments.* Sensors and Actuators A: Physical, 2012. **184**: p. 64-71.

71. Cohen, L., *Time-frequency analysis*. Vol. 1406. 1995: Prentice Hall PTR Englewood Cliffs, NJ:.

72. Papandreou-Suppappola, A., *Applications in time-frequency signal processing*. Vol. 10. 2010: CRC press.

73. Rubio, E., R. Teti, and I. Baciu. *Advanced signal processing in acoustic emission monitoring systems for machining technology*. in *Intelligent Production Machines and Systems-2nd I* PROMS Virtual International Conference 3-14 July 2006*. 2011. Elsevier.

74. Worden, K., G. Manson, and N.R.J. Fieller, *Damage detection using outlier analysis.* Journal of Sound and Vibration, 2000. **229**(Compendex): p. 647-667.

75. Rizzo, P., et al., *Wavelet-based outlier analysis for guided wave structural monitoring: Application to multi-wire strands.* Journal of Sound and Vibration, 2007. **307**: p. 52-68.

76. Sohn, H., et al., *Structural Health Monitoring using statistical pattern recognition techniques.* Jounnal of Dynamic Systems, Measurement and Control, 2001. **123**: p. 706-711.

77. Kaphle, M., et al., *A Study on the Use of Acoustic Emission Technique as a Structural Health Monitoring Tool*, in *Engineering Asset Management and Infrastructure Sustainability*. 2012, Springer. p. 459-469.

78. Adams, D., *Health monitoring of structural materials and components: methods with applications*. 2007: John Wiley & Sons.

79. Vanniamparambil, P.A., *A Novel Cross-Validated Nondestructive Evaluation Framework for Damage Detection using Acoustic Emission*, in *Mechanical Engineering and Mechanics*. 2014, Drexel University: Philadelphia, PA.

80. Ohtsu, M. and K. Ono, *A Generalized Theory of Acoustic Emission and Green's Function in a Half Space.* Journal of Acoustic Emission, 1984. **3**: p. 27-40.

81. Naber, R.R., H. Bahai, and B.E. Jones, *A reciprocal band-limited Green's function approach for modelling acoustic emission using finite element method.* Journal of Sound and Vibration, 2006. **292**: p. 802-823.

82. Rice, J.R., *Elastic Wave Emission from Damage Processes.* Journal of Nondestructive Evaluation, 1980. **1**(4): p. 215-224.

83. Achenbach, J., *Wave propagation in elastic solids*. 2012: Elsevier.

84. Rose, J.L., *Ultrasonic waves in solid media*. 2004: Cambridge university press.

85. Rice, J., *Elastic wave emission from damage processes.* Journal of Nondestructive Evaluation, 1980. **1**(4): p. 215-224.

86. Derode, A., et al., *How to estimate the Green's function of a heterogenous medium between two passive sensors? Application to acoustic wavesq.* Applied Physics Letter, 2003. **83**(15): p. 3054-3056.

87. Wapenaar, K., J. Fokkema, and R. Snieder, *Retrieving the Green's function in an open system by cross correlation: A comparison of approaches (L).* Journal of Acoustic Society of America, 2005. **118**(5): p. 2783-2786.

88. Giordano, M., L. Condelli, and L. Nicolais, *Acoustic emission wave propagation in a viscoelastic plate.* 1999. **59**: p. 1735-1743.

89. Minozzi, M., et al., *Dynamic fracture model for acoustic emission.* The European Physical Journal B, 2003. **36**: p. 203-207.

90. Landa, M., et al., *Acoustic Emission Sources By Atomistic Simulations.* Journal of Acoustic Emission, 2002. **20**: p. 25-38.

91. Ono, K., H. Cho, and T. Matsuo, *Transfer functions of acoustic emission sensors.* J. Acoust. Emiss, 2008. **26**: p. 72-90.

92. Holian, B.L. and R. Ravelo, *Fracture simulations using large-scale molecular dynamics.* Physical Review B, 1995. **51**(17): p. 11275.

93. Hora, P., et al., *Stress wave radiation from brittle crack extension by molecular dynamics and FEM.* 2013.

94. Uhnáková, A., et al., *Stress wave radiation from the cleavage crack extension in 3D bcc iron crystals.* Computational Materials Science, 2010. **50**(2): p. 678-685.

95. Wilcox, P.D., et al. *Progress towards a forward model of the complete acoustic emission process*. in *Advanced Materials Research*. 2006. Trans Tech Publ.

96. Wilcox, P.D., et al. *Quantitative structural health monitoring using acoustic emission*. in *Smart Structures and Materials*. 2006. International Society for Optics and Photonics.

97. Sause, M.G. and S. Richler, *Finite Element Modelling of Cracks as Acoustic Emission Sources.* Journal of Nondestructive Evaluation, 2015. **34**(1): p. 1-13.

98. Silling, S.A. and E. Askari, *A meshfree method based on the peridynamic model of solid mechanics.* Computers & Structures, 2005. **83**(17–18): p. 1526-1535.

99. Krueger, R., *Virtual crack closure technique: history, approach, and applications.* Applied Mechanics Reviews, 2004. **57**(2): p. 109-143.

100. Hillerborg, A., M. Modéer, and P.E. Petersson, *Analysis of crack formation and crack growth in concrete by means of fracture mechanics and finite elements.* Cement and Concrete Research, 1976. **6**(6): p. 773-781.

101. Rice, J., *Thermodynamics of the quasi-static growth of Griffith cracks.* Journal of the Mechanics and Physics of Solids, 1978. **26**(2): p. 61-78.

102. Chaboche, J.-L., *Continuum damage mechanics: Part II—Damage growth, crack initiation, and crack growth.* Journal of applied mechanics, 1988. **55**(1): p. 65-72.

103. Wang, H., et al., *A constitutive model of twinning and detwinning for hexagonal close packed polycrystals.* Materials Science and Engineering: A, 2012. **555**: p. 93-98.

104. Gain, A.L., et al., *A hybrid experimental/numerical technique to extract cohesive fracture properties for mode-I fracture of quasi-brittle materials.* International Journal of Fracture, 2011. **169**(2): p. 113-131.

105. Park, K. and G.H. Paulino, *Computational implementation of the PPR potential-based cohesive model in ABAQUS: Educational perspective.* Engineering Fracture Mechanics, 2012. **93**: p. 239-262.

106. Elices, M., et al., *The cohesive zone model: advantages, limitations and challenges.* Engineering Fracture Mechanics, 2002. **69**(2): p. 137-163.

107. Réthoré, J., S. Roux, and F. Hild, *An extended and integrated digital image correlation technique applied to the analysis of fractured samples: The equilibrium gap method as a mechanical filter.* European Journal of Computational Mechanics/Revue Européenne de Mécanique Numérique, 2009. **18**(3-4): p. 285-306.

108. *ASTM E1316-04, Standard Terminology for Nondestructive Examinations, ASTM International, West Conshohocken, PA, 2004,* www.astm.org.

109. Muravin, B., *Physical principals of acousti emission,* S.M.o.A.i. Metals, Editor. 2011: Israel.

110. Heiple, C. and S. Carpenter, *Acoustic emission produced by deformation of metals and alloys-A review.* Journal of Acoustic Emission, 1987. **6**: p. 177-204.

111. Godinez, V., *AE and applications,* L.o.A. Energy, Editor. 2012, Physical Acoustics - MISTRAS Group: Philadelphia, PA.

112. Broberg, K.B., *Cracks and fracture*. 1999: Academic Press.

113. Anderson, T.L., *Fracture mechanics: fundamentals and applications*. 2005: CRC press.

114. Cotterell, B., *The past, present, and future of fracture mechanics.* Engineering fracture mechanics, 2002. **69**(5): p. 533-553.

115. Sethian, J.A., *Level set methods and fast marching methods: evolving interfaces in computational geometry, fluid mechanics, computer vision, and materials science*. Vol. 3. 1999: Cambridge university press.

116. Wells A. A., *The condition of fast fracture in aluminum alloys with particular reference to comet failure,* in *British Welding Research Association*. 1955.

117. Winne, D. and B. Wundt, *Application of the Griffith-Irwin theory of crack propagation to the bursting behavior of disks, including analytical and experimental studies.* Trans. ASME, 1958. **80**(8): p. 1643-1658.

118. Irwin, G., *Analysis of stresses and strains near the end of a crack traversing a plate.* Journal of Applied Mechanics, 1957. **24**: p. 361-364.

119. Rice, J.R. and G.F. Rosengren, *Plane strain deformation near a crack tip in a power-law hardening material.* Journal of the Mechanics and Physics of Solids, 1968. **16**(1): p. 1-12.

120. Rice, J.R., *A path independent integral and the approximate analysis of strain concentration by notches and cracks.* Journal of applied mechanics, 1968. **35**(2): p. 379-386.

121. Hutchinson, J., *Singular behaviour at the end of a tensile crack in a hardening material.* Journal of the Mechanics and Physics of Solids, 1968. **16**(1): p. 13-31.

122. A., W.A. *Unstable Crack Propagation in Metals: Cleavage and Fast Fracture*. in *Proceedings of the Crack Propagation Symposium*. 1961. Cranfield, UK.

123. Freund, L.B., *The Initial Wave Front Emitted by a Suddenly Extending Crack in an Elastic Solid.* Journal of Applied Mechanics, 1972. **39**(2): p. 601-602.

124. Aki, K. and P. Richards, *1980: Quantitative Seismology: Theory and Methods.* Volume I: WH Freeman & Co.

125. Lysak, M., *Development of the theory of acoustic emission by propagating cracks in terms of fracture mechanics.* Engineering fracture mechanics, 1996. **55**(3): p. 443-452.

126. Andreykiv, O., et al., *Acoustic emission estimation of crack formation in aluminium alloys.* Engineering Fracture Mechanics, 2010. **77**(5): p. 759-767.

127. Belikov, V.T., *Modeling of acoustic-emission processes in a solid.* Russian Journal of Nondestructive Testing, 2008. **44**(6): p. 429-435.

128. Khalifa, W.B., et al., *Analytical modelling of acoustic emission from buried or surface-breaking cracks under stress.* Journal of Physics: Conference Series, 2012. **353**: p. 012016-012016.

129. Auld, B.A., *Acoustic fields and waves in solids*. 1973: Рипол Классик.

130. Promboon, Y., *Acoustic emission source location.* 2000.

131. Southampton, U.o. *Animations of Acoustic Waves*. 2015 [cited 2015; Available from:

http://resource.isvr.soton.ac.uk/spcg/tutorial/tutorial/Tutorial_files/Web-further-dispersive.htm.

132. Aggelis, D., E. Kordatos, and T. Matikas, *Acoustic emission for fatigue damage characterization in metal plates.* Mechanics Research Communications, 2011. **38**(2): p. 106-110.

133. Grondel, S., et al., *Fatigue crack monitoring of riveted aluminium strap joints by Lamb wave analysis and acoustic emission measurement techniques.* Ndt & E International, 2002. **35**(3): p. 137-146.

134. Bartoli, I., *Lamb Waves*, M.-L. 2, Editor. 2012, Drexel University: Philadelphia, PA.

135. Mazzotti, M., *Geometry scale and time domain of wave modes*, in *Power Point*, M.o.E.W. Propagation, Editor. 2015: Philadelphia, PA.

136. Cuadra, J., et al., *Acoustic emission source modeling using a data-driven approach.* Journal of Sound and Vibration, 2015. **341**(0): p. 222-236.

137. *ASTM E8 / E8M-13a, Standard Test Methods for Tension Testing of Metallic Materials, ASTM International, West Conshohocken, PA, 2013, www.astm.org.*

138. *ASTM E1820-13, Standard Test Method for Measurement of Fracture Toughness, ASTM International, West Conshohocken, PA, 2013, www.astm.org.*

139. Vanniamparambil, P.A., et al., *Novel optico-acoustic nondestructive testing for wire break detection in cables.* Structural Control and Health Monitoring, 2013. **20**(11): p. 1339-1350.

140. Vanniamparambil, P.A., et al. *In-situ acousto-ultrasonic monitoring of crack propagation in Al2024 alloy*. in *SPIE Smart Structures and Materials+ Nondestructive Evaluation and Health Monitoring*. 2012. International Society for Optics and Photonics.

141. Vanniamparambil, P.A., et al., *An integrated structural health monitoring approach for crack growth monitoring.* Journal of Intelligent Material Systems and Structures, 2012. **23**(14): p. 1563-1573.

142. Hazeli, K., et al., *In situ identification of twin-related bands near yielding in a magnesium alloy.* Scripta Materialia, 2013. **68**(1): p. 83-86.

143. Cuadra, J., et al., *Damage quantification in polymer composites using a hybrid NDT approach.* Composites Science and Technology, 2013. **83**: p. 11-21.

144. Chu, T., W. Ranson, and M. Sutton, *Applications of digital-image-correlation techniques to experimental mechanics.* Experimental mechanics, 1985. **25**(3): p. 232-244.

145. Hild, F. and S. Roux, *Digital Image Correlation: from Displacement Measurement to Identification of Elastic Properties – a Review.* Strain, 2006. **42**(2): p. 69-80.

146. McCormick, N. and J. Lord, *Digital Image Correlation.* Materials Today, 2010. **13**(12): p. 52-54.

147. Pan, B., *Recent progress in digital image correlation.* Experimental mechanics, 2011. **51**(7): p. 1223-1235.

148. Sutton, M.A., J.J. Orteu, and H.W. Schreier, *Image correlation for shape, motion and deformation measurements: basic concepts, theory and applications*. 2009: Springer Verlag.

149. Sutton, M.A., et al., *The effect of out-of-plane motion on 2D and 3D digital image correlation measurements.* Optics and Lasers in Engineering, 2008. **46**(10): p. 746-757.

150. Pan, B., et al., *Two-dimensional digital image correlation for in-plane displacement and strain measurement: a review.* Measurement science and technology, 2009. **20**: p. 062001.

151. Garcia, D., J. Orteu, and L. Penazzi, *A combined temporal tracking and stereo-correlation technique for accurate measurement of 3D displacements: application to sheet metal forming.* Journal of Materials Processing Technology, 2002. **125**: p. 736-742.

152. Orteu, J.-J., *3-D computer vision in experimental mechanics.* Optics and Lasers in Engineering, 2009. **47**(3–4): p. 282-291.

153. Sutton, M.A., J.-J. Orteu, and H.W. Schreier, *Image correlation for shape, motion and deformation measurements: basic concepts, theory and applications*. 2009: Springer.

154. Niendorf, T., et al., *Monitoring the fatigue-induced damage evolution in ultrafine-grained interstitial-free steel utilizing digital image correlation.* Materials Science and Engineering: A, 2009. **517**(1): p. 225-234.

155. Halim, H., D.S. Wilkinson, and M. Niewczas, *The Portevin–Le Chatelier (PLC) effect and shear band formation in an AA5754 alloy.* Acta Materialia, 2007. **55**(12): p. 4151-4160.

156. Lagattu, F., J. Brillaud, and M.-C. Lafarie-Frenot, *High strain gradient measurements by using digital image correlation technique.* Materials characterization, 2004. **53**(1): p. 17-28.

157. Broughton, W.R., et al., *An experimental assessment of open-hole tension–tension fatigue behaviour of a GFRP laminate.* Composites Part A: Applied Science and Manufacturing, 2011. **42**(10): p. 1310-1320.

158. Crevoisier, J., et al., *Identification of In Situ Frictional Properties of Bolted Assemblies with Digital Image Correlation.* Experimental mechanics, 2012. **52**(6): p. 561-572.

159. Vanniamparambil, P.A., U. Guclu, and A. Kontsos, *Identification of Crack Initiation in Aluminum Alloys using Acoustic Emission.* Experimental Mechanics, 2015: p. 1-14.

160. GOM-mbH, *ARAMIS User Manual - Software*, GOM-mbH, Editor. 2010: Braunshweig, Germany.

161. Felippa, C.A., *Introduction to finite element methods.* University of Colorado, Boulder, http://www.colorado.edu/engineering/CAS/courses.d/IFEM.d, 2004.

162. Rao, S.S., *The finite element method in engineering*. 2005: Butterworth-heinemann.

163. Dhatt, G., E. Lefrançois, and G. Touzot, *Finite element method*. 2012: John Wiley & Sons.

164. Nielsen, C., et al., *Modeling of Thermo-Electro-Mechanical Manufacturing Processes*. 2013: Springer.

165. Barenblatt, G.I., *The mathematical theory of equilibrium cracks in brittle fracture.* Advances in applied mechanics, 1962. **7**(1): p. 55-129.

166. Elices, M., et al., *The cohesive zone model: advantages, limitations and challenges.* Engineering fracture mechanics, 2002. **69**(2): p. 137-163.

167. Hillerborg, A., M. Modéer, and P.-E. Petersson, *Analysis of crack formation and crack growth in concrete by means of fracture mechanics and finite elements.* Cement and concrete research, 1976. **6**(6): p. 773-781.

168. Chandra, N., et al., *Some issues in the application of cohesive zone models for metal–ceramic interfaces.* International Journal of Solids and Structures, 2002. **39**(10): p. 2827-2855.

169. Rabinovitch, O., *Debonding analysis of fiber-reinforced-polymer strengthened beams: cohesive zone modeling versus a linear elastic fracture mechanics approach.* Engineering fracture mechanics, 2008. **75**(10): p. 2842-2859.

170. Song, S.H., *Fracture of asphalt concrete: a cohesive zone modeling approach considering viscoelastic effects*. 2006.

171. Kregting, R., *Cohesive zone models.* preprint, 2005.

172. Schwalbe, K.-H., I. Scheider, and A. Cornec, *Guidelines for applying cohesive models to the damage behaviour of engineering materials and structures*. 2013: Springer.

173. Klein, P., et al., *Physics-based modeling of brittle fracture: cohesive formulations and the application of meshfree methods.* Theoretical and Applied Fracture Mechanics, 2001. **37**(1): p. 99-166.

174. Feih, S., *Development of a user element in ABAQUS for modelling of cohesive laws in composite structures*. 2006.

175. Belytschko, T. and T. Black, *Elastic crack growth in finite elements with minimal remeshing.* International journal for numerical methods in engineering, 1999. **45**(5): p. 601-620.

176. Sukumar, N., et al., *Extended finite element method for three-dimensional crack modelling.* International Journal for Numerical Methods in Engineering, 2000. **48**(11): p. 1549-1570.

177. Zhu, Y., K.M. Liechti, and K. Ravi-Chandar, *Direct extraction of rate-dependent traction–separation laws for polyurea/steel interfaces.* International Journal of Solids and Structures, 2009. **46**(1): p. 31-51.

178. Shen, B. and G.H. Paulino, *Direct Extraction of Cohesive Fracture Properties from Digital Image Correlation: A Hybrid Inverse Technique.* Experimental Mechanics, 2011. **51**(2): p. 143-163.

179. Moosbrugger, C., *Atlas of stress–strain curves.* Materials Park, OH: ASM international, 2002.

180. de Groot, P.J., P.A.M. Wijnen, and R.B.F. Janssen, *Real-time frequency determination of acoustic emission for different fracture mechanisms in carbon/epoxy composites.* Composites Science and Technology, 1995. **55**(4): p. 405-412.

181. Sikorskha, J. and J. Pan, *The Effect of waveguide material and shape on AE transmission characteristics*

Part 2: Frequency and joint-time-frequency characteristics. Journal of Acoustic Emission, 2004. **22**: p. 274-287.

182. Khalifa, W.B., et al. *Analytical modelling of acoustic emission from buried or surface-breaking cracks under stress*. in *10th Anglo-French Physical Acoustics Conference, AFPAC 2011, January 19, 2011 - January 21, 2011*. 2012. Villa Clythia, Frejus, France: Institute of Physics Publishing.

183. Green, E.R., *Propagation of impact-induced stress waves in composite plates.* Journal of Nondestructive Evaluation, 1994. **13**(2): p. 45-54.

184. Giordano, M., L. Condelli, and L. Nicolais, *Acoustic emission wave propagation in a viscoelastic plate.* Composites Science and Technology, 1999. **59**: p. 1735-1743.

185. Aberg, M., *Numerical modeling of acoustic emission in laminated tensile test specimens.* International Journal of Solids and Structures, 2001. **38**(36-37): p. 6643-6663.

186. Sause, M.G.R. and S. Horn, *Simulation of Acoustic Emission in Planar Carbon Fiber Reinforced Plastic Specimens.* Journal of Nondestructive Evaluation, 2010. **29**(2): p. 123-142.

187. Döll, W., *Kinetics of crack tip craze zone before and during fracture.* Polymer Engineering & Science, 1984. **24**(10): p. 798-808.

188. Ernst, H., et al., *Analysis of load-displacement relationship to determine J-R curve and tearing instability material properties.* Fracture Mechanics, 1978: p. 581-599.

189. Gross, S.P., et al., *Acoustic emissions from rapidly moving cracks.* Physical review letters, 1993. **71**(19): p. 3162.

190. Sharon, E., S.P. Gross, and J. Fineberg, *Energy dissipation in dynamic fracture.* Physical review letters, 1996. **76**(12): p. 2117.

191. Hack, J.E., S.P. Chen, and D.J. Srolovitz, *A kinetic criterion for quasi-brittle fracture.* Acta Metallurgica, 1989. **37**(7): p. 1957-1970.

192. Muralidhara, S., R.B. Prasad, and R. Singh, *Analysis of acoustic emission data to estimate true fracture energy of plain concrete.* Current Science, 2013. **105**(9): p. 1213-1216.

193. Jungk, J., et al., *Indentation fracture toughness and acoustic energy release in tetrahedral amorphous carbon diamond-like thin films.* Acta materialia, 2006. **54**(15): p. 4043-4052.

194. Boler, F.M., *Measurements of radiated elastic wave energy from dynamic tensile cracks.* Journal of Geophysical Research: Solid Earth (1978–2012), 1990. **95**(B3): p. 2593-2607.

195. Bosia, F., et al., *Mesoscopic modeling of Acoustic Emission through an energetic approach.* International journal of solids and structures, 2008. **45**(22): p. 5856-5866.

196. King, R., G. Herrmann, and G.S. Kino, *Acoustic Nondestructive Evaluation of Energy Release Rates in Plane Cracked Solids.* 1981.

197. Sause, M., et al., *Quantification of failure mechanisms in mode-I loading of fiber reinforced plastics utilizing acoustic emission analysis.* Composites Science and Technology, 2012. **72**(2): p. 167-174.

198. Muravin, B., *Acoustic emission science and technology.* Journal of Building and Infrastructure Engineering of the Israeli Association of Engineers and Architects, 2009.

199. Rice, J. *An examination of the fracture mechanics energy balance from the point of view of continuum mechanics*. in *ICF1, Japan 1965*. 2012.

200. Hutchinson, J.W., *Singular behaviour at the end of a tensile crack in a hardening material.* Journal of the Mechanics and Physics of Solids, 1968. **16**(1): p. 13-31.

201. Rice, J. and G. Rosengren, *Plane strain deformation near a crack tip in a power-law hardening material.* Journal of the Mechanics and Physics of Solids, 1968. **16**(1): p. 1-12.

202. Griffith, A.A., *The phenomena of rupture and flow in solids.* Philosophical transactions of the royal society of london. Series A, containing papers of a mathematical or physical character, 1921: p. 163-198.

203. Cherepanov, G.P., *Crack propagation in continuous media: PMM vol. 31, no. 3, 1967, pp. 476–488.* Journal of Applied Mathematics and Mechanics, 1967. **31**(3): p. 503-512.

204. Li, F.Z., C.F. Shih, and A. Needleman, *A comparison of methods for calculating energy release rates.* Engineering Fracture Mechanics, 1985. **21**(2): p. 405-421.

205. Merkle, J. and H. Corten, *A J integral analysis for the compact specimen, considering axial force as well as bending effects.* Journal of Pressure Vessel Technology, 1974. **96**(4): p. 286-292.

206. Clarke, G. and J. Landes, *Evaluation of the J integral for the compact specimen.* Journal of Testing and Evaluation, 1979. **7**: p. 264-269.

207. Deng, M., *Cumulative second-harmonic generation of Lamb-mode propagation in a solid plate.* Journal of Applied Physics, 1999. **85**(6): p. 3051.

208. Hikata, A., B.B. Chick, and C. Elbaum, *Dislocation Contribution to the Second Harmonic Generation of Ultrasonic Waves.* Journal of Applied Physics, 1965. **36**(1): p. 229.

209. Kim, J.Y., et al., *Acoustic Nonlinearity Parameter Due to Microplasticity.* Journal of Nondestructive Evaluation, 2006. **25**(1): p. 28-36.

210. Pruell, C., et al., *A nonlinear-guided wave technique for evaluating plasticity-driven material damage in a metal plate.* NDT & E International, 2009. **42**(3): p. 199-203.

211. Pruell, C., et al., *Evaluation of fatigue damage using nonlinear guided waves.* Smart Materials and Structures, 2009. **18**(3): p. 035003.

212. Croxford, A.J., et al., *The use of non-collinear mixing for nonlinear ultrasonic detection of plasticity and fatigue.* J Acoust Soc Am, 2009. **126**(5): p. EL117-22.

213. Li, W., Y. Cho, and J.D. Achenbach, *Detection of thermal fatigue in composites by second harmonic Lamb waves.* Smart Materials and Structures, 2012. **21**(8): p. 085019.

214. Kim, J.-Y., et al., *Experimental characterization of fatigue damage in a nickel-base superalloy using nonlinear ultrasonic waves.* The Journal of the Acoustical Society of America, 2006. **120**(3): p. 1266.

215. Nucera, C. and F. Lanza di Scalea, *Nonlinear wave propagation in constrained solids subjected to thermal loads.* Journal of Sound and Vibration, 2014. **333**(2): p. 541-554.

216. Liu, Y., V.K. Chillara, and C.J. Lissenden, *On selection of primary modes for generation of strong internally resonant second harmonics in plate.* Journal of Sound and Vibration, 2013. **332**(19): p. 4517-4528.

217. Greenhalgh, E., et al., *The effects of defects on the performance of post buckled CFRP stringer-stiffened panels.* Composites Part A: applied science and manufacturing, 2003. **34**: p. 623-633.

218. Higgins, A., *Adhesive bonding of aircraft structures.* International Journal of Adhesion and Adhesives, 2000. **20**: p. 367-376.

219. Weller, T. and J. Singer, *Durability of stiffened composite panels under repeated buckling.* International Journal of Solids Structures, 1990. **26**(9): p. 1037-1069.

220. Vanniamparambil, P.A., et al., *An active–passive acoustics approach for bond-line condition monitoring in aerospace skin stiffener panels.* Aerospace Science and Technology, 2015. **43**(0): p. 289-300.

221. Matt, H., I. Bartoli, and F.L. di Scalea, *Ultrasonic guided wave monitoring of composite wing skin-to-spar bonded joints in aerospace structures.* The Journal of the Acoustical Society of America, 2005. **118**(4): p. 2240-2252.

222. Rudd, R.E. and J.Q. Broughton, *Concurrent Coupling of Length Scales in Solid State Systems.* physica status solidi (b), 2000. **217**(1): p. 251-291.

223. Yamakov, V., et al., *Multiscale modeling of sensory properties of Co–Ni–Al shape memory particles embedded in an Al metal matrix.* Journal of Materials Science, 2015: p. 1-13.

224. Saether, E., V. Yamakov, and E.H. Glaessgen, *An embedded statistical method for coupling molecular dynamics and finite element analyses.* International Journal for Numerical Methods in Engineering, 2009. **78**(11): p. 1292-1319.

225. Sause, M.G.R. and S. Horn, *AEWG 2010*. 2010.

226. Heidary, Z. and D. Ozevin, *On the Influences of Boundary Reflections and Piezoelectric Sensors to the Characteristics of Elastic Waves for Pattern Recognition Methods.* Journal of Nondestructive Evaluation, 2014. **34**(1): p. 1-10.

227. Yalcinkaya, H. and D. Ozevin, *The design and calibration of particular geometry piezoelectric acoustic emission transducer for leak detection and localization.* Measurement Science and Technology, 2013. **24**(9): p. 095103-095103.

228. Sause, M., *Identification of failure mechanisms in hybrid materials utilizing pattern recognition techniques applied to acoustic emission signals*. 2010: Mensch und Buch Verlag.

229. McLaskey, G. and S. Glaser, *Acoustic Emission Sensor Calibration for Absolute Source Measurements.* Journal of Nondestructive Evaluation, 2012. **31**(2): p. 157-168.

230. Jacobs, L.J. and C.A. Woolsey, *Transfer functions for acoustic emission transducers using laser interferometry.* The Journal of the Acoustical Society of America, 1993. **94**(6): p. 3506-3508.

231. Hochhalter, J.D., et al., *Coupling Damage-Sensing Particles to the Digitial Twin Concept*. 2014.

232. Saboonchi, H. and D. Ozevin, *In-Plane MEMS Acoustic Emission Sensors Development and Experimental Characterization*, in *MEMS and Nanotechnology, Volume 5*. 2014, Springer. p. 81-87.

233. Hsu, S.-Y. and R.-B. Cheng, *Modeling geometry and progressive interfacial damage in textile composites.* Journal of Composite Materials, 2012: p. 0021998312447207.

234. Sherburn, M., *Geometric and mechanical modelling of textiles*. 2007, University of Nottingham.

235. Wang, H.W., et al., *Application of extended finite element method in damage progress simulation of fiber reinforced composites.* Materials & Design, 2014. **55**(0): p. 191-196.

236. Kanouté, P., et al., *Multiscale Methods for Composites: A Review.* Archives of Computational Methods in Engineering, 2009. **16**(1): p. 31-75.

237. Liu, P.F. and J.Y. Zheng, *Recent developments on damage modeling and finite element analysis for composite laminates: A review.* Materials & Design, 2010. **31**(8): p. 3825-3834.

238. Orifici, A.C., I. Herszberg, and R.S. Thomson, *Review of methodologies for composite material modelling incorporating failure.* Composite Structures, 2008. **86**(1–3): p. 194-210.